The University of Nottingham

UNITED KINGDOM · CHINA · MALAYSIA

PERYLENE DERIVATIVES AND SILICON NANOSHEETS

Thesis submitted to the University of Nottingham for the Degree of Doctor of Philosophy

Sarah Louise Haddow, MSci

April 2017

Declaration

Except where specific reference is made to other sources, the work presented in this thesis is the original work of the author. It has not been submitted, in whole or in part, for any other degrees.

Signed: Sarah Louise Haddow

Date:

Abstract

The work presented in this thesis explores two different topics of interest, firstly a synthetic project fabricating small building blocks for supramolecular arrays. The building blocks are a series of perylene monoimide monoahydride (PMIA) compounds, synthesised by a four step process. The PMIA compounds belong to a family of dyes called the rylenes which are known in literature for their optical properties and use in optoelectronic devices. Chapter 2 begins with the description of the synthesis and characterisation of these molecules, where Hirshfeld surface analysis is used to investigate the solid state intermolecular forces between adjacent molecules. This is followed by the details of connecting two PMIA through organic linkers and it explores the structural and physical properties of the so called dimer. The physical properties investigated include, optical and electronic properties utilizing spectroelectrochemistry, cyclic voltammetry and electron paramagnetic resonance techniques. The chapter also explores the asymmetric feature of the building blocks with the aid of X-ray crystallography.

The second topic of interest is silicon nanosheets (SiNS). There are many types of these two dimensional (2D) materials published in literature, however one type which has had minimal attention is a buckled sheet structure known as layered polysilane. A synthetic and structural investigation into layered polysilane and closely related siloxene, are carried out in Chapter 3, identifying their bonding arrangement and topographic assembly through a range of analytical techniques. Like many other SiNS, it is proposed that this material can be used in nanotechnology devices in the future, and this thesis makes some way towards identifying the structure which is important in order to use them in such devices. Chapter 4 leads on to discuss the investigation into the modification of SiNS fabricated in Chapter 3, *via* a range of small organic molecules. This is another area in literature which has great

scope for investigation and exciting potential for use in nanodevices. An important difference once the SiNS have been functionalised with small organic groups is their enhanced solubility, in comparison to being insoluble before functionalisation. This opens up a wealth of applications which require solution phase activity. A range of surface analytical techniques aid in identification of functionalised sheets and Chapter 4 details the challenges and successes.

Acknowledgements

First and foremost I would like to thank my Heavenly Father for His unconditional love and for the daily reminder that I can do all things through Christ who strengthens me!

I would like to thank Professor Neil Champness for being a fantastic supervisor, for his constant encouragement, support and advice throughout my PhD. It has been a pleasure to work for him and I have learnt so much.

A special thanks to all of the specialist scientists at Nottingham University, for their expert knowledge; Dr Michael Fay for the countless hours he has put in to helping me with TEM amd SEM results, Dr Emily Smith for XPS results, the 'MALDI men', aka Dr Mick Cooper and Ben Point-Gleadhill for their support with MS and for their cheery faces, Dr Shaz Alsam and Kev Butler for NMR assistance, Prof. Jonathan McMaster for DFT calculations, Dr Stephen Davies for electrochemistry and lastly Prof. Andrei Khlobystov for advice.

A big thank you to all the post-docs in the groups, past and present; Dr Stephen Argent for hosting the BBQs, Dr Lixu Yang for her comedy, and Dr Connie Pfeiffer for being on TEAM GIRLS and beating the boys at monopoly deal. Obviously a big thank you to them for their help with science as well! Especially thank you to Connie for the help with crystallography.

A special thanks to my family. Their constant love and support has been quite simply over whelming throughout the course of my PhD. A special thanks to my Dad for handing me the tissues when required, my Mum for all the coffee and cake breaks, and to my three older brothers, James, Chris and Paul, for giving me 'tough love' to make me stronger! A special thanks to aunties and uncles, and cousins for general support and prayers. A special thanks to my sissy (in-law) Lucy, for her supportive messages, for taking so many selfies with me, and joining in my 'oh just one more'. Other people I should mention who have supported me include; David-Stretton-Downes for love and support when PhD morale was low, my church connect group for countless prayers/Thursday night fellowship and a big thank you to Boots Hockey club- true friendships made and a whole lot of good hockey played! Jess, Sophie, Kate, Helen, Kimmy, Jonty, Laura and the awesome 3s!

A special mention to all my besties for the continuous love and support especially when PhD times were tough; Bethany, Nat, Caz, Wilders, Abby, Nicola. You girls mean the world to me! Thanks to all my Uni gals for the BEST undergrad years in Nottingham; Bry, Bizzle, Len, Bel, Spannah, Hatti, Dooley, Becky, Pips, Jess, Holly. Thanks to Chantal and Luke for being my chemistry partners in crime during undergrad years and for the hard-core library sessions, and for sharing in my revision games!

A big big BIG thank you to all the wonderful people in B52; Nic for being the best B52 Lab dancing partner, Harry McDog for making me laugh, Sam for the great hugs, Charlie for teaching me how to love dogs, Tim for just being happy, Harry number 2 for the amusing Chemistry Summer party episode and Ben for taking me on in my master's year. Hawazan thank you for being you! Thanks to my awesome master students; Philllippp and Hena. Thanks to Jan for making me chuckle- sorry to admit it, but I still have absolutely no idea what you're doing! A special thank you to my fumehood 'Saz12'- you never let me down, you never laughed at me when I smashed one too many things in a day and you never had a leak!

List of Symbols and Abbreviations

α	Alpha
θ	Angle between incident ray and scattering plane
Å	Armstrong
°	Degrees
hv	Photon
π	Pi
λ	Wavelength
ø	Work function
1D	One-Dimensional
2D	Two-Dimensional
3D	Three-Dimensional
AFM	Atomic Force Microscopy
aq	Aqueous
ATR	Attenuated Total Reflectance
BSE	Back Scattered Electron
CIF	Crystallographic Information File
cm	Centimetre
CNT	Carbon Nanotubes
COSY	Homonuclear Correlation Spectroscopy
CV	Cyclic Voltammetry
CVD	Chemical Vapour Deposition
d	*d*-spacing
d	Doublet
DCTB	Trans-2-[3-(4-tert-butylphenyl)-2-methyl-2-propenylidene]malonitrile
DFT	Density Functional Theory
DNA	Deoxyribonucleic Acid
$E_{binding}$/BE	Binding Energy
EDG	Electron Donating Group
EDX	Energy Dispersive X-ray
EELS	Electron Energy Loss Spectroscopy
EI	Electron Ionization
$E_{kinetics}$	Kinetic Energy
eq	Equivalent
ESI	Electrospray Ionization
EWG	Electron Withdrawing Group
FD	Field Desorption
FT	Fourier Transform
g_{iso}	Isotropic *g*-factor
GoF	Goodness of Fit
HOMO	Highest Occupied Molecular Orbital
HR	High Resolution
HSQC	Heteronuclear Single Quantum Correlation
IR	Infrared
l	Longitudinal
LUMO	Lowest Unoccupied Molecular Orbital
m	Multiplet
m/z	Mass-to-charge ratio
MALDI	Matrix Assisted Laser Desorption Ionisation

MD	Molecular Dynamics
MS	Mass Spectrometry
n	Integer
nm	Nanometres
NMR	Nuclear Magnetic Resonance
OFET	Organic Field Effect Transistor
OTFT	Organic Thin Film Transistor
PDA	Perylene-3,4,9,10-tetracarboxylic Dianhydride
PDI	Perylene-3,4,9,10-tetracarboxylic Diimide
PET	Photoinduced Electron Transfer
PMIA	Perylene Monoimide Monoanhydride
PTFE	Polytetrafluoroethylene
q	Quartet
qd	Quartet of doublets
s	Singlet
SE	Secondary Electron
SEM	Scanning Electron Microscopy
SiNP	Silicon Nanoparticles
SiNR	Silicon Nanoribbons
SiNS	Silicon Nanosheets
SiNT	Silicon Nanotubes
SiNW	Silicon Nanowires
t	Transverse
t	Triplet
TEM	Transmission Electron Microscopy
TLC	Thin Layer Chromatography
TOF	Time Of Flight
UV	Ultraviolet
V	Voltage
vis	Visible
vs	Versus
XANES	X-ray Absorption Near Edge Structure
XPS	X-ray Photoelectron Spectroscopy
XRD	X-ray Diffraction

Table of Contents

Declaration i
Abstract ii
Acknowledgements iv
List of Symbols and Abbreviations vi
Table of Contents viii
Chapter 1 1
1.1 Supramolecular Building Blocks 2
1.1.1 Perylene Derivatives 3
1.1.2 Silicon Nanosheets 5
1.1.3 Functionalisation of Silicon Nanosheets 6
1.2 Aim and Objectives 7
1.3 Thesis Overview 8
1.4 References 9
Chapter 2 11
2.1 Introduction 12
2.1.1 Structure of Perylene Diimides (PDIs) 14
2.1.2 Physical Properties of PDI Derivatives 17
2.1.3 Asymmetric PDIs 21
2.1.4 Examples of PDI Supramolecular Arrays 22
2.2 Results and Discussion 25
2.2.1 Synthetic Methodologies toward Asymmetric PMIA 25
2.2.2 Dimerisation of Two PMIA Units 45
2.3 Conclusions 60
2.4 Experimental 62
2.4.1 Materials 62
2.4.2 General Equipment 62
2.4.3 Synthesis of Asymmetric Perylene Derivatives 68
2.4.4 Synthesis of Dimerised PDIs 75
2.5 References 78
Chapter 3 82
3.1 Introduction 83
3.1.1 Silicon Nanomaterials 83
3.1.2. Silicene: Type I 89
3.1.3. Buckled Silicon Nanosheets: Type II 93
3.1.4 History and Review of Layered Polysilane 96

3.1.5 Applications of Silicon Nanomaterials 100
3.2 Results and Discussion 102
3.2.4 Preparation of Siloxene and Layered Polysilane 102
3.2.5 Evidence for Silicon Nanosheets 106
3.3 Conclusions 133
3.4 Experimental 136
3.4.1 Materials 136
3.4.2 General Equipment 136
3.4.3 Synthesis of Siloxene 138
3.4.4 Synthesis of Layered Polysilane 138
3.5 References 139
Chapter 4 146
4.1 Introduction 147
4.1.1 Amine Modified Silicon Nanosheets 148
4.1.2 Phenyl Modified Silicon Nanosheets using a Grignard Reagent 150
4.1.3 Hexyl Modified Silicon Nanosheets using an alkene 155
4.1.4 Mechanochemical Lithiation of Silicon Nanosheets 157
4.1.5 Cross-Linking Silicon Nanosheets *via* Amines 159
4.1.6 Modifications of Silicon Nanosheets *via* Si-O Bond 160
4.2 Results and Discussion 162
4.2.1 Modification of Silicon Nanosheets using an Alkene 162
4.2.2 Functionalisation of Silicon Nanosheets *via* Amine Moieties 181
4.2.3 Functionalisation *via* Si-O Bonds in Silicon Nanosheets 199
4.3 Conclusions 206
4.4 Experimental 209
4.4.1 Materials 209
4.4.2 General Equipment 209
4.4.3 Synthesis of Functionalised Silicon Nanosheets 211
4.5 References 216
Chapter 5 218
5.1 Conclusion and Future Outlook 219
5.2 References 223
Appendix 224

Chapter 1

Introduction

1.1 Supramolecular Building Blocks

> "Supramolecular chemistry is the chemistry of the intermolecular bond, covering the structures and functions of the entities formed by the association of two or more chemical species."
>
> ~ J. M. Lehn[1]

The laboratory of Jean-Marie Lehn introduced the concept of supramolecular chemistry in 1988 which later was awarded a Nobel prize.[2] This quote by Jean-Marie Lehn describes supramolecular chemistry where non-covalent bonds such as electrostatic interactions, hydrogen bonding, π-π stacking, metal-ligand interactions, ion-dipole interactions, dipole-dipole interactions including van der Waals allows individual molecules to connect together in elaborate supramolecular arrays.[3] Bonding may vary from weak to strong and self-assembly strategies are employed for the supramolecular arrays to form.[4] The concept of self-assembly was developed by Whitesides in 1990 particularly focusing on nanoscale structures[5-7] and the self-assembly of functional bulk materials was later developed in 1993 by Stupp and co-workers.[8, 9] Since then supramolecular chemistry has enabled the development of such a large variety of sophisticated systems which are all dependent on the design of the molecular structure. Only last year were Jean-Pierre Sauvage, Fraser Stoddart and Bernard Feringa jointly awarded the 2016 Nobel Prize in Chemistry for their work on the design and synthesis of molecular machines which are recognised supramolecular arrays.[10-12]

Supramolecular structures can be fabricated through simple organic or inorganic molecules connected to each other to form two-dimensional (2D) or three-dimensional (3D) systems.

Importantly, it is the molecular structure which determines the supramolecular array. The properties of the molecule such as the size, symmetry and functional groups influence the systems fabricated. The molecules, often known as building blocks or subunits, can be tailored and designed to synthesise elaborate supramolecular arrays with specific chemical and physical properties if desired.

1.1.1 Perylene Derivatives

Perylene derivatives, such as perylene diimide (PDI) and perylene monoimide monoanhydride (PMIA) are interesting examples of supramolecular building blocks. The structure of these compounds enables them to be designed in different shapes and sizes, with different functional groups added for specific tailoring. This thesis details the synthesis and characterisation of a series of asymmetric PMIA suitable for application as supramolecular building blocks. A brief introduction is provided below, with a more informative and comprehensive review documented in the introduction to Chapter 2.

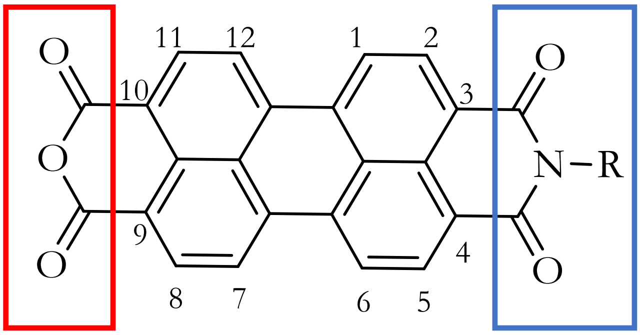

Figure 1.1 Asymmetric PMIA featuring an anhydride moiety (red box) and an imide moiety (blue box).

The general structure of the PMIA series synthesised in this thesis is shown in *Figure 1.1*. The structure consists of two naphthalene rings connected by single bonds, featuring two different functional groups at either end. The functional group highlighted in the red box is an anhydride moiety and the functional group highlighted in the blue box is an imide moiety (often called N-terminal position). The synthesis of this novel series of PMIAs involves a four step procedure with multiple purification steps. The characteristic polyaromatic perylene core, with five fused benzene rings allows for π-π stacking between adjacent molecules which makes them excellent candidates for the synthesis of supramolecular structures. Different functional groups at the N-terminal position (imide moiety) can be substituted, and depending on their size and conformational arrangement can disrupt the π-π interactions between adjacent molecules.[13] The strong ability of such polyaromatic molecules to stack can present a significant disadvantage in terms of low solubility or insolubility of such systems, sometimes presenting challenges when characterising the molecules using solution-based analytical techniques.

The molecules discussed so far (PDIs and PMIAs) belong to the rylene family of compounds, and asymmetric species such as PMIA have received less academic attention compared to symmetrical species such as symmetrical PDIs. PDIs in particular are known for their unique characteristics such as their strong and efficient fluorescence with up to 100 % quantum yields, high chemical and thermal stability, and intense absorbance in the UV-visible range. Over the last century many PDIs have been intensely studied and are now used in industrial applications including a range of optical and electronic devices.[14]

1.1.2 Silicon Nanosheets

In 2004, Novoselov and Geim reported the isolation of graphene, a 2D carbon nanosheet material.[15] The unique properties of graphene have enhanced research of the synthesis and characterisation of other 2D nanosheets. There is now a huge variety of nanosheets ranging from graphene to metal oxide and chalcogenide glasses,[16-19] and more recently carbon nitride nanosheets.[20] The properties observed in nanomaterials in comparison to their bulk analogues continues to draw attention from scientists. An important difference is the increase in surface area to volume ratio in nanomaterials, compared to their conventional forms, and this increases the reactivity and strength.[21] Nanosheets have a 2D structure and are characterised by having a thickness in the order of nanometres. They are expected to bridge the gap between one-dimensional (1D) structures and 3D bulk materials.[22]

Significant developments over the past few years have been focused on silicon nanosheets (SiNS) in particular. A full review of silicon nanomaterials is provided in Chapter 3, however a brief introduction is given here. There are many types of SiNS with each form falling into two categories, either; a) buckled SiNS or b) silicene. Briefly discussing the latter, silicene is a relatively new allotrope of silicon.[23, 24] It is viewed as a silicon version of graphene, where silicon layers obtain a sp^2-sp^3 hybridisation, and the structure's backbone is composed of six-membered rings of silicon joined together. Free-standing silicene has yet to be synthesised but rather the sheets are supported by a surface substrate, for example Ag(111).[25] This exciting material has potential for use in nanomaterial devices including thermoelectric devices, chemical sensors, hydrogen storage and electrode material for lithium batteries.[23]

The other category of SiNS, buckled SiNS, covers a wide range of materials, including structures which have other elements rather than just silicon present in the framework. This thesis concentrates on two particular types of SiNS namely layered polysilane and siloxene which belong to the buckled SiNS category and a full literature review is reported in the introduction to Chapter 3. The silicon backbone is terminated by either hydrogens or hydroxyl groups which protrude perpendicular to the plane of the sheets. The silicon atoms have sp^3 hybridisation allowing the sheets to feature a buckled arrangement. The unique physical and electronic properties make them promising candidates for a variety of applications in nanoscience and nanotechnology.[26]

1.1.3 Functionalisation of Silicon Nanosheets

Surface functionalisation of SiNS can be defined as the act of modifying the silicon surfaces by bringing physical, chemical or biological changes to the material. Recently, modifications of SiNS have been explored by the research group of Nakano and are described in the introduction to Chapter 4. Different methods to functionalise the sheets have been attempted by Nakano, including; amine functionalisation,[27, 28] the use of a Grignard reagent,[29] hydrosilyation,[30] and lithiation of sheets.[31] Modification of SiNS typically improves the stability and dispersion of the functionalised sheets in organic solvents. In addition, new characteristics are revealed and there is potential for application in devices such as Li-ion batteries, ultrathin semiconductors and energy conversion and storage devices.[31]

1.2 Aim and Objectives

The long-term goal of this project is to create PMIA functionalised SiNS systems. It has been reported in the literature that functionalised SiNS have the tendency to produce unique characteristics and can be used in nanoscale devices.[32] One example is the ability of phenyl-functionalised SiNS to produce a light-induced photocurrent giving scope for use in electronic devices.[29] This project was designed to research fundamental information which is required and will contribute to achieve the long-term goal. The key objectives involved:

i. Synthesis and the full characterisation of SiNS produced from calcium disilicide. The characterisation of the structure of these sheets are important for establishing the most suitable pathway to functionalise them. There are conflicting characterisation reports in the literature which will be repeated, in addition to new microscopy studies to aid in identification and understanding of these structures.

ii. Test reactions using small organic compounds (which represent perylene derivative molecules) to achieve a facile route for functionalisation of SiNS.

iii. Synthesis of asymmetric PMIA molecules ready for use in functionalisation of SiNS. Asymmetric PMIA derivatives are good candidates for functionalisation of SiNS since the N-terminus of the molecule can purposely be functionalised with an end group suitable for attachment to the nanosheets, while the other anhydride end of the PMIA can remain inactive towards the sheets. This will prevent cross-linking between the sheets, which would make analysis of structures more complex. Additionally the synthesis of PMIA molecules is required such that asymmetry functionalised PDIs can be prepared with appendages that can be attached to SiNS.

1.3 Thesis Overview

This thesis contains two parts. Firstly, Chapter 2 details the fabrication of a series of PMIA compounds, discussing the synthetic strategies and characterisation. Hirshfeld surface analysis was used to investigate the intermolecular forces between neighbouring molecules in crystal structures. A compound in the series was cross-linked with itself using different organic linkers to form larger molecular dimers. Optical and electronic properties were investigated for one of the dimers utilizing spectroelectrochemistry, cyclic voltammetry (CV) and electron paramagnetic resonance (EPR) techniques. The intention of synthesising the PMIAs was to attempt connecting them to the SiNS.

Secondly, the thesis focuses on the fabrication of SiNS. Chapter 3 investigates the synthesis and characterisation of SiNS. A range of methods were used to investigate the structure of the sheets including infrared (IR) spectroscopy and Raman spectroscopy. These interesting materials were probed using a variety of surface techniques including powder X-ray diffraction (XRD), X-ray photoelectron spectroscopy (XPS), scanning electron microscopy (SEM) and transmission electron microscopy (TEM).

Chapter 4 explores the functionalisation of the previously synthesised SiNS in Chapter 3. SiNS were modified using a range of small organic groups, such as alkenes, imidazole, amines and trioxysilanes, investigating the attachment of the organic groups to the sheets as well as the structure of the sheets.

Chapter 5 summaries the results presented in this thesis, evaluating the outcomes and revealing the scope for future work. The appendix at the end of the thesis details the theory of some of the characterisation techniques used.

1.4 References

1. J.-M. Lehn, in *Supramolecular Chemistry*, Wiley-VCH, Germany, 2006, pp. 1-9.
2. J.-M. Lehn, *Angew. Chem. Int. Ed.*, 1988, **27**, 89-112.
3. J.-M. Lehn, *PNAS*, 2002, **99**, 4763-4768.
4. J.-M. Lehn, *Science*, 2002, **295**, 2400-2403.
5. G. Whitesides, J. Mathias and C. Seto, *Science*, 1991, **254**, 1312-1319.
6. C. T. Seto and G. M. Whitesides, *J. Am. Chem. Soc.*, 1993, **115**, 905-916.
7. J. P. Mathias, E. E. Simanek, C. T. Seto and G. M. Whitesides, *Angew. Chem. Int. Ed.*, 1993, **32**, 1766-1769.
8. S. I. Stupp, S. Son, H. C. Lin and L. S. Li, *Science*, 1993, **259**, 59-63.
9. S. I. Stupp, V. LeBonheur, K. Walker, L. S. Li, K. E. Huggins, M. Keser and A. Amstutz, *Science*, 1997, **276**, 384-389.
10. J. F. Stoddart, *Nat. Chem.*, 2009, **1**, 14-15.
11. W. R. Browne and B. L. Feringa, *Nat. Nanotechnol.*, 2006, **1**, 25-35.
12. J.-P. Sauvage, *Acc. Chem. Res.*, 1998, **31**, 611-619.
13. S. Chen, P. Slattum, C. Wang and L. Zang, *Chem. Rev.*, 2015, **115**, 11967-11998.
14. F. Würthner, C. R. Saha-Möller, B. Fimmel, S. Ogi, P. Leowanawat and D. Schmidt, *Chem. Rev.*, 2016, **116**, 962-1052.
15. K. S. Novoselov, A. K. Geim, S. V. Morozov, D. Jiang, Y. Zhang, S. V. Dubonos, I. V. Grigorieva and A. A. Firsov, *Science*, 2004, **306**, 666-669.
16. C. N. R. Rao, H. S. S. Ramakrishna Matte and U. Maitra, *Angew. Chem. Int. Ed.*, 2013, **52**, 13162-13185.
17. H. S. S. R. Matte, B. Plowman, R. Datta and C. N. R. Rao, *Dalton Trans.*, 2011, **40**, 10322-10325.
18. A. Nag, K. Raidongia, K. P. S. S. Hembram, R. Datta, U. V. Waghmare and C. N. R. Rao, *ACS Nano.*, 2010, **4**, 1539-1544.
19. H. S. S. Ramakrishna Matte, A. Gomathi, A. K. Manna, D. J. Late, R. Datta, S. K. Pati and C. N. R. Rao, *Angew. Chem. Int. Ed.*, 2010, **49**, 4059-4062.
20. J. Zhang, Y. Chen and X. Wang, *Energy Environ. Sci.*, 2015, **8**, 3092-3108.
21. O. Manasreh, *Introduction to Nanomaterials and Devices*, Wiley, New Jersey, 2012.
22. R. Q. Zhang, *Growth Mechanisms and Novel Properties of Silicon Nanostructures from Quantum-Mechanical Calculations*, Springer Berlin Heidelberg, 2013.
23. J. Zhao, H. Liu, Z. Yu, R. Quhe, S. Zhou, Y. Wang, C. C. Liu, H. Zhong, N. Han, J. Lu, Y. Yao and K. Wu, *Prog. Mater. Sci.*, 2016, **83**, 24-151.
24. M. J. S. Spencer and T. Morishita, *Silicene: Structure, Properties and Applications*, Springer International Publishing, Switzerland, 2016.

25. P. Vogt, P. De Padova, C. Quaresima, J. Avila, E. Frantzeskakis, M. C. Asensio, A. Resta, B. Ealet and G. Le Lay, *Phys. Rev. Lett.*, 2012, **108**, 155501.
26. H. Nakano and T. Ikuno, *Appl. Phys. Rev. 3*, 2016, **3**, 040803.
27. H. Okamoto, Y. Kumai, Y. Sugiyama, T. Mitsuoka, K. Nakanishi, T. Ohta, H. Nozaki, S. Yamaguchi, S. Shirai and H. Nakano, *J. Am. Chem. Soc.* , 2010, **132**, 2710-2718.
28. H. Okamoto, Y. Sugiyama, K. Nakanishi, T. Ohta, T. Mitsuoka and H. Nakano, *Chem. Mater.*, 2015, **27**, 1292-1298.
29. Y. Sugiyama, H. Okamoto, T. Mitsuoka, T. Morikawa, K. Nakanishi, T. Ohta and H. Nakano, *J. Am. Chem. Soc.*, 2010, **132**, 5946-5947.
30. H. Nakano, M. Nakano, K. Nakanishi, D. Tanaka, Y. Sugiyama, T. Ikuno, H. Okamoto and T. Ohta, *J. Am. Chem. Soc.*, 2012, **134**, 5452-5455.
31. M. Ohashi, H. Nakano, T. Morishita, M. J. S. Spencer, Y. Ikemoto, C. Yogi and T. Ohta, *Chem. Commun.*, 2014, **50**, 9761-9764.
32. H. Okamoto, Y. Sugiyama and H. Nakano, *Chem. - Eur. J.*, 2011, **17**, 9864-9887.

Chapter 2

Synthesis of Building Blocks for Supramolecular Structures

2.1 Introduction

Perylenes are an interesting class of colourants, featuring a polycyclic aromatic hydrocarbon core shown in *Figure 2.2a.* Colourants are characterised by their capability to absorb or emit light in the visible range of the electromagnetic spectrum, with wavelengths within 400-700 nm. Becoming apparent in the 19th century, colourants have played an important role in many industries, with over *ca.* 15,000 colourants produced on a manufacturing scale in the last 150 years.[1] The particular colourants researched in this thesis belong to the rylene family, which are a group of organic dyes and pigments once used for colouring textiles and are now of great interest to materials and supramolecular chemists. *Figure 2.2* shows a range of rylene derivatives which have attractive features such as, tuneability of colours and solubility, resistance to weather, chemical robustness and heat stability.[2]

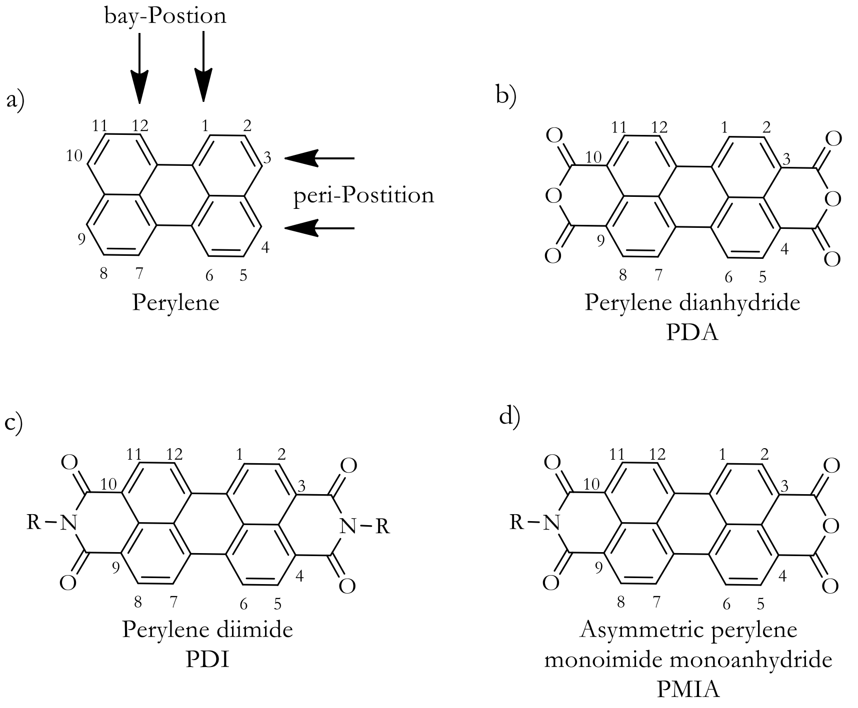

a) Perylene

b) Perylene dianhydride
PDA

c) Perylene diimide
PDI

d) Asymmetric perylene
monoimide monoanhydride
PMIA

Figure 2.2 The numbering system for structures of a) perylene, b) PDA, c) PDI and d) PMIA.

Perylene-3,4:9,10-tetracarboxylic dianhydride (PDA) (*Figure 2.2b)* can be considered as the parent compound for this family of dyes, often used as the starting material for synthesis of perylene derivatives.[3] PDA consists of two anhydride moieties at either end of the perylene core, with four carboxylic groups giving a planar rectangular structure belonging to the D_{2h} point group.[4] The structure and morphology of PDA has been well studied, however insolubility in typical organic solvents has limited its utility.[5, 6]

In the rylene diimide series, the most intensely studied dyes are perylene-3,4:9,10-tetracarboxylic diimide (PDI) (*Figure 2.2c*), and the first was reported in 1913 by a German chemist named Kardos.[7] PDIs consist of two imide functional groups at either end of the molecule, commonly known as the N-terminal positions.[8] PDIs are broadly used as dyes and pigments due to their outstanding photochemical properties, such as high absorption in the visible to near IR-region and their ability to fluoresce with quantum yields near unity.[9, 10] Optical applications include fluorescence solar collectors,[11] electrophotographic devices,[12] light-emitting diodes,[13] photovoltaic devices[14, 15] and dye lasers.[16-18] Moreover, many PDI derivatives are favourable for the construction of electronic devices[19] due to their electron mobilities (2.10 $cm^2V^{-1}s^{-1}$).[19-21] PDIs are used in the active layer of n-type semiconductors for applications in organic thin film transistors (OTFTs)[19, 22, 23] and organic field-effect transistors (OFETs).[24]

The interesting properties of PDIs have led to research into asymmetric PDIs and perylene monoimide monoanhydrides (PMIAs). There are two types of asymmetric perylene cores; the first feature different functional groups at the bay positions on the perylene core[25] and the second feature different functional groups at the peri positions on the perylene core (*Figure 2.2d*). Asymmetric PDIs/PMIAs can be intentionally designed for synthesis of specific supramolecular systems. An example of this is by Liu *et al.* who synthesised an asymmetrical PDI to form a nanocoiled assembly with promising applications in optoelectronics, fluorescent sensors and biological imaging.[26] Asymmetric PDI and PMIA are further discussed in Section 2.1.3.

2.1.1 Structure of Perylene Diimides (PDIs)

PDIs consist of a planar aromatic core of five fused rings.[27] There are 12 functionalisable positions on the core, four peri- (3, 4, 9, 10), four bay (1, 6, 7, 12) and four ortho- (2, 5, 8, 11) positions.[7] The framework consists of two naphthalene half units joined together by two carbon-carbon single bonds shown by X-ray diffraction studies displayed in *Figure 2.3.*[27-30] The single bond character connecting the two units has been suggested due to a longer bond length of 1.46 Å in comparison to the delocalised carbon-carbon bonds within the naphthalene units, which have a shorter average bond of 1.40 Å.[30] The single bond character can allow twisting of the perylene core, as illustrated in *Figure 2.4a.*

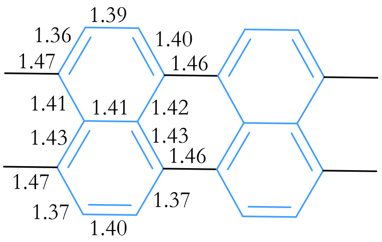

Figure 2.3 Selected bond lengths of the perylene core in the solid state.[30]

The most noticeable feature in solid state is the stacking of the molecules due to π-π interactions where the molecules form stacks parallel to the molecular plane. The planarity of these molecules facilitates aromatic interactions, and an offset of one molecule to an adjacent occurs as illustrated in *Figure 2.4*. Moreover, the planar structure increases the packing density and therefore the van der Waals interactions. An interplanar distance of approximately 3.5 Å is commonly observed between the PDI molecules,[31, 32] which is comparable to the interplanar distance between layers of graphene in graphite at 3.337 Å.[33]

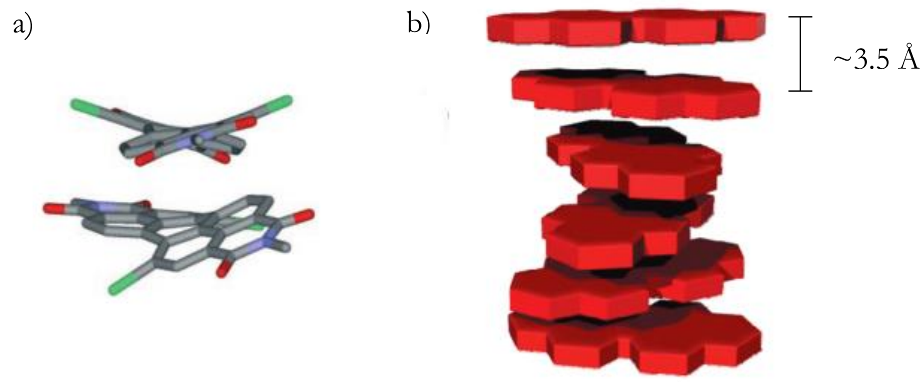

Figure 2.4 Two views of PDI molecules showing a) twist in the aromatic core[34] *and b) an illustration of π-π stacking between PDI molecules with an interplanar distance of ~3.5 Å.*[35]

The properties of PDIs previously discussed, are readily tuneable by functionalisation at two distinct locations; the bay- and N-terminal positions. Functionalisation allows tailoring of the molecule for specific uses, and differentiates the interplanar *d*-spacing from ~3.5 Å for different PDI derivatives. Different substituents on the PDI molecule can lead to dramatic changes in the colour of these dyes due to the aggregation effect in which the PDI stack.[31]

2.1.1.1 *Functionalisation at the Bay Region*

Facile synthetic routes have been reported for core functionalisation. The first introduction to this concept was by Seybold *et al.* in 1989, where the core positions on the PDI were chlorinated with sulfuryl chloride in nitrobenzene.[11] With the use of X-ray crystallography, a distortion in the structure was reported because of a twist between the two halves of the perylene backbone.

2.1.1.2 Terminal Group Effects

Functionalisation at the N-terminal position of the PDI opens up a facile route to tune solubility.[7] Imidization is typically performed where a condensation reaction between PDA and a specific amine occurs, to afford the desired derivative.[36] The first major imidization approach was reported in the 1990s by Langhals and co-workers.[37] 'Swallow-tail' hydrocarbon imide groups were added to PDA, in different media depending on the amine, the likes of water or benzene for reactive primary aliphatic amines, and imidazole for less reactive amines.[37] Depending on the size of the N-substituent, different degrees of transverse (*t*) and longitudinal (*l*) displacement of a PDI unit relative to another PDI unit can occur (*Figure 2.5*). The coordinates *t* and *l* describe the displacement of a given atom in a PDI molecule, relative to the corresponding atom in the preceding molecule. These measurements were used in a study by Graser *et al.* to describe the relationship of the crystal colour with the bathochromic shift in regard to the π-π contact area between the stacked molecules within a crystal lattice.[28, 29, 38] For smaller transverse shifts such as those seen in *Figure 2.5b*, a greater bathochromic shift is seen and darker maroon coloured pigments are observed. However, PDIs which have larger transverse shifts, such as those seen in *Figure 2.5a,* red shades are exhibited. Often, PDIs with a greater longitudinal displacement (such as *Figure 2.5c*) have increased coupling between adjacent molecules, exhibiting stronger electronic interactions between neighbouring π-systems and consequently are often black dyes.[30] The extent of the transverse and longitudinal shifts can be controlled by the choice of N-terminal groups. Packing interactions can be engineered to alter the pigment properties and crystallochromy of the PDI molecule.

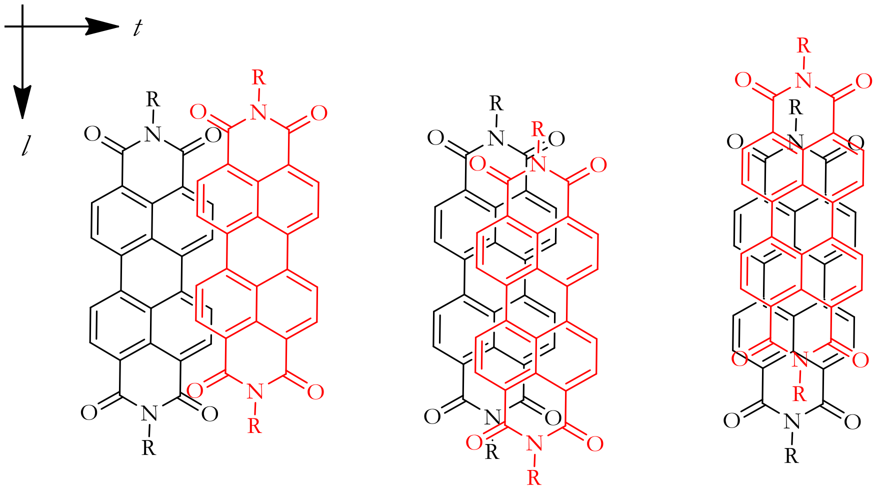

R = Azobenzene
a)

R = p-CH_3OPhCH_2
b)

R = Me
c)

Figure 2.5 Transverse (t) and longitudinal (l) displacement of stacked π-systems in a variety of PDIs with different N-terminal groups.[30]

2.1.2 Physical Properties of PDI Derivatives

2.1.2.1 Optical Properties

An attractive feature of PDIs is their absorption and emission properties and they can be regarded as a closed chromophoric system. The most common approach for investigation into such properties is with UV-vis and fluorescence spectroscopy and example spectra are shown in *Figure 2.6*.[36] The major feature observed in an absorption spectrum of a PDI is a broad $S_0 \rightarrow S_1$ absorption band in the visible region, which displays vibrational structure.[36] Emission profiles of PDIs are usually mirror images of the corresponding absorption band as displayed in *Figure 2.6* (dashed line) and high quantum yields (of up to 100 %) are common.[39] The nature of different bay substitutions have an influence on absorption and emission spectra, compared to different imide substitutions which cause little change to the spectra. For example, the bands usually display less vibronic structure and are broader due to the loss of planarity and symmetry of the perylene core upon substitution with large bay groups.[36]

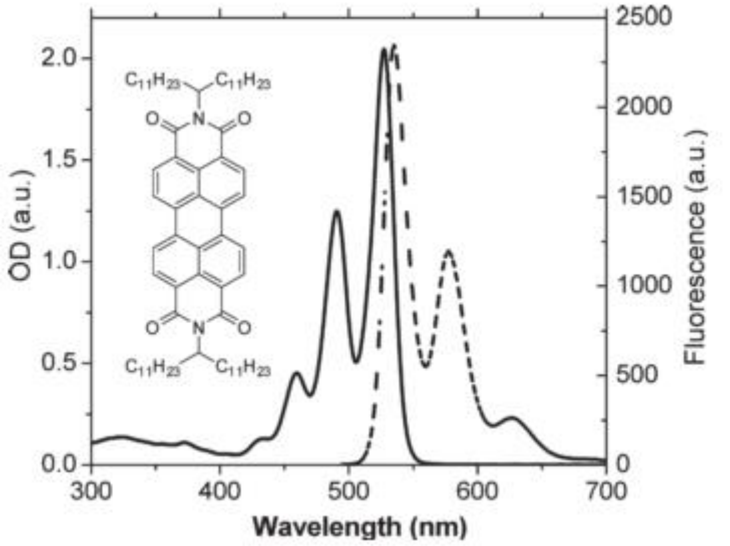

Figure 2.6 UV-vis absorption (solid line) and fluorescence spectrum (dashed line) of a perylene diimide derivative in toluene.[36]

The DFT (density functional theory) is a computational quantum mechanical modelling method often used to calculate the LUMO and HOMO energies.[40] DFT-calculated HOMO and LUMO of a typical PDI are shown in *Figure 2.7*.[36] The first key feature to observe is the symmetry along the molecular (N-N) axis, with nodes present in both the HOMO and LUMO. Thus, functionalisation at the imide position has negligible effects on the absorption and emission wavelength because effects are minimal for both the LUMO and the HOMO resulting in little change to the π-system.[41]

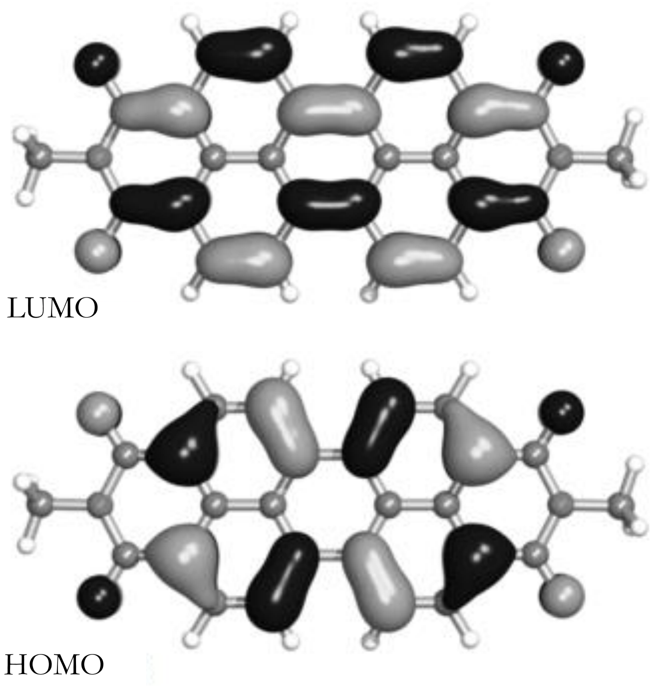

Figure 2.7 DFT calculations of a) LUMO and b) HOMO of a simple PDI. (Light and dark shading correspond to positive and negative phases of the wave function respectively).[36]

There are significant HOMO and LUMO contributions in the bay area causing absorption and emission peaks to shift when different bay substituents are incorporated into the molecule. In general, electron donating groups (EDGs) such as nitro- or oxy- destabilize the HOMO and electron withdrawing groups (EWGs) such as cyano- bromo-, with less effect, destabilize the LUMO. Both these effects lead to bathochromic shifts in the absorption spectrum.[36] In certain cases, the effect of core twisting in the PDI due to steric properties can lead to hypsochromic shifts.[36]

2.1.2.2 Redox Properties

In general, PDIs have a low lying LUMO and are fairly electron-deficient making them easily reducible but hard to oxidise.[30] Cyclic voltammetry (CV) is a useful method for measuring electrochemical behaviour and determining HOMO and LUMO energy levels.[42] For most perylene derivatives, two reversible one-electron reduction potentials are detected without any oxidations (*Figure 2.8).*

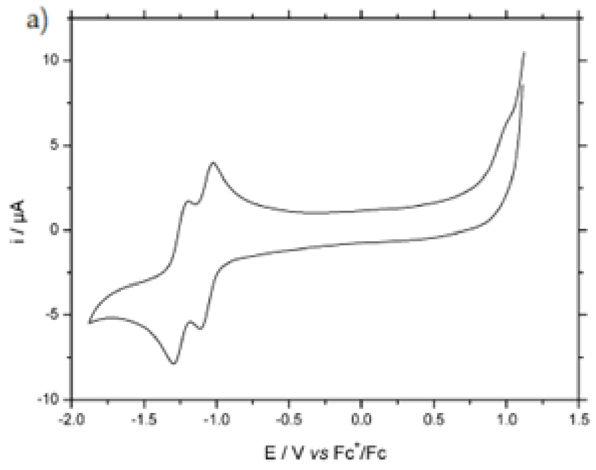

Figure 2.8 A typical cyclic voltammogram for PDI showing two reversible reduction potentials. Obtained from PDI (10^{-3} M) in DCM containing Bu_4NPF_6 (0.1 M), measured with a scan rate of 100 mVs^{-1}.[42]

Different substituents at the N-terminal position have similar redox properties due to the nodes present in the frontier orbitals. Redox properties are affected by the functional groups in the bay region, where substitution with redox active groups can add extra reductive or oxidative waves. Generally, PDIs with strong EDGs (such as phenoxy-) at the bay positions lowers the reduction potentials (*i.e.* become more negative) and are less readily reduced, which is comparative to EWGs (such as chloro or cyano groups) which increase the reduction potentials causing easier reductions.

2.1.3 Asymmetric PDIs

Asymmetric PDIs can be used in complicated molecular engineering of organic functional systems. Examples include use in; optoelectronic devices,[43] fluorescent sensors,[44-46] photoinduced electron transfer (PET) devices[47-50] and as side chains in polymer architectures.[51, 52] Asymmetric PDIs can have different functional groups at the peri-position. Synthetic strategies to install different peri-position substitution groups in an asymmetric fashion have been discovered and are briefly detailed below:

a. The simultaneous condensation of PDA with two different amines of similar reactivity in stoichiometric equivalents, however undesired symmetrical PDIs form and are difficult to isolate.[53]
b. Nagao *et al.* prepared asymmetric PDIs *via* a two-step procedure involving condensation with an amine at one end of the PDA, followed by condensation with a different amine at the other terminal end of the molecule. This approach is often unsuccessful because of the difference in reactivity of the amines with the PDA.[54]
c. Coupling between two 1,8-napthalic imides (two half units of PDI) *via* a palladium-catalysed Suzuki reaction where the two units have different N-terminal groups.[55]
d. Langhals *et al.* prepared a symmetrical PDI and removed one of the imides with KOH in *tert*-butyl alcohol to make an asymmetric PMIA.[56] Other research groups have also used similar methods.[57]
e. Synthesis of perylene diester monoimides *via* condensation of a perylene monoanhydride diester.[43] This was first introduced by Xue and utilizes a symmetrical tetraester species.

Asymmetric PDIs can also be synthesised *via* different substitutions in the conjugated aromatic core which fine-tunes the optoelectronic properties.[58] The most common examples found in the literature are asymmetric 1,7-disubstitued PDIs with a variety of functional groups attached.[25, 49, 59, 60]

2.1.4 Examples of PDI Supramolecular Arrays

Supramolecular Chemistry, described by Jean-Marie Lehn as 'Chemistry beyond the molecule'[61] is a concept suggesting complexity can be controlled by the power of intermolecular forces.[62] Intricate architectures are designed by tailoring these non-covalent forces. PDIs are perfect examples of building blocks for supramolecular arrays and a comprehensive review has been reported by Wüthner and co-workers.[63] Importantly, molecular structure determines the features of the supramolecular array, and changing the substituents on the perylene core and N-terminal position will vary the structural growth and intermolecular interactions.

A common theme in PDI supramolecular structures are intermolecular π-π interactions between neighbouring molecules. An intriguing example in the literature is the incorporation of PDI molecules into DNA illustrated in *Figure 2.9*.[64, 65] It is the π-π interactions between the perylene core and the DNA bases which stabilise the structure, along with the hydrogen interactions between one PDI imide terminus and thymine bases in the DNA strands (*Figure 2.9b*). Molecular modelling studies show six PDI units are arranged in a zipper-like stacking mode (*Figure 2.9c*), and the DNA acts as a scaffold for the structure. Evidence of PDI-PDI interactions is seen in UV-vis absorption and fluorescence spectral features.

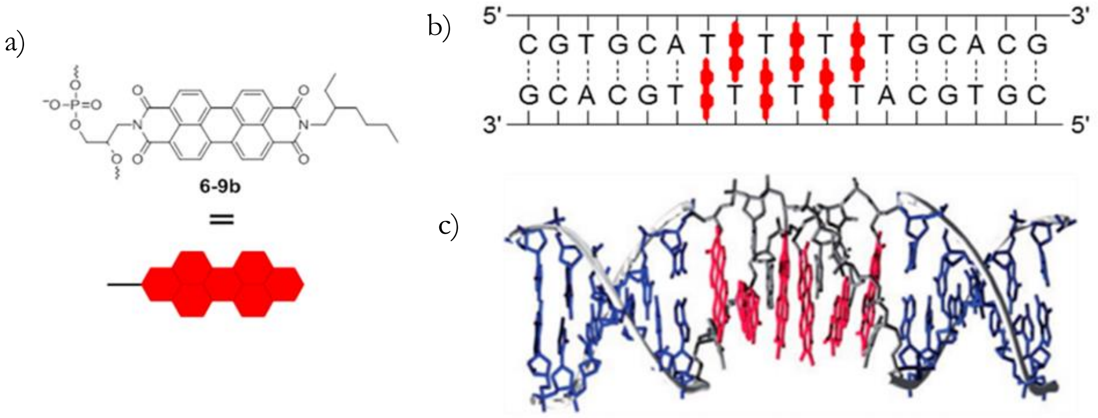

Figure 2.9 a) PDI unit, b) duplex DNA strand with six PDI units incorporated and c) calculated energy-minimised structure of duplex DNA-PDI complex.[64, 65]

Self-assembled metallosupramolecular boxes using PDIs were published in 2010 by Indelli *et al.*[66] Unique PDI derivatives were co-ordinated to zinc ion centres in ruthenium-bridged porphyrins shown in *Figure 2.10*.

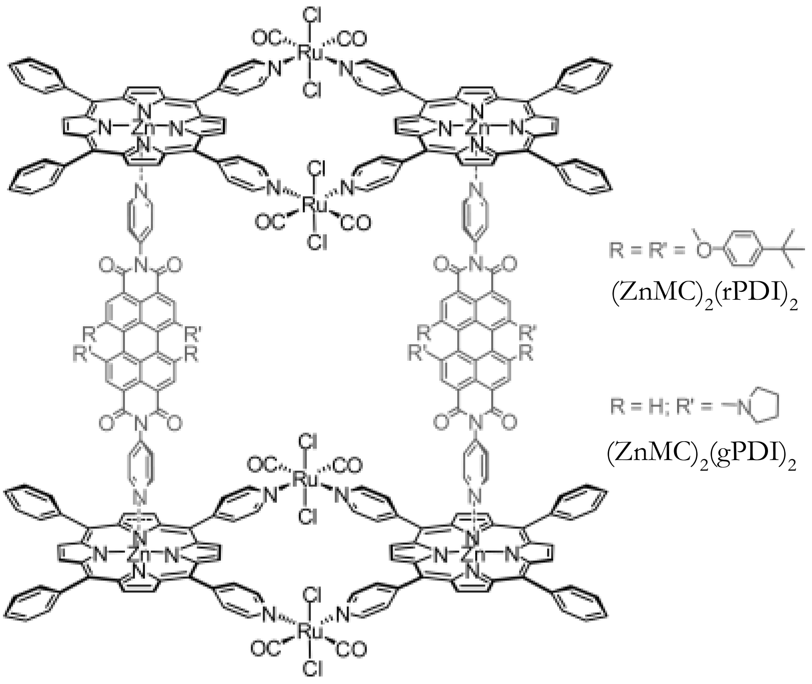

Figure 2.10 Metallosupramolecular boxes with ruthenium-bridged zinc porphyrins coordinated to PDI units.[66]

Generally, the coordination of pyridine ligands to zinc porphyrins are intrinsically weak, however due to four pyridine-zinc bonds present in the structure the supramolecular box is remarkably stable. The PDIs act as pillars for the box, and two different PDI derivatives have been probed with either phenoxy- (rPDI) or pyrrolidino- (gPDI) bay functionalised groups. The g(PDI) has an almost perfect rectangular scaffold, compared to the r(PDI) box which has a highly distorted twisted structure. The two PDI units in the r(PDI) box are at a very short distance of 3.9 Å in a co-facial π stacking arrangement.[66]

Numerous assemblies of water soluble PDIs have been published since the 1980s, with the biggest challenge being the dye's tendency to aggregate in aqueous solutions causing insolubility.[67] The introduction of polar, water soluble (hydrophilic) sites on the PDI molecules is crucial for water solubility, and this can occur at the bay or N-terminal positions. Water is a suitable aqueous medium for PDIs to portray a supramolecular π-system amongst the molecules themselves or with other π-systems present. An example that stands out is the interaction of water soluble PDI units with carbon nanostructures such as graphene,[68] and carbon nanotubes (*Figure 2.11*).[69, 70]

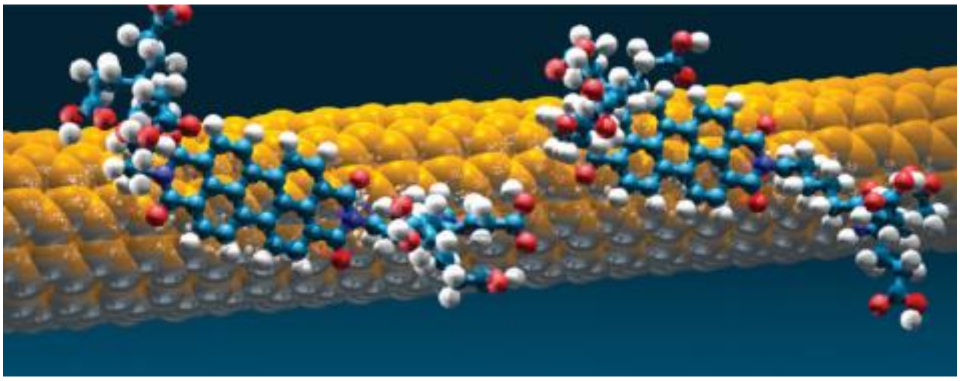

Figure 2.11 Schematic illustration of the interactions of PDIs and carbon nanotubes.[70]

2.2 Results and Discussion

2.2.1 Synthetic Methodologies toward Asymmetric PMIA

In this section, the synthesis of a series of novel asymmetric PMIAs are detailed and discussed and a variety of characterisation techniques used for confirmation of synthesis. All compounds are characterised by mass spectrometry (MS), often using a softer ionisation technique called matrix-assisted laser desorption/ionisation (MALDI). This technique uses a matrix compound which absorbs the laser's energy which is used to ionise the analyte molecules. Other MS techniques used include field desorption (FD) and field ionisation (FI). Compounds which are soluble are characterised by nuclear magnetic resonance (NMR) and crystallographic evidence is reported for some structures.

*2.2.1.1 Synthesis of a Simple Tetraester, **1***

The first synthetic step starts with commercially available PDA. The targeted intermediate is a symmetrically tetrasubstituted perylene **1**, synthesised using an approach first reported by Chen and co-workers.[71] The reaction (*Scheme 2.1*) proceeds *via* the use of a strong base, KOH, opening up the two anhydrides in the PDA forming a tetrapotassium salt which dissolves in water. A phase transfer catalyst, aliquat-336, facilitates the migration of the perylene tetracarboxylic anions into the organic phase, where a nuclear displacement reaction with 1-bromodecane can occur. The ammonium cations from aliquat-336 dissociate and replace the potassium cations co-ordinated with the perylene tetracarboxylic anions to allow this to happen.

Scheme 2.1 Synthesis of symmetrical tetraester perylene.

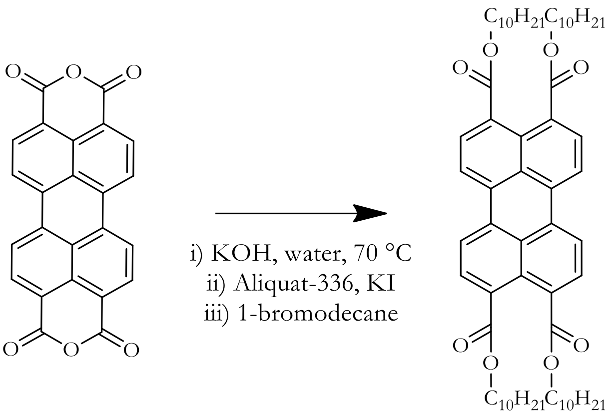

PDA

1

1-bromodecane was the chosen reactant, using bromine as an excellent leaving group, and decyl chains which are long and flexible increasing solubility in organic solvents. The bulky decyl aliphatic chains reduce π-π aggregation, minimising the stacking of the perylene molecules giving a fully soluble product. The product was extracted with chloroform, and washed with an aqueous solution of sodium chloride followed by precipitation with methanol to yield the tetraester product **1** in a solid state as a deep orange colour. This reaction was completed multiple times with an average yield of 61 %. The ^{1}H NMR spectrum of **1** in deuterated chloroform is shown in *Figure 2.12*, and the regions relating to the aromatic core protons, the CH_2 adjacent to the ester functional group and protons in the alkyl chain have been labelled. A further confirmation of **1** is seen by MALDI-TOF in which a peak at m/z 988.63 is seen which is the expected mass of **1**$^-$.

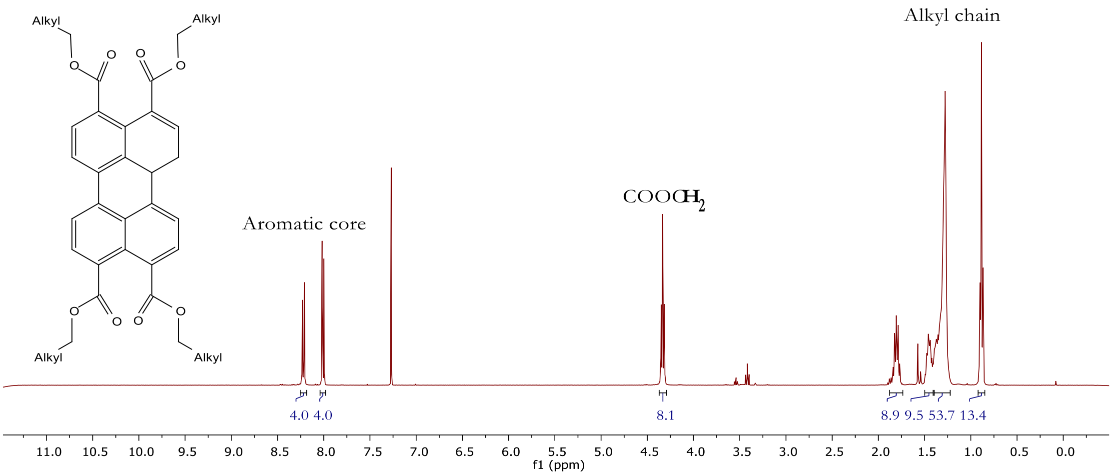

Figure 2.12 ^{1}H NMR of tetraester species ***1*** *in chloroform-d. Integration for each signal is given below the respective spectra.*

2.2.1.2 Synthesis of a Perylene Diester Monoanhydride, ***2***

The formation of **2** utilises an acid catalysed hydrolysis outlined in *Scheme 2.2,* an approach taken from Xue.[43] The reaction is reversible and chosen as it has an esterification hydrolysis equilibrium. If the initial bond cleavage in **1** does not occur in the 'correct' position *i.e. route b* is taken, product **2** would not form. The equilibrium can '*right*' itself so that two esters at the same end of the molecule (*route a*) are hydrolysed. When *route a* is undertaken at a high temperature, a fast cyclisation occurs between two adjacent carbonyl groups giving the six-membered anhydride ring of **2**. It is then removed from the equilibrium because the anhydride species is only sparingly soluble in the reaction solvent system *n*-dodecane : toluene (5 : 1) and therefore precipitates after formation.

*Scheme 2.2 Hydrolysis of perylene tetraester **1**, showing the two routes possible in the reaction equilibrium. Only route a leads to the formation of **2**.*

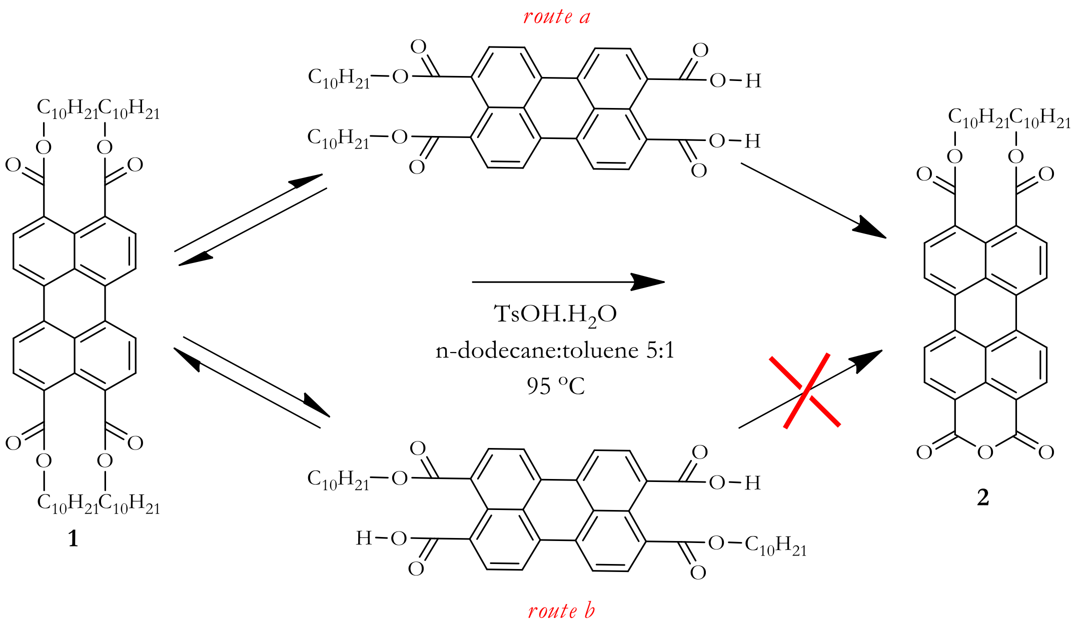

One equivalent of *p*-toluenesulphonic acid monohydrate acts as the acid catalyst and water source for hydrolysis and reacts with a high concentration of **1** at 95 °C for 5 hours producing a red, sticky, crude product. Thin layer chromatography (TLC) (silica, chloroform:acetone [9:1]) displayed two distinct spots, a yellow spot with Rf of 0.8 (**1**, tetraester species) and a red spot with Rf of 0.3 (**2**, diester product). The crude product was purified *via* silica gel column chromatography using a wet loading technique. The yellow unreacted starting material was isolated first, followed by a streaked red band. During the course of this column, the initial mobile phase was chloroform and polarity was increased by the addition of acetone to ~5 %.

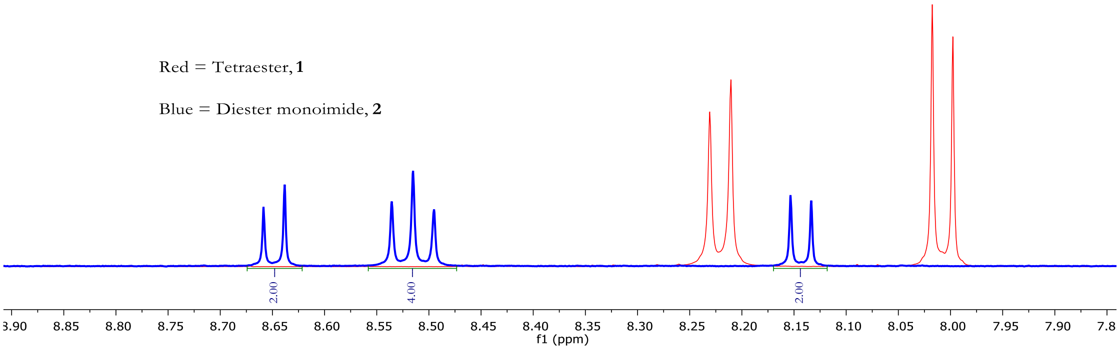

*Figure 2.13 ¹H NMR spectra comparing the aromatic region of **1** (red) and **2** (blue) in chloroform-d. Integration for each signal is given below the respective spectra.*

Species **2**, diester monoanhydride, is intrinsically unsymmetrical and its identity was confirmed by ^{1}H NMR. A clear difference in the peaks resulting from the aromatic hydrogen atoms between **1** and **2** are shown in *Figure 2.13*. **2** has four resonances, including two doublets at 8.15 and 8.65 ppm and two doublets which overlap to appear as a triplet at 8.53 ppm. This can be compared to **1** which has only two resonances of two doublets at 8.00 and 8.22 ppm. Other confirmations of synthesis include ^{13}C NMR, HRMS and IR.

*2.2.1.3 Synthesis of Perylene Diester Monoimides **3***

The next step in the synthesis involved the introduction of imide functionality. **2** was condensed with four different alkyl amines including; n-butylamine **a**, 3-aminopentane **b**, cyclohexylamine **c** and bis(diphenylmethyl)-4-methylphenyl amine **d**. The reactivity difference between the two different functional groups at either end of perylene species **2** allows a nucleophile, such as amines **a** to **d** to selectively attack the anhydride rather than the esters. The general procedure involved an inert atmosphere, with one equivalent of **2** and 2-4 equivalents of the amine, molten imidazole as the solvent, a temperature of 130 °C and approximately 18 hours of reaction time. The reaction mixture was extracted into chloroform, washed with deionised water to remove the imidazole solvent, and subsequently dried over anhydrous magnesium sulphate. These perylene species were highly soluble in most organic solvents, e.g. chloroform, dichloromethane, acetone, THF, toluene and others. After each reaction, multiple chromatographic steps were necessary to remove impurities formed in the reaction. The eluent usually started as 100 % chloroform and acetone was added accordingly (usually up to 3 %) to increase the polarity and movement of product through the column.

Scheme 2.3 Synthesis of asymmetric diester monoimide using four different amines.

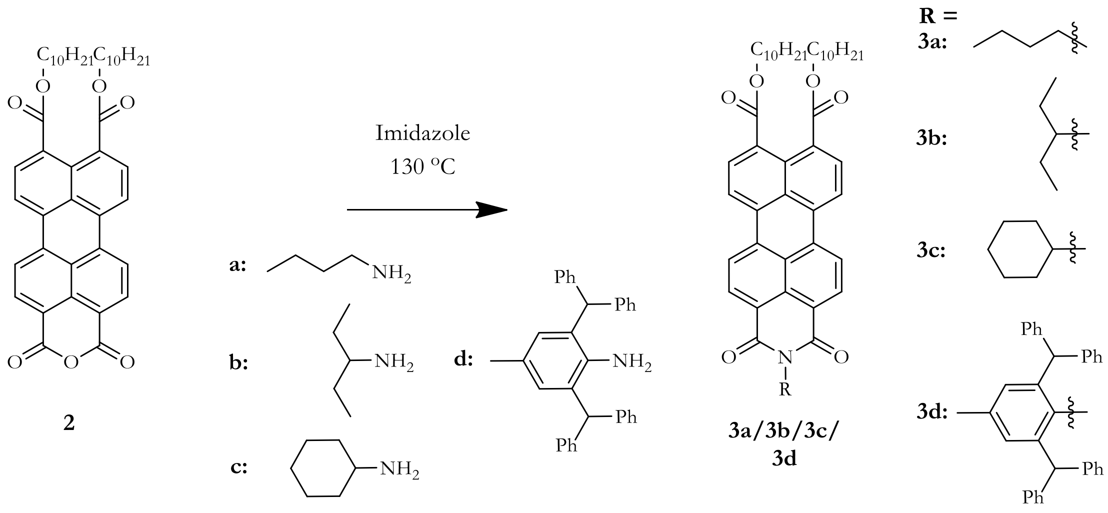

Satisfactory yields of 66, 41, 87 and 28 % were obtained for **3a**, **3b**, **3c** and **3d** respectively. **3d** produced the lowest yield which is most likely due to the size of the N-terminal group having steric effects, consequently limiting the rate of reaction. Additionally, **3d** was synthesised from an aniline, compared to **3a** to **c** which were synthesised from more nucleophilic alkyl amines. Characterisation using ^{1}H NMR (*Figure 2.14*), ^{13}C NMR, HRMS and IR provided evidence for products. The ^{1}H NMRs shown in *Figure 2.14* of the perylene diester monoimide species display the aromatic hydrogens in the downfield region, presenting four resonances for the protons on the aromatic core. In **3a**, **3b** and **3d**, two resonances overlap and in **3c** three resonances overlap.

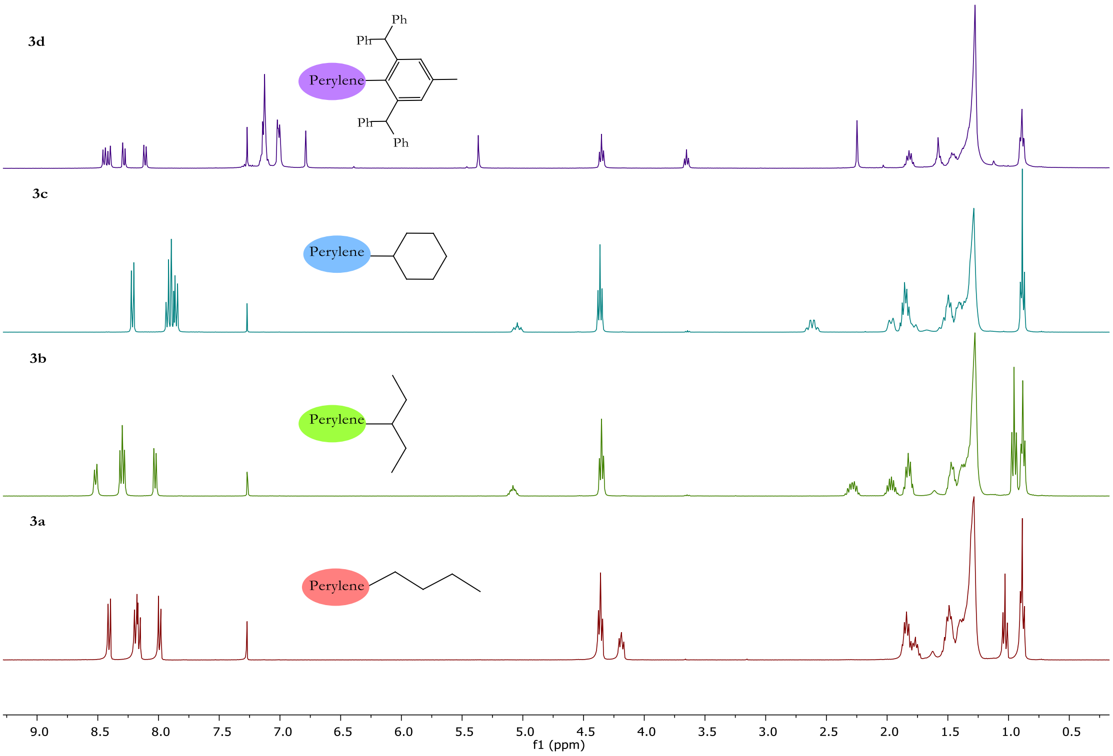

Figure 2.14 ^{1}H NMR of perylene diester monoimide, ***3a*** *to* ***d*** *in chloroform-d.*

Crystals of **3a** were attained for X-ray diffraction. They were grown through slow diffusion of hexane through an equal volume of solution composed of chloroform and **3a**. X-ray diffraction data confirmed the connectivity within the molecule and revealed the structure crystallised in the *P*-1 space group (*Figure 2.15*). Also revealed was the decyl and butyl chains both lie out of plane with the perylene core, as highlighted in *Figure 2.15b*. A slight torsion angle between the two naphthalene rings in the aromatic core was observed at 5.99°.

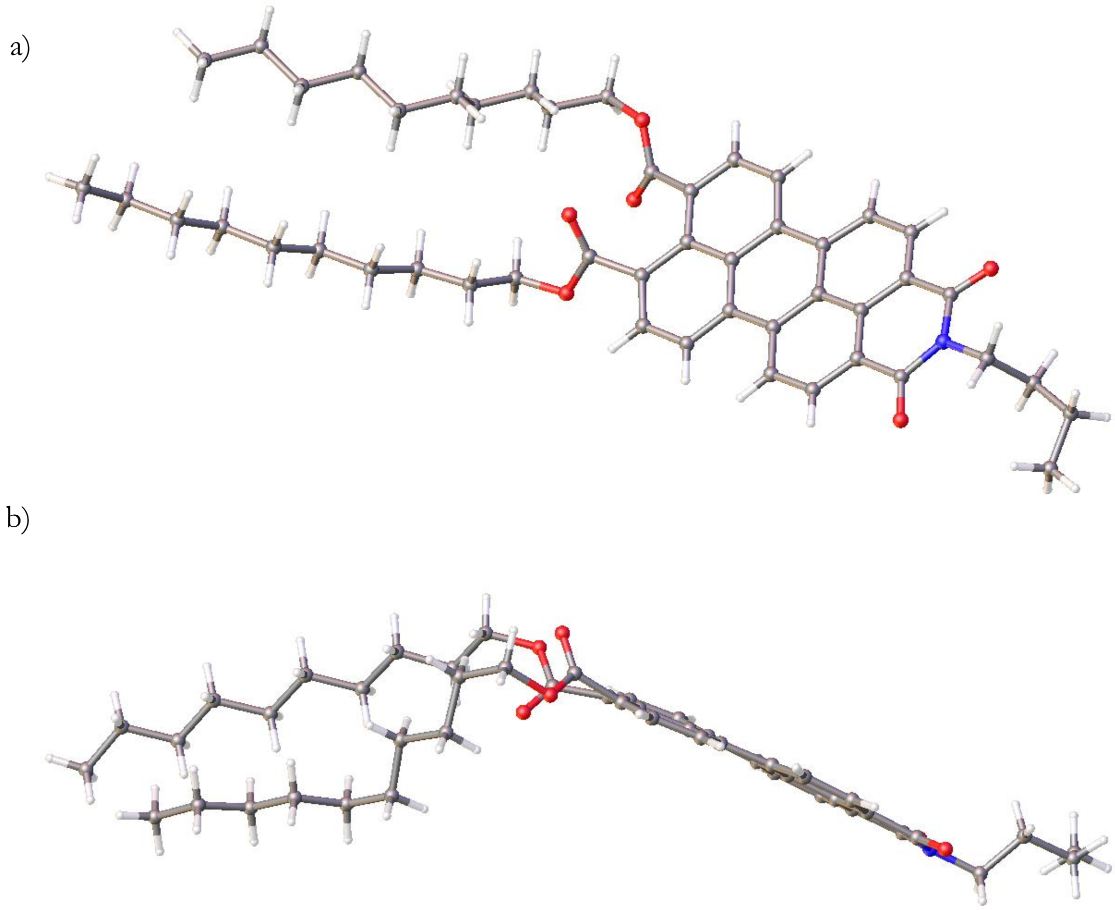

*Figure 2.15 Two different views of the single crystal structure of **3a**. Atom colours; carbon = grey, hydrogen = white, oxygen = red and nitrogen = blue.*

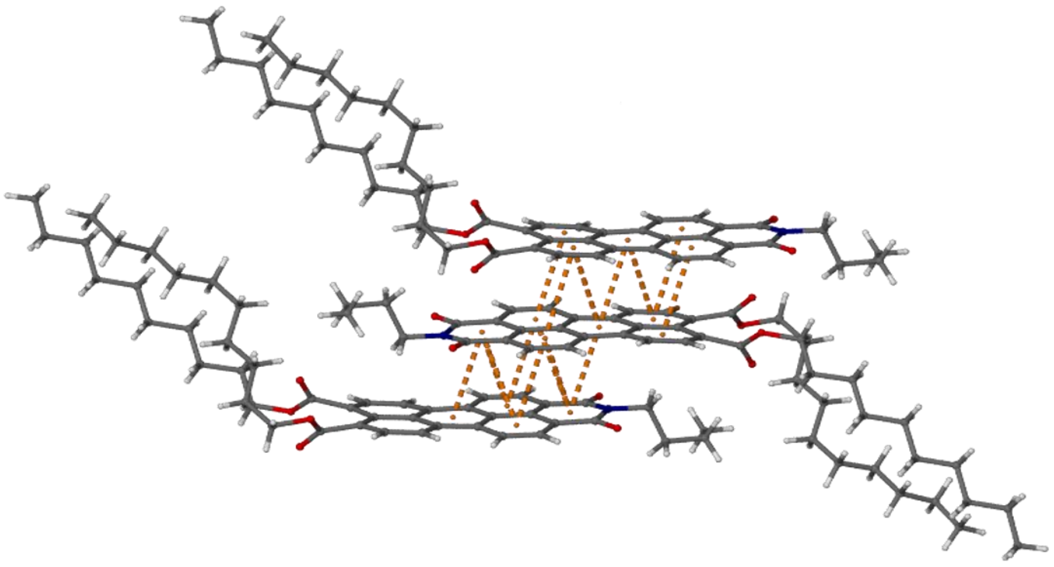

Figure 2.16 Example of the π-π interactions (dashed orange bonds) found in **3a** *(reference is middle molecule). Atom colours; carbon = grey, hydrogen = white, oxygen = red and nitrogen = blue.*

Within the crystal, there is an extensive network of π-π interactions (*Figure 2.16*) (3.63-3.93 Å, shift 1.16-1.91 Å). The shift distance is measured *via* the movement, or shift of centroid points with corresponding centroid points in adjacent molecules. Molecules stack in an anti-parallel fashion with the ester groups pointing in opposite directions to adjacent molecules. The packing motif, *Figure 2.17*, shows the arrangement of molecules in the solid states packing into neat stacks. *Figure 2.17b* highlights the transverse offset of one molecule to the next. The crystal structure is further investigated with the use of Hirshfeld surfaces.

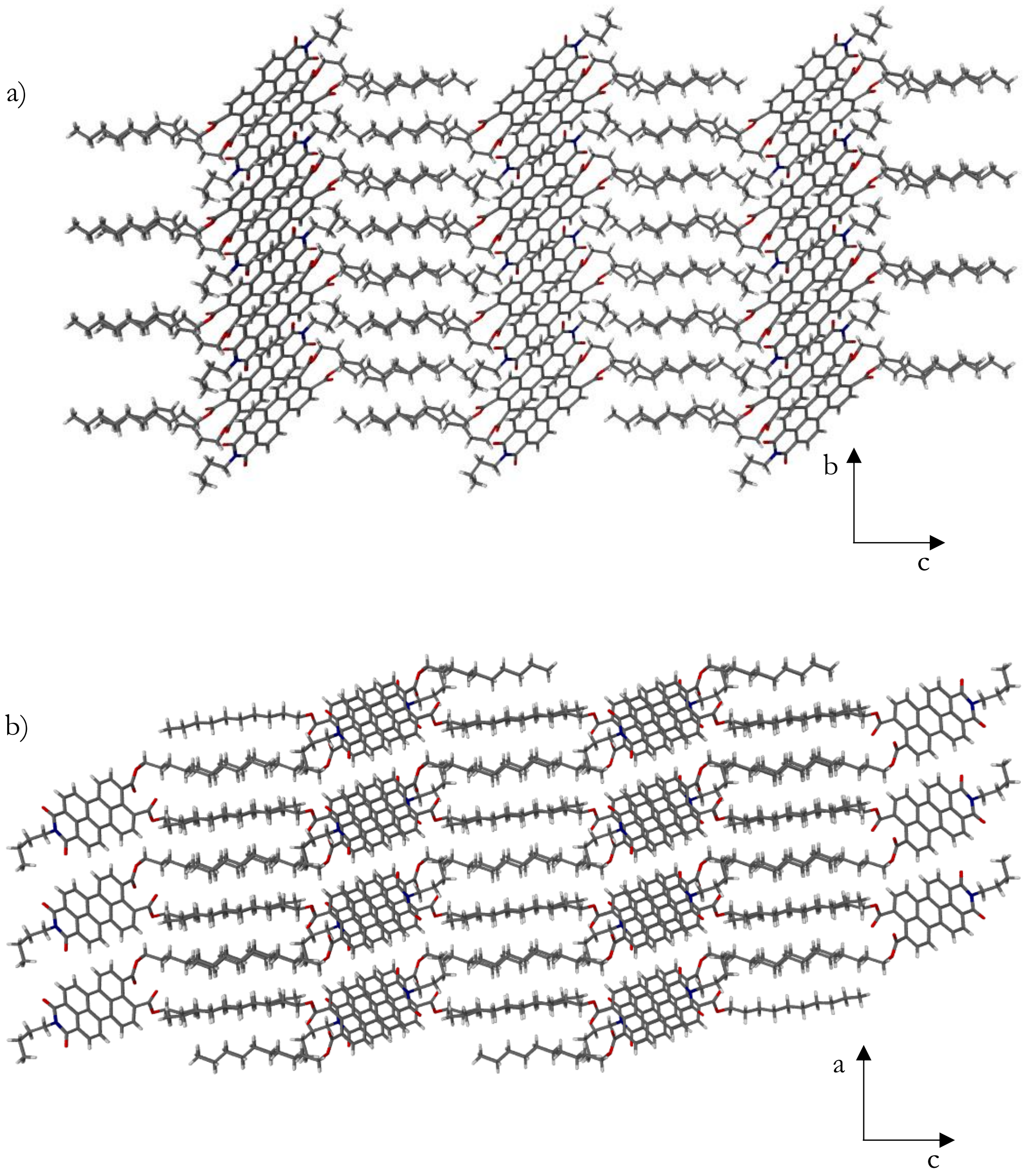

Figure 2.17 Packing motif of ***3a*** *displaying along the a) bc axis and c) ac axis. Atom colours; carbon = grey, hydrogen = white, oxygen = red and nitrogen = blue.*

For further understanding of the supramolecular structure of **3a**, Hirshfeld surface analysis was a method used to identify the individual types of intermolecular interactions between the molecules in the crystal packing.[72] CrystalExplorer was used to calculate the Hirshfeld surfaces and is a useful tool for visualising, by colour plots, the various interactions of compounds.[73] Hirshfeld surfaces are assembled by the partitioning of space in a crystal into smooth, non-overlapping regions associated with electron density of the molecule, and the surface reflects the proximity of nearest neighbouring molecules.[74] The construction of the surfaces is based on the electron density of the promolecule, $\varrho_{int}(\mathrm{r})$ dominating over the electron density of the surrounding molecules $\varrho_{ext}(\mathrm{r})$. Calculations of the surfaces are defined by the molecule and the proximity of its nearest neighbouring atoms, whilst maintaining a whole of molecule approach.[75] A Hirshfeld surface is represented by tens of thousands of surface points and is obtained by two parameters; i) the distance, d_i, from the Hirshfeld surface to the nearest atom interior to the surface and ii) the distance, d_e, from the Hirshfeld surface to the nearest nucleus in another molecule exterior to the surface. These parameters can be plotted as a surface and with the use of a red-green-blue colour scheme, properties and patterns for structural analysis are identified.

D_{norm} is an extension of d_e and d_i mapping, where the pairs, d_e and d_i, are normalised with respect to the van der Waals radii of their corresponding atoms. It requires for each surface point, both the distance and identity of the nearest atoms internal and external to the surface.[76] *Figure 2.18* shows the d_{norm} mapping of **3a** and it graphically highlights regions of the surface involved in different intermolecular bonding *via* colour; red regions represent contacts shorter than the sum of the van der Waals of the two atoms, white regions highlight contacts around the van der Waals separation and blue regions represents longer contacts. The closest point of contact in the crystal packing is highlighted in *Figure*

2.18 by point **1** and is found between the edges of the molecules in the perylene plane featuring a hydrogen bonding (C=O···H-C) with a distance of 2.255 Å. Closely following this is another weak hydrogen bond between hydrogen on a decyl chain and a carbonyl (C-H···O=C contacts) with a distance of 2.778 Å (point **2** in *Figure 2.18*). Other close points of contact can be seen in the inset in *Figure 2.18* (point **3**) which shows a different orientation of the Hirshfeld surface of **3a**. The increased distance between the decyl chains provide an increased blue coloured surface representing longer intermolecular forces. This can be compared to the aromatic core featuring a whiter surface due to the shorter intermolecular interactions (π-π stacking).

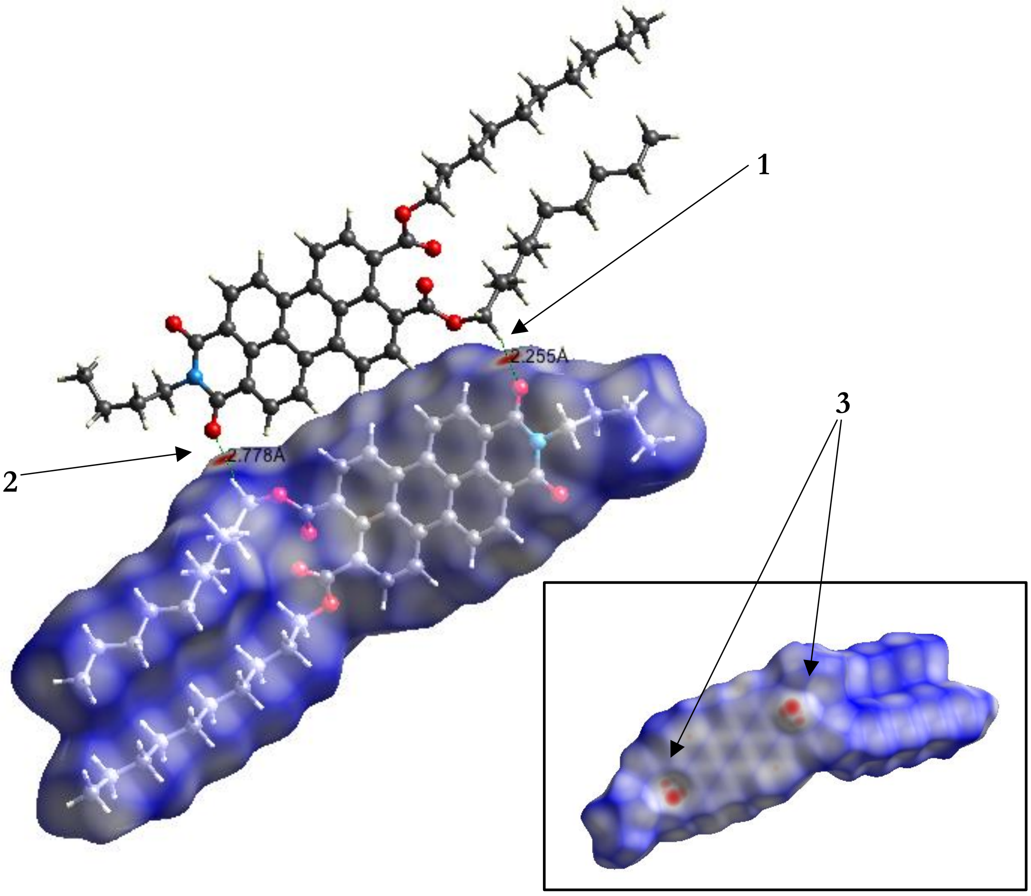

*Figure 2.18 d_{norm} surface showing the pairwise O···H interactions of **3a** at points **1**, **2** and **3**. The inset shows a different orientation of the Hirshfeld surface. Atom colours in the crystal structure; carbon = grey, hydrogen = white, oxygen = red and nitrogen = blue.*

Hirshfeld surfaces can also be represented as a histogram which summarises and provides a 2D ‘fingerprint’ of the intermolecular interactions in a crystal. The full fingerprint plot for the Hirshfeld surface of **3a** is shown in *Figure 2.19a*. Each point on the plot corresponds to a unique d_e and d_i pair and the colouring (increasing from blue to green to red) relates to the frequency of occurrence of the interaction.[77] A characteristic of these plots is the mirror image reflection along the $d_e = d_i$ diagonal. It is also possible to plot the contribution of different types of interactions separately and this is shown for the major contacts C···H, C···C, O···H, H···H and C···O in *Figure 2.19b-f*. An important feature, especially highlighted in *Figure 2.19b* at point **4**, are the ‘wings’ in the fingerprint plots and these are a common characteristic of C-H···C_π (C···H) interactions.[78] The two sharp spikes revealed in *Figure 2.19d* (**5**) pointing to the lower left of the plot are characteristics of hydrogen bonding (O···H contacts). An example of this in **3a** is the carbonyls interacting with the hydrogens in close proximity. The upper spike (where $d_e > d_i$) corresponds to the hydrogen bond donor (C-H···O=C) in comparison to the lower spike (where $d_e < d_i$) which corresponds to hydrogen bond acceptor (C=O···H-C). The shape of the spike arises from a small amount of points on the Hirshfeld surface concentrated in a small area which corresponds to the donor and acceptor regions. These are the closest points of contact occupying the smallest d_e/d_i sum and have already been highlighted in *Figure 2.18*. The C···C contacts (*Figure 2.19c*), found in the top right corner of the fingerprint, have a large distance, however cover a small area of the plot and therefore have a small range.

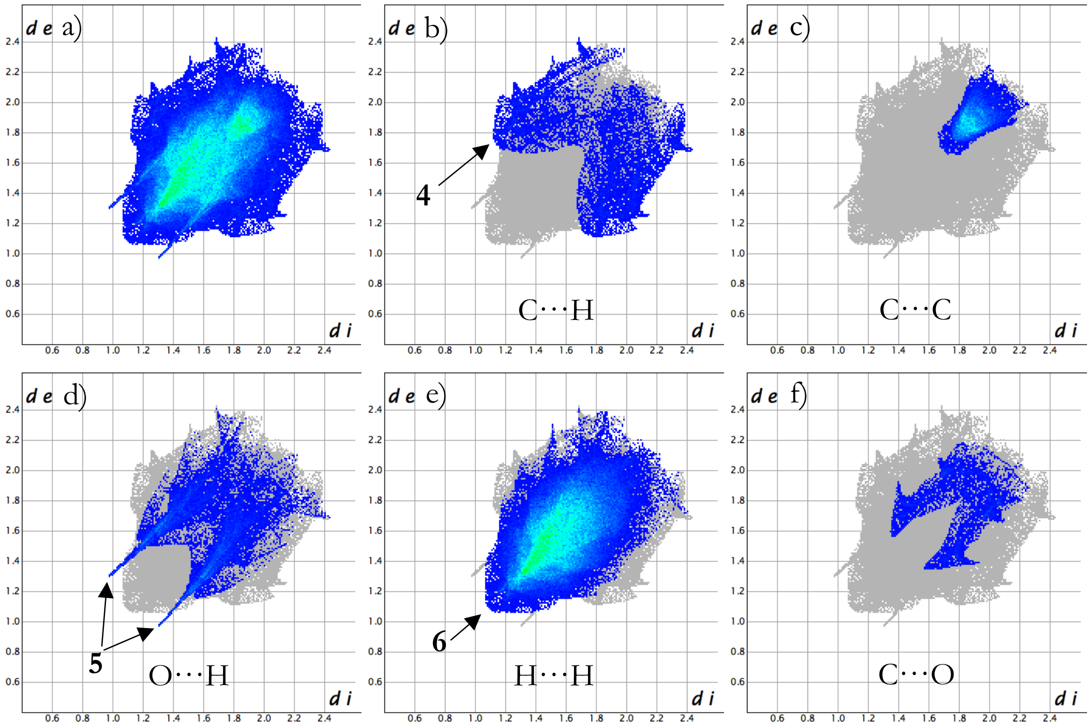

Figure 2.19 a) The full fingerprint of the Hirshfeld surfaces for ***3a****. Fingerprint plots for* ***3a*** *resolved into b) C···H, c) C···C, d) O···H, e) H···H and f) C···O contacts. The full fingerprint appears beneath each decomposed plot as a grey shadow. Numbered labels referred to in the text.*

Moreover, it is possible to highlight specific areas of contacts on the Hirshfeld surface. Quantitative analysis involving the sum of the area of these highlighted surface patches can be calculated as percentages. This has been performed for the major contacts in the Hirshfeld surface of **3a** (mapped with d_e) and are shown in *Figure 2.20*. Other interactions which are not shown include C···N, N···O, N···H and O···O which all contributed less than 1 % to the Hirshfeld surface area. H···H contacts compromise the greatest surface area of the Hirshfeld surface with 71.3 % and therefore it is suggested that these, essentially van der Waals contacts, play a large role in the stabilisation of the crystal structure. *Figure 2.20e* shows that a major contribution of H···H contacts are interactions between the decyl chains. From the fingerprint plot it is observed that the H···H contacts (*Figure 2.19e,* point **6**) have a 'nose' feature and cover a wide range of distances. This is expected considering the bends in the long chain which vary the intermolecular distances between the decyl groups as shown in the crystal structure. C···H contacts (*Figure 2.20b*) between the hydrogens on the butyl groups/perylene core and a carbon from the aromatic core in an adjacent molecule contribute 6.3 % to the Hirshfeld surface. The C···C contacts (*Figure 2.20c*) are the π-π interactions between adjacent aromatic cores contribute 8.2 % to the Hirshfeld surface. Closer inspection of the aromatic core reveals numerous hexagonal shapes in a wheel-like pattern, each with six blue 'spokes' radiating from the centre. This is a characteristic feature which arises from overlapping aromatic cores due to the stacking of molecules in the crystal structure.

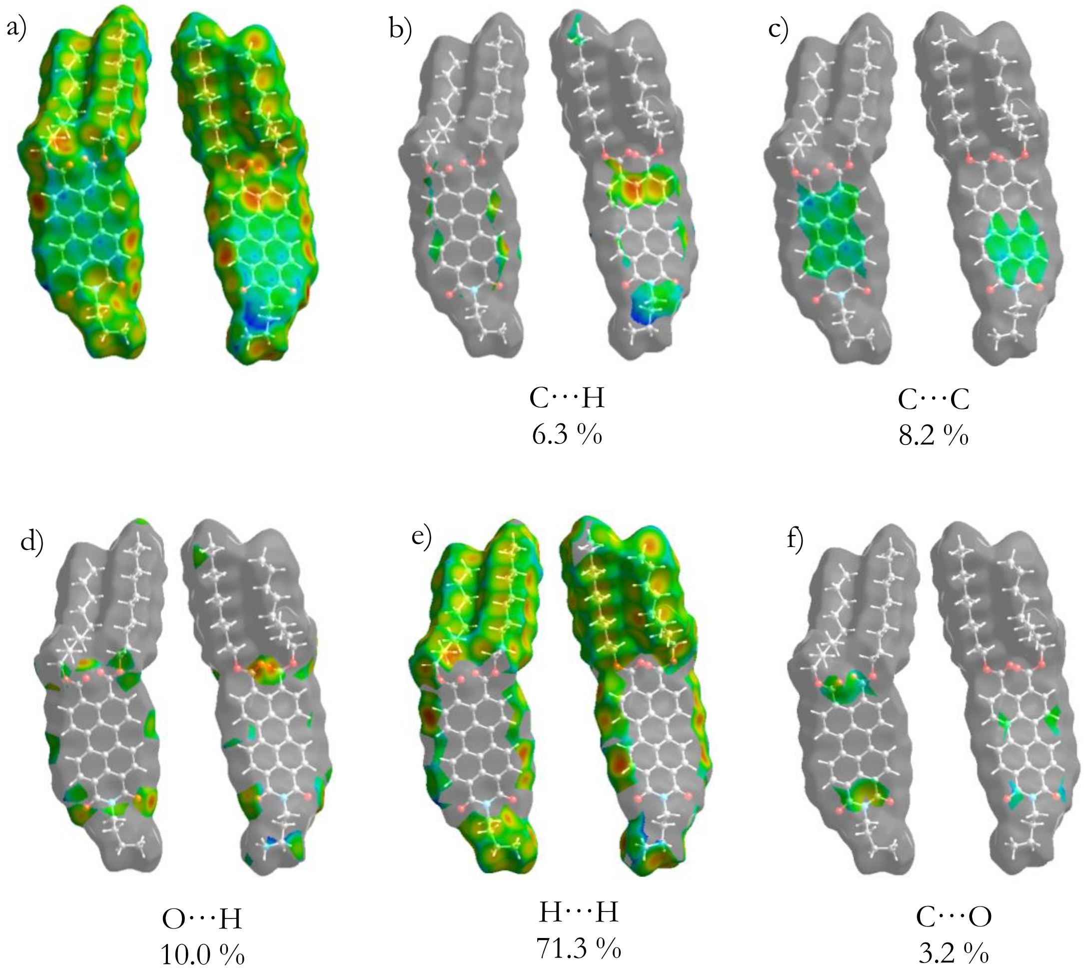

*Figure 2.20 a) d_e mapping of **3a** and the relative contributions of different types of interactions, including b) C···H, c) C···C, d) O···H, e) H···H and f) C···O contacts, showing both front and back profiles. The percentages below are the relative contributions to the Hirshfeld surface for the major intermolecular contacts in **3a.***

2.2.1.4 *Final Step: Synthesis of Perylene Monoimide Monoanhydride, PMIA* **4**

The final step is the conversion of monoimide diester species into a PMIA **4** *via* a de-esterification reaction as outlined in *Scheme 2.4*. Similarly as before, selectivity plays a key role. Ester groups are selectively cleaved by *p*-toluenesulphonic acid monohydrate. The reaction commenced with one equivalent of **3a** and 1.5 equivalents of acid.

Scheme 2.4 Synthesis of asymmetric PMIA, ***4a*** *to* ***d****.*

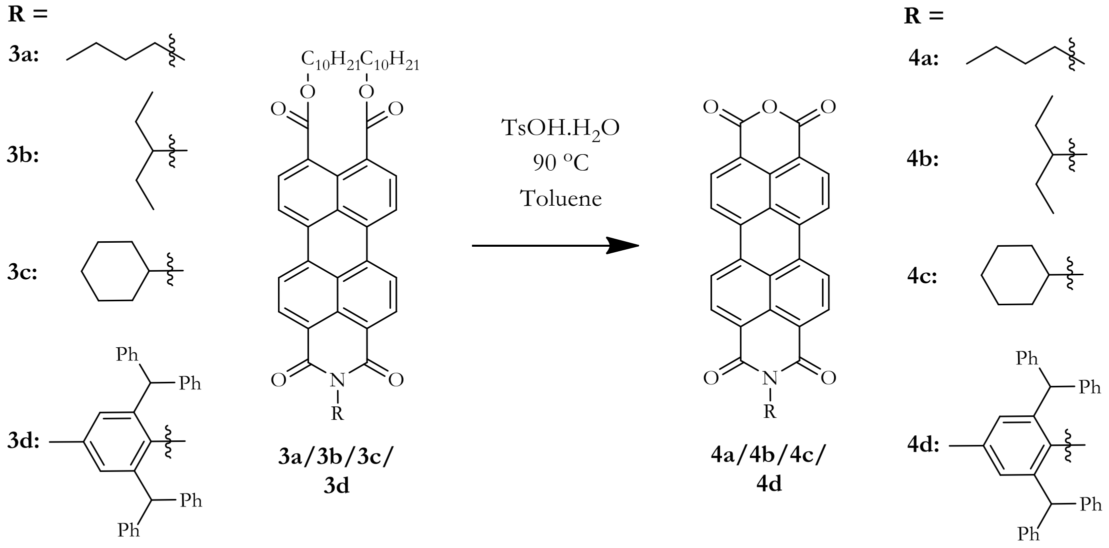

Careful monitoring throughout the course of the reaction *via* TLC showed the development of a darker coloured spot (**4**) and diminution of a yellow/orange reactant spot. Acid was added accordingly to ensure this process occurred and the saponification reaction often took a few hours. MALDI MS was a useful technique to monitor the reactions, where peaks with a *m*/*z* of 446.3, 461.6, 473.1 and 813.1 appeared confirming the presence of **4a**, **4b**, **4c** and **4d** respectively. A comparison of MALDI MS spectra of **3d** and **4d** is shown in *Figure 2.21*. During the course of the reaction the depletion of a peak at 1111.5 (*Figure 2.21a*) and the appearance of a peak at 813.5 (*Figure 2.21b*) corresponding to **3d** and **4d** respectively was evident.

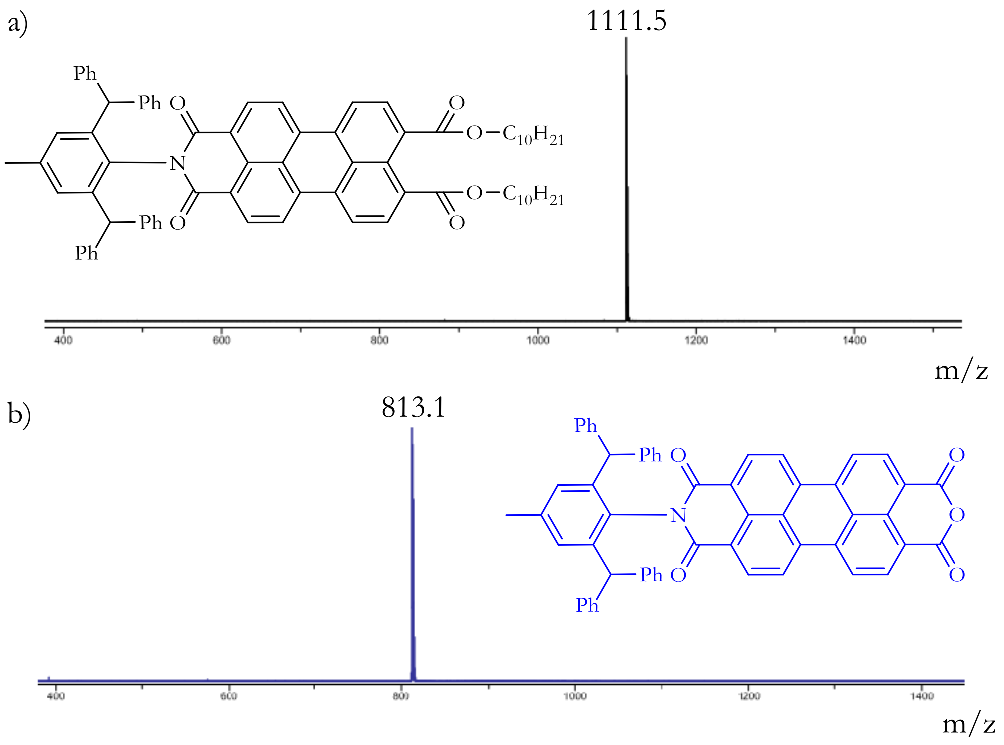

*Figure 2.21 MALDI MS of compound **3d** (a) and **4d** (b).*

Solubility was dramatically reduced after removal of the decyl chains limiting usual solution phase characterisation methods for some of the species. The solubility varied greatly depending on which imide group was attached at the N-terminal position, with the most soluble species being the largest, most bulky group, **4d**. Unsurprisingly, the most insoluble species was **4a** with a simple butyl group at the N-terminal position. ^{1}H NMR and ^{13}C NMR was used where possible, and HRMS was obtained for all (**4a**, **4b**, **4c** and **4d**) products.

Single crystals of **4b**, suitable for single crystal X-ray crystallographic studies, were grown by slow diffusion of a layered hexane and a chloroform solution of the compound. Single crystal diffraction data confirmed the molecular structure of **4b** (see *Figure 2.22*). *Figure 2.22a* highlights the aromatic core and *Figure 2.22b* displays the 1-ethylpropyl group perpendicular to the aromatic core. A small torsion angle of 2.83° is observed between the two naphthalene rings in the perylene core.

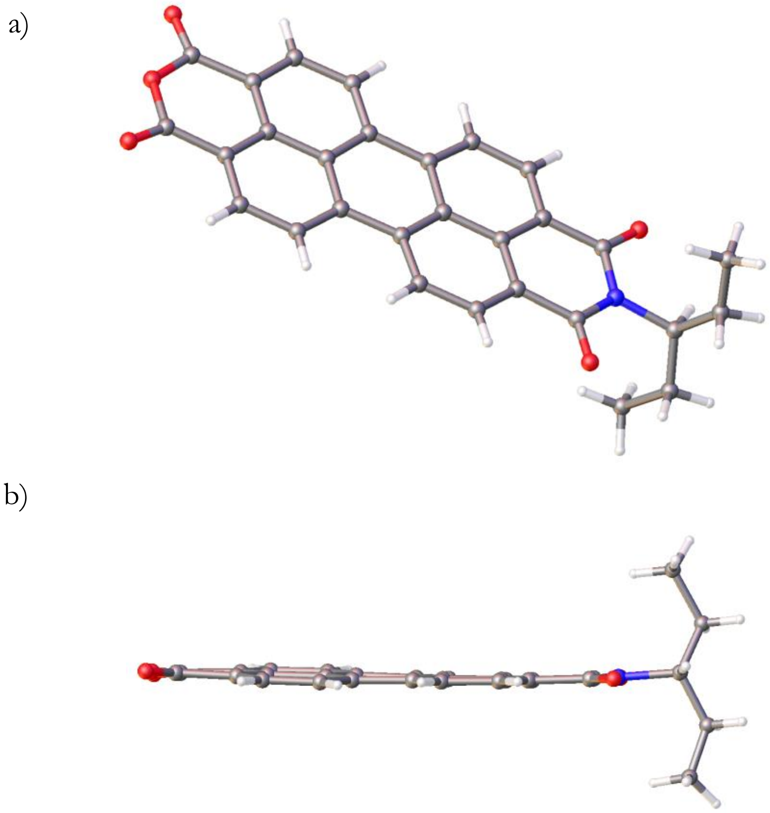

*Figure 2.22 Single crystal structure of **4b** a) showing the molecular structure and b) highlighting the 1-ethylpropyl group perpendicular to the aromatic core. Atom colours; carbon = grey, hydrogen = white, oxygen = red and nitrogen = blue.*

The molecules stack with an antiparallel orientation as demonstrated in *Figure 2.23*. The extended aromatic core allows for an extensive network of π-π interactions (3.50-3.81 Å, shift 0.99-1.83 Å). The π- π interactions are highlighted by orange dashed lines in *Figure 2.23* and full details of the corresponding distances can be found in Section 2.4.2.6. The π-π distances reported are typical of PDI species, at 3.4 Å.[30] The packing motif is shown in *Figure 2.24* along the ac and ab axes. It is interesting to note the closeness of the 1-ethylpropyl groups to the neighbouring carbonyl in the anhydride moiety on an adjacent molecule with a distance of 3.37 Å (C···O). Another, close point of contact is between two CH_3 groups in the 1-ethylpropyl terminus with a distance of 3.99 Å (C···C).

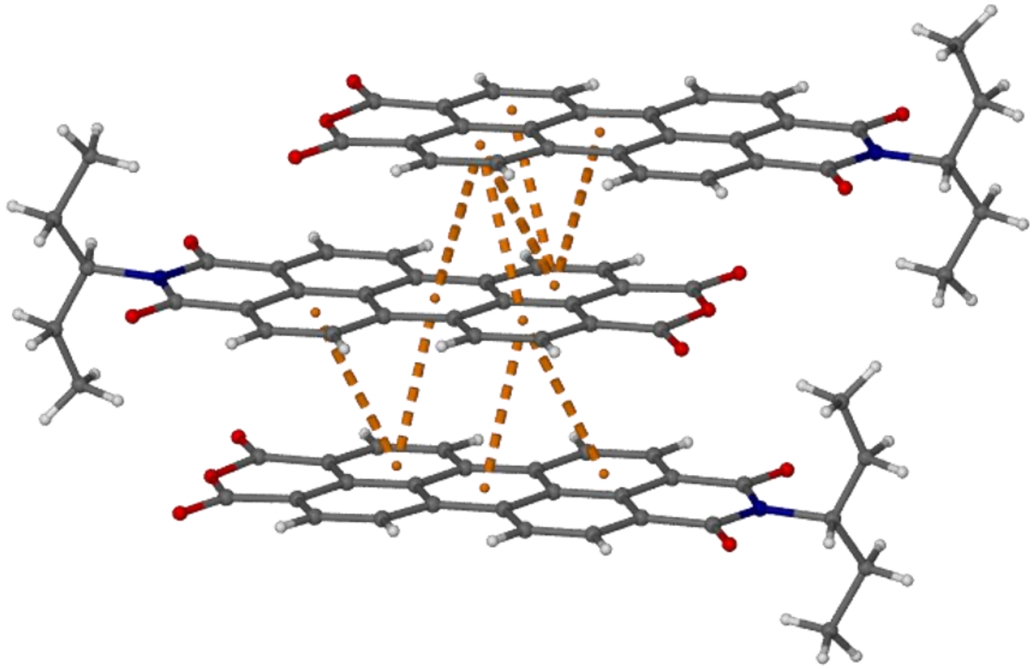

Figure 2.23 Example of π-π interactions (dashed orange bonds) in **4b** *(reference is middle molecule). Atoms colours; carbon = grey, hydrogen = white, oxygen = red and nitrogen = blue.*

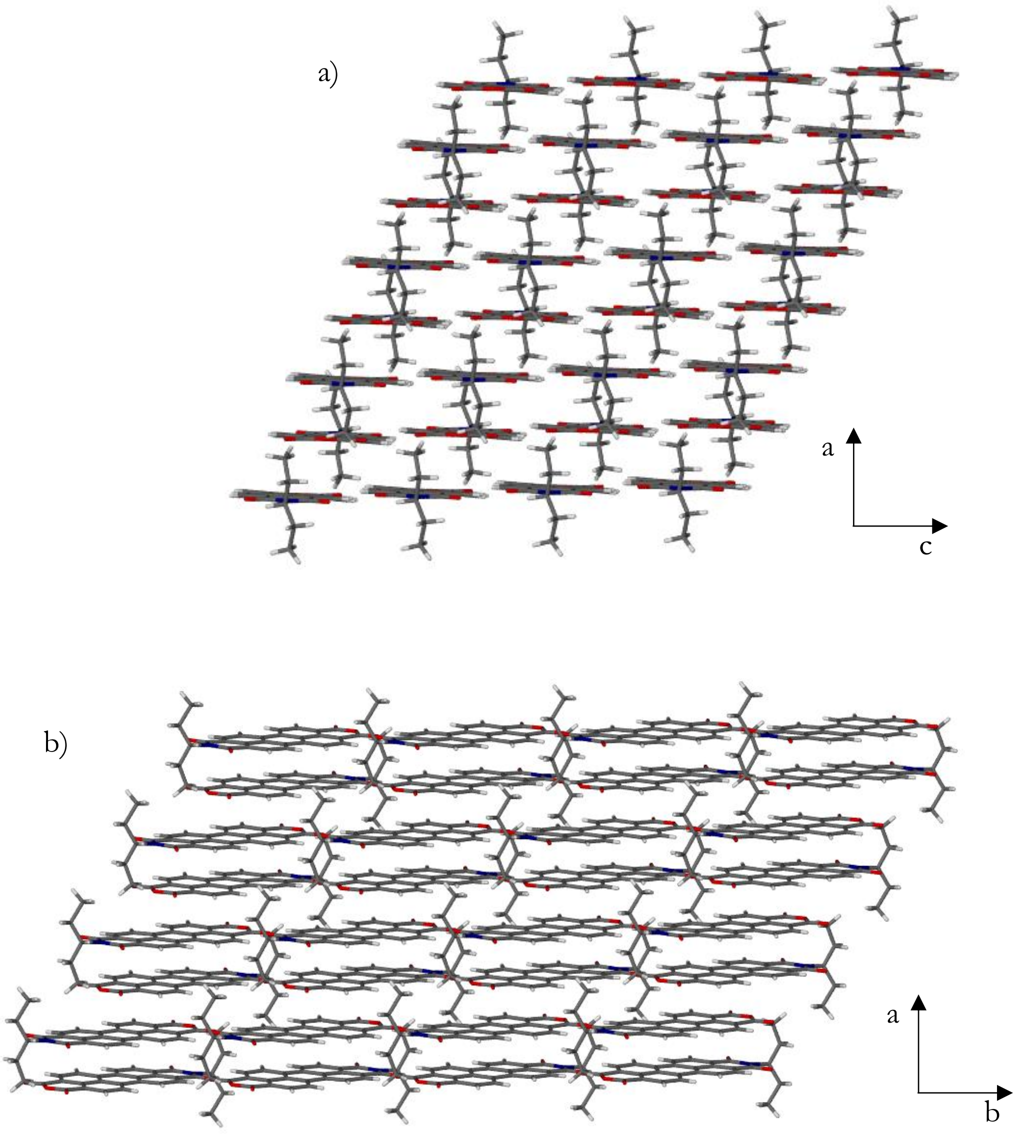

Figure 2.24 Packing motifs of ***4b*** *along the a) ac axis and b) ab axis. Atoms colours; carbon = grey, hydrogen = white, oxygen = red and nitrogen = blue.*

2.2.2 Dimerisation of Two PMIA Units

This section describes the successful connection of two asymmetric PMIA units with different linkers. For synthesis of these dimers, the most soluble asymmetric PMIA in the series was used, **4d**, which features a bulky N-terminal group, which prohibits stacking of molecules.

*2.2.2.1 Dimerisation using p-Xylylenediamine as a Linker, **5***

The synthesis for the first dimer is outlined in *Scheme 2.5*. It involves two equivalents of **4d** and one equivalent of the commercially available linker, *p*-xylylenediamine and the reaction was left for 22 hours at 130 °C in imidazole and toluene. Similar to before with the imidization, the reaction follows an S_N2 mechanism. The solid content of the reaction was dissolved in chloroform and washed with water and the organic layer dried over magnesium sulphate. MALDI MS revealed the presence of an asymmetric PDI, **5a** at *m/z* 931.3 and also the expected asymmetric dimer **5** at *m/z* 1727.24. Multiple purification steps were required including another purification technique, preparative thin layer chromatography (prepTLC). Due to the multiple purification steps a low yield of 7 mg, 8 % was obtained.

*Scheme 2.5 Reaction scheme for the synthesis of dimer **5** and asymmetric PDI **5a**.*

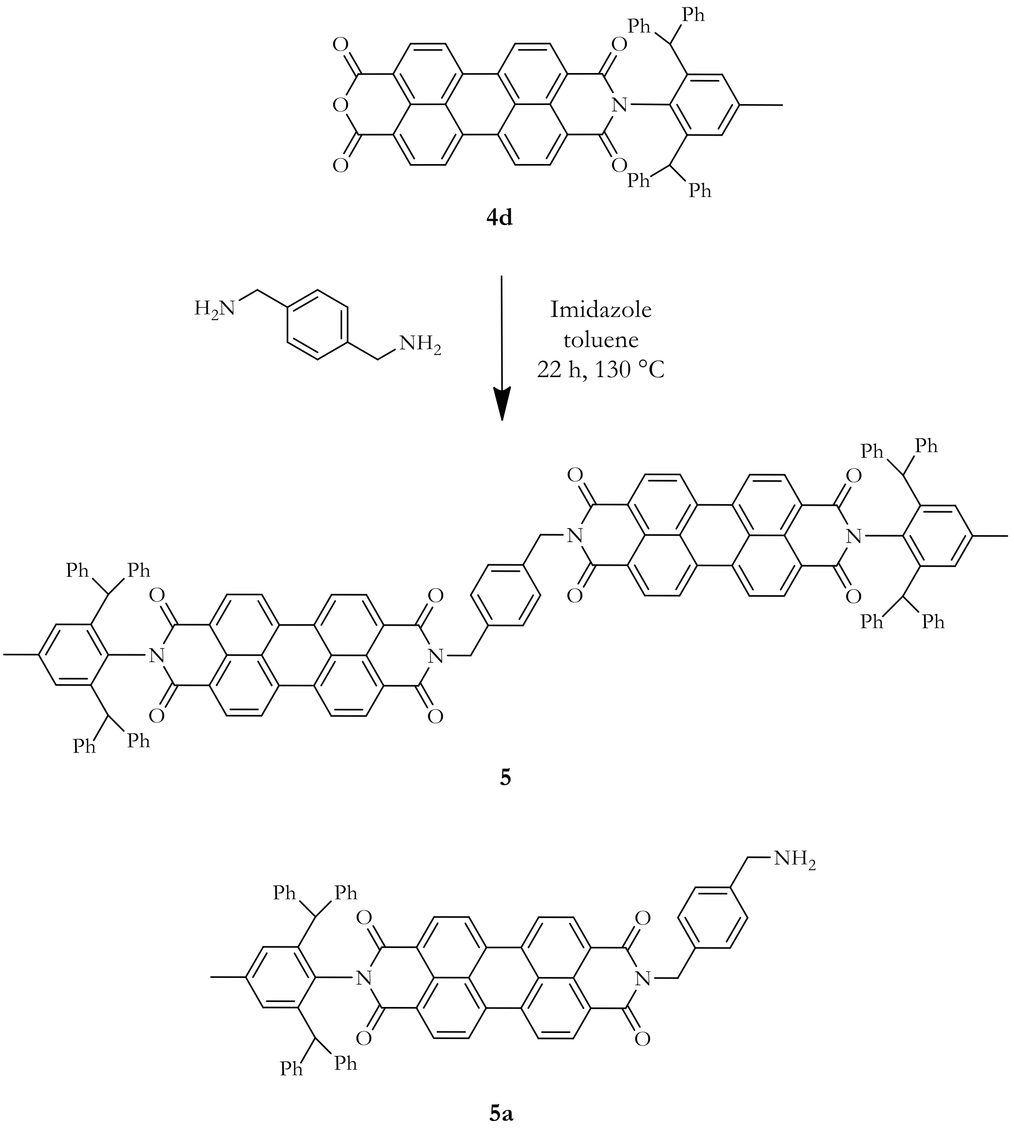

^{1}H NMR (shown in *Figure 2.26*) and ^{13}C NMR both gave evidence for the synthesis of **5**, however this compound had low solubility and other solution phase analytical techniques, such as cyclic voltammetry, could not be performed. Optical absorption spectra for dimer **5** were recorded in DCM. The dimer exhibits an absorbance profile typical for a PDI featuring three vibronic peaks with an absorbance maximum of 529 nm and a molar extinction coefficient of 66,500 mol^{-1}dm^{3}cm^{-1} (*Figure 2.28*).

DFT geometry optimisations were performed on the a model of dimer **5** derived from the crystal structure of N-(2,6-bis(diphenylmethyl)-4-methylphenyl)-perylene-3,4-dicarboximide-9,10-anhydride to predict the gas phase structure of dimer **5**. The structure is shown in *Figure 2.25* and it is assumed that this is the most thermodynamically stable structure. The geometry optimised molecular structure compares well to the crystal structures of **3a** and **4b** previously reported in this chapter in the fact that the perylene core is essentially planar. The large bulky group at the imide positions protrudes from the perylene plane as expected. The organic linker connecting the two subunits creates an angle of 114.3° with the perylene plane as shown in *Figure 2.25*. As previously mentioned, this compound is insoluble and this is somewhat surprising due to the prediction of the molecular structure, where one would expect that it disrupts π-π stacking between adjacent molecules potentially enhancing solubility.

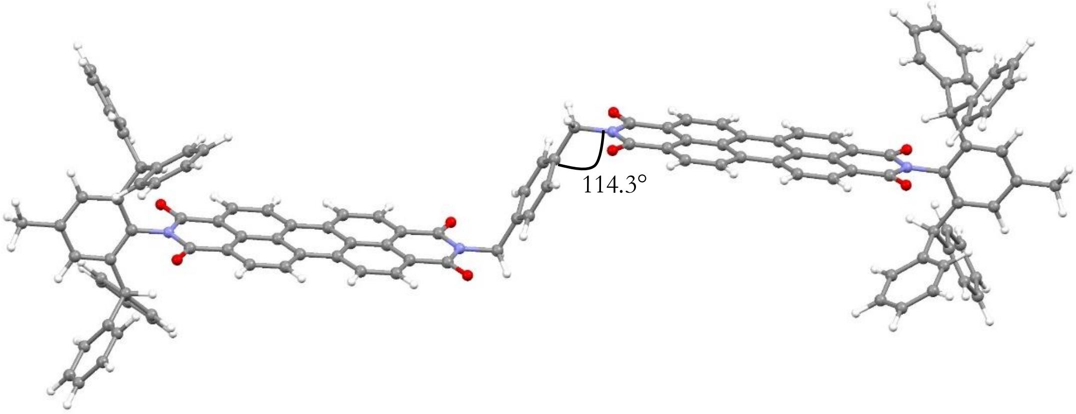

*Figure 2.25 The minimised molecular structure of dimer **5** calculated using DFT. Atom colours; carbon = grey, hydrogen = white, oxygen = red and nitrogen = blue.*

2.2.2.2 *Dimerisation using Bis(4-aminophenyl)ethyne as a Linker*

A second dimer was synthesised using bis(4-aminophenyl)ethyne linker. The organic linker was prepared *via* a cross coupling reaction of a terminal alkyl and an aryl halide bearing an amino group using a known procedure (outlined in *Scheme 2.6*).[79] The reaction gave **6** in 89 % yield after stirring at room temperature for 4 hours.

*Scheme 2.6 Synthesis of organic linker bis(4-aminophenyl)ethyne, **6**.*

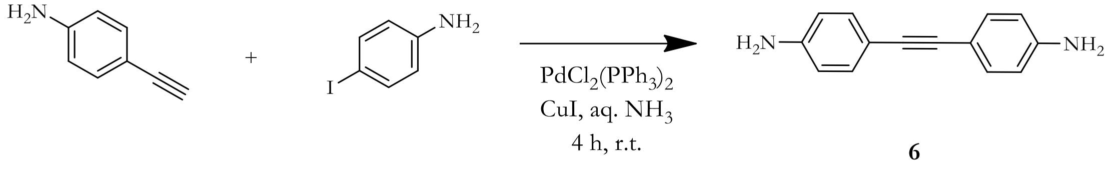

Bis(4-aminophenyl)ethyne **6** was used to bridge two PMIA units. One equivalent of **6** and two equivalents of **4d** were heated in imidazole for 18 hours at 130 °C. MALDI MS revealed a peak at m/z 1798.58 however multiple purification steps were required to obtain dimer **7** pure, giving a low yield of 4.1 mg, 9 %. The two dimers were probed *via* ^{1}H NMR and the downfield region of the spectra are shown in *Figure 2.26*. Each dimer revealed four resonances downfield, between 8.2-8.8 ppm, corresponding to the protons from the aromatic core. Resonances between 6.7 and 7.2 ppm integrated to a total of 44 and are from the aromatic protons in the N-terminal group. 2D NMR (^{1}H-^{1}H COSY) spectroscopy, which features a chemical shift correlation map between neighbouring protons, aided in assignments of the peaks and dimer **7**'s 2D NMR is shown in *Figure 2.27*.

*Scheme 2.7 Outline of synthesis for dimer **7**.*

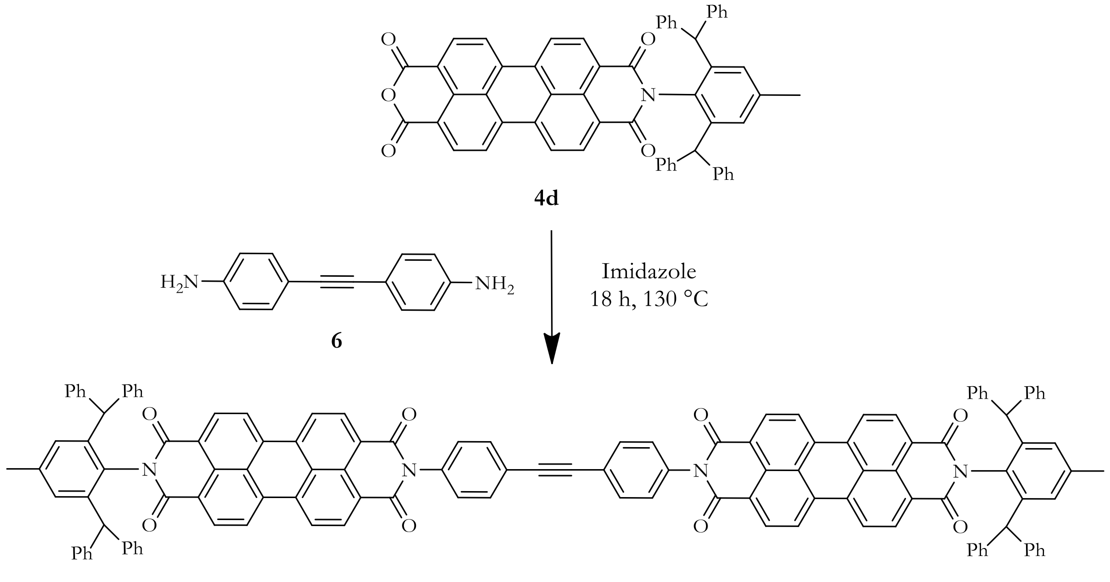

7

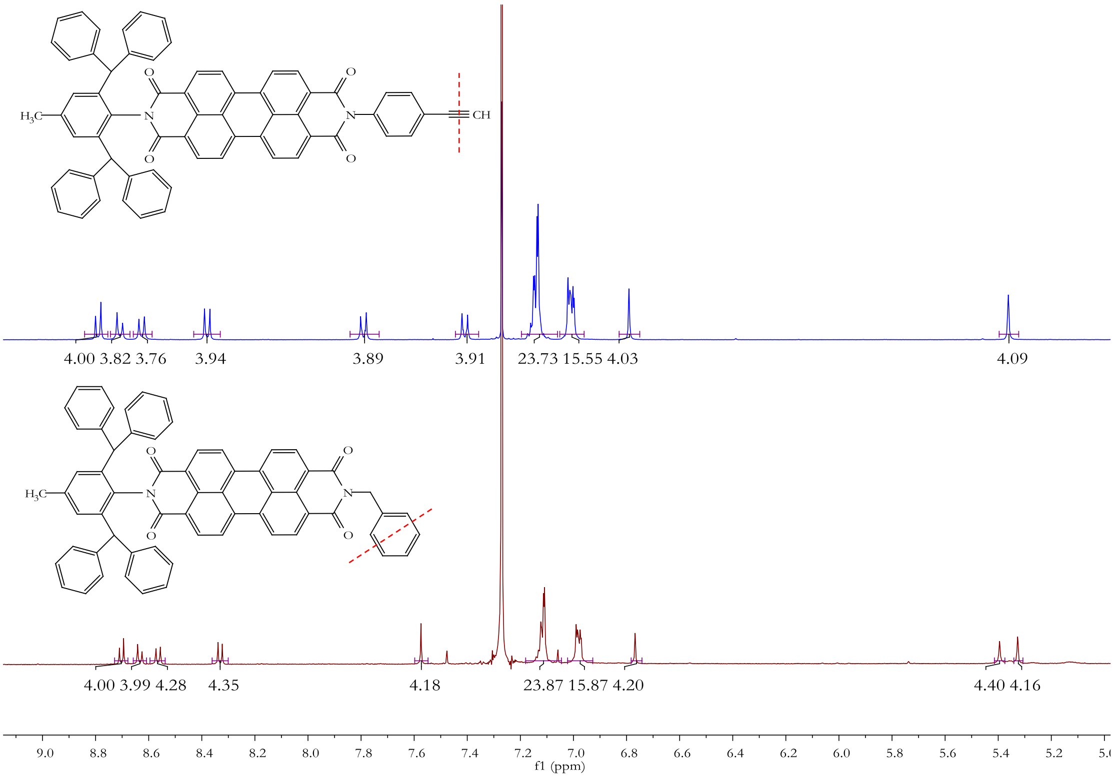

*Figure 2.26 ^{1}H NMR spectra of the aromatic region of **5** (red) and **7** (blue) in chloroform-d. Integration for each signal is given below the respective spectra.*

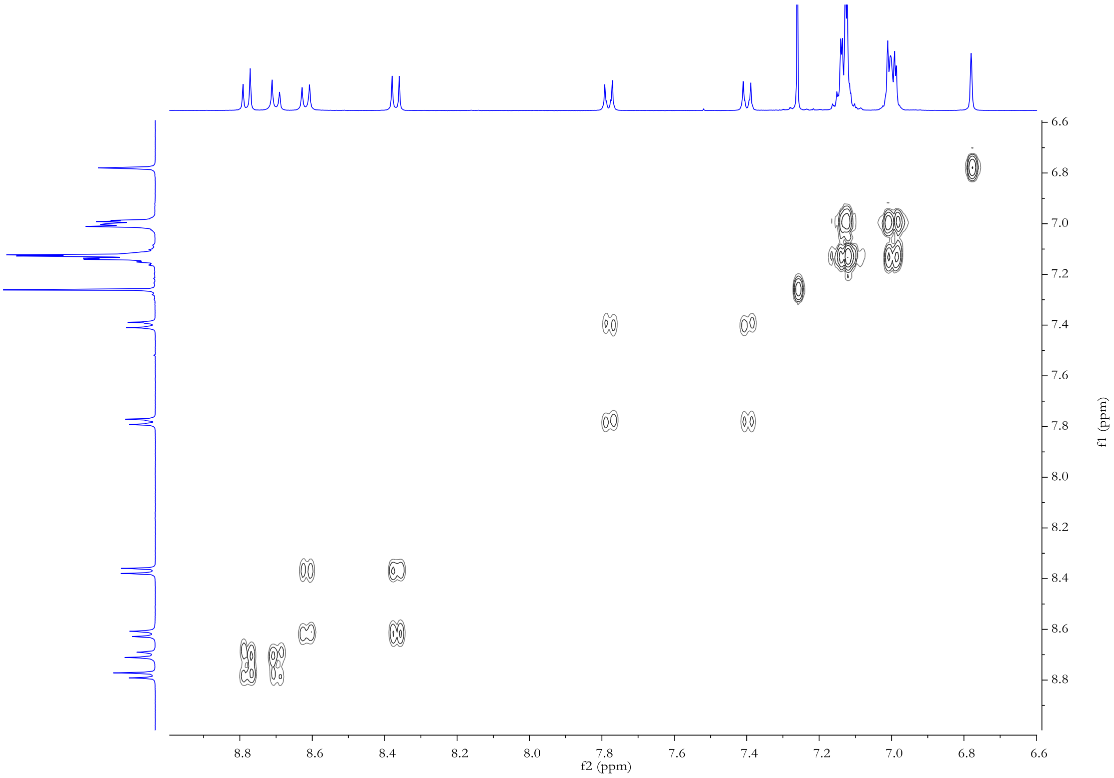

*Figure 2.27 ^{1}H-^{1}H COSY NMR spectrum of the aromatic region of **7** in chloroform-d.*

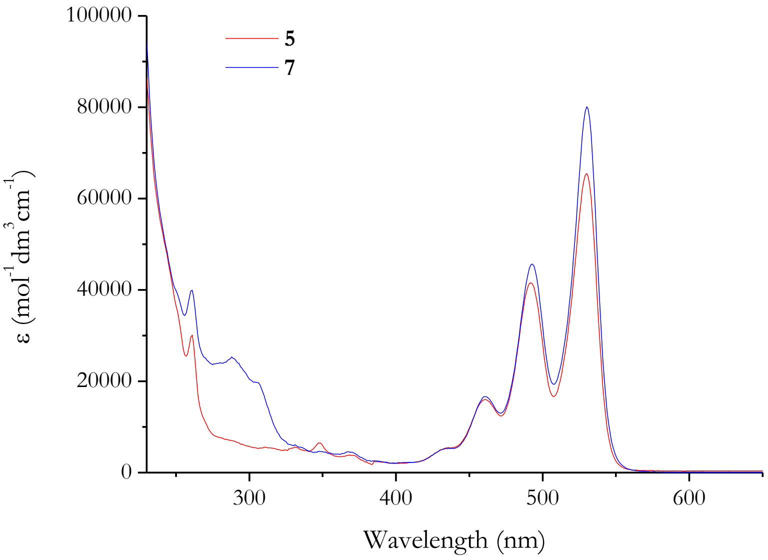

Figure 2.28 Comparison of UV-vis spectra for dimers ***5*** *(red) and* ***7*** *(blue) in DCM at concentration of* 5×10^{-6} *moldm*$^{-3}$.

The UV-vis spectra of **5** and **7** are compared in *Figure 2.28*. Both dimers exhibit an absorption band at 529 nm and look similar in profile except in the 260-340 nm region where the band structure changes. Dimer **7** was considerably more soluble than dimer **5**. UV-vis spectra of **7** was investigated with different solvent systems; 100 % DCM, 80 % DCM/20 % MeOH, 50 % DCM/50 % MeOH and 10 % DCM/90 % MeOH and are shown in *Figure 2.29*. A higher percentage of methanol causes the perylene dimer to experience pronounced spectral change where the three vibronic features usually ranging between 450 and 550 nm broadens to a range between 450 and 600 nm. DCM is classed as a non-polar solvent (dielectric constant of 8.91)[80] exhibiting strong solvent-molecule interactions. Competition of intermolecular forces between molecules of **7** and DCM, result in less aggregation of **7** and π-π stacking energy is reduced. Contrary, methanol has weaker solvent-molecule interactions due to its high polarity (dielectric constant of 32.66).[80] Strong hydrogen bonds form between methanol molecules resulting in less interaction between the methanol molecules and dimer units, allowing stacking of **7** and causing a broadening of the absorption bands.

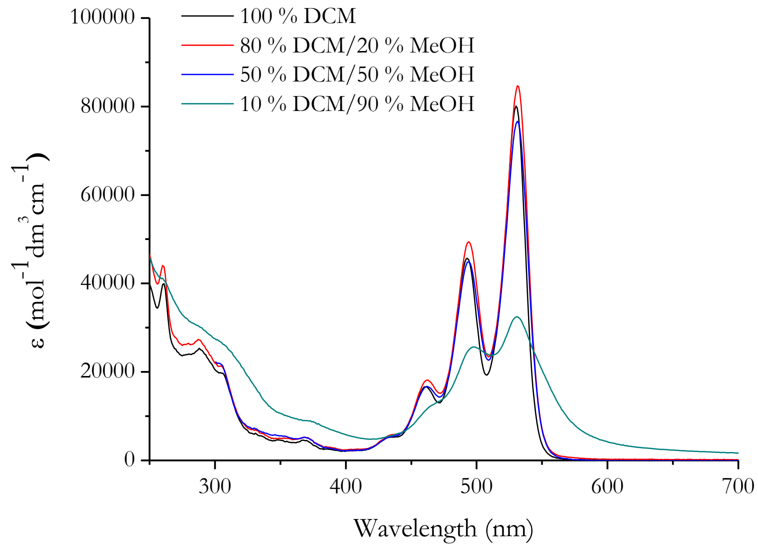

*Figure 2.29 UV-vis absorption spectra of **7** in different solvent system. Concentration of **7** is $5x10^{-6}$ moldm^{-3}. (Black = 100 % DCM, red = 80 % DCM/20 % MeOH, blue = 50 % DCM/50 % MeOH and green = 10 % DCM/90 % MeOH).*

Cyclic voltammetry was used to investigate the redox processes of dimer **7** (*Figure 2.30*). Experiments of **7** were performed in DCM with supporting electrolyte tetrabutylammonium tetrafluoroborate ($[Bu_4N][BF_4]$). The electrolysis cell had a three electrode setup including; a platinum/rhodium gauze working electrode, platinum wire secondary electrode, and a silver/silver chloride reference electrode. The voltammogram exhibits two two-electron reduction processes, and each process was studied at five different scan rates: 20, 50, 100, 200 and 300 mVs^{-1}. The processes were reversible shown by the overall shape of the curve.

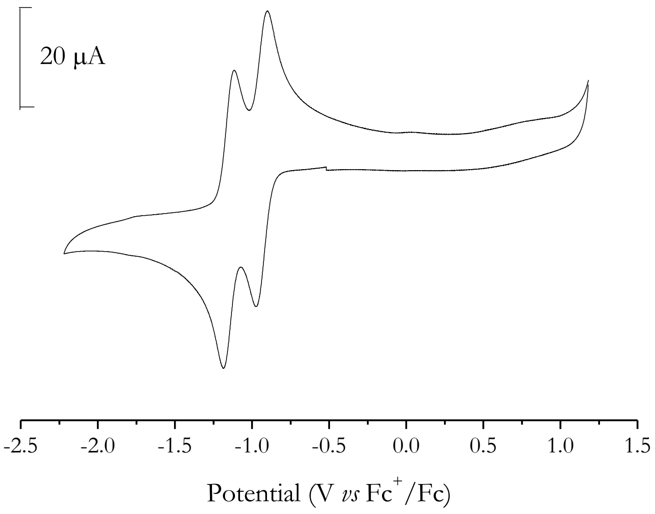

Figure 2.30 Cyclic voltammogram of dimer ***7*** *in DCM containing 0.4 M [Bu_4N][BF_4] supporting electrolyte, with a scan rate of 100 mVs^{-1}.*

The first reduction potential for dimer **7** occurs at -0.97 V (*vs* Fc^+/Fc) and the second reduction at -1.18 V providing a difference of 0.21 V between the reduction potentials. The redox potentials for a symmetrical PDI featuring the same N-terminal groups as dimer **7**, shown in *Figure 2.31*, have previously been examined in the Champness lab.[81] This compound showed two reduction processes, the first at -0.99 V and the second at -1.24 V (*vs* Fc^+/Fc). Comparison of the redox potentials between dimer **7** and symmetrical PDI shows that dimer **7** has a more electron deficient perylene core due to bis(4-aminophenyl)ethyne in dimer **7** having a greater electron withdrawing effect than bis(diphenylmethyl)-4-methylphenyl.

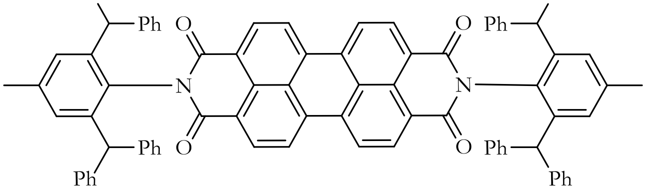

Figure 2.31 Symmetrical PDI featuring N-terminal group of bis(diphenylmethyl)-4-methylphenyl.

Species **7** was probed further by spectroelectrochemistry investigating the absorbance profiles of the electrogenerated species. The neutral compound was regenerated after reduction which was shown by the return of the absorption spectrum of the neutral species. The UV-vis absorption spectra showing the inter-conversion from neutral (blue) to monoanionic (red) species of dimer **7** is shown in *Figure 2.32* and the black arrows indicate the progression of the reduction. Upon first reduction the vibronic feature corresponding to the neutral perylene species ($S_0 \rightarrow S_1$ transition) in the wavelength range 450-550 nm is diminished, and new bands arise in the region 600-850 nm, with similar molar extinction coefficients for both features.

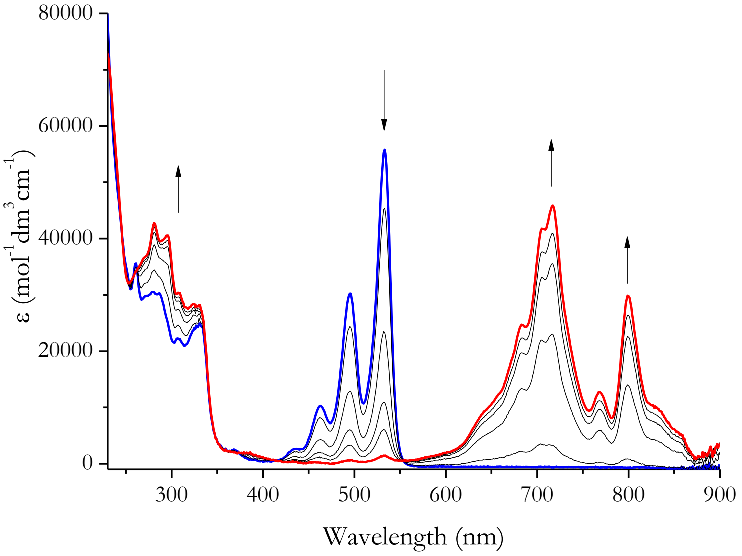

*Figure 2.32 UV-vis absorption spectra showing the inter-conversion from neutral (blue) to monoreduced (red) species of dimer **7**, arrows indicate the progress of the reduction. Spectra were recorded in DCM containing [Bu_4N][BF_4] (0.4 M) as the supporting electrolyte at 273 K.*

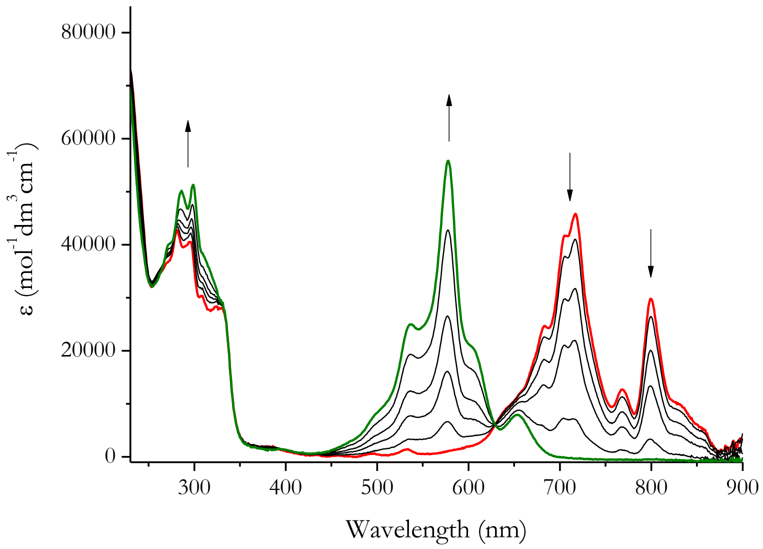

Figure 2.33 UV-vis absorption spectra showing the inter-conversion from monoanionic (red) to dianionic (green) species of dimer **7***, arrows indicate the progress of the reduction. Spectra were recorded in DCM containing* $[Bu_4N][BF_4]$ *(0.4 M) as the supporting electrolyte at 273 K.*

The spectroelectrochemical interconversion between the monoanionic (red) and dianionic (green) forms of dimer **7** are shown in *Figure 2.33* and formation of the dianionic species show a decrease in absorption bands in the lower energy region, and a rise in an intense sharp band at 577 nm. The blue shift from the monoanionic to the dianionic species has been previously reported.[82-84] The main feature for the dianion is observed in the middle of the main neutral and monoreduced absorption bands highlighted in *Figure 2.34*. The optical absorbance data for neutral, monoreduced and direduced forms of **7** are summarized in *Table 2.1*.

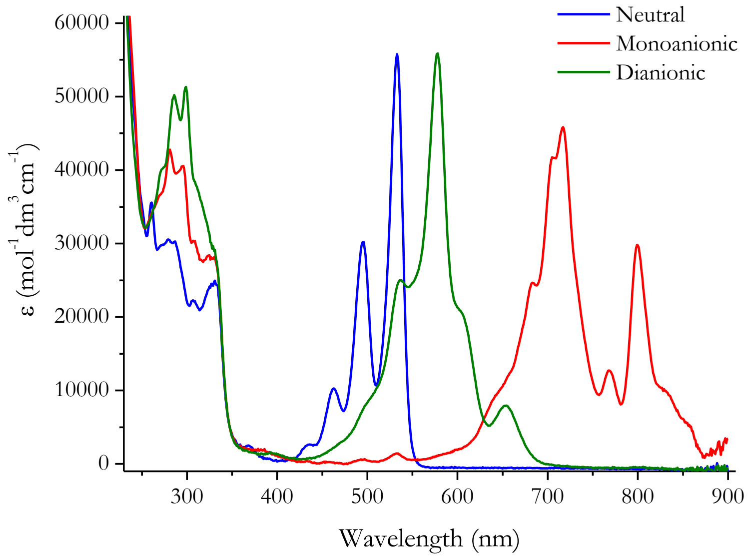

Figure 2.34 UV-vis absorption spectra of neutral (blue), monoanionic (red) and dianionic (green) forms of dimer ***7****. Spectra were recorded in DCM containing [Bu_4N][BF_4] (0.4 M) as the supporting electrolyte at 273 K.*

Table 2.1 Summary of UV-vis spectroscopic data for dimer ***7****.*

λ_{abs} (nm) [ε (10^3mol^{-1}dm^{3}cm^{-1})]		
Neutral	*Monoanionic*	*Dianionic*
259 (35.4), 286 (30.1), 307 (22.3), 330 (25.0), 434 (2.7), 462 (10.4), 495 (30.3), 533 (55.6)	280 (42.6), 295 (40.5), 308 (30.3), 329 (28.0), 533 (1.4), 682 (24.7), 705 (41.8), 717 (45.5), 768 (12.6), 799 (29.6)	270 (40.1), 285 (50.0), 298 (51.4), 331 (29.1), 537 (25.0), 577 (55.6), 605 (20.6), 653 (8.3)

Obtained at an optically transparent electrode cell in dichloromethane, containing [Bu_4N][BF_4] (0.4 M) at 273 K, spectral range 230 – 900 nm.

Infrared electrochemistry was investigated for dimer **7** and the spectra recorded in DCM in the presence of the supporting electrolyte, [Bu$_4$N][BF$_4$]. The monoreduced species of **7** was electrogenetated and the infrared spectrum measured to investigate changes in the carbonyl region of the neutral and monoreduced species (*Figure 2.35*). Neutral species **7** features two C=O absorption stretches at 1667 and 1704 cm^{-1}, however these peaks disappear in the IR spectrum of monoreduced **7**. A series of new bands arise at a lower wavenumber in the reduced species due to the C=O bonds occupying less energy. On reduction of species **7** there is an addition of an electron and bond strength (bond order) is reduced.

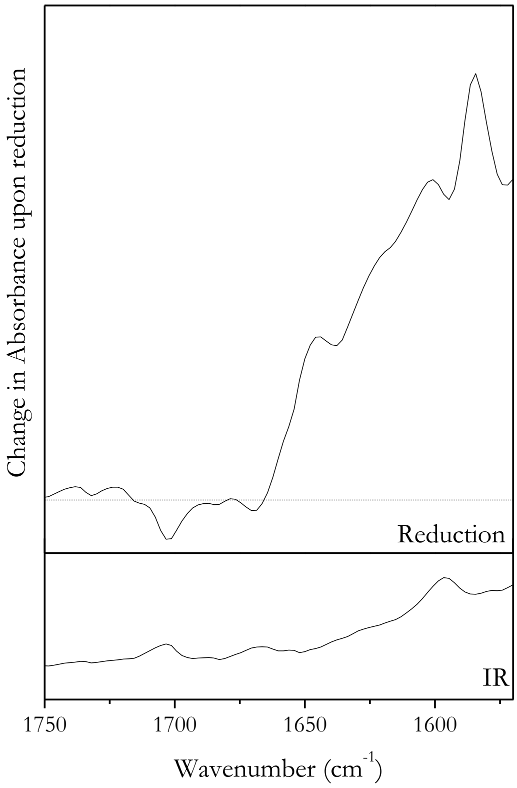

Figure 2.35 Infrared spectra showing the change in absorption that occurs upon reduction for 7. Spectra recorded in solution phase containing [Bu$_4$N][BF$_4$] in DCM at r.t.

Bulk electrolysis and electron paramagnetic resonance spectroscopy was performed on dimer **7** to investigate the location of unpaired electrons in the electrogenerated species. Bulk electrolysis was used to generate the dianion of **7** in DCM containing $[Bu_4N][BF_4]$ (0.4 M) and the solution was found to be EPR active and blue in colour. The EPR spectrum is shown in *Figure 2.36* recorded at ambient temperature. A g_{iso} value of 2.0034 was measured and the spectrum represents a diradical species, resembling that of a S = ½ system. It is suggested that there are two unpaired electrons in the molecule, one in each of two equivalent orbitals, on each of the PDI units which are not interacting with each other and therefore forming a 2 x s = ½ system.

Since there are two unpaired electrons present in the system, further investigation into the EPR spectroscopy of dimer **7** was completed. If the unpaired electrons are aligned antiparallel, the multiplicity is a singlet (S= 0) and therefore is EPR silent. However, if the spins are aligned parallel (S = 1), the multiplicity is a triplet which would be EPR active. Triplet states are typically only seen in a frozen solution rather than fluid solution, due to the increased relaxation time and therefore the frozen solution of **7** was investigated. From the results of the frozen solution spectrum the presence of any significant amount of triplet state is eliminated.

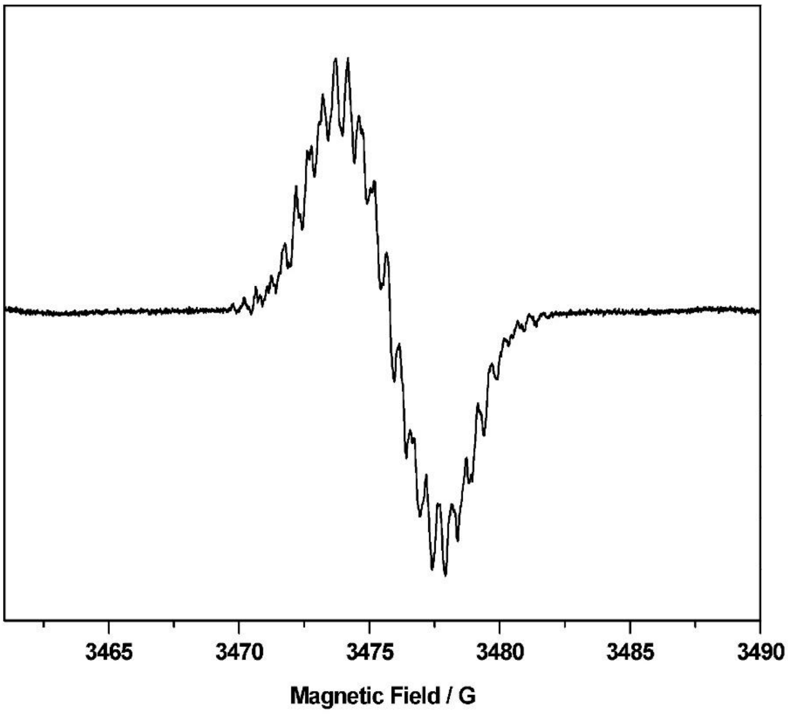

Figure 2.36 X-band fluid solution EPR spectrum of reduced ***7*** *in DCM containing [Bu_4N][BF_4] (0.4 M) recorded at ambient temperature.*

The gas phase structure for dimer **7** was predicted from DFT geometry optimization calculations. Two views of the predicted structure are shown in *Figure 2.37* and from the two views it can be seen that the plane of the organic linker (bis(4-aminophenyl)ethyne) is approximately perpendicular to the perylene core planes. Further analysis of the structure reveals that the two PDI subunits have a torsion angle of 8.17°.

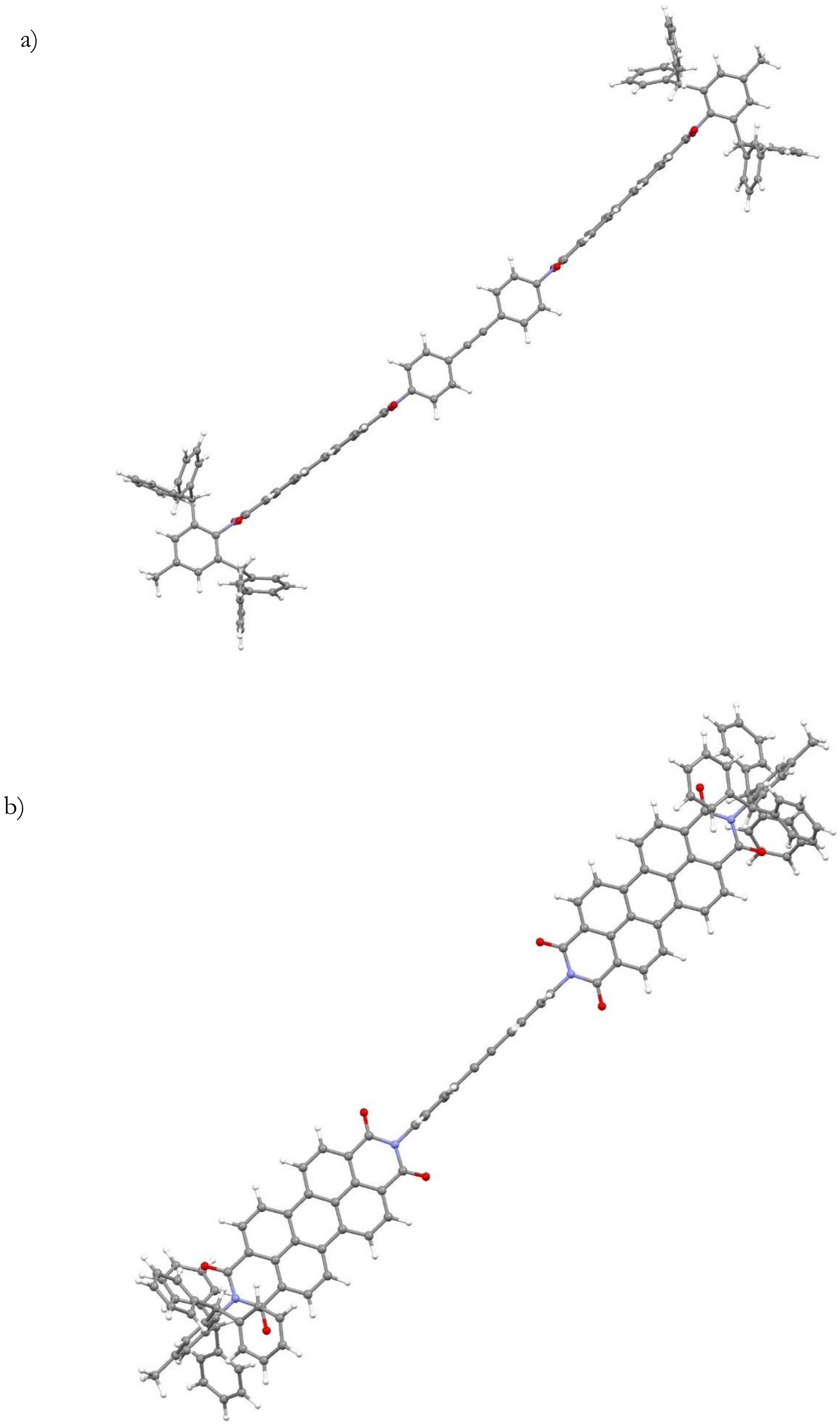

Figure 2.37 The minimised molecular structure of dimer ***7*** *calculated using DFT. Atom colours; carbon = grey, hydrogen = white, oxygen = red and nitrogen = blue.*

2.3 Conclusions

A series of asymmetric PMIAs have been synthesised and characterised. The synthesis involved a series of steps with multiple purification columns and each compound is characterised when possible by ^{1}H NMR, ^{13}C NMR and MS. Single crystals were grown for **3a** and **4b**, both crystallising in the *P*-1 space group. The monoimide diester species **3a** was investigated using Hirshfeld surface analysis which probed the various intermolecular forces present in the crystal structure. The closest point of contact was at the edges of two adjacent molecules where hydrogen interactions (C=O···H-C) took place with a distance of 2.26 Å. Fingerprint plots of **3a** informed that the largest contribution of intermolecular forces were from H···H contacts contributing 71 %. The deconvolution of different interactions on the Hirshfeld surface indicates that a large contribution of H···H contacts was from interactions of decyl chains in adjacent molecules.

4d was used to build larger molecular systems by dimerizing two PMIA units with organic linkers. Two different linkers were used including *p*-xylylenediamine and *bis(4*-aminophenyl)ethyne to synthesise dimers **5** and **7** respectively. The molecular structure of the dimers were predicted using DFT calculations showing that dimer **5** consisted of the two perylene units in different planes compared to dimer **7** where the units were in the same planes with a torsion angle of 8.17°.

A combination of electroanalytical techniques were investigated for dimer **7** including CV, spectroelectrochemistry and EPR spectroscopy. CV revealed two reversible two-electron reduction processes on each of the PDI units at -0.97 V and -1.18 V (*vs* Fc$^+$/Fc). Spectroelectrochemical investigations revealed the direduced species possesses an absorption band placed between the neutral and monoreduced absorption bands. EPR spectroscopy showed that species **7** forms a stable diradical, where unpaired electrons sit on each of the PDI units and do not communicate with each other and form a 2 x $s = ½$ system.

2.4 Experimental

2.4.1 Materials

All chemicals were obtained from commercial suppliers, (Alfa Aesar, Fisher Scientific, Sigma-Aldrich, or VWR international) and used without further purification. Column chromatography was performed on silica gel (Merck silica gel 60, 0.2 - 0.5 mm, 50 - 130 mesh). Preparative thin layer chromatography was also employed, using silica gel as the stationary phase on plates purchased from AnalTech. Anhydrous dichloromethane was purchased from Sigma-Aldrich (Fluka) and stored over 4 Å molecular sieves in a nitrogen atmosphere. Reactions sensitive to air and moisture were performed using a standard Schlenk line, with nitrogen as the inert gas. Glassware was flame dried under vacuum and backfilled with dinitrogen.

2.4.2 General Equipment

2.4.2.1 NMR Spectroscopy

Proton and carbon NMR experiments were carried out using either a JEOL EX270 (270 MHz), Bruker DPX400 (400 MHz), Bruker AV(III)400hd (400 MHz), Bruker AV(III)400 (400 MHz) or AV(III)500 (500 MHz) instrument at room temperature. Chemical shifts are reported with respect to the $CDCl_3$ residual peak at 7.26 ppm (^1H) and 77.00 ppm (^{13}C) or DMSO-d_6 residual peak at 2.50 ppm. For ^1H spectroscopy, splitting patterns are described in brackets after the chemical shift as s = singlet, d = doublet, t = triplet, q = quartet, m = multiplet, or qd = quartet of doublets. Coupling constant (*J* = Hz) and the number of atoms in that environment follow after.

2.4.2.2 Mass Spectrometry

Electrospray ionisation (ESI) spectra were recorded on a Bruker MicroTOF II spectrometer (Bruker Daltonik, Bremen, Germany), operating in Flow Injection mode, using methanol or acetonitrile as the solvent. Field desorption (FD) spectra were acquired on a JEOL AccuTOF GCX (JEOL Corp., Tokyo, Japan) time-of-flight mass spectrometer, employing an appropriate (poly)ethylene glycol as a mass reference. Field ionisation (FI) spectra were acquired on a JOEL GCv4G spectrometer. Nominal mass matrix-assisted laser desorption/ionisation (MALDI) spectra were recorded with a Bruker Ultraflex III mass spectrometer (Bruker Daltonik, Bremen, Germany) using trans-2-[3-(4-tert-butylphenyl)-2-methyl-2-propenylidene]-malononitrile (DCTB) as the matrix. High resolution (HR) MALDI spectra were obtained by co-calibrating the recorded spectrum against that of an appropriate (poly)ethylene glycol standard.

2.4.2.3 Elemental Analysis

Elemental analysis was performed using an automated CE-440 Elemental Analyser.

2.4.2.4 Infrared Spectroscopy

Infrared spectra were obtained with a Bruker Tensor 27 FTIR spectrometer at room temperature (with an ATR attachment if necessary).

2.4.2.5 UV-vis Absorption

UV-vis absorption spectra were recorded on a Perkin-Elmer Lambda 25 spectrometer.

2.4.2.6 X-ray Crystallography

Single crystals of **3a** ($C_{48}H_{59}NO_6$) were grown *via* a layering technique where **3a** was dissolved in chloroform and an equivalent amount of hexane was carefully layered on top. Slow diffusion of the layers resulted in suitable crystals. Data was collected on a **GV1000, Atlas** diffractometer at 120(2) K. Using Olex2,[85] the structure was solved with the ShelXT[86] structure solution program using Intrinsic Phasing and refined with the ShelXL[87] refinement package using Least Squares minimisation.

Crystal Data for **3a** (*M* =745.96 g/mol): triclinic, space group *P*-1 (no. 2), $a = 9.1597(2)$ Å, $b = 9.5135(3)$ Å, $c = 24.8583(5)$ Å, $\alpha = 89.1998(19)°$, $\beta = 89.7837(18)°$, $\gamma = 67.143(2)°$, $V = 1995.88(9)$ Å^3, $Z = 2$, $T = 120(2)$ K, μ(CuKα) = 0.636 mm^{-1}, $Dcalc = 1.241$ g/cm^3, 27492 reflections measured ($7.112° \leq 2\Theta \leq 149.84°$), 7961 unique ($R_{int} = 0.0294$, $R_{sigma} = 0.0217$) which were used in all calculations. The final R_1 was 0.0364 ($I > 2\sigma(I)$), wR_2 was 0.1048 (all data) and GoF = 1.031.

π-π interactions

Plane	**Interacting Plane**	**Centroid-centroid distance (Å)**	**Shift distance (Å)**
C3-C16-C15-C14-C1-C2	C4-C16-C15-C17-C6-C5@2_686 (1-X,3-Y,1-Z)	3.673	1.161
C3-C16-C15-C14-C1-C2	C18-C19-C20-C9-C8-C7@2_676 (1-X,2-Y,1-Z)	3.628	1.355
C3-C16-C15-C14-C1-C2	N31-C24-C4-C16-C3-C23@2_686 (1-X,3-Y,1-Z)	3.930	1.913
C4-C16-C15-C17-C6-C5	C13-C19-C20-C10-C11-C12@2_676 (1-X,2-Y,1-Z)	3.783	1.313
C4-C16-C15-C17-C6-C5	N31-C24-C4-C16-C3-C23@2_686 (1-X,3-Y,1-Z)	3.724	1.379

Single crystals of **4b** ($C_{41}H_{47}NO_5$) were grown *via* a layering technique where **4b** was dissolved in chloroform and an equivalent amount of hexane was layered on top. Slow diffusion of the layers resulted in suitable crystals. The data was collected on a **SuperNova,**

Dual, Cu at zero, Atlas diffractometer kept at 120(2) K during data collection. Using Olex2[85], the structure was solved with the ShelXT[86] structure solution program using Intrinsic Phasing and refined with the ShelXL[87] refinement package using Least Squares minimisation.

Crystal Data for **4b** (*M* =633.79 g/mol): triclinic, space group *P*-1 (no. 2), a = 7.4950(5) Å, b = 10.3064(7) Å, c = 15.4279(12) Å, α = 94.346(6)°, β = 90.326(6)°, γ = 98.863(6)°, V = 1173.95(15) Å^3, Z = 2, T = 120(2) K, μ(CuKα) = 0.922 mm^{-1}, $Dcalc$ = 1.793 g/cm^3, 8530 reflections measured (8.71° $\leq$ 2Θ $\leq$ 149.526°), 4599 unique (R_{int} = 0.0368, R_{sigma} = 0.0459) which were used in all calculations. The final R_1 was 0.0947 (I > 2σ(I)), wR_2 was 0.2837 (all data) and GoF = 1.045.

π-π interactions

Plane	Interacting Plane	Centroid-centroid distance (Å)	Shift distance (Å)
C14-C15-C16-C17-C22-C13	C7-C6-C3-C4-C9-C8@2_566 (-X,1-Y,1-Z)	3.670	1.503
C13-C22-C21-C10-C9-C8	C7-C6-C3-C4-C9-C8@2_566 (-X,1-Y,1-Z)	3.498	0.987
C13-C22-C21-C10-C9-C8	C11-C12-C5-C4-C9-C10@2_666 (1-X,1-Y,1-Z)	3.548	1.153
C7-C6-C3-C4-C9-C8	C11-C12-C5-C4-C9-C10@2_666 (1-X,1-Y,1-Z)	3.617	1.366
C11-C12-C5-C4-C9-C10	C11-C12-C5-C4-C9-C10@2_666 (1-X,1-Y,1-Z)	3.814	1.832
C14-C15-C16-C17-C22-C13	C7-C6-C3-C4-C9-C8@2_566 (-X,1-Y,1-Z)	3.670	1.503

C13-C22-C21-C10-C9-C8	C7-C6-C3-C4-C9-C8@2_566 (-X,1-Y,1-Z)	3.498	0.987
C13-C22-C21-C10-C9-C8	C11-C12-C5-C4-C9-C10@2_666 (1-X,1-Y,1-Z)	3.548	1.153
C7-C6-C3-C4-C9-C8	C11-C12-C5-C4-C9-C10@2_666 (1-X,1-Y,1-Z)	3.617	1.366
C11-C12-C5-C4-C9-C10	C11-C12-C5-C4-C9-C10@2_666 (1-X,1-Y,1-Z)	3.814	1.832

2.4.2.7 Molecular Hirshfeld Surfaces

The molecular Hirshfeld surfaces of **3a** were generated using a standard (high) surface resolution using the program CrystalExplorer.[73] The 3D d_e surfaces were mapped over a fixed colour scale of 0.966 (red) to green to 2.409 Å (blue). The 3D d_{norm} surfaces were mapped over a fix colour scale of -0.265 (red) to 1.396 a.u. (blue). The surfaces were shown to be transparent for aid in visualization of interactions.

2.4.2.8 Cyclic Voltammetry

Cyclic voltammetry was carried out using an Autolab PGSTAT20 potentiostat under an argon atmosphere using a three-electrode arrangement in a single compartment cell. Glassy carbon was used as the working electrode, platinum wire as the secondary electrode and a silver/silver chloride reference electrode, chemically isolated from the test solution *via* a fritted bridge tube containing electrolyte solution, in the cell. An analyte concentration of 1 mM was used with $[Bu_4N][BF_4]$ (400 mM) as a supporting electrolyte. Redox potentials are referenced to the ferrocenium/ferrocene couple, which was implemented as an internal reference.[88]

2.4.2.9 *Spectroelectrochemistry*

UV-vis spectroelectrochemical measurements were performed using an optically transparent quartz electrochemical cell, with a 0.5 mm path length. A three-electrode configuration of a platinum/rhodium gauze working electrode, platinum wire secondary electrode and a silver/silver chloride reference electrode (chemically isolated *via* a fritted bridge tube) were used in the cell. The potential at the working electrode was regulated with a Sycopel Scientific Ltd DD10M potentiostat and the spectra recorded with a Perkin Elmer 16 spectrophotometer. Temperature control was achieved with a stream of chilled nitrogen gas (cooled by passing through a tube submerged in liquid nitrogen) across the surface of the cell, adjusting the flow rate as necessary in response to a temperature sensor (±0.1 °C). $[Bu_4N][BF_4]$ (400 mM) was used as the supporting electrolyte for the experiments.

2.4.2.10 *Infrared Spectroscopy of Electrogenerated Species*

Samples of reduced compound were electrogenerated using the bulk electrolysis technique described above, with a working electrode compartment containing the analyte at (0.84 mM) and $[Bu_4N][BF_4]$ (400 mM) as the supporting electrolyte at 0 °C. After electrolysis, the prepared solution was transferred by cannula to an argon-purged adjustable path-length IR cell with KBr windows for analysis on a Bruker IR spectrometer. The spectra were recorded at ambient temperature.

2.4.2.11 *Bulk Electrolysis and Electron Paramagnetic Resonance*

Bulk electrolysis was performed under an argon atmosphere at 0 °C in a two-component cell: a platinum/rhodium gauze working electrode and secondary electrode are separated by a glass frit. A silver/silver chloride reference electrode was bridged to the test solution through a vycor frit, oriented at the centre of the working electrode. The working electrode compartment, containing analyte (0.84 mM), was stirred rapidly with a magnetic stirrer bar during electrolysis. $[Bu_4N][BF_4]$ (400 mM) was used as the supporting electrolyte for the experiments.

After electrolysis was completed, the prepared solution was transferred by cannula to a quartz EPR tube for analysis on a Bruker EMX spectrometer. Solution phase (fluid) spectra were recorded at room temperature and frozen (glass) spectra were recorded by freezing the electrogenerated radical solution in liquid nitrogen within an additional quartz dewar. Spectra were simulated when possible using WIN EPR SimFonia software.

2.4.2.12 Density Functional Calculations

DFT calculations were performed using Gaussian 09 software with the B3LYP exchange-correlation function and a 6-311g(d,p) basis set for all atoms.[89-91] Geometry optimizations on models of A and B were performed in a dichloromethane solvent field using a polarizable continuum model. The calculated geometries were recognized as local minima by frequency calculations.

2.4.3 Synthesis of Asymmetric Perylene Derivatives

Synthesis of 3,4,9,10-tetra(decyloxycarbonyl)perylene 1

The synthesis of this compound was carried out according to a literature procedure.[71] To a stirred solution of potassium hydroxide (3.00 g, 53.5 mmol) in deionised water (50 mL), 3,4,9,10-perylenetetracarboxylic dianhydride (3.92 g, 10.0 mmol) was added, and the mixture heated to 70 °C for 1 h. To this, aliquat-336 (1.35 g, 3.30 mmol) and potassium iodide (0.25 g, 1.50 mmol) were added and the mixture was vigorously stirred for 10 min. 1-Bromodecane (17.8 g, 80.2 mmol) was added and the mixture heated under reflux for

4 h. The reaction product was extracted with chloroform and washed with an aq. solution of sodium chloride (15 % (w/v), 3 x 100 mL). Methanol was added to precipitate the desired orange solid, which was collected by filtration (6.00 g, 61 %).

^{1}H NMR (400 MHz, Chloroform-*d*) δ 8.22 (d, *J* = 8.1 Hz, 4H), 8.01 (d, *J* = 7.9 Hz, 4H), 4.33 (t, *J* = 6.9 Hz, 8H), 1.81 (m, 8H), 1.49 – 1.42 (m, 8H), 1.38 – 1.26 (m, 48H), 0.91 – 0.86 (m, 12H). ^{13}C NMR (101 MHz, $CDCl_3$) δ 168.5, 133.0, 130.4, 130.4, 129.0, 128.8, 121.3, 65.6, 31.9, 29.6, 29.5, 29.4, 29.3, 28.6, 26.0, 22.7, 14.1. IR (ATR): 2917, 2849, 1717, 1277, 1169, 746 cm^{-1}. MS (MALDI)$^-$ m/z 988.63 ($C_{64}H_{92}O_8$ [M]$^-$ requires 988.68). Elemental Analysis calc'd for $C_{64}H_{92}O_8$: C 77.69 %, H 9.37 %, found: 77.6 %, H 9.35 %.

Synthesis of perylene-3,4-anhydride-9,10-di-(decyloxycarbonyl) 2

The synthesis of this compound was carried out according to a literature procedure.[43] To a solution of **1** (2.92 g, 2.95 mmol) in toluene (0.79 mL), n-dodecane (3.88 mL) was added and heated to 95 °C. *p*-toluenesulfonic acid monohydrate (0.56 g, 2.95 mmol) was added over a period of 5 h at 95 °C with monitoring *via* TLC. The red reaction mixture was transferred to a cellulose tube and dissolved in chloroform (250 mL) *via* a Soxhlet extractor overnight. This was purified by column chromatography (silica, chloroform: acetone [95:5]) to afford **2** as a red solid (1.35 g, 66 %).

^{1}H NMR (400 MHz, Chloroform-*d*) δ 8.65 (d, *J* = 8.1 Hz, 2H), 8.52 (t, *J* = 8.1 Hz, 4H), 8.14 (d, *J* = 7.9 Hz, 2H), 4.35 (t, *J* = 6.9 Hz, 4H), 1.81 (m, 4H), 1.49 – 1.42 (m, 4H), 1.32 – 1.26 (m, 24H), 0.90 – 0.86 (m, 6H). ^{13}C NMR (101 MHz, $CDCl_3$) δ 168.0, 160.3, 137.3, 133.6, 132.8, 131.9, 131.5, 130.4, 129.3, 129.2, 128.5, 123.5, 122.1, 118.0, 66.0, 31.9, 29.7, 29.6, 29.5, 29.4, 28.6, 26.0, 22.7, 14.1. IR (ATR): 2921, 2852, 1766, 1707, 1592, 1282, 1124, 1009, 805, 736 cm^{-1}. HRMS (FI)$^-$ m/z 690.3580 ($C_{44}H_{50}O_7$ [M]$^-$ requires 690.3562).

Synthesis of *N*-(butyl)-perylene-3,4-dicarboximide-9,10-di-(decyloxycarbonyl) 3a

A flame-dried two-neck flask with a condenser fitted was purged three times with N_2 and charged with **2** (0.221 g, 0.319 mmol), *n*-butylamine (0.11 mL, 0.959 mmol) and imidazole (1 g) and heated to 130 °C for 3.5 h with stirring. After cooling to room temperature, the solid contents of the reaction were dissolved in chloroform (55 mL) and washed with deionised water (3 x 40 mL). The organic layer was dried over anhydrous $MgSO_4$, filtered under gravity, and the solvent removed under vacuum. The red product was purified by column chromatography (silica, chloroform: acetone [99.9:0.1]) to afford **3a** as a red solid (0.157 g, 66 %).

^{1}H NMR (400 MHz, Chloroform-*d*) δ 8.41 (d, *J* = 8.0 Hz, 2H), 8.17 (dd, *J* = 11.1, 8.1 Hz, 4H), 7.99 (d, *J* = 7.9 Hz, 2H), 4.36 (t, *J* = 6.9 Hz, 4H), 4.19 (t, *J* = 8 Hz, 2H), 1.84 (m, 4H), 1.79 – 1.71 (m, 2H), 1.54-1.44 (m, 6H), 1.43 – 1.20 (m, 24H), 1.03 (t, *J* = 7.4 Hz, 3H), 0.89 (t, *J* = 6.8 Hz, 6H). ^{13}C NMR (101 MHz, $CDCl_3$) δ 168.2, 163.4, 135.1, 131.8, 131.1, 130.2, 130.2, 129.1, 128.8, 128.8, 125.6, 122.4, 121.9, 121.6, 65.9, 40.3, 31.9, 30.2, 29.4, 29.3, 28.6, 28.6, 26.0, 22.7, 20.4, 20.0, 14.1, 13.9. HRMS (FD)$^+$ m/z 745.4337 ($C_{48}H_{59}NO_6$ [M]$^+$ requires 745.4337).

Synthesis of *N*-(1-ethylpropyl)-perylene-3,4-dicarboximide-9,10-di-(decyloxycarbonyl) 3b

A flame-dried 2-neck flask with a condenser fitted was purged three times with N_2 and charged with **2** (0.235 g, 0.34 mmol), 3-aminopentane (0.11 mL, 1.02 mmol) and imidazole (1 g) and heated to 130 °C for 5 h with stirring. After cooling, the solid contents of the reaction were dissolved in chloroform (70 mL) and washed with deionised water (3 x 70 mL). The organic layer was dried over anhydrous $MgSO_4$, filtered under gravity and the solvent removed under vacuum to afford a red solid. This was purified by column chromatography (silica, chloroform: acetone [99.9:0.1]) to afford **3b** as a red solid (0.107 g, 41 %).

^{1}H NMR (400 MHz, Chloroform-*d*) δ 8.52 (d, *J* = 7.9 Hz, 2H), 8.30 (t, *J* = 7.7 Hz, 4H), 8.03 (d, *J* = 7.8 Hz, 2H), 5.12-5.04 (m, 1H), 4.35 (t, *J* = 6.8 Hz, 4H), 2.35-2.23 (m, 2H), 2.01-1.91 (m, 2H), 1.83 (m, 4H), 1.49-1.44 (m, 4H), 1.38-1.28 (m, 24H), 0.96 (t, *J* = 7.4 Hz, 6H), 0.88 (t, *J* = 6.3 Hz, 6H). ^{13}C NMR (126 MHz, $CDCl_3$) δ 168.2, 163.9, 135.1, 132.0, 131.8, 131.4, 131.3, 130.2, 129.3, 129.1, 129.0, 125.8, 122.4, 121.7, 65.9, 57.5, 31.9, 29.6, 29.6, 29.3, 29.3, 28.6, 26.0, 25.0, 22.7, 14.1, 11.4. HRMS (FD)$^+$ m/z 759.4461 ($C_{49}H_{61}NO_6$ [M]$^+$ requires 759.4493).

Synthesis of *N*-(cyclohexyl)-perylene-3,4-dicarboximide-9,10-di-(decyloxycarbonyl) 3c

A flame-dried two-neck flask with a condenser fitted was purged three times with N_2 and charged with **2** (0.208 g, 0.301 mmol), 3-aminopentane (0.10 mL, 0.904 mmol) and imidazole (1 g) and heated to 130 °C for 5 h with stirring. After cooling to room temperature, the solid contents of the reaction were dissolved in chloroform (70 mL) and washed with deionised water (3 x 70 mL). The organic layer was dried over anhydrous $MgSO_4$, filtered under gravity and the solvent removed *in vacuo* to produce a red solid. This was purified by column chromatography (silica, chloroform: acetone [99.9:0.1]) *via* wet loading to afford **3c** as a red solid (0.203 g, 87 %).

^{1}H NMR (400 MHz, Chloroform-*d*) δ 8.21 (d, *J* = 8.0 Hz, 2H), 7.95 – 7.83 (m, 6H), 5.05 (tt, *J* = 12.1, 3.6 Hz, 1H), 4.36 (t, *J* = 7.0 Hz, 4H), 2.62 (qd, *J* = 13.5, 12.8, 4.8 Hz, 2H), 1.97 (d, *J* = 12.8 Hz, 2H), 1.89-1.79 (m, 6H), 1.54 – 1.24 (m, 32H), 0.93 – 0.84 (m, 6H). ^{13}C NMR (101 MHz, $CDCl_3$) δ 168.1, 163.6, 134.3, 131.6, 131.6, 130.7, 130.0, 128.9, 128.6, 128.4, 125.1, 122.3, 122.0, 121.3, 65.9, 53.8, 31.9, 29.6, 29.6, 29.4, 29.3, 29.1, 28.6, 26.6, 26.0, 25.5, 22.7, 14.1. HRMS (FD)$^+$ m/z 771.4492 ($C_{50}H_{61}NO_6$ [M]$^+$ requires 771.4493).

Synthesis of *N*-(2,6-bis(diphenylmethyl)-4-methylphenyl)-perylene-3,4-dicarboximide-9,10-di-(decyloxycarbonyl) 3d

A flame-dried two-neck flask with a condenser fitted was purged three times with N_2 and charged with **2** (0.466 g, 0.675 mmol), *n*-2,6-bis(diphenylmethyl)-4-methylphenyl amine (0.445 g, 1.01 mmol) and imidazole (0.63 g) and heated to 130 °C for 19 h with stirring. After cooling to room temperature, the solid contents of the reaction were dissolved in chloroform (55 mL) and washed with deionised water (3 x 40 mL). The organic layer was dried over anhydrous $MgSO_4$, filtered under gravity, and the solvent removed *in vacuo* to afford **3d** as a red solid (0.21 g, 28 %).

^{1}H NMR (400 MHz, Chloroform-*d*) δ 8.45 (d, *J* = 8.0 Hz, 2H), 8.41 (d, *J* = 8.0 Hz, 2H), 8.28 (d, *J* = 8.0 Hz, 2H), 8.11 (d, *J* = 7.9 Hz, 2H), 7.16-7.10 (m, 12H), 7.05 – 6.97 (m, 8H), 6.79 (s, 2H), 5.37 (s, 2H), 4.35 (t, *J* = 6.8 Hz, 4H), 2.25 (s, 3H), 1.82 (m, 4H), 1.58 (m, 4H), 1.48 – 1.30 (m, 24H), 0.89 – 0.86 (m, 6H). ^{13}C NMR (101 MHz, $CDCl_3$) δ 168.3, 162.5, 142.2, 142.2, 141.6, 137.9, 135.5, 132.5, 132.3, 132.1, 131.8, 131.3, 131.1, 130.4, 129.6, 129.5, 128.1, 126.2, 122.5, 122.2, 121.7, 65.9, 63.1, 60.7, 52.5, 32.8, 31.9, 28.6, 26.0, 25.7, 22.7, 21.8, 14.1. MS (MALDI)$^-$ m/z 1111.61 ($C_{77}H_{77}NO_6$ [M]$^-$ requires 1111.57). HRMS (MALDI)$^+$ m/z 1111.5756 ($C_{77}H_{77}NO_6$ [M]$^+$ requires 1111.5745).

Synthesis of *N*-(butyl)-perylene-3,4-dicarboximide-9,10-anhydride 4a

To a solution of N-(butyl)-perylene-3,4-dicarboximide-9,10-di-(decyloxycarbonyl) **3a** (90 mg, 0.12 mmol) in toluene (7 mL), heated to 90 °C, *p*-toluenesulphonic acid monohydrate (30 mg, 0.157 mmol) was added. The solution was stirred at 90 °C for 4 h to produce a red solid which was dissolved in chloroform and subsequently purified by column chromatography (silica, chloroform: acetone [99.5:0.5] to afford **4a** as a red solid (9 mg, 16 %). HRMS (FI)$^-$ m/z 447.1109 ($C_{28}H_{17}NO_5$ [M]$^-$ requires 447.1112).

Synthesis of *N*-(1-ethylpropyl)-perylene-3,4-dicarboximide-9,10-anhydride 4b

To a solution of *N*-(1-ethylpropyl)-perylene-3,4-dicarboximide-9,10-di-(decyloxycarbonyl) **3b** (71 mg, 0.093 mmol) in toluene (6 mL), heated to 90 °C, *p*-toluenesulphonic acid monohydrate (17 mg, 0.093 mmol) was added. The solution was stirred at 90 °C for 4 h to produce a dark red solid which was dissolved in chloroform and subsequently purified by column chromatography (silica, chloroform: acetone [97:3]) to afford **4b** as a red solid (13 mg, 30 %).

^{1}H NMR (500 MHz, Chloroform-*d*) δ 8.84 – 8.66 (m, 8H), 5.12-5.06 (m, 1H), 2.34-2.24 (m, 2H), 2.03 – 1.93 (m, 2H), 0.95 (t, *J* = 7.5 Hz, 6H). ^{13}C NMR (126 MHz, $CDCl_3$) δ 160.0, 157.3, 139.2, 136.4, 133.7, 133.6, 131.9, 129.6, 126.9, 126.6, 123.9, 123.5, 123.2, 119.1, 57.9, 25.0, 11.3. HRMS (FI)$^-$ m/z 461.1263 ($C_{28}H_{19}NO_5$ [M]$^-$ requires 461.1269).

Synthesis of *N*-(cyclohexyl)-perylene-3,4-dicarboximide-9,10-anhydride 4c

To a solution of *N*-(cyclohexyl)-perylene-3,4-dicarboximide-9,10-di-(decyloxycarbonyl) **3c** (72 mg, 0.093 mmol) in toluene (6 mL), heated to 90 °C, *p*-toluenesulphonic acid monohydrate (25 mg, 0.13 mmol) was added. The solution was stirred at 90 °C for 4 h to produce a dark red solid which was dissolved in chloroform and subsequently purified by column chromatography (silica, chloroform: acetone [97:3]) to afford **4c** as a dark purple (15 mg, 34 %).

^{1}H NMR (500 MHz, Chloroform-*d*) δ 8.80 – 8.63 (m, 8H), 5.06 (tt, *J* = 12.2, 3.7 Hz, 1H), 2.58 (qd, *J* = 12.5, 3.4 Hz, 2H), 1.93 (d, *J* = 13.5 Hz, 2H), 1.77 (t, *J* = 12.9 Hz, 3H), 0.89 (t, *J* = 6.9 Hz, 3H). ^{13}C NMR (126 MHz, $CDCl_3$) δ 163.6, 160.0, 136.5, 133.6, 133.6, 131.9, 131.4, 129.4, 126.9, 126.5, 124.7, 123.9, 123.2, 119.0, 54.2, 26.5, 25.4, 14.1. HRMS (FI)$^-$ m/z 473.1291 ($C_{30}H_{19}NO_5$ [M]$^-$ requires 473.1269).

Synthesis of *N*-(2,6-bis(diphenylmethyl)-4-methylphenyl)-perylene-3,4-dicarboximide-9,10-anhydride 4d

To a solution of N-(2,6-bis(diphenylmethyl)-4-methylphenyl)-perylene-3,4-dicarboximide-9,10-di-(decyloxycarbonyl) **3d** (0.129 g, 0.116 mmol) in toluene (8 mL), heated to 90 °C, *p*-toluenesulphonic acid monohydrate (0.086 g, 0.45 mmol). The solution was stirred at 90 °C for 5 h in total to produce a red solid. The solvent was removed *in vacuo*. The remaining solid was dissolved in chloroform and subsequently purified by column chromatography (silica, chloroform: acetone [98.5:1.5] to afford **4d** as a bright red solid (56 mg, 59 %).

^{1}H NMR (400 MHz, Chloroform-*d*) δ 8.78 – 8.67 (m, 4H), 8.62 (d, *J* = 8.1 Hz, 2H), 8.37 (d, *J* = 8.0 Hz, 2H), 7.15-7.11 (m, 12H), 7.01-6.98 (m, 8H), 6.78 (s, 2H), 5.33 (s, 2H), 2.25 (s, 3H). ^{13}C NMR (126 MHz, $CDCl_3$) δ 162.1, 160.0, 142.2, 142.0, 138.2, 136.6, 133.8, 133.6, 131.9, 131.3, 131.2, 129.7, 129.5, 129.4, 128.1, 126.9, 126.6, 126.3, 124.0, 123.8, 123.2, 119.0, 52.6, 21.8. HRMS (FD)$^+$ m/z 813.2512 ($C_{57}H_{35}NO_5$ [M]$^+$ requires 813.2510).

2.4.4 Synthesis of Dimerised PDIs

Synthesis of *N,N'*-bis(*N''*-(2,6-bis(diphenylmethyl)-4-methylphenyl)perylene-3,4,9,10-tetracarboxylic diimide)-*p*-xylylene diamine 5

A flame-dried two-neck flask with a condenser fitted was purged three times with N_2 and charged with N-(2,6-bis(diphenylmethyl)-4-methylphenyl)-perylene-3,4-dicarboximide-9,10-di-(decyloxycarbonyl) **4d** (50 mg, 0.0615 mmol), *p*-xylylene diamine (4.18 mg, 0.0301 mmol), imidazole (30 mg) and toluene (1 mL) and heated to 130 °C for 22 h with stirring. After cooling to room temperature, the solid contents of the reaction were dissolved in chloroform (20 mL) and washed with deionised water (20 mL). The organic layer was dried over anhydrous $MgSO_4$, filtered under gravity and the solvent removed under vacuum. This was purified *via* column chromatography (silica, chloroform: acetone ~[99.9:0.1]) to afford **5** as a red solid (7 mg, 13 %).

^1H NMR (500 MHz, Chloroform-*d*) δ 8.70 (d, *J* = 8.0 Hz, 4H), 8.63 (d, *J* = 8.2 Hz, 4H), 8.56 (d, *J* = 8.2 Hz, 4H), 8.33 (d, *J* = 8.0 Hz, 4H), 7.57 (s, 4H), 7.18 – 7.05 (m, 24H), 7.0-6.97 (m, 16H), 6.77 (s, 4H), 5.40 (s, 4H), 5.33 (s, 4H), 2.24 (s, 6H). ^{13}C NMR (126 MHz, $CDCl_3$) δ 163.5, 162.2, 142.2, 142.1, 138.0, 136.4, 136.1, 135.1, 134.5, 131.7, 131.3, 129.6, 129.5, 129.3, 128.4, 128.1, 127.2, 126.4, 126.2, 123.4, 123.1, 121.5, 119.7, 52.6, 22.7, 14.1. HRMS (MALDI)$^+$ m/z 1749.5699 ($C_{122}H_{78}N_4O_8Na$ [M+Na]$^+$ requires 1749.5712).

Synthesis of bis(4-aminophenyl)ethyne 6

The synthesis of this compound was carried out according to a literature procedure.[79] A flame-dried two-neck flask was purged three times with N_2 and charged with $PdCl_2(PPh_3)_2$ (10 mg, 0.015 mmol), CuI (5.7 mg, 0.003 mmol), 4-iodoaniline (0.329 g, 1.5 mmol), THF (6 mL), and 4-ethynyl aniline (0.19 g, 1.5 mmol) and stirred at room temperature for 30 min. An aqueous ammonia (6 mL, 3 mmol, 0.5 M) was added drop-wise to the reaction mixture and stirring was continued for 4 h. Two phases of the resulting mixture were separated and the aqueous layer was extracted with diethyl ether and dried over $MgSO_4$. The combined organic layer was reduced *in vacuo*. Purification of **6** involved recrystallization using ethyl acetate/hexane to afford green-brown needles (0.278 g, 89 %).

^{1}H NMR (400 MHz, DMSO-*d*$_6$) δ 7.10 (d, *J* = 8.5 Hz, 4H), 6.52 (d, *J* = 8.6 Hz, 4H), 5.40 (s, 4H). ^{13}C NMR (101 MHz, DMSO) δ 148.6, 132.0, 113.6, 109.5, 87.7, 39.5. IR (ATR): 3464, 3370, 1613, 1515, 1288, 784 cm^{-1}. MS (ESI) m/z 209.10 ($C_{14}H_{12}N_2$ [M+H] requires 209.1079).

Synthesis of *N,N'*-bis(*N*''-(2,6-bis(diphenylmethyl)-4-methylphenyl)perylene-3,4,9,10-tetracarboxylic diimide)-bis-(4-aminophenyl)ethyne 7

A flame-dried two-neck flask with a condenser fitted was purged three times with N_2 and charged with *N*-(2,6-bis(diphenylmethyl)-4-methylphenyl)-perylene-3,4-dicarboximide-9,10-anhydride **4d** (34 mg, 0.0418 mmol), bis(4-aminophenyl)ethyne **6** (4.3 mg, 0.02 mmol), imidazole (30 mg) and toluene (1 mL) and heated to 130 °C for 18 h with stirring. After cooling to room temperature, the solid contents of the reaction were dissolved in chloroform (30 mL) and washed with deionised water (30 mL). The organic layer was dried over anhydrous $MgSO_4$, filtered under gravity and the solvent removed *in vacuo* to produce a red solid. This was purified *via* column chromatography (silica, chloroform: acetone [99.9:0.1]) to afford **7** as a red solid (4.1 mg, 11 %).

^{1}H NMR (400 MHz, Chloroform-*d*) δ 8.79 (d, *J* = 8.0 Hz, 4H), 8.71 (d, *J* = 8.3 Hz, 4H), 8.63 (d, *J* = 8.3 Hz, 4H), 8.38 (d, *J* = 8.0 Hz, 4H), 7.79 (d, *J* = 8.6 Hz, 4H), 7.41 (d, *J* = 8.5 Hz, 4H), 7.16-7.12 (m, 24H), 7.02-7.0 (m, 16H), 6.79 (s, 4H), 5.36 (s, 4H), 2.26 (s, 6H). ^{13}C NMR (101 MHz, $CDCl_3$) δ 163.5, 162.2, 142.2, 142.1, 138.1, 135.4, 135.0, 134.5, 132.7, 132.0, 131.3, 129.9, 129.6, 129.6, 129.3, 128.8, 128.4, 128.1, 126.8, 126.5, 126.3, 123.9, 123.5, 123.2, 123.1, 89.7, 52.6, 21.8. MS (MALDI)$^+$ m/z 1799.58 ($C_{128}H_{78}N_4O_8$ [M+H]$^+$ requires 1799.58). HRMS (MALDI)$^+$ m/z 1821.5678 ($C_{128}H_{78}N_4O_8Na$ [M+Na]$^+$ requires 1821.5712).

2.5 References

1. H. Zollinger, *Color Chemistry: Syntheses, Properties and Applications of Organic Dyes and Pigments*, 2nd edn., Wiley-VCH, Germany, 1991.
2. W. Herbst and K. Hunger, *Industrial Organic Pigments: Production, Properties and Applications*, 3rd edn., Wiley-VCH, Germany, 2004.
3. J. Ikonomov, O. Bauer and M. Sokolowski, *Surface Science*, 2008, **602**, 2061-2068.
4. B. A. Paez, G. Salvan, R. Scholz, T. U. Kampen and D. R. T. Zahn, *Proc. SPIE*, 2003, **5217**, 210-218.
5. F. Hiroyuki, T. Sachiko, U. Yasushi, K. Tetsuyuki and T. Sei, *Jpn. J. Appl. Phys.*, 1995, **34**, 3852-3857.
6. I. G. Hill, A. Kahn, Z. G. Soos and R. A. Pascal, *Chem. Phys. Lett.*, 2000, **327**, 181-188.
7. C. Li and H. Wonneberger, *Adv. Mater.*, 2012, **24**, 613-636.
8. S. Chen, P. Slattum, C. Wang and L. Zang, *Chem. Rev.*, 2015, **115**, 11967-11998.
9. Y. Avlasevich, C. Li and K. Mullen, *J. Mater. Chem.*, 2010, **20**, 3814-3826.
10. D. Dotcheva, M. Klapper and K. Müllen, *Macromol. Chem. Phys.*, 1994, **195**, 1905-1911.
11. G. Seybold and G. Wagenblast, *Dyes Pigm.*, 1989, **11**, 303-317.
12. K. Law, *Chem. Rev.*, 1993, **93**, 449-486.
13. J. Kalinowski, P. Di Marco, V. Fattori, L. Giulietti and M. Cocchi, *J. Appl. Phys.*, 1998, **83**, 4242-4248.
14. Y. Li, N. Wang, X. He, S. Wang, H. Liu, Y. Li, X. Li, J. Zhuang and D. Zhu, *Tetrahedron*, 2005, **61**, 1563-1569.
15. D. Schlettwein, D. Wohrle, E. Karmann and U. Melville, *Chem. Mater.*, 1994, **6**, 3-6.
16. M. Sadrai and G. R. Bird, *Opt. Commun.*, 1984, **51**, 62-64.
17. R. Gvishi, R. Reisfeld and Z. Burshtein, *Chem. Phys. Lett.*, 1993, **213**, 338-344.
18. M. Sadrai, L. Hadel, R. R. Sauers, S. Husain, K. Krogh-Jespersen, J. D. Westbrook and G. R. Bird, *J. Phys. Chem.*, 1992, **96**, 7988-7996.
19. R. Schmidt, J. H. Oh, Y.-S. Sun, M. Deppisch, A.-M. Krause, K. Radacki, H. Braunschweig, M. Könemann, P. Erk, Z. Bao and F. Würthner, *J. Am. Chem. Soc.*, 2009, **131**, 6215-6228.
20. S. Tatemichi, M. Ichikawa, T. Koyama and Y. Taniguchi, *Appl. Phys. Lett.*, 2006, **89**, 112108.
21. R. J. Chesterfield, J. C. McKeen, C. R. Newman, P. C. Ewbank, D. t. A. d. S. Filho, J.-L. Bre´das, L. L. Miller, K. R. Mann and C. D. Frisbie, *J. Phys. Chem. B*, 2004, **108**, 19281-19292.
22. P. R. L. Malenfant, C. D. Dimitrakopoulos, J. D. Gelorme, L. L. Kosbar, T. O. Graham, A. Curioni and W. Andreoni, *Appl. Phys. Lett.*, 2002, **80**, 2517-2519.

23. C. D. Dimitrakopoulos and P. R. L. Malenfant, *Adv. Mater.*, 2002, **14**, 99-117.
24. S. Hüttner, M. Sommer and M. Thelakkat, *Appl. Phys. Lett.*, 2008, **92**, 093302.
25. X. Zhang, C. Zhan, X. Zhang and J. Yao, *Tetrahedron*, 2013, **69**, 8155-8160.
26. X. Liu, Y. Zhang, X. Pang, Y. E, Y. Zhang, D. Yang, J. Tang, J. Li, Y. Che and J. Zhao, *J. Phys. Chem. C*, 2015, **119**, 6446-6452.
27. P. Zugenmaier, J. Duff and T. L. Bluhm, *Cryst. Res. Technol.* , 2000, **35**, 1095-1115.
28. F. Graser and E. Hadicke, *Acta Cryst. C*, 1986, **42**, 195-198.
29. E. Hädicke and F. Graser, *Acta Cryst. C*, 1986, **42**, 189–195.
30. F. Würthner, *Chem. Commun.*, 2004, 1564-1579.
31. P. M. Kazmaiergt and R. Hoffmannt, *J. Am. Chem. Soc.*, 1994, **116**, 9684-9691
32. G. Klebe, F. Graser, E. Hädicke and J. Berndt, *Acta Cryst.*, 1989, **B45**, 69-77.
33. J. C. Charlier, X. Gonze and J. P. Michenaud, *Europhys. Lett.*, 1994, **28**, 403-408.
34. Z. Chen, U. Baumeister, C. Tschierske and F. Wurthner, *Chem. - Eur. J.*, 2007, **13**, 450-465.
35. Z. Chen, B. Fimmel and F. Wurthner, *Org. Biomol. Chem.*, 2012, **10**, 5845-5855.
36. C. Huang, S. Barlow and S. R. Marder, *J. Org. Chem.*, 2011, **76**, 2386-2407.
37. H. Langhals, *Heterocycles*, 1995, **40**, 477-500.
38. G. Klebe, F. Graser, E. Hadicke and J. Berndt, *Acta Cryst. B*, 1989, **45**, 69-77.
39. N. I. Georgiev, A. R. Sakr and V. B. Bojinov, *Dyes Pigm.*, 2011, **91**, 332-339.
40. W. Kohn, A. D. Becke and R. G. Parr, *J. Phys. Chem.*, 1996, **100**, 12974-12980.
41. M. C. R. Delgado, E.-G. Kim, D. A. Filho and J.-L. Bredas, *J. Am. Chem. Soc.*, 2010, **132**, 3375-3387.
42. M. Queste, C. Cadiou, B. Pagoaga, L. Giraudetc and N. Hoffmann, *New J. Chem.*, 2010, **34**, 2537-2545.
43. C. Xue, R. Sun, R. Annab, D. Abadi and S. Jin, *Tetrahedron Lett.*, 2009, **50**, 853-856.
44. L. Zang, R. Liu, M. W. Holman, K. T. Nguyen and D. M. Adams, *J. Am. Chem. Soc.*, 2002, **124**, 10640-10641.
45. N. Soh, T. Ariyoshi, T. Fukaminato, K. Nakano, M. Irie and T. Imato, *Bioorg. Med. Chem. Lett.*, 2006, **16**, 2943-2946.
46. T. Fukaminato and M. Irie, *Adv. Mater.*, 2006, **18**, 3225-3228.
47. R. Gómez, J. L. Segura and N. Martín, *Org. Lett.*, 2005, **7**, 717-720.
48. S. Fukuzumi, K. Ohkubo, J. Ortiz, A. M. Gutierrez, F. Fernandez-Lazaro and A. Sastre-Santos, *Chem. Commun.*, 2005, 3814-3816.
49. E. E. Neuteboom, S. C. J. Meskers, E. H. A. Beckers, S. Chopin and R. A. J. Janssen, *J. Phys. Chem. A*, 2006, **110**, 12363-12371.
50. E. E. Neuteboom, E. H. A. Beckers, S. C. J. Meskers, E. W. Meijer and R. A. J. Janssen, *Org. Biomol. Chem.*, 2003, **1**, 198-203.

51. J. Hernando, P. A. J. de Witte, E. M. H. P. van Dijk, J. Korterik, R. J. M. Nolte, A. E. Rowan, M. F. Garca-Parajo and N. F. van Hulst, *Angew. Chem. Int. Ed.*, 2004, **43**, 4045-4049.
52. J. L. Segura, R. Gómez, E. Reinold and P. Bäuerle, *Org. Lett.*, 2005, **7**, 2345-2348.
53. R. Sun, C. Xue, M. Owak, R. M. Peetz and S. Jin, *Tetrahedron Lett.*, 2007, **48**, 6696-6699.
54. Y. Nagao, Y. Abe and T. Misono, *Dyes Pigm.*, 1985, **6**, 303-311.
55. A. G. Slater, University of Nottingham, 2007.
56. H. Langhals and J. Gold, *J. prakt. Chem.*, 1996, **338**, 654-659.
57. A. Wicklein, P. Kohn, L. Ghazaryan, T. Thurn-Albrecht and M. Thelakkat, *Chem. Commun.*, 2010, **46**, 2328-2330.
58. M.-H. Luo and K.-Y. Chen, *Dyes Pigm.*, 2013, **99**, 456-464.
59. H.-Y. Tsai, C.-W. Chang and K.-Y. Chen, *Molecules*, 2014, **19**, 327-341.
60. F. Wurthner, V. Stepanenko, Z. Chen, C. R. Saha-Moller, N. Kocher and D. Stalke, *J. Org. Chem.*, 2004, **69**, 7933-7939.
61. J.-M. Lehn, in *Supramolecular Chemistry*, Wiley-VCH, Germany, 2006, pp. 1-9.
62. J.-M. Lehn, *PNAS*, 2002, **99**, 4763-4768.
63. F. Würthner, C. R. Saha-Möller, B. Fimmel, S. Ogi, P. Leowanawat and D. Schmidt, *Chem. Rev.*, 2016, **116**, 962-1052.
64. D. Baumstark and H.-A. Wagenknecht, *Chem. Eur. J.*, 2008, **14**, 6640-6645.
65. F. Menacher, V. Stepanenko, F. Wurthner and H.-A. W. necht, *Chem. - Eur. J.*, 2011, **17**, 6683-6688.
66. M. T. Indelli, C. Chiorboli, F. Scandola, E. Iengo, P. Osswald and F. Würthner, *J. Phys. Chem. B*, 2010, **114**, 14495-14504.
67. D. Görl, X. Zhang and F. Würthner, *Angew. Chem. Int. Ed.*, 2012, **51**, 6328-6348.
68. J. M. Englert, J. Rohrl, C. D. Schmidt, R. Graupner, M. Hundhausen, F. Hauke and A. Hirsch, *Adv. Mater.*, 2009, **21**, 4265-4269.
69. C. Backes, F. Hauke and A. Hirsch, *Adv. Mater.*, 2011, **23**, 2588-2601.
70. C. Oelsner, C. Schmidt, F. Hauke, M. Prato, A. Hirsch and D. M. Guldi, *J. Am. Chem. Soc.*, 2011, **133**, 4580-4586.
71. X. Mo, H.-Z. Chen, M.-M. Shi and M. Wang, *Chem. Phys. Lett.*, 2006, **417**, 457-460.
72. M. A. Spackman and D. Jayatilaka, *CrystEngComm*, 2009, **11**, 19-32.
73. S. K. Wolff, D. J. Grimwood, J. J. McKinnon, M. J. Turner, D. Jayatilaka and M. A. Spackman, *CrystalExplorer (Version 3.1)*, (2012) University of Western Australia, Australia.
74. J. J. McKinnon, A. S. Mitchell and M. A. Spackman, *Chem. – Eur. J.*, 1998, **4**, 2136-2141.
75. J. J. McKinnon, M. A. Spackman and A. S. Mitchell, *Acta Crystallographica Section B*, 2004, **60**, 627-668.
76. J. J. McKinnon, D. Jayatilaka and M. A. Spackman, *Chem. Commun.*, 2007, 3814-3816.

77. A. D. Martin, J. Britton, T. L. Easun, A. J. Blake, W. Lewis and M. Schröder, *Crys. Growth Des.*, 2015, **15**, 1697-1706.

78. M. A. Spackman and J. J. McKinnon, *CrystEngComm*, 2002, **4**, 378-392.

79. M. M. S. Ahmed and A. Mori, *Tetrahedron*, 2004, **60**, 9977-9982.

80. G. Wypych, *Handbook of Solvents, Volume 1*, 2nd edn., ChemTec Publishing, 2014.

81. N. Pearce, University of Nottingham, 2016.

82. T. W. Chamberlain, E. S. Davies, A. N. Khlobystov and N. R. Champness, *Chem. - Eur. J.*, 2011, **17**, 3759-3767.

83. A. G. Slater, E. S. Davies, S. P. Argent, W. Lewis, A. J. Blake, J. McMaster and N. R. Champness, *J. Org. Chem.*, 2013, **78**, 2853-2862.

84. B. A. Llewellyn, A. G. Slater, G. Goretzki, T. L. Easun, X.-Z. Sun, E. S. Davies, S. P. Argent, W. Lewis, A. Beeby, M. W. George and N. R. Champness, *Dalton Trans.*, 2014, **43**, 85-94.

85. O. V. Dolomanov, L. J. Bourhis, R. J. Gildea, J. A. K. Howard and H. Puschmann, *J. Appl. Crystallogr.*, 2009, **42**, 339-341.

86. G. Sheldrick, *Acta Cryst. A*, 2015, **71**, 3-8.

87. G. Sheldrick, *Acta Cryst. A*, 2008, **64**, 112-122.

88. R. R. Gagne, C. A. Koval and G. C. Lisensky, *Inorg. Chem.*, 1980, **19**, 2854-2855.

89. M. J. Frisch, G. W. Trucks, H. B. Schlegel, G. E. Scuseria, M. A. Robb, J. R. Cheeseman, G. Scalmani, V. Barone, B. Mennucci, G. A. Petersson, H. Nakatsuji, M. Caricato, X. Li, H. P. Hratchian, A. F. Izmaylov, J. Bloino, G. Zheng, J. L. Sonnenberg, M. Hada, M. Ehara, K. Toyota, R. Fukuda, J. Hasegawa, M. Ishida, T. Nakajima, Y. Honda, O. Kitao, H. Nakai, T. Vreven, J. A. Montgomery Jr., J. E. Peralta, F. Ogliaro, M. J. Bearpark, J. Heyd, E. N. Brothers, K. N. Kudin, V. N. Staroverov, R. Kobayashi, J. Normand, K. Raghavachari, A. P. Rendell, J. C. Burant, S. S. Iyengar, J. Tomasi, M. Cossi, N. Rega, N. J. Millam, M. Klene, J. E. Knox, J. B. Cross, V. Bakken, C. Adamo, J. Jaramillo, R. Gomperts, R. E. Stratmann, O. Yazyev, A. J. Austin, R. Cammi, C. Pomelli, J. W. Ochterski, R. L. Martin, K. Morokuma, V. G. Zakrzewski, G. A. Voth, P. Salvador, J. J. Dannenberg, S. Dapprich, A. D. Daniels, Ö. Farkas, J. B. Foresman, J. V. Ortiz, J. Cioslowski and D. J. Fox, *Gaussian 09 Revision E. 01*, (2009) Gaussian, Inc., Wallingford, CT, USA.

90. C. Lee, W. Yang and R. G. Parr, *Phys. Rev. B*, 1988, **37**, 785-789.

91. T. Yanai, D. P. Tew and N. C. Handy, *Chem. Phys. Lett.*, 2004, **393**, 51-57.

Chapter 3

Synthesis and Analysis of Silicon Nanosheets

3.1 Introduction

Silicon nanomaterials and nanostructures are of both industrial and academic interest due to silicon being one of the most important materials for nanoscale devices.[1] In comparison to bulk silicon material, which has been studied in depth,[2-4] silicon nanomaterials are a relatively new field of research, exhibiting many advantageous properties.[5] Silicon nanomaterials can take many different arrangements, examples include; fullerene-like silicon nanoparticles (SiNP), silicon nanotubes (SiNT), silicon nanowires (SiNW), silicon nanoribbons (SiNR) and silicon nanosheets (SiNS).[5] These materials have lately become more topical in the literature. However, the conditions employed for their fabrication have produced challenges for academic researchers as well as for industry.

3.1.1 Silicon Nanomaterials

Silicon nanomaterials have attracted attention due to their unique characteristics, which are not seen in bulk silicon materials. Their photoelectric effects, lower thermal conductivity and higher chemical activities compared to bulk silicon give them a wide scope for use in a range of applications.[1] A brief overview of the main silicon nanomaterials are described below.

3.1.1.1 Silicon Nanoparticles (SiNP)

Low-dimensional materials have been specifically targeted for particular nanoscale devices.[6] Firstly, one might consider zero-dimensional (0D) silicon material such as SiNP.[7, 8] Their average size ranges between 1-10 nm and they are often referred to as nanodots, quantum dots, nanocrystals or nanoclusters. SiNP can have a range of surface groups and a typical TEM image of them is shown in *Figure 3.38a*.

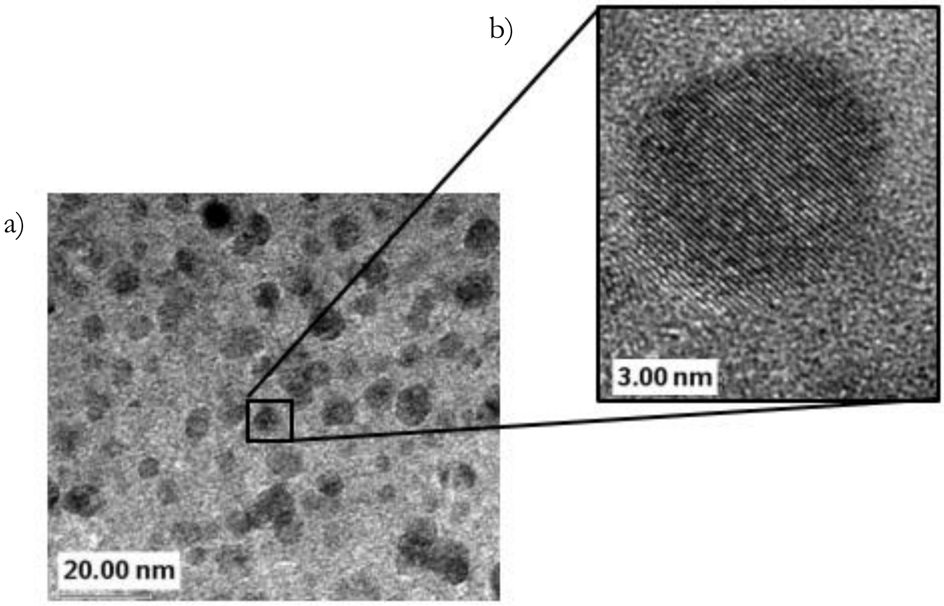

Figure 3.38 TEM image of organo-capped SiNP a) displaying a group of particles and b) high resolution image of one particle.[9]

Many synthetic procedures have been published to fabricate SiNP and the key methods are listed below.

A. Gas phase synthesis:

   i. Pyrolysis of silane: SiNP are produced by microwave plasma decomposition of silane (SiH_4) with hydrogen (H_2) in a flow reactor. Silicon particles are blown through a conical nozzle to a collecting chamber where they are deposited on a substrate, such as a fine stainless steel mesh, or liquid cooled quartz tube.[10-14]

   ii. Synthesis of SiNP by thermal decomposition of dilute silane in helium at 700-1000 °C with subsequent oxidation. The SiNP are collected as a suspension in organic solvents, such as ethylene glycol.[15-17]

iii. Laser ablation method generates SiNP by irradiation of a solid target of silicon, followed by deposition on a hard solid surface substrate by a "nanoparticle beam".[18, 19]

B. Solution phase synthesis:

i. The reduction of $SiCl_4$ and trihalosilanes by sodium metal in a non-polar organic solvent at high temperature and pressure produces SiNP.[20]

ii. Low temperature solution-phase routes have also been reported by reduction of $SiCl_4$ but with different reducing agents such as $LiAlH_4$.[21]

Functionalisation of SiNP *via* capping with a variety of organic groups such as alkyl,[20, 22-24] alkoxy,[24] alcohol,[9, 25] (*Figure 3.38*), organothio[26] and alkylamine[27] has also been reported.

3.1.1.2 Silicon Nanowires (SiNW) and Silicon Nanotubes (SiNT)

SiNW and SiNT both have a one-dimensional (1D) structure. SiNW consist of a diamond arrangement, whereas SiNT take a tubular formation.[28] SiNW have a diameter of less than 100 nm and have stimulated extensive research due to their physical and chemical properties for use in nanodevices.[29] A computational model of a single SiNW is shown in *Figure 3.39a* displaying the diamond-type structure. The Si-Si bonds in the model take an average of 2.35 Å which is expected for Si-Si single bonds. The most common growth techniques for SiNW are thermal evaporation, laser ablation and chemical vapour deposition (CVD).[6]

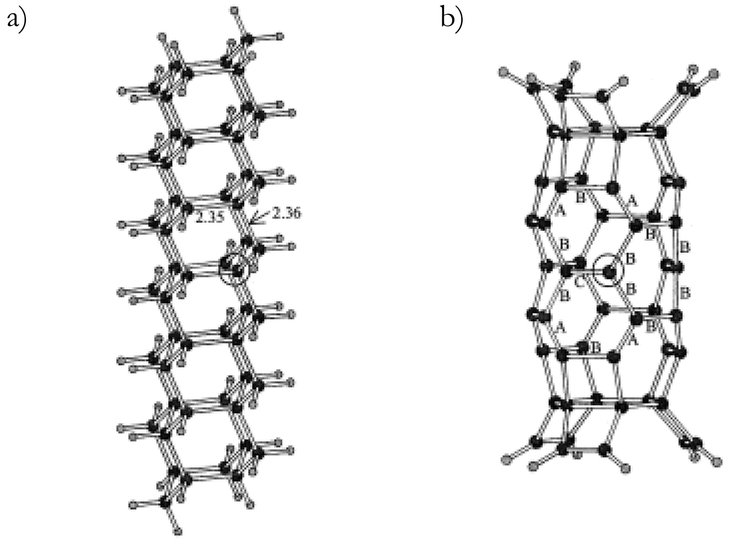

Figure 3.39 Computational model of a) a SiNW ($Si_{54}H_{60}$) and b) a SiNT ($Si_{54}H_{12}$).[28] *All calculations were carried out using the Gaussian 98 package of programs.*[30]

Electronic and structural properties of SiNT have been studied theoretically[28, 31-36] and a computational model is shown in *Figure 3.39b*. SiNT can be considered as a chemical analogue of carbon nanotubes (CNT), a material which has been extensively researched and reported in literature.[37-41] Carbon and silicon are both in Group 14 of the periodic table and have four electrons in their outer valence shell. Both elements are similar in many ways but exhibit different nanostructures due to major differences in their structural, chemical and physical properties. Silicon has an electron configuration of $1s^22s^22p^33s^24s^23p^2$ that favours sp^3 hybridisation compared to carbon which has a configuration of $1s^22s^22p^2$ that favours sp^2 hybridisation.[28, 32] There is a significant increase in the interatomic distance from carbon to silicon radii and the π-π overlap decreases in silicon, resulting in weaker π-bonding.[42] It is for this reasons that the synthesis of SiNT presents more of a challenge than the relative ease with which CNT are synthesised.[28] Computational studies show that there is a large bond length alteration in SiNT with the shortest Si-Si length being 1.85 Å and the longest being 2.25 Å, a variation of 0.4 Å.[28] This suggests there is a strong tendency for bond localisation (Si=Si *vs* Si-Si) and less electron delocalisation due to the poor π-π overlap between silicon atoms. This results in an extremely puckered structure, shown in *Figure 3.39b*, which according to computational studies may be formed under appropriate conditions.

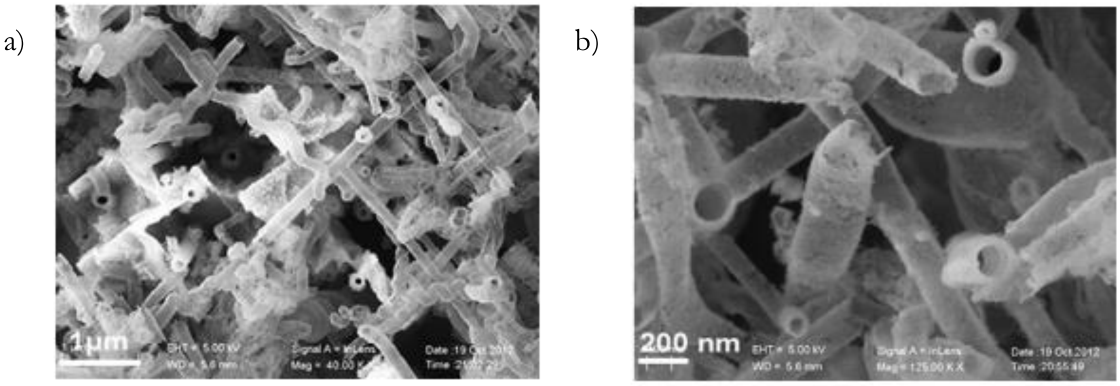

Figure 3.40 SEM images of SiNT on silicon substrates with scales of a) 1 μm and b) 200 nm.[43]

Sophisticated experimental procedures have been utilised to synthesise SiNT,[44-49] where sometimes the nanotubes (NT) are stabilised by the use of a substrate as in *Figure 3.40*.[43] As the synthesis of stable sp^2 coordination structures is impossible with silicon, these tubular structures adopt alternating tetrahedral sp^3 and trigonal-planar sp^2 coordination structures (sp^2-sp^3 tubes). Characterisation methods including electron energy loss spectroscopy (EELS) and transmission electron microscopy (TEM) give evidence for SiNT with single or few layer walls.[47] SiNT have diameters ranging from 2 nm upwards and are hundreds of nanometers in length. Application to date of SiNT concentrate on electronic devices such as potential use in batteries.[45, 50, 51]

3.1.1.3 Silicon Nanoribbons (SiNR)

SiNR are two-dimensional (2D) silicon structures with a buckled hexagonal structure studied both theoretically and experimentally.[52] Nanoribbons have a thickness of 10 to 20 nm, a width of 50 to several 100 nm and lengths of many micrometres.[53, 54] Some SiNR have rippling edges (*Figure 3.41a)* and others have smooth edges (*Figure 3.41b).* This rippling and unique curling feature examined in TEM make them distinctly different to 1D SiNW previously discussed in Section 3.1.1.2.

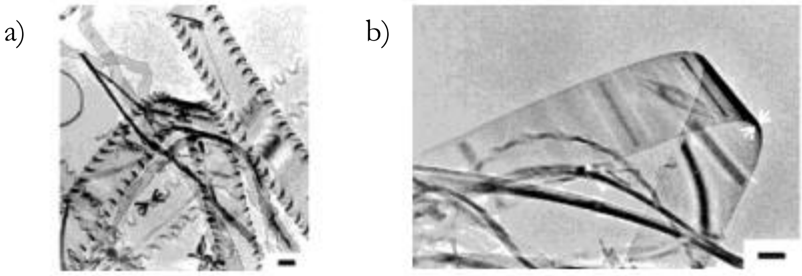

Figure 3.41 TEM images of a) rippling-edge and b) smooth-edge SiNR (scale bar 100 nm).[54]

Common synthetic procedures for SiNR are oxide-assisted growth (OAG) methods.[5, 55] For example, silicon monoxide (SiO) powder is placed in a tube furnace at 1150 °C and the evaporated material is carried down the reactor tube by a gas mixture of 5 % hydrogen in argon.[54] SiNR are grown on substrates placed in the tube, and a typical growth procedure takes approximately two hours. Silicon-carbon nanoribbons (SiCNR) have also been synthesised by a reaction of silicon vapour and carbon black powder at 1,500 °C in argon at atmospheric pressure.[56] A vapour-solid growth mechanism was proposed and the SiCNR were several microns in width.[56]

Often surfaces of SiNR are terminated with hydrogen, however recent investigation into fluorine-terminated analogues has been published.[57] SiNR have been investigated for their application in electronic, photoelectric and chemical-sensing devices,[53, 58, 59] as they show interesting electronic and magnetic properties for use in such devices.[60, 61] Ding and Ni[60] investigated the electronic structures of SiNR which have a buckled geometry, providing spatial control on elastic substrates, and have been reported for use in stretchable electronics.[62, 63] In addition, SiNR can be used as highly specific sensors for biomolecules and therefore are promising candidates for biosensors.[64] Recently, SiNR have been incorporated into prosthetic skin instruments to exploit pressure, strain, humidity and temperature sensors for artificial systems.[65] This prosthetic skin contains stretchable multi-electrode arrays, and a stretchable heater that makes it behave like real skin.

3.1.1.4 Silicon Nanosheets (SiNS)

Since the discovery of graphene, much attention has been focused on 2D nanosheets. Examples include; silicon (Si), molybdenum sulphide (MoS_2) and related dichalcogenides,[66-68] boron nitrides (BN),[69] metal oxide (such as SnO_2 and TiO_2)[70, 71] and metal-organic framework (MOF)[72] nanosheets.[73, 74] A crucial feature of these nanosheets is their incredibly high surface area. SiNS have a thickness of one or a few atomic layers and there are two prominent types of SiNS:

i. Type I: A graphene-like honeycomb lattice structure of silicon known as silicene (discussed in Section 3.1.2).
ii. Type II: A buckled-sheet structure with sp^3 hybridised silicon atoms (discussed in Sections 3.1.3 and 3.1.4).

3.1.2. Silicene: Type I

Silicene (*Figure 3.42*) features a hexagonal lattice in a single atomic layer of silicon, making it the thinnest possible form of silicon.[75] Whilst studies are still in their infancy, silicene has been described as the silicon equivalent of graphene, the material which has gripped the nanomaterial world since 2004.

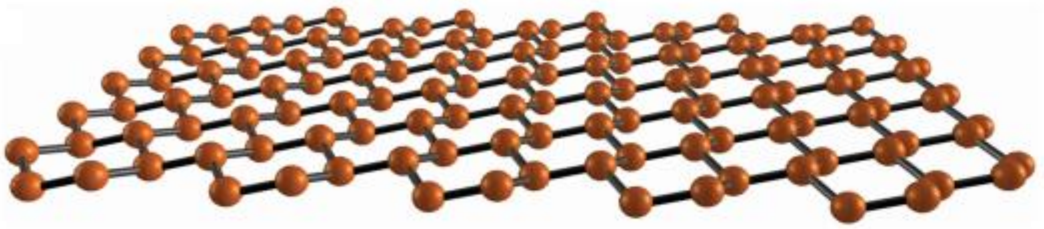

Figure 3.42 Honeycomb lattice structure of sp^2 silicon atoms called silicene. Atom colour; silicon = bronze.[76]

Silicene has yet to be synthesised free-standing, therefore the proposed structures of free-standing silicene are currently theoretical. However, silicene has been fabricated with support of a substrate and these results are not expected to differ significantly for free-standing silicene.[76] Controversial results have been reported for the hypothetical structure of free-standing silicene, with some reports stating the material as a pure sp^2 hybridization of silicon, whereas others claim it has a sp^2-sp^3 nature.[77, 78] Some studies, including Suzuki and Yokomizo's work have simply assumed a planar silicene surface.[79] Kaltsas and Tsteseris have reported stability for reconstructed silicon surfaces.[80]

Most theoretical studies of silicene have used density functional theory (DFT) calculations, assuming the layered structure has a hexagonal lattice similar to graphene.[81] Silicon is not known to form flat sp^2 bonding and therefore silicon atoms opposite to each other in a 6-membered ring (*i.e.* A and B in *Figure 3.43a*) would not be in the same plane. Consequently, lattice constant *a* will vary, producing a buckled surface (*Figure 3.43b*) and therefore the total energy relative to a flat silicon surface (*Figure 3.43c*) is minimised.

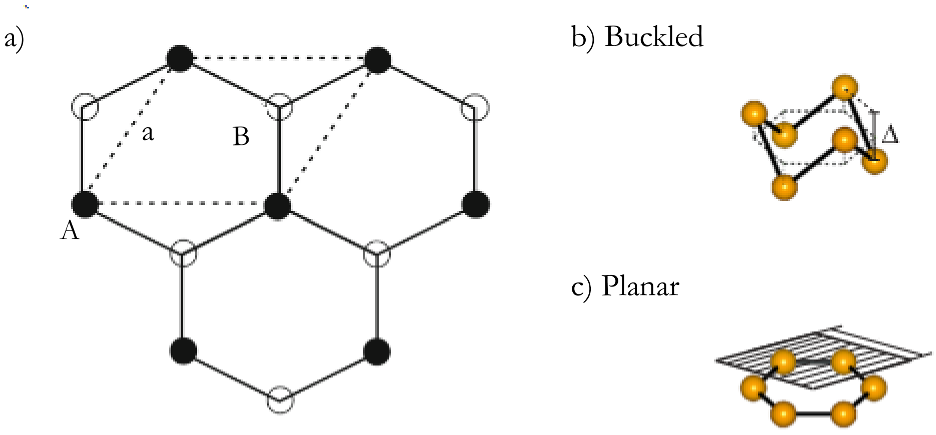

Figure 3.43 a) The crystal lattice of silicene. Illustrations of b) buckled and c) planar silicene.[61, 75]

The buckled surface in silicene can be explained in two ways:

i. the large separation of silicon atoms giving rise to minimised orbital overlap and therefore weaker π-bonds.

ii. the pseudo Jahn-Teller instability on each of the planar Si_6 membered rings causing distortion into a chair-like formation, minimising the overall energy of the species.[82]

Structural parameters for out-of-plane silicon atoms marked as Δ in *Figure 3.43b* have been calculated for silicene.[83] The buckling height for silicene was found to be ~0.4 Å, compared to bulk silicon where the out of plane silicon atom is 0.78 Å from the (111) plane.[61, 83] Thus, due to the height of the buckling in silicene the bonding indicates a behaviour between sp^2 and sp^3.

Silicene has received a great deal of attention since it was first fabricated in 2012 when sheets were grown on a Ag(111).[84-88] Silicene was synthesised under ultra-high vacuum (UHV) conditions, where a slow deposition of silicon onto a silver substrate was employed at different temperatures (150-300 °C). Silver is a good substrate on which to grow silicene because of low reactivity between itself and silicon, as well as the ideal compatibility of the lattice constants within the crystal structure. Silicene has also been reported on other metallic substrates such as ZrB_2(0001),[89] Ir (111),[90] and chalcogenide templates.[91, 92]

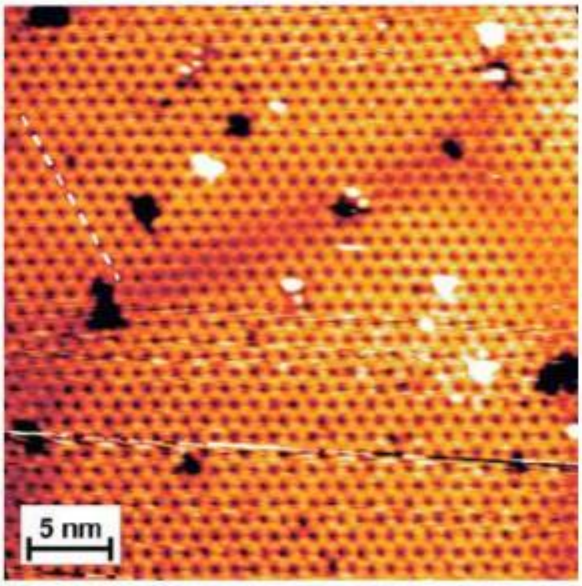

Figure 3.44 Scanning tunnelling microscopic (STM) image of silicene on Ag(111).[84]

Due to the great similarities between silicene and graphene, many of the same potential applications of graphene have been considered for silicene, with nanoelectronics being the most obvious.[75] However, experimental studies of silicene are still new and therefore far from any device fabrication.[86]

3.1.3. Buckled Silicon Nanosheets: Type II

There are many different types of buckled SiNS and most are based on the Si(111) structure. Different routes have been employed to synthesise buckled SiNS and the main ways are detailed below:

i. A soft synthesis technique where calcium disilicide is used as a precursor and is mixed with hydrochloric acid. This method is further discussed in Section 3.1.4. Other Group 14 elements have also been investigated using this method for fabrication of nanosheets.[93]

ii. Kim *et al.* synthesised free standing SiNS *via* CVD using silicon tetrachloride as a precursor and hydrogen as the carrier gas.[94] The reported thickness of the sheets was between 1 to 100 nm and the SiNS grew in three stages on a silicon substrate. A schematic illustration of the growth mechanism is shown in *Figure 3.45e.* First, 1D seed growth in a SiNW fashion was observed in SEM, where free-standing stick-like structures protruded from the substrate as shown in *Figure 3.45a.* The next stage was 2D sheet growth which branched from the seed nanowires, filling the interdendritic space (*Figure 3.45b/c*). The first two stages occurred fairly quickly compared to the last stage, which was the thickening of the nanosheets (*Figure 3.45d*). The thickness of the SiNS increased with growth time, and can be controlled depending on the $SiCl_4/H_2$ gas ratio.

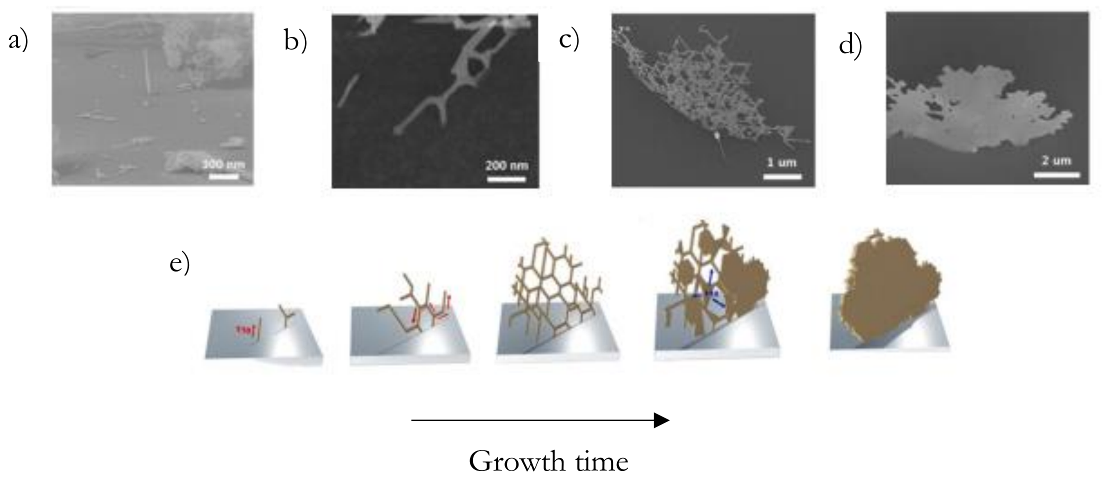

Figure 3.45 Synthesis of SiNS via CVD. a-d) SEM images showing the different growth stages of SiNS and e) is a schematic illustration of the growth mechanism.[95]

Photoluminescence and absorption studies showed SiNS have enhanced characteristics when compared to bulk silicon, portraying potential application in silicon optoelectronics. The SiNS show strong thickness-dependent photoluminescence in the visible range including red, green and blue emissions with wavelengths of 765, 550 and 430 nm respectively.[95] Kim *et al.* proposed that the thickness of the SiNS is the reason for the range in colour, as no other significant physical or chemical factors changed with increasing growth time.[95]

iii. Recently, SiNS have been synthesised from sand.[96] The study used magnesiothermic reduction starting with commercial sand and a schematic illustration of the process is shown in *Figure 3.46*. Commercial sand was crushed by planetary ball milling and subsequently washed with deionised water, dried and calcined at 600 °C (step 1). The resulting calcined sand was hand-mixed with magnesium and then treated at 700 °C for 4 hours under a 5 % H_2/N_2 atmosphere, a method known as magnesiothermic reduction (step 2). The resulting SiNS were washed with hydrochloric acid (HCl) to dissolve the magnesium containing compounds MgO and $MgSi_2$ (step 3), and then washed with hydrofluoric acid (HF) solution to remove the unreacted SiO_2 (step 4). Lastly, SiNS were encapsulated with reduced graphene oxide (step 5). This last step enhances electrochemical properties for potential use in Li-ion batteries.

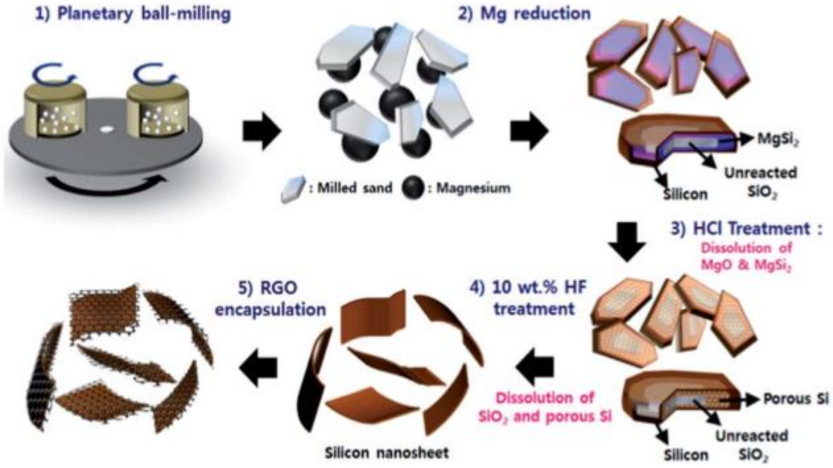

Figure 3.46 Schematic illustration of the synthesis of graphene oxide- encapsulated SiNS.[96]

iv. Another interesting method to synthesise SiNS, introduced last year, is the use of natural clay as a silicon source.[97] Natural clays commonly exist as layered silicate structures in bulk sized particles which must be exfoliated to obtain ultrathin sheets. An all-in-one strategy is used, where a molten salt is penetrated into the silicate structure to act as an exfoliation-inducing agent and to simultaneously assist with chemical reduction of the natural clays. The sheets synthesised have a narrow size distribution (1-5 μm), are ultrathin (~5 nm) and have a high surface area. The sheets exhibit a photo-assisted hydrogen production rate from a water-methanol mixture (486 μmol H_2 per hour per gram of silicon). Moreover, platinum nanoparticles can be added as a co-catalyst, increasing the hydrogen evolution rate further.[97]

3.1.4 History and Review of Layered Polysilane

Layered polysilane is a type of SiNS synthesised and characterised in this thesis. An introduction to the material is reported below. The fabrication of layered polysilane utilises calcium disilicide ($CaSi_2$) shown in *Figure 3.47*.[98] $CaSi_2$ is a stable binary Zintl material with an extreme formulation of $Ca^{2+}(Si^-)_2$. Binary Zintl materials were named after Eduard Zintl, who first studied these compounds in the early 1930s.[99] These materials are stabilised due to ionic interactions between strongly electropositive metals (Ca^{2+}) and less electropositive metals (Si^-).[100] $CaSi_2$ is made of anionic layers, comprised of Si_6 rings compacted between planar monolayers of calcium ions (cationic layer), as shown in *Figure 3.47*.

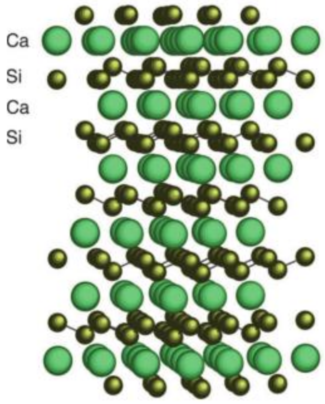

Figure 3.47 Ball and stick illustration of $CaSi_2$. Atom colours; calcium = light green and silicon = dark green.[101]

Si-Si covalent bonds within $CaSi_2$ have high stability and can undergo deintercalation of calcium ions (Ca^{2+}) from the interlayer spacing. This topochemical transformation leaves the polyanion $(Si_n)^{n-}$ structure unchanged and can be seen as the backbone of the layered polysilane sheets.[102] Different methods have been explored to produce SiNS in this approach and a timeline of proceedings is summarised below.

In 1863, Wöhler reported for the first time a stable silicon sheet polymer.[102] Wöhler studied the effects of different acids with $CaSi_2$ including HCl. Treating $CaSi_2$ with ice-cold concentrated aqueous acid produces an insoluble yellow compound which Wöhler called 'silicon'.[102, 103] Kautsky later modified the reaction conditions to obtain a grey-green product which he called 'siloxene'.[103] Kautsky proposed a layered structure model in which six-membered rings are isolated from each other by linear Si-O-Si bridges, shown in *Figure 3.48a* to afford a composition of $Si_6O_3H_6$.[103] Wiberg proposed a slightly different model illustrated in *Figure 3.48b* where one dimensional silicon chains are interconnected by Si-O bonds.[103]

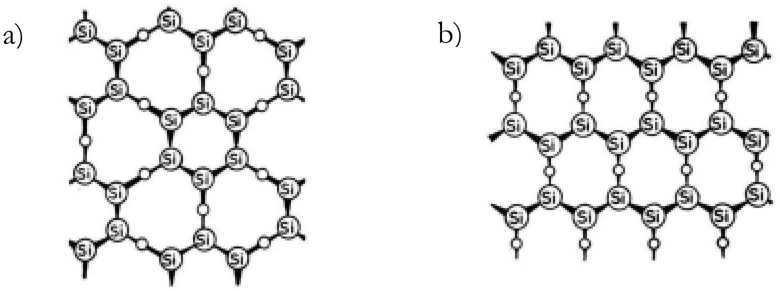

Figure 3.48 a) Kautsky's and b) Wiberg's proposed siloxene structure.[103]

In 1979, Weiss *et al.* claimed to synthesise a sheet polymer product which was made of puckered Si 2D layers.[103] He used a similar method to Wöhler previously discussed by taking $CaSi_2$ and reacting it with different acids at low temperatures. Weiss and co-workers proposed that the structure consisted of six-membered silicon rings connected together, with each silicon atom bearing three equivalent silicon neighbours at a distance very close to that observed in silicon. Weiss *et al.* compared the lattice dimensions of their material, Kautsky's siloxene, $CaSi_2$ and bulk silicon to prove that Si-O-Si bridges were not present in their new material. The silicon layers, with a composition of $Si_6H_3(OH)_3$, are stabilised by termination though alternating hydrogen and hydroxide groups pointing perpendicular from the plane (*Figure 3.49*).[103]

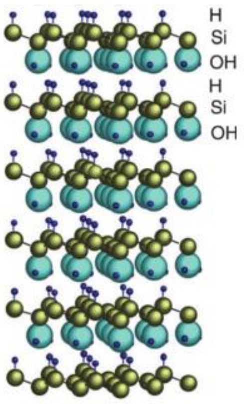

Figure 3.49 Illustration of Weiss et al. siloxene, $Si_6H_3(OH)_3$.[101]

When $CaSi_2$ reacts with concentrated HCl, hydrogen gas is produced *via* the following reaction:

$$3CaSi_2 + 6HCl + 3H_2O \rightarrow Si_6H_3(OH)_3 + 3CaCl_2 + 3H_2 \qquad [1]$$

The first oxygen-free SiNS were reported by Dahn, Way and Fuller in 1993.[104] Dahn confirmed Weiss's structure and adapted the synthesis so that silicon sheets were terminated by hydrogen only, rather than hydroxyl groups. Aqueous HCl was reacted with $CaSi_2$ at two different temperatures 0 °C and 80 °C for 30 minutes. Dahn *et al.* concluded that preparing the NS (nanosheets) at a lower temperature of 0 °C reduces the oxygen content and produces silicon layers which are terminated with hydrogen only. Dahn identified that if oxidation does not occur, the reaction is an ion exchange:

$$3CaSi_2 + 6H^+ \rightarrow Si_6H_6 + 3Ca^{2+} \qquad [2]$$

Furthermore, the SiNS were rinsed with hydrofluoric acid to remove silicon oxide. The samples were found to spontaneously combust upon exposure to air. Dahn *et al.* called this new material layered polysilane and stated it has an elemental composition of Si_6H_6.[105] Van de Walle and Northrup established that layered polysilane has a direct band gap of about 3 eV from first principle electronic calculations.[106]

In 1996 Yamanaka investigated the synthesis and analysis of layered polysilane and concluded

> "*the structural types of resulting siloxenes vary depending on the preparation conditions such as the concentration and temperature of HCl solutions, reaction period, and aging in water and air*".[98]

Yamanaka completed experiments at temperatures of -30 °C (#1), 0 °C (#2) and 30 °C (#3/#4) in an argon filled glove box to avoid oxidation and contamination with water. The volume of hydrogen gas evolved was measured to find the degree of oxidation in silicon layers, where an increase in evolution of hydrogen meant an increase in the oxidation of sheets. Yamanaka plotted a graph of the amount of hydrogen evolved as a function of reaction time at different temperatures which is shown in *Figure 3.50*.

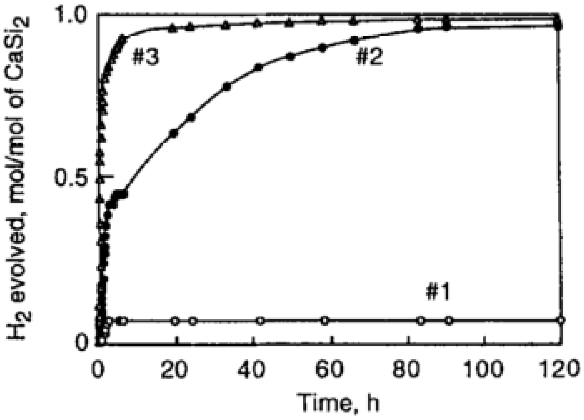

Figure 3.50 The volume of hydrogen evolved during the reaction of $CaSi_2$ with HCl solutions at different temperatures of -30 °C (#1), 0 °C (#2) and 30 °C (#3).[98]

Reacting concentrated HCl and $CaSi_2$ at -30 °C for 5 days gave the most promising results for layered polysilane (#1 in *Figure 3.50*). The calcium ions were deintercalated without evolution of hydrogen and Yamanaka proposed this reaction:

$$3CaSi_2 + 6HCl \rightarrow Si_6H_6 + 3CaCl_2 \qquad [3]$$

Furthermore, investigations into chemical analysis, infrared spectroscopy (IR), electron paramagnetic resonance (EPR) spectroscopy, differential thermal analysis (DTA) and optical absorption were completed, though results differ greatly amongst the few published papers.[98, 107, 108]

In recent years, functionalisation of layered polysilane has drawn greater attention as one limitation of layered polysilane is its inability to disperse in typical organic and inorganic solvents.[5] Modification *via* capping with small organic groups discourages aggregation and allows for good dispersion in organic solvents. This is discussed in detail in Chapter 4.

3.1.5 Applications of Silicon Nanomaterials

As previously mentioned, silicon nanomaterials have been fabricated into nanodevices for application in areas such as energy, catalysis, optoelectronics and biotechnology, to name a few.[109] The biotechnology applications are highlighted in *Figure 3.51* and an exciting advance in the silicon nanomaterial field is detailed in this section.

SiNW have unique electronic, optical, thermoelectric and mechanical properties and developments in the research of these materials have led to interesting application in biosensors.[110] SiNW biosensors are often prepared by metal-assisted chemical etching (MACE). They can be incorporated with metal nanoparticles such as gold nanoparticles and utilised for the destruction of tumour cells with hyperthermia agents.[111] The tumour phototherapy studies proceeded *in vivo* where mice were treated with a specific SiNW material *via* an injection, followed by irradiation using an 808 nm laser. A caliper was used to measure the tumour size and within two days of irradiation, the mice were free of tumours and went on to live for more than 8 months.[111] The findings of these investigations bring exciting opportunities for cancer treatment. The use of silicon nanomaterials is increasing rapidly in biotechnologies as they are known to have little or no toxicity.

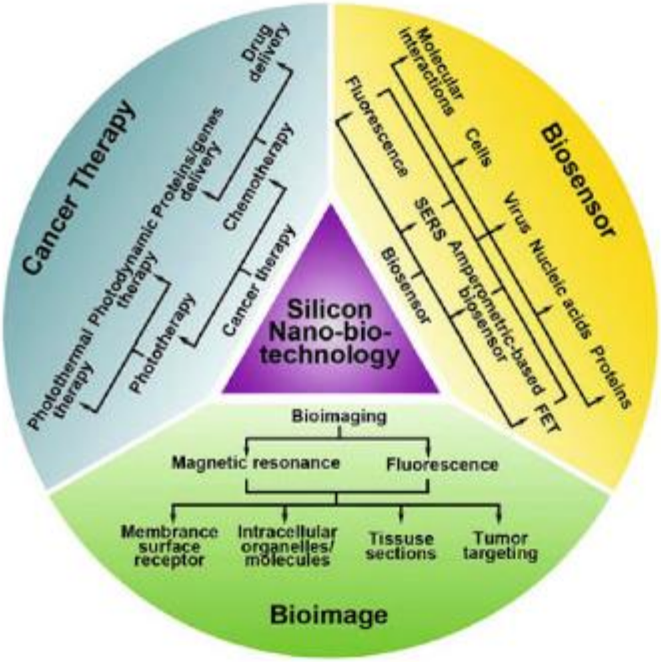

Figure 3.51 Silicon nanobiotechnology holds great promise for biological and biomedical applications, particularly for biosensors, bioimaging and cancer therapy.[112]

3.2 Results and Discussion

As discussed throughout this Chapter, there are many different ways to synthesise SiNS in their various forms. The approach taken in this Chapter is one similar to Yamanaka,[98] using calcium disilicide as the silicon source. The synthesis is detailed and analysis fully discussed.

3.2.4 Preparation of Siloxene and Layered Polysilane

Layered polysilane was synthesised by reacting powdered $CaSi_2$ with an excess of concentrated HCl using a topochemical method. During synthesis, all procedures, where possible, were performed under an inert atmosphere to avoid oxidation and contamination with water. $CaSi_2$ (1 g, 1 eq.), a dark black powder, was transferred from a glove box to a sealed Schlenk flask. The starting material $CaSi_2$, has a strong heteropolar bonding character, which leads to the formation of puckered $(Si_n)^{n-}$ polyanion layers separated from each other by planar Ca^{2+} monolayers.[113, 114] Si^- in $CaSi_2$ formally has six valence electrons and three non-polar Si-Si bonds per silicon atom (shown in *Figure 3.52a*). However, it is described as a heteropolar material due to the polar interactions between Si^- and the Ca^{2+} ions which contribute to the heteropolar bonding character.

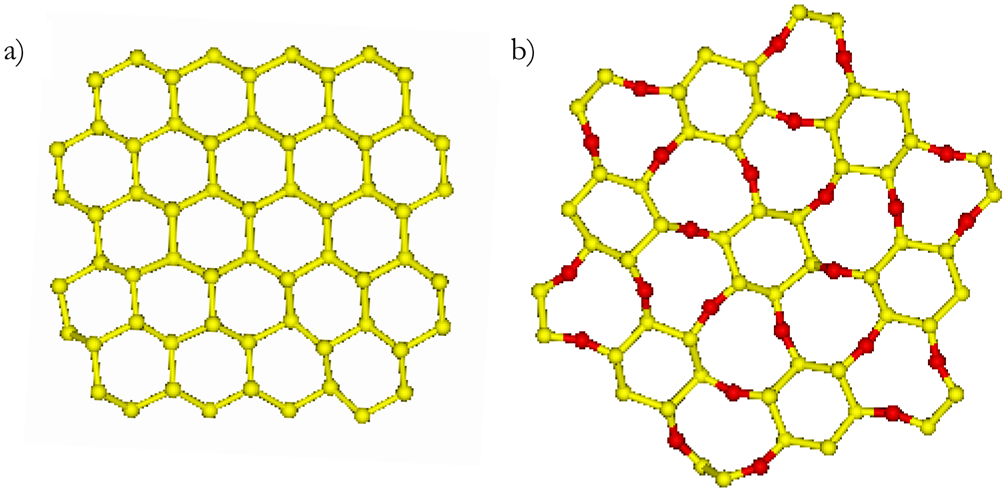

Figure 3.52 a) A model of the puckered $(Si_n)^{n-}$ *polyanion framework in the starting material,* $CaSi_2$*. b) A model of the proposed silicon framework for siloxene and layered polysilane whereby layers of six-membered silicon rings are bridged together by Si-O-Si linkers. Atom colours; silicon = yellow and oxygen = red.*

Excess concentrated HCl (100 mL, ~100 eq.) was added to the Schlenk flask containing $CaSi_2$ *via* a cannula procedure while under dinitrogen. HCl removes Ca^{2+} ions from the anionic layers of silicon, without destroying the silicon layers. On initial addition of the acid, hydrogen gas evolved, and fizzing was observed on the surface of the liquid. For the course of this reaction the Schlenk flask was kept cool utilising an immersion cooler and a dewar filled with a solvent system of water, ethylene glycol, and alcohol, 40 %, 40 %, 20 % respectively to ensure the reaction remained at -30 °C. The reaction was continuously stirred for 5 days at -30 °C under an atmosphere of dinitrogen and a green slurry formed with a small amount of floating white solid observed, which we suggest is calcium chloride. The reaction mixture was allowed to heat to room temperature before washing with acetone and subsequently filtered *via* Büchner filtration. The wet green-yellow product which remained on the filter paper was transferred to a vial and left under vacuum at 110 °C overnight. The product appeared as a fine green-yellow powder and at this stage the product is called siloxene. A model of siloxene is shown in *Figure 3.52b* whereby layers of six-membered silicon rings are bridged together by Si-O-Si linkers. The fourth sp^3 valence of the silicon atoms are terminated by either a hydrogen or hydroxyl group pointing from the layers. The solubility was tested and as expected the product did not dissolve in any typical organic solvents, such as chloroform or hexane. The overall reaction proposed is:

$$CaSi_2 + HCl + H_2O \rightarrow siloxene + CaCl_2 + H_2 \qquad [4]$$

Hydrofluoric acid (HF) etching is reported in literature to aid the removal of carbon contamination and glassy oxide impurities from a surface.[115] Siloxene was purified *via* rinsing with HF to reduce the oxygen content and the new product is called layered polysilane. The suggested reaction is:

$$siloxene + \mathrm{HF}\ (5\ \%) \rightarrow \text{layered polysilane} + \mathrm{H_2O} + \text{fluoride byproducts} \qquad [5]$$

It is proposed that layered polysilane has a similar silicon backbone structure to siloxene (*Figure 3.52b*), however two key differences are present after rinsing with HF:

i) Firstly, removal of the hydroxyl groups which are terminating the silicon surface so that the surfaces are fully terminated with hydrogen.
ii) Secondly, elimination of some of the Si-O-Si bridges which link the Si_6 rings.

During rinsing, H^+ ions passivate the silicon surface and the concentration of HF plays a key role in determining the hydrogen coverage of the sheets. Different concentrations of HF and a variety of rinsing procedures were attempted to find the technique which achieved most surface hydrogen coverage. One method attempted involved suspending siloxene in HF in a plastic beaker and stirring for different lengths of time ranging from 1 minute to overnight, followed by filtration using a Büchner funnel. Another method involved careful decantation of HF solution onto siloxene powder while on filter paper in a Büchner funnel. Other techniques involved the use of glass frits or special glass-membrane filter paper. In addition, different concentrations of HF were used, ranging from 1 % to concentrated (49 %). It was concluded that the optimum conditions for highest hydrogen coverage involved 5 % HF solution decanted onto siloxene while on filter paper in a Büchner funnel. The colour of the powder indicated the level of hydrogen coverage; a lighter shade of green-yellow powder indicated a higher degree of hydrogen coverage (layered polysilane), compared to siloxene which featured a darker green colour. Rinsing with 5 % HF solution produced a lighter coloured powder. The powder from the filter paper was rapidly collected into a Schlenk flask and left overnight under vacuum at 110 °C. The resulting product is shown in *Figure 3.53* and was stored under dinitrogen before analysis. Exposure to the atmosphere caused the exposed surface to turn a grey/white colour within approximately 24 hours. It is interesting to note that Si-F bond energies are almost twice that of Si-H bond energies (5.6 and 3.1 eV respectively)[6] and therefore one might expect the surfaces to be terminated with fluorine rather than hydrogen. This was investigated using a variety of analytical techniques described in Section 3.2.5.

Figure 3.53 Green-yellow powdered sample of layered polysilane.

3.2.5 Evidence for Silicon Nanosheets

Many analytical techniques were used in order to identify and fully characterise siloxene and layered polysilane. Evidence gathered during this study was compared to published literature and further analysed using additional techniques, which, to our knowledge have not been reported previously. Techniques applied to the system for the first time include; scanning emission microscopy (SEM) (Section 3.2.5.5), transmission electron microscopy (TEM) (Section 3.2.5.6) and energy dispersive X-ray spectroscopy (EDX) (Sections 3.2.5.5 and 3.2.5.6). The chemical and physical properties of the material were also studied using infrared spectroscopy (IR) (Section 3.2.5.1), Raman spectroscopy (Section 3.2.5.2), powder X-ray diffraction (XRD) (Section 3.2.5.3) and X-ray photoelectron spectroscopy (XPS) (Section 3.2.5.4) which have previously been published in literature, however show conflicting reports.

3.2.5.1 Infrared Spectroscopy

IR spectroscopy was used to identify bonds such as Si-H, Si-O and O-H in the silicon samples. Attenuated total reflectance (ATR) was a sampling tool used to analyse a powdered material, where an IR beam is directed into an ATR crystal before going into the solid sample. Other methods used included a KBr pellet method where the sample is pressed into a KBr pellet, however easiest interpretation of results came from the ATR-IR. The IR spectrum of layered polysilane can be seen in *Figure 3.54* and a list of absorptions with their corresponding assigned bonds is summarised in *Table 3.2*.

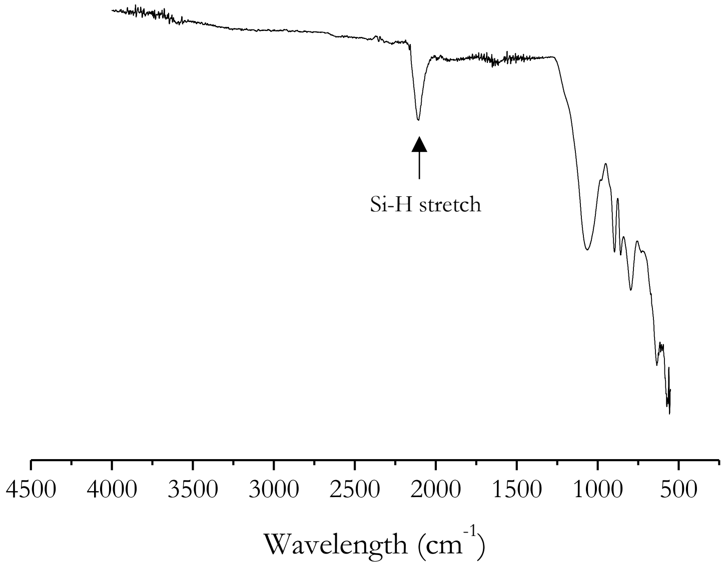

Figure 3.54 IR spectrum of layered polysilane highlighting the absorption assigned to the Si-H stretch.

The absorption band at 2110 cm^{-1} corresponds to Si-H stretching mode. This peak is also observed in IRs reported in the literature for layered polysilane with two example spectra in *Figure 3.55*.[98, 108] The #1 in these two spectra represents polysilane synthesised with similar conditions to the synthesis herein (-30 °C, for 5 days, rinsing with HF).

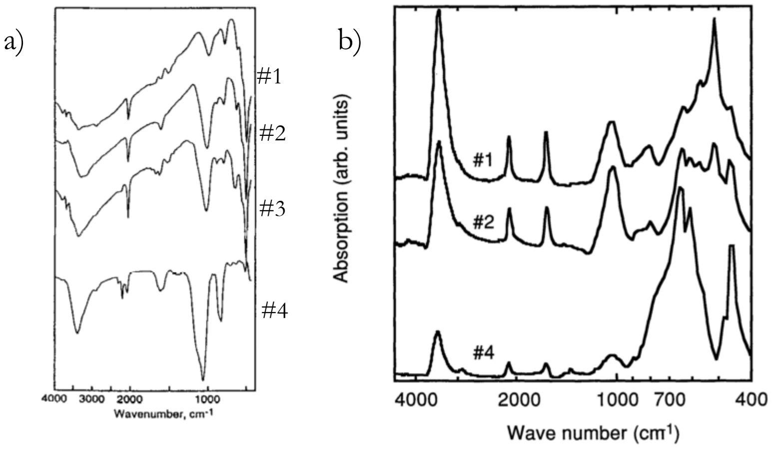

Figure 3.55 IR spectra of layered polysilane (#1) found in literature. a)[98]and b)[108].

Table 3.2 Assignments of absorption bands of layered polysilane and siloxene.

Absorption (cm^{-1})		**Assignment**
Polysilane	**Siloxene**	
556	561	Si-Si stretch
634	632	Si-H bend
796	797	Si-O-Si bend
860	-	?
895	-	C-F stretch
1066	1028	Si-O-Si stretch
-	1632	Hydrocarbon stretch
2110	2102	Si-H stretch
-	3289	O-H stretch

In layered polysilane the absorptions at 556 cm^{-1} and 634 cm^{-1} correspond to Si-Si stretching and Si-H bending vibrations respectively. The strong absorptions at 1066 cm^{-1} are attributed to the symmetrical vibrational stretch Si-O-Si which is paired with an antisymmetric stretch at 796 cm^{-1}.[116] These absorptions, especially at 1066 cm^{-1}, are fairly strong and in the literature they are considered to be silicon dioxide impurities.[98] However, it is suggested that they are too large to be an impurity and the Si-O-Si bonds are actually part of the nanosheets structure. This is later confirmed by Raman spectroscopy and discussed in Section 3.2.5.2. It is presumed that, to some extent, silicon dioxide impurities are present in the sample, which makes quantification of the IR spectrum challenging. These impurities may have arisen when transferring the sample for analysis or during the synthetic procedures.

In order to probe the hydrogen coverage of the sheets, IR spectroscopy was used to compare the SiNS both before HF rinsing (siloxene) and after HF rinsing (layered polysilane). A comparison of the IR spectra can be seen in *Figure 3.56*. Siloxene has a broad absorption band at 3289 cm^{-1}, which is assigned to O-H stretching vibrations from the terminating hydroxyl groups protruding from the silicon plane. The O-H stretch is absent in layered polysilane as the sheets are terminated by hydrogen only. Referring back to published IR data (in *Figure 3.55*), it is interesting to observe the large O-H peak at ~3350 cm^{-1} especially after rinsing the material with HF which, according to authors, eliminates the terminating hydroxyl groups.

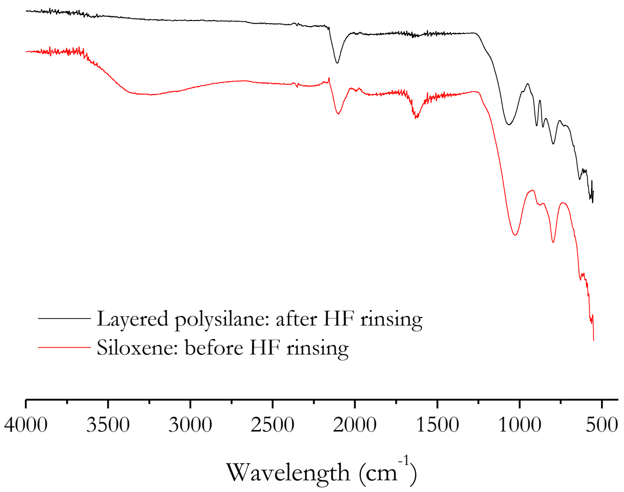

Figure 3.56 IR spectra comparing siloxene (red) and layered polysilane (black).

There is an increase in the Si-O-Si absorption band (at 1028 cm^{-1}) relative to the Si-H band (2102 cm^{-1}) in siloxene compared to polysilane. In siloxene, the Si-O-Si absorption band is approximately five times greater in intensity than the Si-H band, compared to layered polysilane where the Si-O-Si band is only three times greater in intensity than the Si-H band. It can therefore be concluded that HF rinsing removes either some of the Si-O-Si bonds within the silicon layers or the silicon dioxide impurities, however not all. Lastly, an absorption band at 1632 cm^{-1}, attributed to hydrocarbon stretches (such as C=C/C=O), is depleted after HF rinsing. It is suggested that this absorption band is accounted for by the synthetic work-up where siloxene is rinsed with acetone before being placed under vacuum. These impurities are removed during HF rinsing.

A closer examination of the IR "fingerprint" region is shown in *Figure 3.57*. The main observation is the addition of a band at 895 cm^{-1} after rinsing the product with HF. This new peak is found in the region where Si-F stretching modes are likely to absorb, which would suggest that some of the surface is terminated by Si-F bonds.[117, 118] The IR spectra disclosed in the literature for layered polysilane (*Figure 3.55*) also shows this band, however it is neither recognised nor discussed. Further analysis of the material using XPS (see below), investigates and discusses the nature of this bonding. The origin of the additional band in polysilane at 860 cm^{-1} is unknown.

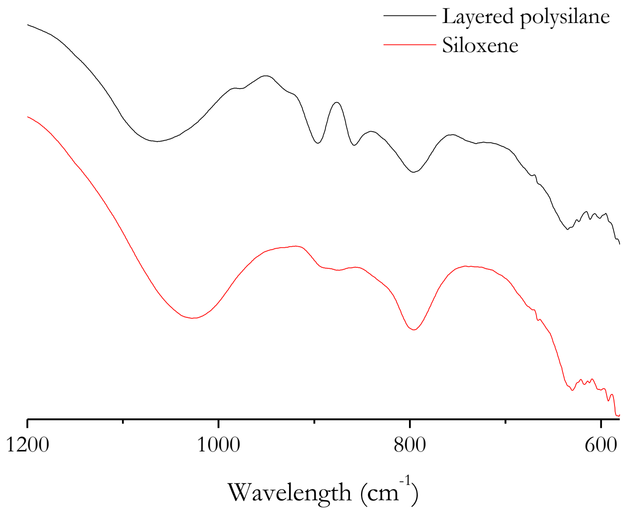

Figure 3.57 Closer examination of the "fingerprint" region in IR spectra comparing siloxene (red) and layered polysilane (black).

3.2.5.2 Raman Spectroscopy

Raman spectroscopy was used to investigate the vibration, rotational and other-low frequency modes in SiNS both before HF rinsing (siloxene) and after HF rinsing (layered polysilane). Raman spectra were recorded for the solid samples directly without any pre-treatment/deposition and the spectra are shown in *Figure 3.58*, along with a list of Raman shifts and their corresponding assignments, shown in *Table 3.3*.

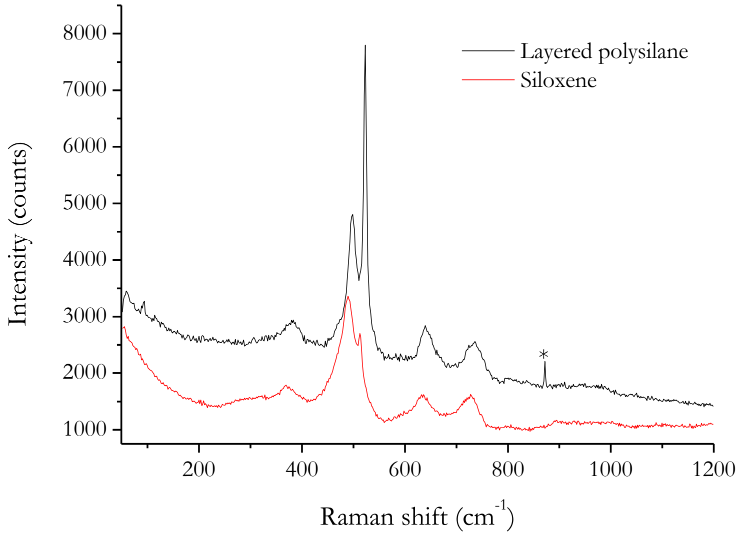

*Figure 3.58 The Raman spectra of siloxene (red) and layered polysilane (black). * denotes a peak due to an artefact.*

Both siloxene and layered polysilane exhibit similar Raman spectra and the only main difference is the relative intensities of the two bands in the range of 400-600 cm^{-1}. There is an increase in intensity and sharpness of the band positioned at 523 cm^{-1} in polysilane. In Raman spectroscopy, intensity and sharpness of signals are usually greater for products with high symmetry.[119] Comparison of siloxene, where silicon atoms are terminated by two different groups (-OH and -H), to layered polysilane, one would expect the latter to have greater symmetry due to silicon atoms being terminated by hydrogen only.

Raman modes at ~375 and ~520 cm^{-1} in both siloxene and layered polysilane are assigned to the corrugated Si(111) planes. Raman data reported in the early 1990s compares the starting material calcium disilicide, a type of siloxene and porous silicon.[120] Both calcium disilicide and siloxene exhibit Raman shifts at 380, 410 and ~515 cm^{-1} and therefore, since the only feature these two materials share are the Si(111) corrugated planes, these peaks are assigned to this structural feature. Modes at 638/636 cm^{-1} and 736/727 cm^{-1} are assigned to Si-H vibrations, which are similar in value to Raman shifts which occur in a pristine polysilane polymer chain reported in the literature.[121]

Table 3.3 Raman shifts for polysilane and siloxene and their assignments.

Raman shift (cm^{-1})		**Assignment**
Polysilane	**Siloxene**	
380	369	Si-Si planes
497	490	Si-O vibrations
523	512	Si-Si planes
638	636	Si-H vibrations
736	727	Si-H vibrations
964	967	TO mode

The peak with a Raman shift of ~495 cm^{-1} has a greater intensity in siloxene compared to polysilane. It is suggested that this peak is due to the insertion of oxygen into the silicon planes which would suggest that siloxene has a large proportion of oxygen compared to layered polysilane.[120] This also coincides with the IR results where comparing the Si-H peak with the Si-O-Si peak, there is a larger ratio (1 : 5) in siloxene compared to polysilane (1 : 3). It has been reported that gentle heating leads to the insertion of oxygen into the silicon planes.[120] In the material synthesised herein, this might have occurred when the product was warmed to room temperature after being kept at -30 °C for 5 days and the oxygen may have come either from the -OH groups terminating the structure or from atmospheric oxygen. The peaks at 523 and 512 cm^{-1} in polysilane and siloxene respectively, correspond to silicon sp^3, similar to that in bulk silicon. This peak is assigned to the silicon framework which features sp^3 hybridisation, where the silicon atoms occupy three bonds in the plane, whether they be Si-Si or Si-O-Si bonds, and one bond (Si-H or Si-OH) terminating the sheets.

It is reported in the literature that amorphous silicon exhibits broad bands centred at ~480 cm^{-1}, compared to crystalline silicon which present a narrow peak at 519 cm^{-1} in Raman spectroscopy.[122, 123] Peaks centred at these Raman shifts are observed in both siloxene and layered polysilane which implies that both materials are part amorphous and part crystalline, which is later confirmed by other analytical techniques. The ratio of crystalline to amorphous material increases after HF rinsing.

All samples showed inhomogeneity and also produced spectra similar to that shown in *Figure 3.59*, featuring a sharp peak at 519 cm^{-1}. These spectra reveal the presence of silicon impurities in the material, evident due to the absence of peaks at ~380, ~490, ~635 and 730 cm^{-1}, which correspond to either silicon planes or Si-H vibrations. The spectrum also features a weak transverse optical (TO) mode at ~960 cm^{-1} similar to bulk silicon. In general, IR spectroscopy shows a better selection of strong characteristic bands for silicon compounds than Raman spectroscopy.[124] One example is the O-H stretch which is not normally present or is rather weak in Raman spectroscopy, however is observed in IR spectroscopy.

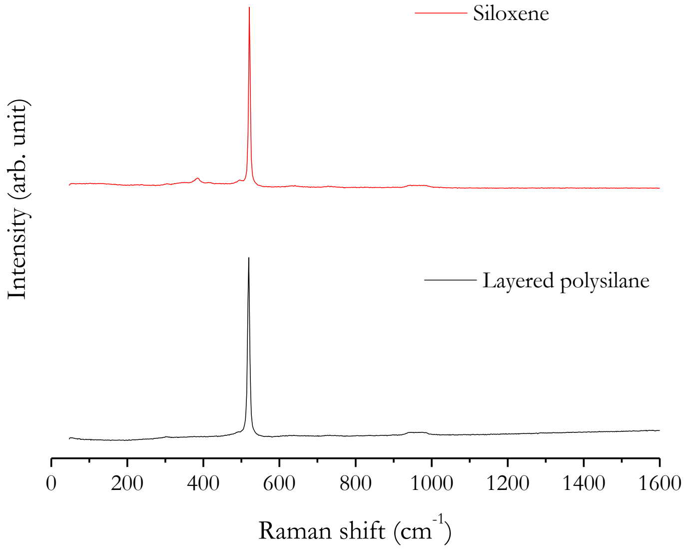

Figure 3.59 The Raman spectra observed for both siloxene and layered polysilane.

3.2.5.3 Powder X-ray Diffraction

Powder XRD is an analytical technique which was used to help identify the crystallinity of material, and provide information about the atomic arrangement. Powdered samples were placed on circular zero background silicon plates to record the XRD pattern. The sample was bombarded with X-rays which were produced from a copper anode source (Kα radiation is 1.54 Å). The angle of diffraction, which is called theta angle, is measured in degrees. For practical reasons the diffractometer measures an angle twice that of the theta angle and this angle is called '2-theta'. The powder XRD patterns shown in *Figure 3.60* compare the starting material, calcium disilicide, and layered polysilane, highlighting their differences. The assignment of lattice planes is adapted from a previously reported calculated XRD pattern for SiNS.[104]

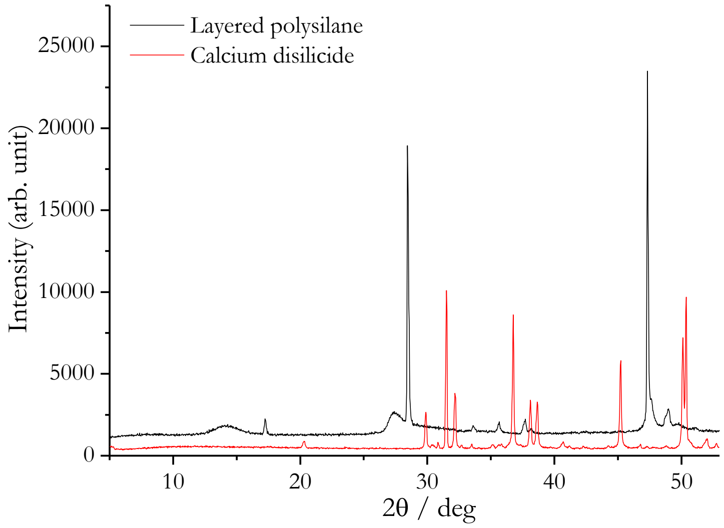

Figure 3.60 Powder XRD of layered polysilane (black) and calcium disilicide (red).

The powder XRD pattern of layered polysilane has four key features (*Figure 3.60*). Firstly, broader peaks at 14.29° and 27.39°, indicating an amorphous-type structure and secondly, sharp peaks at 28.44° and 47.32°, identifying a more crystalline component. This suggests layered polysilane is a material with both amorphous and crystalline parts, which is later confirmed by high resolution TEM (HRTEM).

The first broad peak at a low angle of 2θ = 14.29° is assigned to the periodicity of the layered structure of polysilane which has an interlayer spacing (*d*) of 6.19 Å, calculated using Braggs law (λ = 1.54 Å and n = 1):

$$d = \frac{n\lambda}{2sin\theta} = \frac{1.54}{2sin7.1465} = 6.19\ \text{Å} \qquad [6]$$

The broadness of this peak indicates minimal stacking of sheets. However, another diffraction peak which also corresponds to the layered structure of polysilane is at 2θ = 28.44°. This peak is sharp, showing crystallinity in the stacked structure, and has a periodic layer-to-layer spacing of 3.13 Å, calculated using Braggs law as before. The larger periodic spacing of 6.19 Å is designated to the periodicity between adjacent silicon frameworks and the smaller interplanar distance of 3.13 Å is assigned to spacing between the terminating hydrogens pointing from the silicon framework in adjacent sheets.

The model in *Figure 3.61* illustrates the interplanar distances of layered polysilane, assuming the Si-H bonds have lengths of 1.46 Å. Using the interplanar distance of 3.13 Å and the Si-H bond length [(1.46 x 2) + 3.13], it is calculated that the distance between the silicon frameworks of two adjacent sheets is 6.05 Å. However, looking at the results of the XRD, the interplanar spacing is slightly larger than expected at 6.19 Å (a difference of 0.14 Å). The larger distance of 6.19 Å is most likely due to the presence of some hydroxyl groups instead of complete hydrogen termination of sheets, thus enlarging the interplanar space.

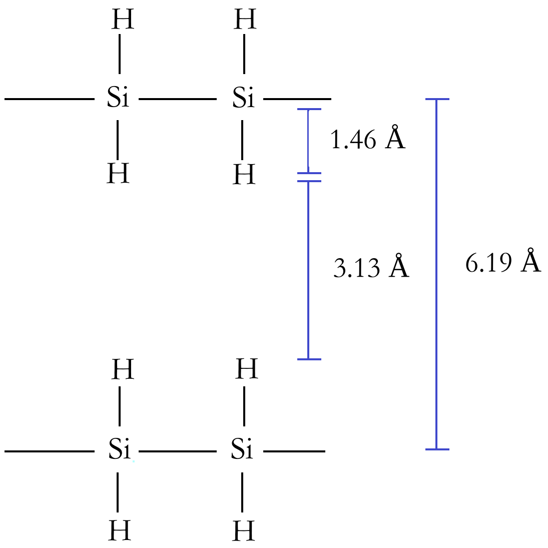

Figure 3.61 Representation of layered polysilane displaying the interplanar distances between two adjacent SiNS. Si-H bonds occupy lengths of 1.46 Å.

The structure within the silicon framework of a sheet corresponds to peaks at 2θ = 27.39° and 47.32°. The peak at 27.39° provides a *d*-spacing of 3.25 Å (using Bragg's law) which is related to the spacing observed in analysis of HRTEM images of layered polysilane (see Section 3.2.5.6). Several weak peaks in the powder XRD can be assigned to residual silicon or carbon, which is likely to be from the starting material.

3.2.5.4 X-ray Photoelectron Spectroscopy

XPS is a surface technique used in this thesis to provide elemental identity, chemical state information and quantity of detected elements from the outer 5 to 10 nm of a solid surface.[125] For XPS analysis of materials in this Chapter, powdered samples covering an area of approximately 0.5 by 0.5 mm, were placed on non-conducting double sided sticky tape stuck to one end of the sample holder. *Figure 3.62* shows the widescan spectra of layered polysilane (black) and siloxene (red), providing an overview of the whole energy range and giving an insight as to which elements are present in the two samples. Data analyses were performed using Kratos Vision processing software and CasaXPS Version 2.3.16 PR 1.6. The spectra have not been charge corrected as they are adequately aligned.

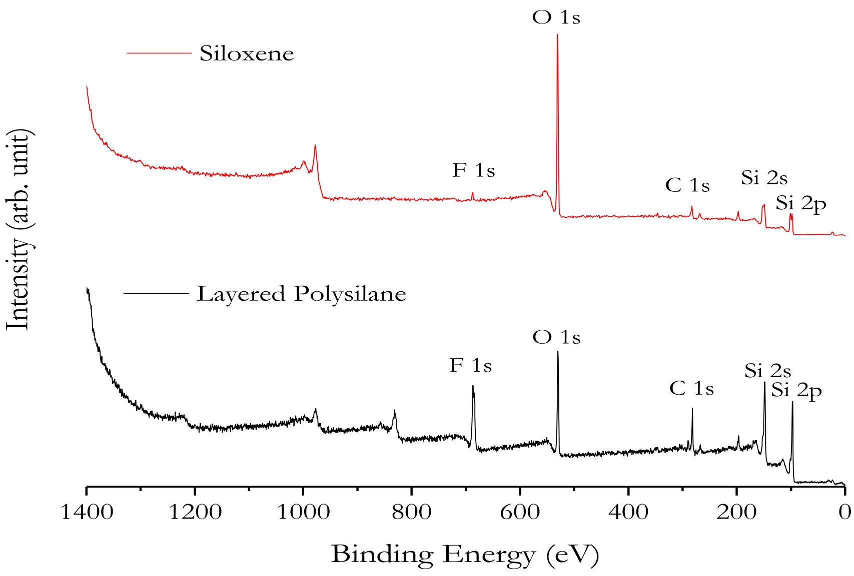

Figure 3.62 Widescan XPS of siloxene and layered polysilane.

The atomic percentages of the orbitals labelled in *Figure 3.62* are recorded in *Table 3.4* and *Table 3.5*. The first observation is the difference in ratio of silicon to oxygen between the two samples. In siloxene the silicon to oxygen ratio is approximately 1 : 1.3 compared to layered polysilane, where the ratio is 3.5 : 1. This is most probably due to the replacement of hydroxyl groups with Si-H bonds after HF rinsing. It is important to note here that even after HF rinsing there is still oxygen present (~15 %) in the sample. This is expected, as some degree of oxygen will always be present in samples exposed to air, even if only for a short period, either due to contamination or oxidation from the atmosphere. Both samples have carbon present, which is often the case with air exposed samples and is often known as adventitious carbon.[126] This is usually a thin layer of carbonaceous material built up on the sample surface and is most likely composed of hydrocarbons. This carbon material may also be oxidised, which increases the percentage of oxygen present.

Table 3.4 Atomic percentage of elements in siloxene from XPS data analysis.

Element	**Binding Energy (eV)**	**Atomic %**
F 1s	687	1.2
O 1s	531	50.2
C 1s	282	9.9
Si 2p	99	38.6

Table 3.5 Atomic percentage of elements in layered polysilane from XPS data analysis.

Element	**Binding Energy (eV)**	**Atomic %**
F 1s	685	12.2
O 1s	530	15.1
C 1s	282	19.6
Si 2p	99	53.1

A closer examination of the silicon 2p orbitals in *Figure 3.63* allows extraction of chemical state information. Siloxene has two peaks present, each with different binding energies (101.2 and 97.6 eV), and therefore two different chemical environments. The peak with the higher binding energy of 101.2 eV is in an environment that has increased deshielding due to an electronegative atom, such as an oxygen. The withdrawal of valence electron charge by an electronegative atom causes a chemical shift, altering the energy of the orbital and increasing the binding energy. Therefore, this peak most likely corresponds to silicon oxide (Si-O) environments. The second peak with lower binding energy is most likely to be from the silicon framework (Si-Si bonds) terminated with hydrogen. After rinsing with HF, the silicon 2p peak with a binding energy of 101.2 eV significantly reduces in intensity due to the removal of oxygen from the sheets. The very small shift in the silicon framework peak at ~97 eV after rinsing with HF may be due to the overall decrease in electronegativity of the sheets after removal of oxygen or sample charging.

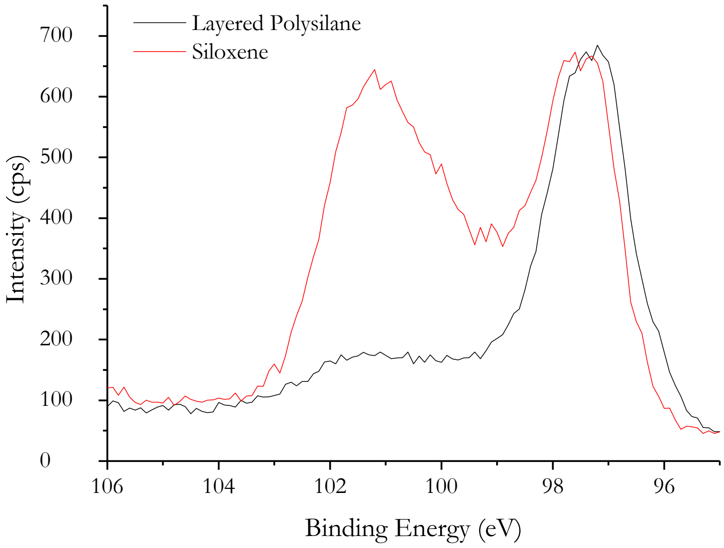

Figure 3.63 High resolution XPS spectra of Si 2p orbital in siloxene (red) and layered polysilane (black).

The widescan spectra of siloxene and layered polysilane both show the presence of fluorine in the sample. There is an increase in fluorine, from ~1 to 12 %, after rinsing the sample with HF. It is important to clarify that fluorine was not attached to the sheets. The trace amount of fluorine present in the sample pre-HF treatment is from an unknown source, potentially the vacuum chamber. Fluorine is an electronegative atom and if it were chemically attached to the sheets (Si-F), a clear peak would easily be detected in the Si 2p orbital area. This characteristic peak would have a higher binding energy, however there was no peak observed. Moreover, probing the high resolution carbon 1s component showed a small peak at higher binding energy, which can be assigned to CF_3 residues and accounts for the 12 % fluorine after HF treatment.

3.2.5.5 Scanning Electron Microscopy and Elemental Mapping

SEM was used to obtain images of layered polysilane, with a resolution of up to 10 nm, revealing information about the surface topography, sheet structure and composition.[127] The insoluble material was dispersed in organic solvent, such as hexane, and sonicated for 10 minutes. The material was deposited onto a variety of grids *via* a drop-casting method, where a dilute solution is pipetted drop-wise onto the grid and subsequently dried. The disadvantage of this method is the production of artefacts on the surface through the drying process.[128]

For the images shown in this section, copper grids with a diameter of 3 mm were used, fashioning a mesh of systematically arranged squares, as shown in *Figure 3.64a*. These grids feature a lacey carbon support film which has a wide range of hole sizes (*Figure 3.64b*) and can be described as a 'mini-mesh', acting as a support for the sample being deposited.

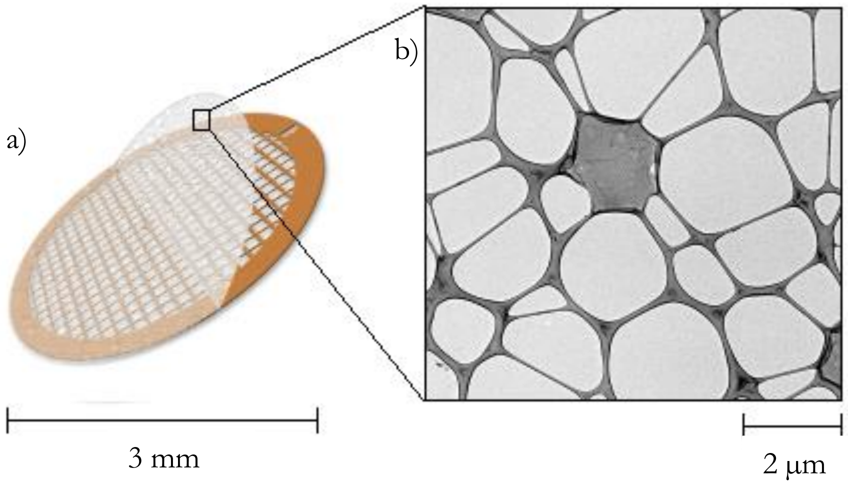

Figure 3.64 a) Copper mesh grid of systematically arranged squares showing the lacey carbon support film and b) SEM image of the lacey carbon film.

A variety of signals, including backscattered electrons (BSE), secondary electrons (SE), X-rays and other photons of various energies are emitted after a beam of electrons has irradiated the sample.[129] SE are emitted by atoms near the surface of the sample when their electrons become excited and have sufficient energy to escape the sample surface and these electrons provide topographic information about the sample surface. Two secondary electron-scanning electron microscopy (SE-SEM) images are shown in *Figure 3.65* and the detail of the surfaces demonstrates the sensitivity of this technique. *Figure 3.65a* is a low magnification SE-SEM image displaying the copper grid as well as the sample, which is highlighted in a white box. *Figure 3.65b* illustrates a high magnification SEM image of free standing layered polysilane. In this microscopy image, nanosheets with a laminar structure, seen particularly at the edge of the sheets, are observed. When investigating layered polysilane *via* SEM, it was found that nanosheets ranged within 5-20 μm and the example image shown in *Figure 3.65b* exhibits nanosheets with a size of 10 μm. In general the surface of the sheets appears smooth, however artefacts are present on their surface, most probably from the drop-cast deposition method.

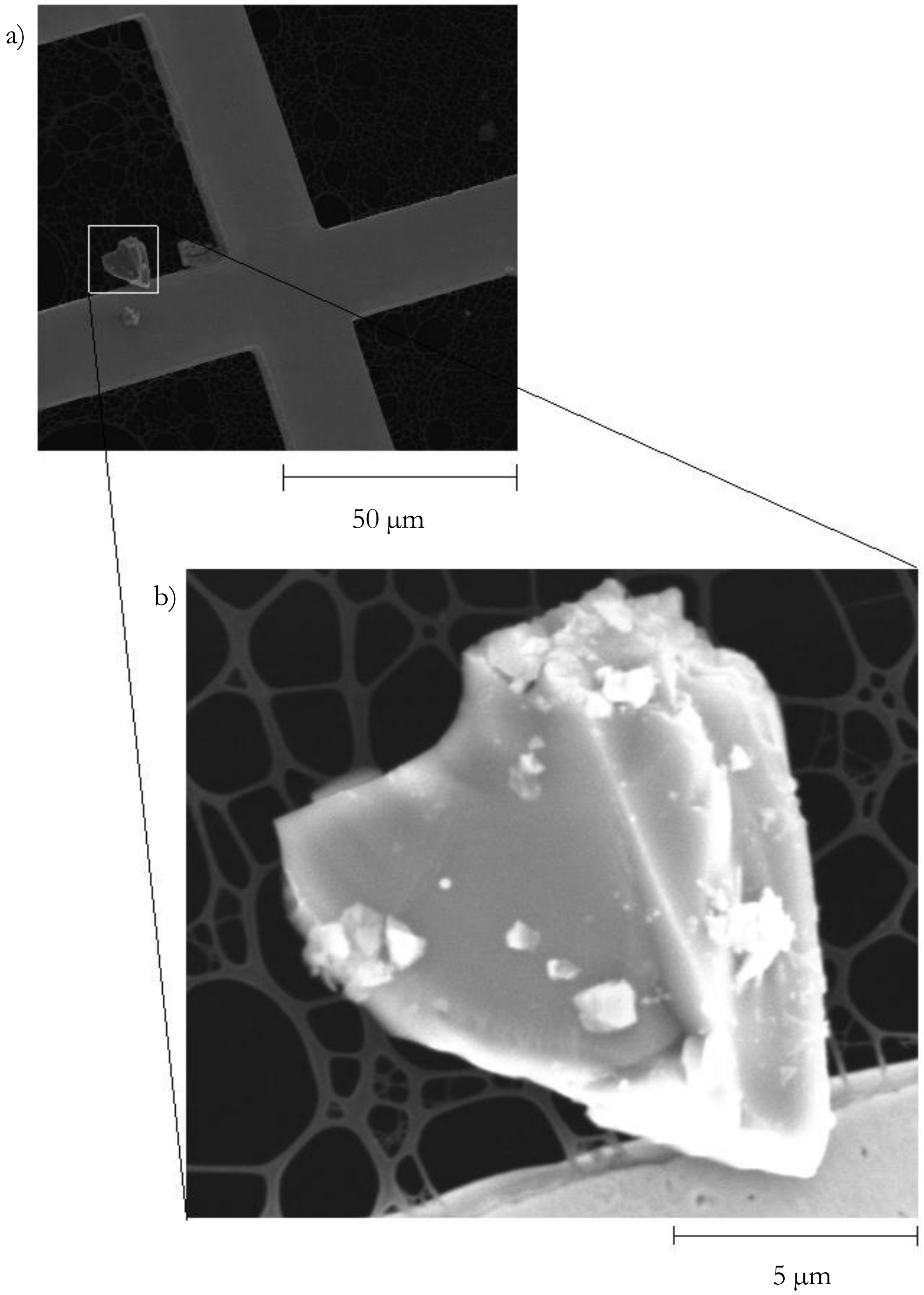

Figure 3.65 a) Low and b) high magnification SE-SEM images of layered polysilane highlighting the laminar structure around the edge of the material and the lacey carbon film underneath.

BSE images were also obtained for polysilane. A unique feature of these images was the colour contrast between the light and heavier elements detected, and can be explained by the fact that BSE are sensitive to the atomic mass (z) of the nuclei they scatter from. Comparatively heavier elements such as silicon, which backscatter more efficiently appear brighter in colour relative to lighter elements such as carbon (from the support film). The advantage of these images is that they are obtained nearly instantly at any magnification within the instrument range and provide information on elemental analysis. However, these images do not convey as much elemental information as is obtained from energy-dispersive X-ray spectroscopy (EDX) and therefore EDX was used to an analyse the elemental composition.

Compositional maps of silicon, aluminium, carbon, oxygen and copper with colour superposition are shown in *Figure 3.66*. Elemental distribution maps of polysilane revealed silicon as the main element. The aluminium detected in this experiment is from the sample holder and the copper comes from the grid. Additionally, a trace amount of carbon is detected and this is most probably from the lacey carbon support film or the vacuum chamber. The oxygen detected may be either from handling the grids in air when depositing the sample followed by atmospheric storage or from Si-O-Si bridges present in the silicon framework. However, the detection of these elements are minimal and therefore we can distinguish that from SEM analysis that the polysilane sheets have a very low oxygen content.

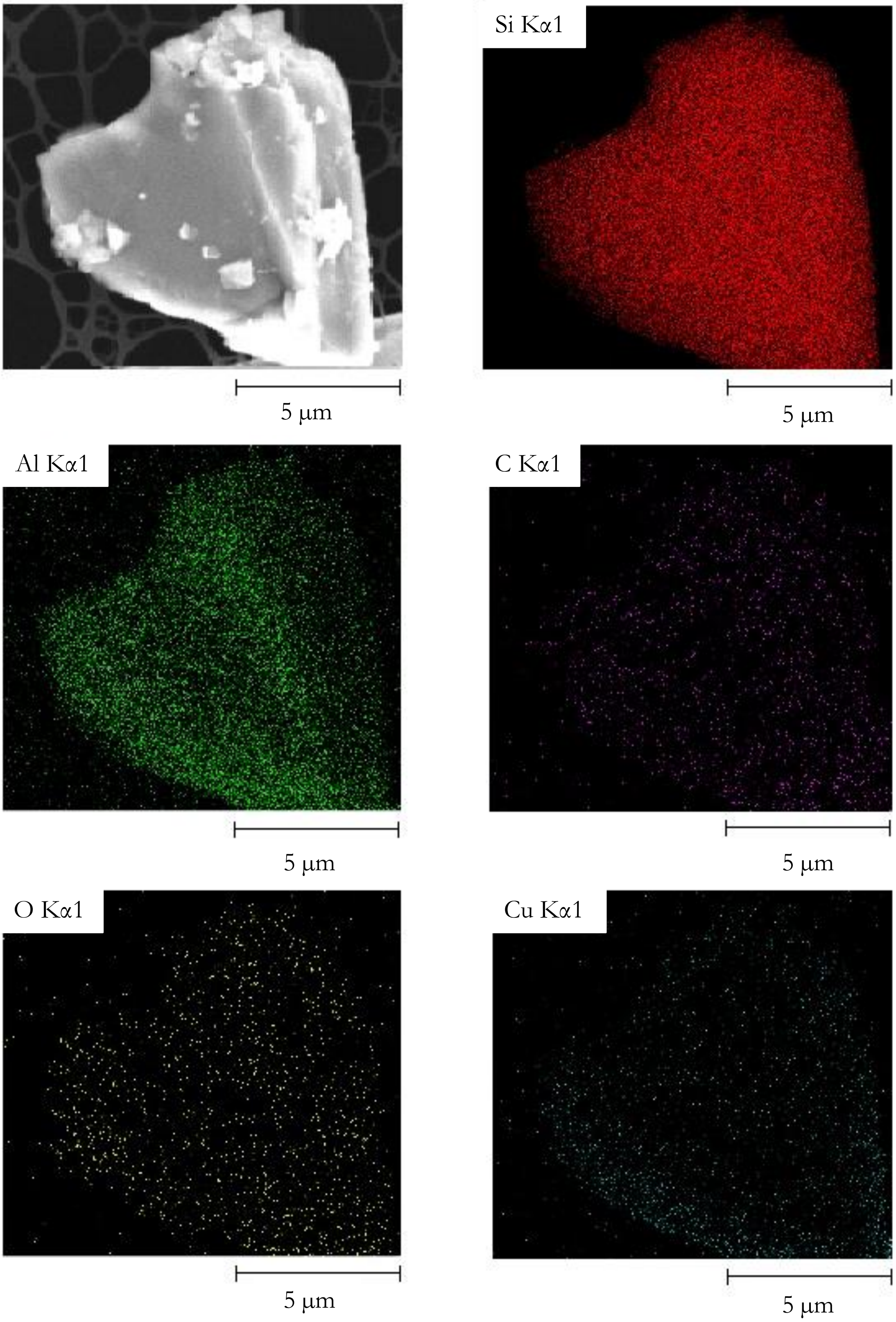

Figure 3.66 Compositional maps for silicon, aluminium, carbon, oxygen and copper with colour superposition showing the silicon rich phases of the sheets relative to other elements detected in trace amounts. Atom colours; silicon = red, aluminium = green, carbon = purple, oxygen = yellow and copper = blue.

It is interesting to note that the detection of 'trace' elements take the shape of the SiNS. When the incident electron beam hits a large volume of material on the grid, it produces an increased scattering of X-rays, SE and BSE, compared to when the beam hits the support film. Due to this increased scattering of signals upon hitting material, there is more chance of detection of the signals and therefore electron mapping will reflect the volume and shape of the material, in this case polysilane. The results for elemental distribution mapping show that the artefacts on the surface are silicon.

3.2.5.6 Transmission Electron Microscopy

TEM has a higher resolution than SEM and therefore gives more detail of the topographic structure. TEM grids were prepared in a similar manner to SEM, *via* a drop-cast method. Two different support films on the copper grids were used when analysing the sheets; either a lacey/holey carbon film similar to the one used previously or a graphene oxide film. Lacey carbon support films are usually better than graphene oxide films when analysing elemental composition as they provide more accurate results, however graphene oxide films have a hydrophilic surface that aid sample dispersion, making it easier to obtain more informative images. In addition to copper grids, sample deposited on gold grids was also investigated.

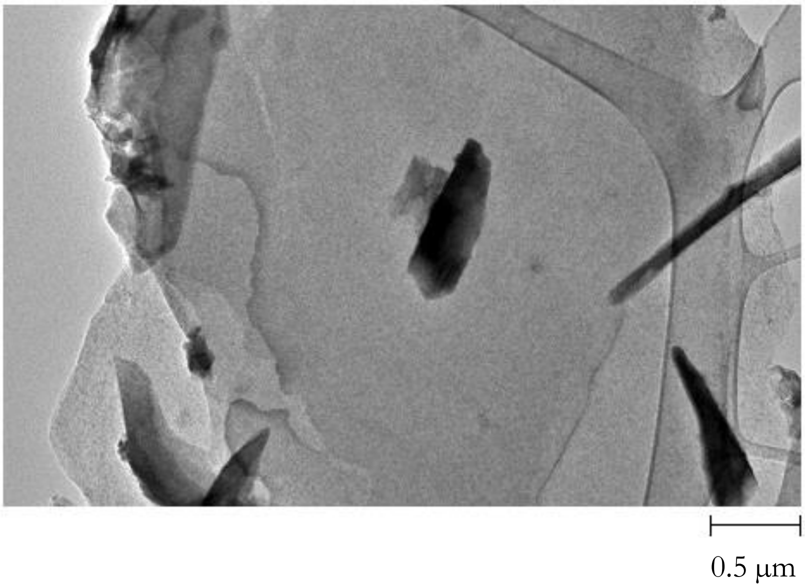

Figure 3.67 A TEM image of polysilane highlighting the thinness of the sheets and the artefacts on the surface.

Figure 3.67 shows a typical TEM image of layered polysilane, which highlights the thinness of the material and also the lacey carbon film supporting the sheets. Another feature observed is the stacking of sheets, with 3-5 sheets stacked on top of one another in *Figure 3.67*. The darker material visible in *Figure 3.67* corresponds to artefacts, probably from when the material was deposited onto the grids.

The sheets behave like, and look similar to, graphene in many ways, and *Figure 3.68* displays a series of images demonstrating the movement of a wave in the sheets over a short space of time when irradiated with an electron beam. In order to show this movement, an artefact on the surface was used as a reference point, highlighted in a red circle in *Figure 3.68a/i*. In picture *a,* it is above the ripple however, after beam irradiation, the artefact is below the ripple in picture *i,* revealing the movement within the sheets.

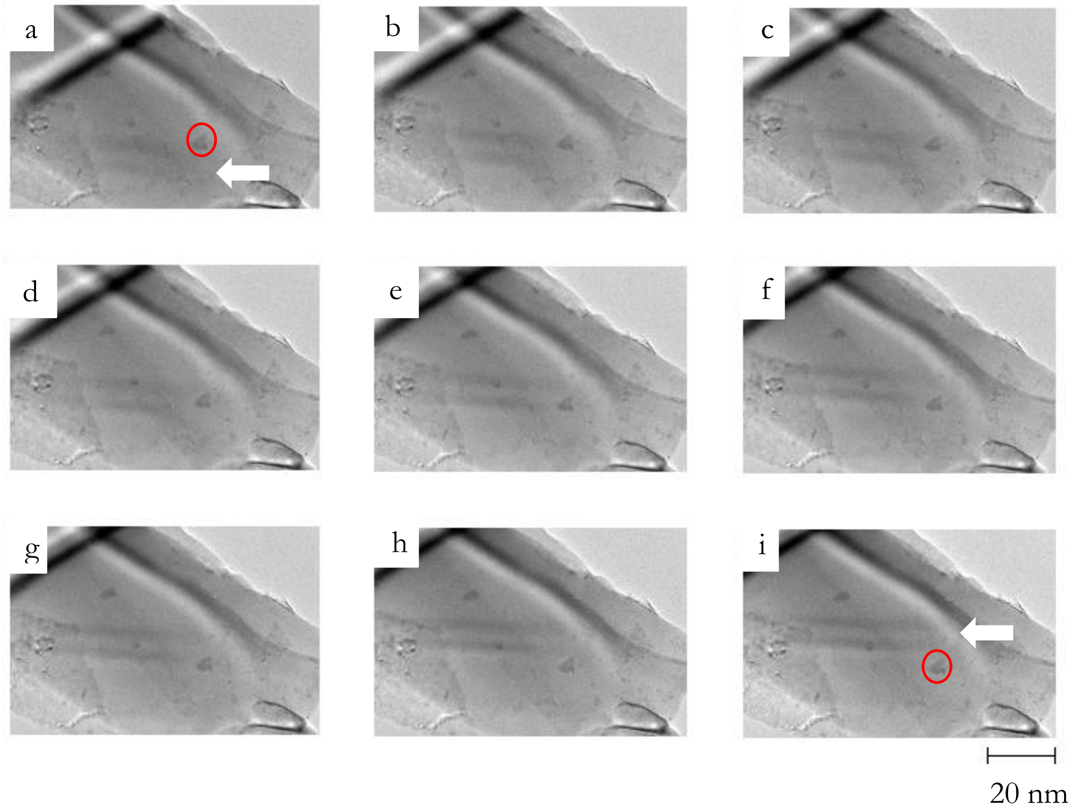

Figure 3.68 A series of TEM images showing a ripple in the sheets over a few seconds. The red circles highlight an artefact used as a reference to track ripple movement. The white arrows highlights the ripple.

Figure 3.69 shows further TEM images of layered polysilane and their characteristic features. In particular, *Figure 3.69e* shows the layer by layer build-up of sheets and laminar structure. From this we can identify that sheets of polysilane have the same lattice type and also have similar lattice spacing, allowing them to fit one layer on top of another. The surfaces of polysilane appear flat and in the cases where the sheets are ordered, for example *Figure 3.69e*, edge displacement of the sheets can be measured using imaging software (Digital Micrograph). The edge displacement is highlighted by two red lines in *Figure 3.69e* and each sheet on average has a 29 nm displacement with the adjacent sheet. The layering of the sheets is stable due to the strong layer-layer interactions, such as van der Waal's forces. The layer-wise deposition results in a crystalline structure as highlighted in powder XRD (Section 3.2.5.3).

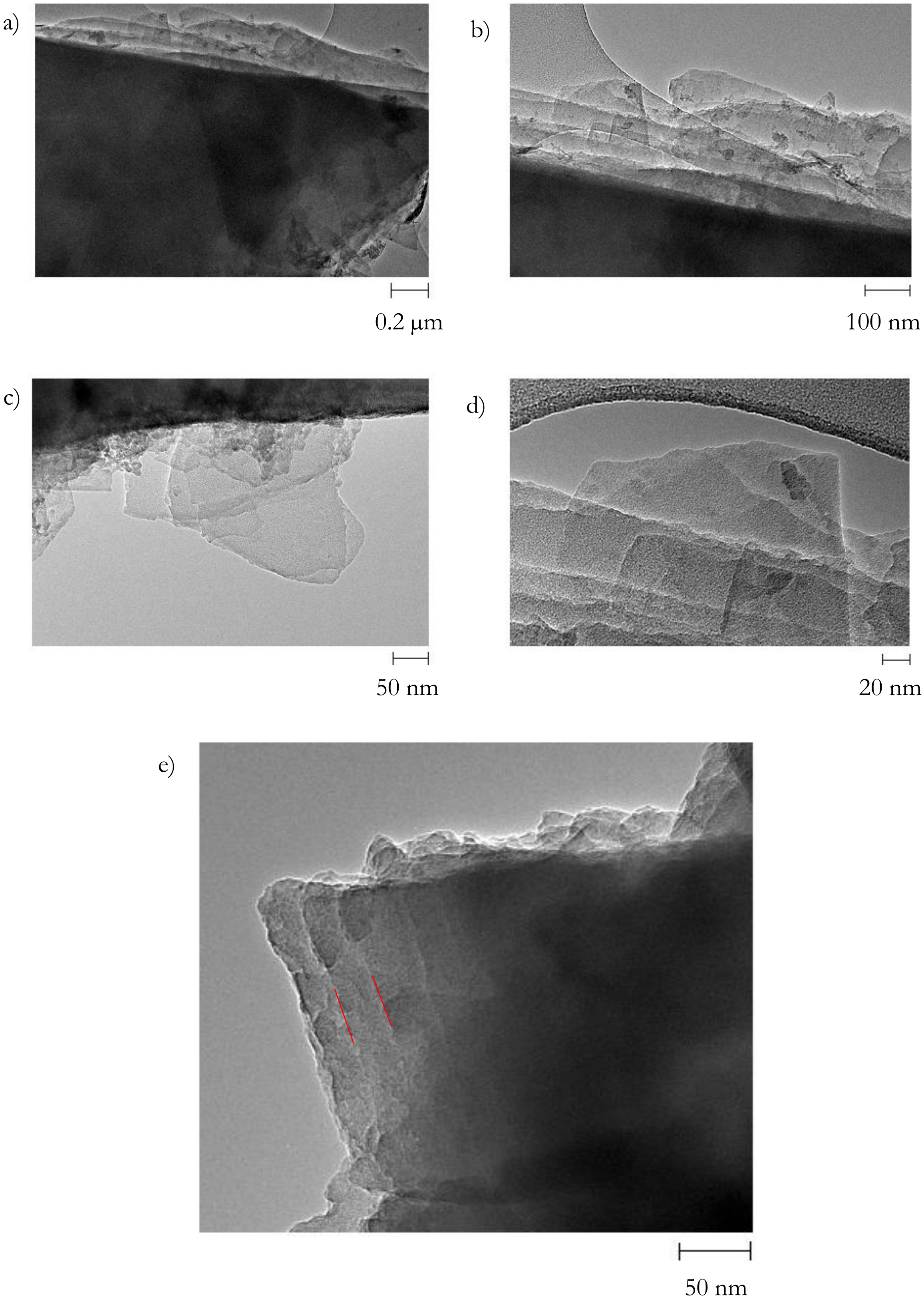

Figure 3.69 TEM images of layered polysilane deposited of a holey carbon film copper grid. The two red lines in image e) highlights an example of edge displacement from adjacent sheets.

In agreement with powder XRD measurements, HRTEM images of polysilane (*Figure 3.70*) show a mixture of both crystalline and amorphous areas within the material. Crystalline areas have been highlighted in a white box in *Figure 3.70a* with different orientations observed within the crystallinity parts. Fourier transform, a tool to look at the periodicity within an image, showed mostly amorphous structure, as diffraction spots were not observed.

Lattice fringes, which can be detected by examining TEM images, are caused when incident electrons are diffracted by the specimen. This is a phase-contrast phenomenon *i.e.* interference of waves.[130] The periodic bright and dark bands in *Figure 3.70c* are lattice fringes and are interpreted as the projection of tunnels between columns of atoms. Whether the dark lines are atoms or the spaces between atoms depends on the parameters, thickness and orientation of the sample. The spacing of the fringe corresponds to that of the lattice plane, and a digital micrograph is used to measure the spacing between adjacent fringes. In the sample, the distance is 0.32 nm (3.2 Å), the distance between neighbouring atoms. This distant correlates to that obtained from powder XRD spacing within the polysilane sheet itself, where a *d*-spacing of 3.25 Å is calculated *via* Braggs law from the peak observed at 27.39° (see Section 3.2.5.3). Accuracy is improved by measuring an average between different fringes.

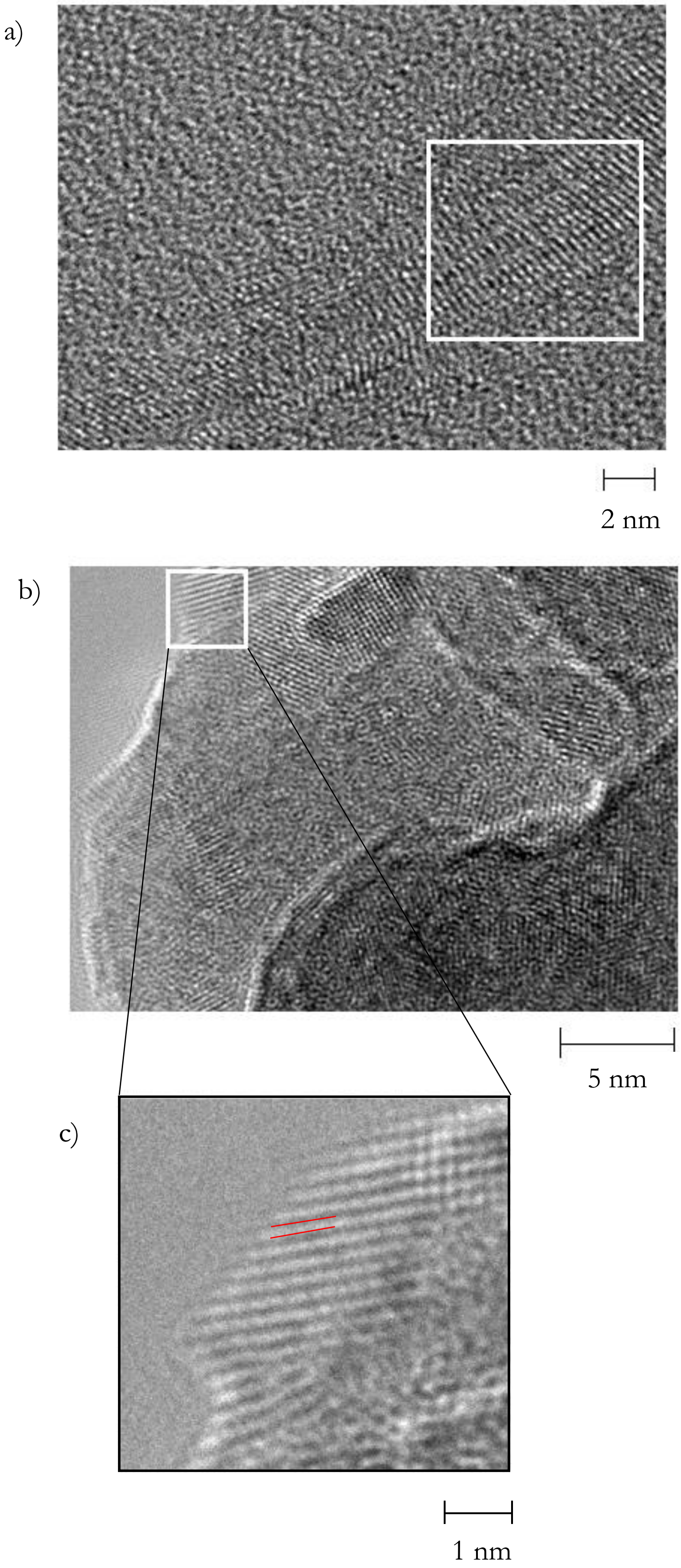

Figure 3.70 HRTEM images highlighting part amorphous and part crystalline structure of polysilane. The lattice fringe is highlighted in image c) by two red lines and was measured at 3.2 Å.

TEM-EDX measurements detail elements present in the sample and their relative percentage detection. When analysing this data we have to take into consideration the support films used and the perturbation that they might have on the results. The EDX data shown in *Table 3.6* is taken from polysilane deposited on a graphene oxide copper grid. There appears to be an approximate 2 : 1 ratio of oxygen to silicon. Taking into consideration oxygen from the graphene oxide film, this would still imply that there is a degree of oxygen in the silicon sheets, most likely from the Si-O-Si bridges. Additionally, the rapid transformation of Si-H bonds to Si-OH groups with exposure to the atmosphere may also contribute to the oxygen detection. A small amount of calcium and chloride are present, which is most probably from the starting materials (calcium disilicide and HCl). As with SEM, trace amounts of aluminium and copper are present from the grid holder and copper mesh grid respectively.

Table 3.6 TEM-EDX results for layered polysilane deposited on a graphene oxide support film copper grid.

Element	**Atomic %**
C	30.8
O	46.0
Si	21.2
Al	0.3
Cl	0.1
Ca	0.3
Cu	1.3

The third type of TEM grids used to analyse the sample were gold grids. These grids hold the advantage that a support film is not present and therefore, when probing elemental composition, only gold needs to be accounted for from the grid. However, the disadvantages of these grids are that the material does not disperse well on them but rather gathers on the metal grid and the large mesh holes allow material to fall through making analysis of the sample difficult. Layered polysilane was dispersed in hexane, and deposited on gold grids using the drop-cast method. The EDX results are shown in *Table 3.7* and this data, when compared to *Table 3.6*, shows an increase in Si : O ratio, which is now approximately 3 : 1 compared to 1 : 2. There is still a fairly large amount of oxygen in the material and the conclusion was drawn that even after HF rinsing, oxygen was still present in the silicon frame.

Table 3.7 TEM-EDX results for layered polysilane deposited on gold grids.

Element	**Atomic %**
C	1.3
O	20.6
Si	63.1
Cl	4.63
Ca	1.70
F	1.82
Al	0.47

3.3 Conclusions

A full characterisation of layered polysilane has been completed, including comparison to literature, and a range of analytical techniques were employed. The synthesis of layered polysilane was achieved *via* deintercalation of calcium disilicide using concentrated hydrochloric acid, adopting a similar method to Yamanaka.[98] The SiNS were terminated with a mixture of hydrogen and hydroxyl groups. Oxygen, either from the atmosphere or hydroxyl groups present on the surface, were inserted into the silicon planes creating Si-O-Si linkers between six-membered silicon rings. However, rinsing with hydrofluoric acid (5 %) removed, to some extent, the hydroxyl bonds and Si-O-Si linkers. The SiNS were sensitive to air overtime, but did not spontaneously combust upon contact with air unlike the claims of some literature reports.[105]

IR spectroscopy revealed removal of an absorption at 3289 cm^{-1} after rinsing siloxene with HF, and it is therefore concluded that all bonds terminating the sheets in layered polysilane are Si-H rather than Si-OH bonds. The absorption band at ~2100 cm^{-1} in both products confirms the Si-H termination of layered polysilane, but also clarifies that siloxene is terminated by a variety of Si-H and Si-OH bonds. A small absorption band at 895 cm^{-1} was observed after HF rinsing, which was assigned to C-F. It is suggested that this is a carbon halide impurity rather than fluorine attached to the sheets, as there is no evidence of Si-F bonding in XPS analysis but rather evidence for C-F with a small peak at higher binding energy in the carbon 1s component. A large absorption at ~1050 cm^{-1} was present in both structures, and therefore we have concluded that oxygen is inserted into the silicon planes to some extent, more so in siloxene than in layered polysilane.

Raman spectroscopy revealed shifts at ~375, ~490, ~520, ~635 and 730 cm^{-1}. Peaks at ~375 and ~520 cm^{-1} correspond to Si-Si plane vibrations, and peaks at ~635 and 730 cm^{-1} correspond to Si-H vibrations. The peak at ~490 cm^{-1} is larger for siloxene than layered polysilane and is assigned to Si-O vibrations, which is in agreement with other techniques that indicate that siloxene has a greater extent of oxygen coverage than polysilane.

Investigation and extrapolation of data from the powder XRD patterns suggested that both amorphous and crystalline structures were present in layered polysilane. Diffraction peaks at 14.92° and 28.44° correspond to the layering of the sheets and utilising Bragg's law gives *d*-spacing of 6.19 Å and 3.13 Å respectively. *d*-spacing of 6.19 Å refers to the spacing between the silicon frameworks with adjacent sheets, and *d*-spacing of 3.13 Å is the spacing between the hydrogen atoms between adjacent sheets. Diffraction peaks at 27.39° and 47.32° correspond to periodicity within the sheet structure. The peak at 27.39° gives a *d*-spacing of 3.25 Å, which agrees with the periodicity spacing calculated in HRTEM images.

XPS investigated the surface of the sheets and revealed that rinsing the sheets with HF changed the ratio of Si : O from 1 : 1.3 in siloxene to 3.5 : 1 in polysilane. There was an increase in fluorine atomic percentage after rinsing with HF, which went up to ~12 %. However, examining the silicon 2p orbital peak confirm that the fluorine was not attached to the silicon in the sheets but was rather a molecular impurity.

Microscopic techniques allowed in-depth studies of the elemental composition and surface detail of layered polysilane. A clear identification of sheets *via* both TEM and SEM was achieved and the images revealed that the sheets were stacked. The sheets had a rippling appearance similar to that of graphene, and ranged in sizes 5-10 μm. HRTEM images displayed crystalline parts where lattice fringe measurements were taken. The average distance between adjacent tunnels of atoms was measured at 3.2 Å, which is in agreement with the periodicity within the silicon framework from powder XRD diffraction patterns with a *d*-spacing of 3.25 Å.

3.4 Experimental

3.4.1 Materials

All chemicals were obtained from commercial suppliers (Alfa Aesar, Fisher Scientific, Sigma-Aldrich, or VWR international) and used without further purification. Cold reactions used a Cole-Parmer immersion cooler, model VLT1000. Preparation of $CaSi_2$ was performed in an MBraun UNIlab glove box operating under a dinitrogen atmosphere. The sample products were exposed to air during synthetic workup, HF rinsing and transfer between measuring equipment. All samples were sealed in vacuum during measurements of XPS, SEM and TEM. IR (~1 minute), Raman (15 minutes) and powderXRD (~20 minutes) measurements had relatively short exposure time.

3.4.2 General Equipment

3.4.2.1 Infrared Spectroscopy

Infrared spectra were obtained with a Bruker Tensor 27 FTIR spectrometer at room temperature with an ATR attachment.

3.4.2.2 Raman Spectroscopy

Raman spectra recorded of the solid samples directly without any pre-treatment/deposition on the Horiba–Jobin–Yvon LabRAM Raman microscope, with a laser wavelength of 532 nm operating at a power of ca. 20 mW and a 600 lines/mm grating.

3.4.2.3 Powder X-ray Diffraction

pXRD data was collected using a PANalytical X'Pert PRO powder diffractometer equipped with a monochromated Cu $K\alpha_1$ radiation source (λ = 1.5432 Å, 40 kV, 40 mA).

The instrument was fitted with 0.04 rad Soller slits on both the diffracted and incident beams as well as programmable divergent slits on both beams that were set to an irradiative length of 20.0 mm. The powder samples analysed in this thesis were placed on circular zero background silicon plates using PW3064/60 sample spinner and a revolution time of four seconds. The experiment parameters for the data collection were typically start angle 5°, end angle 60°, step size 0.026°, and scan speed 0.035 °/s.

3.4.2.4 X-ray Photoelectron Spectroscopy

XPS data was recorded on a XPS Kratos Axis Ultra LiPPS. For the samples in this Chapter, the powder was placed on double sided sticky tape whereby one end was attached to the sample holder and the other held the powder. The powder covered approximately 0.5 by 0.5 cm area. Spectra were acquired using the Al-Kα monochromatic X-ray source (1486.7 eV) with 0° take of angle (normal to analyser). The vacuum pressure in the analysing chamber was maintained at ~$2x10^{-9}$ Torr during the acquisition process. The survey spectra were collected with pass energy 160 eV, and 0.5 eV step wise, dwell time 250 ms. Data analyses were done using Kratos Vision (Kratos Analytical Ltd) processing software and CasaXPS Version 2.3.16 PR 1.6. (Casa Software Ltd).

3.4.2.5 Scanning Electron Microscopy

SiNS materials were dispersed in an organic solvent (usually hexane) using an ultrasonic bath and drop-cast onto SEM grids (Agar). Quanta 650 SEM, equipped with an Oxford Instruments X-Max 150 mm SDD detector for EDX.

3.4.2.6 Transmission Electron Microscopy

SiNS material were dispersed in an organic solvent (usually hexane) using an ultrasonic bath and drop-cast onto TEM grids (Agar). Two transmission electron microscopes were used. JEOL 2100F, field emission source TEM equipped with a Gatan Orius CCD camera for imaging and an Oxford Instruments 80 mm X-Max system for EDX. JEOL 2100 Plus TEM, LaB_6 source, equipped with a Gatan Ultrascan camera for imaging and an Oxford Instruments X-Max 80 TLE system for EDX.

3.4.3 Synthesis of Siloxene

The synthesis of this compound was carried out according to a known literature procedure.[98] $CaSi_2$ (1 g, 10.5 mmol) was prepared in a sealed Schlenk flask in a glove box operating under a dinitrogen atmosphere. Conc. HCl (100 mL) was added and the reaction mixture stirred while purging with dinitrogen for 5 days at -30 °C. The resultant green solid slurry was allowed to heat to room temperature before being washed with acetone (50 mL); subsequently dried under vacuum at 110 °C overnight to reveal a fine green/yellow powder (820 mg).

IR (ATR): 3289, 2102, 1632, 1028, 797, 632, 561 cm^{-1}.

3.4.4 Synthesis of Layered Polysilane

A small amount of siloxene (80 mg) was taken and placed on filter paper in a Büchner funnel. HF (5 %) was poured over the powder and the powder allowed to rapidly dry before immediately placing it in a vial and subsequently under vacuum at 110 °C (40 mg).

IR (ATR): 2110, 1066, 895, 860, 796, 634, 556 cm^{-1}.

3.5 References

1. Z. Lu, J. Zhu, D. Sim, W. Zhou, W. Shi, H. H. Hng and Q. Yan, *Chem. Mater.*, 2011, **23**, 5293-5295.
2. S. K. Bux, R. G. Blair, P. K. Gogna, H. Lee, G. Chen, M. S. Dresselhaus, R. B. Kaner and J.-P. Fleurial, *Adv. Funct. Mater.*, 2009, **19**, 2445-2452.
3. J. Frühauf, *Shape and Functional Elements of the Bulk Silicon Microtechnique: A Manual of Wet-Etched Silicon Structures*, Springer Berlin Heidelberg, 2005.
4. R. Hull, *Properties of Crystalline Silicon*, IET, London, 1999.
5. H. Okamoto, Y. Sugiyama and H. Nakano, *Chem. - Eur. J.*, 2011, **17**, 9864-9887.
6. B. K. Teo and X. H. Sun, *Chem. Rev.*, 2007, **107**, 1454-1532.
7. R. A. Bley and S. M. Kauzlarich, *J. Am. Chem. Soc.*, 1996, **118**, 12461-12462.
8. R. A. Bley, S. M. Kauzlarich, J. E. Davis and H. W. H. Lee, *Chem. Mater.*, 1996, **8**, 1881-1888.
9. R. K. Baldwin, K. A. Pettigrew, E. Ratai, M. P. Augustine and S. M. Kauzlarich, *Chem. Commun.*, 2002, 1822-1823.
10. H. Takagi, H. Ogawa, Y. Yamazaki, A. Ishizaki and T. Nakagiri, *Appl. Phys. Lett.*, 1990, **56**, 2379-2380.
11. L. Mangolini, E. Thimsen and U. Kortshagen, *Nano Lett.*, 2005, **5**, 655-659.
12. R. M. Sankaran, D. Holunga, R. C. Flagan and K. P. Giapis, *Nano Lett.*, 2005, **5**, 537-541.
13. X. Li, Y. He and M. T. Swihart, *Langmuir*, 2004, **20**, 4720-4727.
14. M. Ehbrecht, B. Kohn, F. Huisken, M. A. Laguna and V. Paillard, *Phys. Rev. B*, 1997, **56**, 6958-6964.
15. K. A. Littau, P. J. Szajowski, A. J. Muller, A. R. Kortan and L. E. Brus, *J. Phys. Chem.*, 1993, **97**, 1224-1230.
16. J. L. Heinrich, C. L. Curtis, G. M. Credo, M. J. Sailor and K. L. Kavanagh, *Science*, 1992, **255**, 66-68.
17. L. N. Dinh, L. L. Chase, M. Balooch, W. J. Siekhaus and F. Wooten, *Phys. Rev. B*, 1996, **54**, 5029-5037.
18. I. Umezu, K. Shibata, S. Yamaguchi, A. Sugimura, Y. Yamada and T. Yoshida, *J. Appl. Phys.*, 1998, **84**, 6448-6450.
19. T. Seto, Y. Kawakami, N. Suzuki, M. Hirasawa and N. Aya, *Nano Lett.*, 2001, **1**, 315-318.
20. J. R. Heath, *Science*, 1992, **258**, 1131-1133.
21. R. D. Tilley and K. Yamamoto, *Adv. Mater.*, 2006, **18**, 2053-2056.
22. F. Hua, M. T. Swihart and E. Ruckenstein, *Langmuir*, 2005, **21**, 6054-6062.
23. R. K. Baldwin, K. A. Pettigrew, J. C. Garno, P. P. Power, G.-y. Liu and S. M. Kauzlarich, *J. Am. Chem. Soc.*, 2002, **124**, 1150-1151.

24. K. A. Pettigrew, Q. Liu, P. P. Power and S. M. Kauzlarich, *Chem. Mater.*, 2003, **15**, 4005-4011.
25. J. D. Holmes, K. J. Ziegler, R. C. Doty, L. E. Pell, K. P. Johnston and B. A. Korgel, *J. Am. Chem. Soc.*, 2001, **123**, 3743-3748.
26. D. S. English, L. E. Pell, Z. Yu, P. F. Barbara and B. A. Korgel, *Nano Lett.*, 2002, **2**, 681-685.
27. J. H. Warner, A. Hoshino, K. Yamamoto and R. D. Tilley, *Angew. Chem. Int. Ed.*, 2005, **44**, 4550-4554.
28. R. Q. Zhang, S. T. Lee, C.-K. Law, W.-K. Li and B. K. Teo, *Chem. Phys. Lett.*, 2002, **364**, 251-258.
29. W. Molnar, A. Lugstein, P. Pongratz, N. Auner, C. Bauch and E. Bertagnolli, *Nano Lett.*, 2010, **10**, 3957-3961.
30. M. J. Frisch, G. W. Trucks, H. B. Schlegel, G. E. Scuseria, M. A. Robb, J. R. Cheeseman, G. Scalmani, V. Barone, B. Mennucci, G. A. Petersson, H. Nakatsuji, M. Caricato, X. Li, H. P. Hratchian, A. F. Izmaylov, J. Bloino, G. Zheng, J. L. Sonnenberg, M. Hada, M. Ehara, K. Toyota, R. Fukuda, J. Hasegawa, M. Ishida, T. Nakajima, Y. Honda, O. Kitao, H. Nakai, T. Vreven, J. A. Montgomery Jr., J. E. Peralta, F. Ogliaro, M. J. Bearpark, J. Heyd, E. N. Brothers, K. N. Kudin, V. N. Staroverov, R. Kobayashi, J. Normand, K. Raghavachari, A. P. Rendell, J. C. Burant, S. S. Iyengar, J. Tomasi, M. Cossi, N. Rega, N. J. Millam, M. Klene, J. E. Knox, J. B. Cross, V. Bakken, C. Adamo, J. Jaramillo, R. Gomperts, R. E. Stratmann, O. Yazyev, A. J. Austin, R. Cammi, C. Pomelli, J. W. Ochterski, R. L. Martin, K. Morokuma, V. G. Zakrzewski, G. A. Voth, P. Salvador, J. J. Dannenberg, S. Dapprich, A. D. Daniels, Ö. Farkas, J. B. Foresman, J. V. Ortiz, J. Cioslowski and D. J. Fox, *Gaussian 09*, (2009) Gaussian, Inc., Wallingford, CT, USA.
31. S. B. Fagan, R. J. Baierle, R. Mota, A. J. R. da Silva and A. Fazzio, *Phys. Rev. B*, 2000, **61**, 9994-9996.
32. S. B. Fagan, R. Mota, R. J. Baierle, G. Paiva, A. J. R. da Silva and A. Fazzio, *J. Mol. Struct.: THEOCHEM*, 2001, **539**, 101-106.
33. A. S. Barnard and S. P. Russo, *J. Phys. Chem. B*, 2003, **107**, 7577-7581.
34. K. Jeong Won, B. Ki Ryang and H. Ho Jung, *Modell. Simul. Mater. Sci. Eng.*, 2004, **12**, 1-12.
35. R. Q. Zhang, H.-L. Lee, W.-K. Li and B. K. Teo, *J. Phys. Chem. B*, 2005, **109**, 8605-8612.
36. J. Bai, X. C. Zeng, H. Tanaka and J. Y. Zeng, *Proc. Natl. Acad. Sci. U. S. A.*, 2004, **101**, 2664-2668.
37. S. Iijima, *Nature*, 1991, **354**, 56-58.
38. J. Prasek, J. Drbohlavova, J. Chomoucka, J. Hubalek, O. Jasek, V. Adam and R. Kizek, *J. Mater. Chem.*, 2011, **21**, 15872-15884.
39. T. Belin and F. Epron, *Mater. Sci. Eng. B*, 2005, **119**, 105-118.

40. E. T. Thostenson, Z. Ren and T.-W. Chou, *Compos. Sci. Technol.*, 2001, **61**, 1899-1912.
41. G. Seifert, T. Köhler, H. M. Urbassek, E. Hernández and T. Frauenheim, *Phys. Rev. B*, 2001, **63**, 193409.
42. P. Melinon, B. Masenelli, F. Tournus and A. Perez, *Nat. Mater.*, 2007, **6**, 479-490.
43. C. Zhang, H. Cheng and X. Liu, *Mater. Chem. Phys.*, 2016, **177**, 479-484.
44. M. De Crescenzi, P. Castrucci, M. Scarselli, M. Diociaiuti, P. S. Chaudhari, C. Balasubramanian, T. M. Bhave and S. V. Bhoraskar, *Appl. Phys. Lett.*, 2005, **86**, 231901.
45. T. Song, J. Xia, J.-H. Lee, D. H. Lee, M.-S. Kwon, J.-M. Choi, J. Wu, S. K. Doo, H. Chang, W. I. Park, D. S. Zang, H. Kim, Y. Huang, K.-C. Hwang, J. A. Rogers and U. Paik, *Nano Lett.*, 2010, **10**, 1710-1716.
46. J. Sha, J. Niu, X. Ma, J. Xu, X. Zhang, Q. Yang and D. Yang, *Adv. Mater.*, 2002, **14**, 1219-1221.
47. P. Castrucci, M. Scarselli, M. De Crescenzi, M. Diociaiuti, P. S. Chaudhari, C. Balasubramanian, T. M. Bhave and S. V. Bhoraskar, *Thin Solid Films*, 2006, **508**, 226-230.
48. F. Hongjin, K. Mato, S. Roland, N. Kornelius, P. Eckhard, H. Dietrich, G. Ulrich and Z. Margit, *Nanotechnology*, 2006, **17**, 5157-5162.
49. X. Huang, R. Gonzalez-Rodriguez, R. Rich, Z. Gryczynski and J. L. Coffer, *Chem. Commun.*, 2013, **49**, 5760-5762.
50. M.-H. Park, M. G. Kim, J. Joo, K. Kim, J. Kim, S. Ahn, Y. Cui and J. Cho, *Nano Lett.*, 2009, **9**, 3844-3847.
51. A. T. Tesfaye, R. Gonzalez, J. L. Coffer and T. Djenizian, *ACS Appl. Mater. Interfaces*, 2015, **7**, 20495-20498.
52. X. Zhang, H. Ge, G. Wang and Y. Liao, *Chem. Phys.*, 2016, **469–470**, 72-78.
53. M. Huang, C. S. Ritz, B. Novakovic, D. Yu, Y. Zhang, F. Flack, D. E. Savage, P. G. Evans, I. Knezevic, F. Liu and M. G. Lagally, *ACS Nano*, 2009, **3**, 721-727.
54. W. Shi, H. Peng, N. Wang, C. P. Li, L. Xu, C. S. Lee, R. Kalish and S.-T. Lee, *J. Am. Chem. Soc.*, 2001, **123**, 11095-11096.
55. C. N. R. Rao, A. Müller and A. K. Cheetham, *The Chemistry of Nanomaterials: Synthesis, Properties and Applications*, Wiley-VCH, Germany, 2006.
56. H. Zhang, W. Ding, K. He and M. Li, *Nanoscale Res. Lett.*, 2010, **5**, 1264-1271.
57. Y.-N. Yang, J.-M. Zhang and K.-W. Xu, *Phys. E*, 2014, **57**, 21-27.
58. R. L. Stoop, M. Wipf, S. Müller, K. Bedner, I. A. Wright, C. J. Martin, E. C. Constable, A. Fanget, C. Schönenberger and M. Calame, *Biosensors*, 2016, **6**, 21.
59. D.-B. Lu, C.-Y. Pu, Y.-L. Song, Q.-N. Pan, D.-W. Zhou and H.-R. Xu, *Chin. Phys. B*, 2015, **24**, 127802.
60. Y. Ding and J. Ni, *Appl. Phys. Lett.*, 2009, **95**, 083115.

61. S. Cahangirov, M. Topsakal, E. Aktürk, H. Şahin and S. Ciraci, *Phys. Rev. Lett.*, 2009, **102**, 236804.
62. Y. Sun, W. M. Choi, H. Jiang, Y. Y. Huang and J. A. Rogers, *Nat. Nano.*, 2006, **1**, 201-207.
63. H. Jiang, Y. Sun, J. A. Rogers and Y. Huang, *Appl. Phys. Lett.*, 2007, **90**, 133119.
64. N. Elfström, A. E. Karlström and J. Linnros, *Nano Lett.*, 2008, **8**, 945-949.
65. J. Kim, M. Lee, H. J. Shim, R. Ghaffari, H. R. Cho, D. Son, Y. H. Jung, M. Soh, C. Choi, S. Jung, K. Chu, D. Jeon, S.-T. Lee, J. H. Kim, S. H. Choi, T. Hyeon and D.-H. Kim, *Nat. Commun.*, 2014, **5**, 1-11.
66. J. N. Coleman, M. Lotya, A. O'Neill, S. D. Bergin, P. J. King, U. Khan, K. Young, A. Gaucher, S. De, R. J. Smith, I. V. Shvets, S. K. Arora, G. Stanton, H.-Y. Kim, K. Lee, G. T. Kim, G. S. Duesberg, T. Hallam, J. J. Boland, J. J. Wang, J. F. Donegan, J. C. Grunlan, G. Moriarty, A. Shmeliov, R. J. Nicholls, J. M. Perkins, E. M. Grieveson, K. Theuwissen, D. W. McComb, P. D. Nellist and V. Nicolosi, *Science*, 2011, **331**, 568-571.
67. H. S. S. Ramakrishna Matte, A. Gomathi, A. K. Manna, D. J. Late, R. Datta, S. K. Pati and C. N. R. Rao, *Angew. Chem. Int. Ed.*, 2010, **49**, 4059-4062.
68. H. S. S. R. Matte, B. Plowman, R. Datta and C. N. R. Rao, *Dalton Trans.*, 2011, **40**, 10322-10325.
69. A. Nag, K. Raidongia, K. P. S. S. Hembram, R. Datta, U. V. Waghmare and C. N. R. Rao, *ACS Nano.*, 2010, **4**, 1539-1544.
70. B. Wang, B. Luo, X. Li and L. Zhi, *Mater. Today*, 2012, **15**, 544-552.
71. G. Pacchioni, *Chem. - Eur. J.*, 2012, **18**, 10144-10158.
72. P.-Z. Li, Y. Maeda and Q. Xu, *Chem. Commun.*, 2011, **47**, 8436-8438.
73. C. N. R. Rao, H. S. S. Ramakrishna Matte and U. Maitra, *Angew. Chem. Int. Ed.*, 2013, **52**, 13162-13185.
74. C. N. R. Rao, H. S. S. R. Matte and K. S. Subrahmanyam, *Acc. Chem. Res.*, 2013, **46**, 149-159.
75. M. J. S. Spencer and T. Morishita, *Silicene: Structure, Properties and Applications*, Springer International Publishing, Switzerland, 2016.
76. L. Tao, E. Cinquanta, D. Chiappe, C. Grazianetti, M. Fanciulli, M. Dubey, A. Molle and D. Akinwande, *Nat. Nano.*, 2015, **10**, 227-231.
77. E. F. Sheka, *Int. J. Quantum Chem.*, 2013, **113**, 612-618.
78. E. Cinquanta, E. Scalise, D. Chiappe, C. Grazianetti, B. van den Broek, M. Houssa, M. Fanciulli and A. Molle, *J. Phys. Chem. C*, 2013, **117**, 16719-16724.
79. T. Suzuki and Y. Yokomizo, *Phys. E*, 2010, **42**, 2820-2825.
80. D. Kaltsas and L. Tsetseris, *Phys. Chem. Chem. Phys.*, 2013, **15**, 9710-9715.
81. K. Takeda and K. Shiraishi, *Phys. Rev. B*, 1994, **50**, 14916-14922.
82. J. R. Soto, B. Molina and J. J. Castro, *Phys. Chem. Chem. Phys.*, 2015, **17**, 7624-7628.

83. L. C. Lew Yan Voon, E. Sandberg, R. S. Aga and A. A. Farajian, *Appl. Phys. Lett.*, 2010, **97**, 163114.

84. P. Vogt, P. De Padova, C. Quaresima, J. Avila, E. Frantzeskakis, M. C. Asensio, A. Resta, B. Ealet and G. Le Lay, *Phys. Rev. Lett.*, 2012, **108**, 155501.

85. D. Chiappe, C. Grazianetti, G. Tallarida, M. Fanciulli and A. Molle, *Adv. Mater.*, 2012, **24**, 5088-5093.

86. B. Feng, Z. Ding, S. Meng, Y. Yao, X. He, P. Cheng, L. Chen and K. Wu, *Nano Lett.*, 2012, **12**, 3507-3511.

87. H. Jamgotchian, Y. Colignon, N. Hamzaoui, B. Ealet, J. Y. Hoarau, B. Aufray and J. P. Bibérian, *J. Phys.: Condens. Matter*, 2012, **24**, 172001.

88. L. Chun-Liang, A. Ryuichi, K. Kazuaki, T. Noriyuki, M. Emi, K. Yousoo, T. Noriaki and K. Maki, *Appl. Phys. Express*, 2012, **5**, 045802.

89. A. Fleurence, R. Friedlein, T. Ozaki, H. Kawai, Y. Wang and Y. Yamada-Takamura, *Phys. Rev. Lett.*, 2012, **108**, 245501.

90. L. Meng, Y. Wang, L. Zhang, S. Du, R. Wu, L. Li, Y. Zhang, G. Li, H. Zhou, W. A. Hofer and H.-J. Gao, *Nano Lett.*, 2013, **13**, 685-690.

91. E. Scalise, M. Houssa, E. Cinquanta, C. Grazianetti, B. v. d. Broek, G. Pourtois, A. Stesmans, M. Fanciulli and A. Molle, *2D Mater.*, 2014, **1**, 011010.

92. J. Zhu and U. Schwingenschlogl, *J. Mater. Chem. C*, 2015, **3**, 3946-3953.

93. G. Vogg, M. S. Brandt and M. Stutzmann, *Adv. Mater.*, 2000, **12**, 1278-1281.

94. U. Kim, I. Kim, Y. Park, K.-Y. Lee, S.-Y. Yim, J.-G. Park, H.-G. Ahn, S.-H. Park and H.-J. Choi, *ACS Nano*, 2011, **5**, 2176-2181.

95. S. W. Kim, J. Lee, J. H. Sung, D.-j. Seo, I. Kim, M.-H. Jo, B. W. Kwon, W. K. Choi and H.-J. Choi, *ACS Nano*, 2014, **8**, 6556-6562.

96. W.-S. Kim, Y. Hwa, J.-H. Shin, M. Yang, H.-J. Sohn and S.-H. Hong, *Nanoscale*, 2014, **6**, 4297-4302.

97. J. Ryu, Y. J. Jang, S. Choi, H. J. Kang, H. Park, J. S. Lee and S. Park, *NPG Asia Mater.*, 2016, **8**, e248.

98. S. Yamanaka, H. Matsu-ura and M. Ishikawa, *Mater. Res. Bull.*, 1996, **31**, 307-316.

99. H. Schäfer, B. Eisenmann and W. Müller, *Angew. Chem. Int. Ed.*, 1973, **12**, 694-712.

100. A. Mustapha Ait and T. Mohamed Rachid, *J. Phys.: Conf. Ser.*, 2014, **491**, 012009.

101. H. Nakano, M. Ishii and H. Nakamura, *Chem. Commun.*, 2005, 2945-2947.

102. M. S. Brandt, G. Vogg and M. Stutzmann, in *Silicon- and Germanium-Based Sheet Polymers and Zintl Phases*, Wiley-VCH, Germany, 2007, pp. 194-213.

103. A. Weiss, G. Beil and H. Meyer, *Naturforsch*, 1979, **34b**, 25-30.

104. J. R. Dahn, B. M. Way, E. Fuller and J. S. Tse, *Phys. Rev. B*, 1993, **48**, 17872-17877.

105. J. R. Dahn, B. M. Way, E. W. Fuller, W. J. Weydanz, J. S. Tse, D. D. Klug, T. Van Buuren and T. Tiedje, *J. Appl. Phys.*, 1994, **75**, 1946-1951.
106. C. G. Van de Walle and J. E. Northrup, *Phys. Rev. Lett.*, 1993, **70**, 1116-1119.
107. J. He, J. S. Tse, D. D. Klug and K. F. Preston, *J. Mater. Chem.*, 1998, **8**, 705-710.
108. N. Kohsuke, N. Yasuyuki, Y. Shoji and M.-u. Hiroyuki, *Jpn. J. Appl. Phys.*, 1996, **35**, 293-296.
109. F. Peng, Y. Su, Y. Zhong, C. Fan, S.-T. Lee and Y. He, *Acc. Chem. Res.*, 2014, **47**, 612-623.
110. Q. Yu, H. Liu and H. Chen, *J. Mater. Chem. B*, 2014, **2**, 7849-7860.
111. Y. Su, F. Peng, X. Ji, Y. Lu, X. Wei, B. Chu, C. Song, Y. Zhou, X. Jiang, Y. Zhong, S.-T. Lee and Y. He, *J. Mater. Chem. B*, 2014, **2**, 2892-2898.
112. Y. He and Y. Su, *Silicon Nano-biotechnology*, Springer, Berlin, 2014.
113. F. R. Wagner, D. Bende and Y. Grin, *Dalton Trans.*, 2016, **45**, 3236-3243.
114. S. Fahy and D. R. Hamann, *Phys. Rev. B*, 1990, **41**, 7587-7592.
115. B. R. Weinberger, G. G. Peterson, T. C. Eschrich and H. A. Krasinski, *J. Appl. Phys. Rev.*, 1986, **60**, 3232-3234.
116. S. L. Warring, D. A. Beattie and A. J. McQuillan, *Langmuir*, 2016, **32**, 1568-1576.
117. G. Socrates, *Infrared and Raman Characteristic Group Frequencies: Tables and Charts*, 3rd edn., John Wiley & Sons, Chichester, 2004.
118. P.-F. Wang, S.-J. Ding, W. Zhang, J.-Y. Zhang, J.-T. Wang and W. Lee William, *Chin. Phys. Lett.*, 2000, **17**, 912-914.
119. M. Schmitt, *RSC Adv.*, 2014, **4**, 1907-1917.
120. H. D. Fuchs, M. Stutzmann, M. S. Brandt, M. Rosenbauer, J. Weber, A. Breitschwerdt, P. Deák and M. Cardona, *Phys. Rev. B*, 1993, **48**, 8172-8189.
121. P. Vora, S. A. Solin and P. John, *Phys. Rev. B*, 1984, **29**, 3423-3429.
122. J. W. Swart, *Microelectronics Technology and Devices* Electrochemical Society, New Jersey, 2008.
123. G. Krötz, W. Hellmich, G. Müller, G. Derst and S. Kalbitzer, *Nucl. Instrum. Methods Phys. Res., Sect. B*, 1993, **80**, 927-930.
124. P. Larkin, in *Infrared and Raman Spectroscopy: Principles and Spectral Interpretation*, Elsevier, Oxford, 2011, pp. 73-115.
125. S. Hüfner, in *Photoelectron Spectroscopy: Principles and Applications*, Springer Berlin Heidelberg, 1995, pp. 431-454.
126. T. L. Barr and S. Seal, *J. Vac. Sci. Technol., A*, 1995, **13**, 1239-1246.
127. D. G. Robinson, K. Mühlethaler, U. Ehlers, R. Herken, B. Herrmann, F. Mayer and F. W. Schürmann, *Methods of Preparation for Electron Microscopy: An Introduction for the Biomedical Sciences*, Springer Berlin Heidelberg, 2012.
128. G. van Tendeloo, D. van Dyck and S. J. Pennycook, *Handbook of Nanoscopy: Volume 1*, Wiley-VCH, Germany, 2012.

129. J. Goldstein, D. E. Newbury, D. C. Joy, C. E. Lyman, P. Echlin, E. Lifshin, L. Sawyer and J. R. Michael, *Scanning Electron Microscopy and X-ray Microanalysis*, Plenum, New York, 2003.

130. D. B. Williams and C. B. Carter, *Transmission Electron Microscopy: A Textbook for Materials Science*, 2nd edn., Springer, USA, 2009.

Chapter 4

Functionalisation of Silicon Nanosheets

4.1 Introduction

The synthesis and characterisation of 2D silicon nanosheets (SiNS) have previously been discussed in Chapter 3, in particular layered polysilane and siloxene. When referring to SiNS within this Chapter, this primarily means layered polysilane unless stated otherwise. Chemical modification of SiNS is discussed herein using a variety of groups and methods to functionalise target nanosheets. Studies of organo-modified SiNS are still very much in their infancy, however they are expected to be used in many different fields including electronic applications, photonic devices and lithium ion battery electrodes.[1-3] There are two key purposes for functionalising SiNS including:

i. Promote exfoliation: SiNS easily aggregate and are challenging to disperse in typical organic solvents. Addition of small organic groups to the sheets promotes exfoliation and increases solubility. It is an advantage if SiNS can be used in solution for use as building blocks in different devices.
ii. Control the interlayer spacing: Depending on the size of the organic group attached to the sheets the spacing between adjacent sheets can be controlled.

To date, capping with organic functional groups has been attempted in the literature using four different functional groups, including; amines (Section 4.1.1); Grignard reagents (Section 4.1.2); alkenes (Section 4.1.3); and lithium (Section 4.1.4). There is at present very little data and evidence for the functionalisation of sheets with many questionable results in literature.

4.1.1 Amine Modified Silicon Nanosheets

In 2010, Nakano and co-workers attempted to modify SiNS by chemically attaching straight chain decyl groups to the sheets *via* a Si-N bond using amine moieties.[4] Nakano and co-workers performed the reaction by stirring a mixture of n-decylamine and chloroform for approximately 1 hour at 60 °C in a dinitrogen atmosphere. Nakano suggests that some of the Si-H bonds on the polysilane sheet reacted with the amine molecules to form Si-NH-decyl linkers on both sides of the sheets as displayed in *Figure 4.71a*. Increasing the temperature causes further reaction between the amine residues and adjacent Si-H bonds on the same sheet, forming Si-NR-Si linkers as modelled in *Figure 4.71b*.

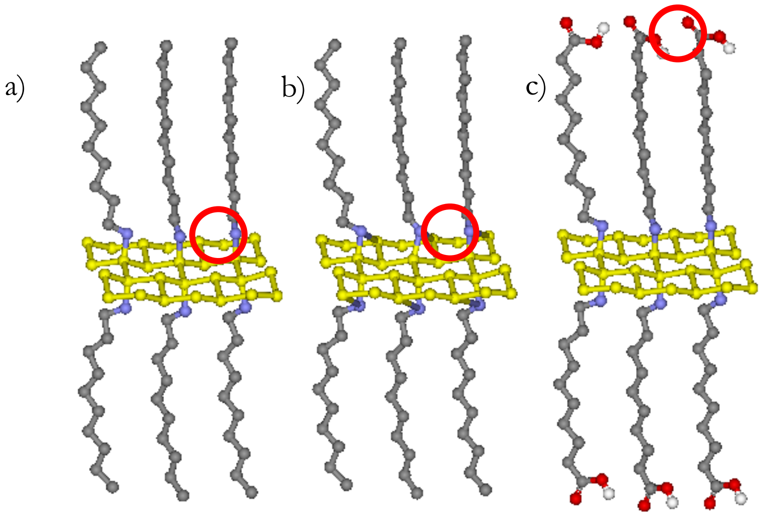

Figure 4.71 Modified SiNS modelling decyl groups attached on both sides of the sheet via a) Si-N bonds, b) Si-NR-Si linkers and c) Si-N bonds with carboxylic acid groups. Most hydrogen atoms have been removed for clarity and the differences between structures are highlighted in red circles. Atom colours; silicon = yellow, carbon = grey, nitrogen = blue, oxygen = red and hydrogen = white.

Furthermore, Nakano reacts amino-carboxylic acids with polysilane, again functionalising *via* amine groups. However, now the chains have carboxylic acids at the other end as displayed in *Figure 4.71c*.[5] Nakano and co-workers used infrared (IR) spectroscopy to study the bonding involved in the functionalised sheets. *Figure 4.72* shows the IR spectrum for a) polysilane, b) decyl-SiNS and c) decylamine. Two differences were observed once the sheets were modified. Firstly, strong C-H stretching vibrations between 2800-3000 cm^{-1} became apparent in the decyl-modified sheets and secondly the disappearance of Si-H stretch at 2100 cm^{-1} in *Figure 4.72b*. The peak at 930 cm^{-1} in *Figure 4.72b* is assigned to Si-N-Si stretching mode, clarifying the attachment of the decyl chains *via* the nitrogen.

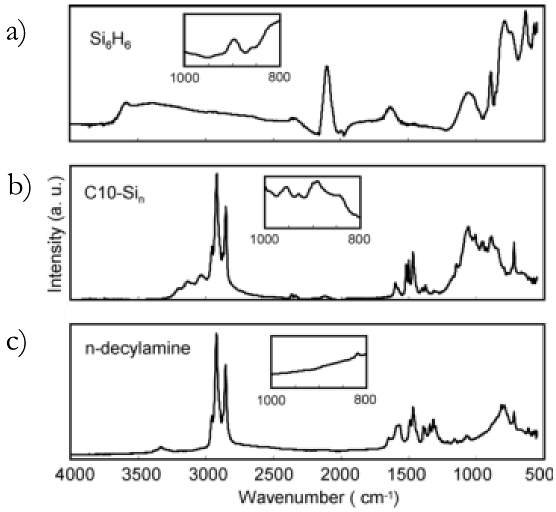

Figure 4.72 IR spectra of a) polysilane, b) decyl-modified SiNS, and c) n-decylamine. The insets show enlarged spectra in the range from 800 to 1000 cm^{-1}.[4]

Nakano and co-workers also used X-ray absorption near-edge structure (XANES) to reveal Si-N linkage by comparing to reference samples such as crystalline silicon, quartz, siloxene and layered polysilane. In addition, AFM and SEM analytical methods were used to investigate the sheet structure. Smooth sheets were observed (*Figure 4.73a*) and thickness of the modified nanosheets were 10 times larger than the thickness of the starting material nanosheets. Powder XRD was studied to reveal characteristics of the modified sheets and their ability to stack in a regular structure by self-assembly. A super-saturated solution of decyl modified sheets in toluene (*Figure 4.73b*) were described as a jelly-like agglomerate material, however fluidity is lost when the solvent slowly evaporates and a flake-like product forms (*Figure 4.73c*).

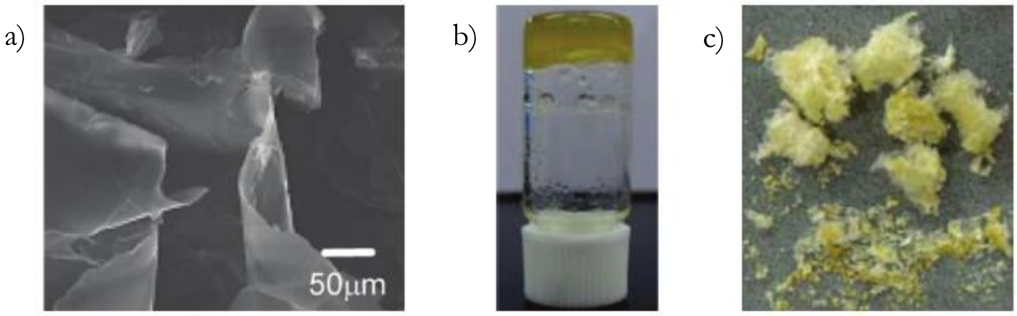

Figure 4.73 a) SEM image of decyl modified sheets. b) Decyl-SiNS dissolved in toluene and slowly evaporating the solvent to concentrate the solution and c) decyl-SiNS dissolved in toluene/chloroform and slowly evaporating the solvent to produce a flake-like product.[4]

4.1.2 Phenyl Modified Silicon Nanosheets using a Grignard Reagent

In 2010 Nakano and co-workers functionalised polysilane sheets creating a stable Si-C bond connecting the sheets and appendages.[6] A model of a phenyl-modified SiNS is shown *Figure 4.74* and Nakano states the sheets were oxygen free and had a thickness of atomic order. The modification of layered polysilane utilised a Grignard reagent where layered polysilane and phenyl magnesium bromide were stirred in THF and heated to 70 °C for two days. The synthesised material was a colourless paste and soluble in organic solvents as predicted.

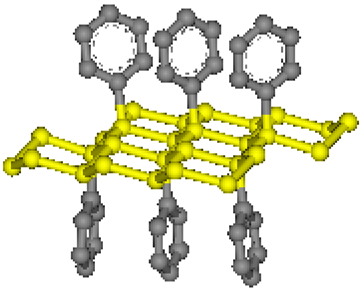

Figure 4.74 A model of phenyl-capped SiNS. All hydrogen atoms have been removed for clarity. Atom colours; silicon = yellow and carbon = grey.

Nakano provided evidence for the functionalised sheets including an IR spectrum shown in *Figure 4.75*. Si-C bonds connecting the phenyl groups to the silicon sheets were assigned to frequencies at 1150 and 1410 cm^{-1} and the peaks between 1700-2000 cm^{-1} correspond to C=C aromatic bonds from the phenyl groups.

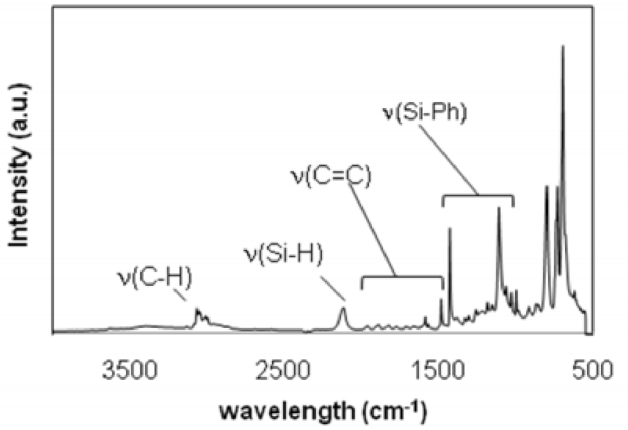

Figure 4.75 IR spectrum for phenyl functionalised sheets highlighting the key bonds involved.[6]

Addition of organic groups to the sheets allows the material to disperse in organic solvents which permits characterisation *via* nuclear magnetic resonance (NMR). *Figure 4.76* shows a ^1H NMR of phenyl functionalised SiNS. The two key resonances at 7.1-7.7 and 2.5-3.0 ppm correspond to the aromatic hydrogens (Si-Ph) and the hydrogens attached to the silicon sheet (Si-H) respectively. Nakano used an integration tool to deduce the coverage of the sheets where an approximate ratio of 2 : 1 for - H/-Ph was found. The sheets were determined to have a $Si_6H_4Ph_2$ composition. Other resonances highlighted in the NMR is a water peak at 2.01 ppm and a resonance at 1.93 ppm corresponding to the *d*-acetonitrile solvent.

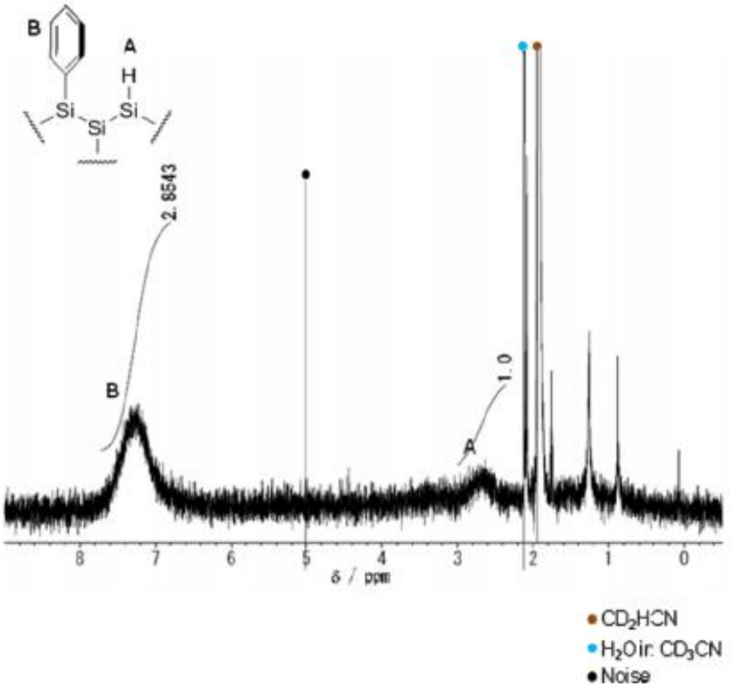

Figure 4.76 ^{1}H NMR *spectrum of phenyl functionalised SiNS in* CD_3CN.[6]

AFM images of phenyl functionalised sheets were studied by Nakano and co-workers and portrayed the sheets occupying a flat surface (*Figure 4.77a*). The images showed a periodic organisation of phenyl groups on the silicon surface by the arrangement of atom-like dots (*Figure 4.77b*) which were measured at a 0.96 nm distance apart. This is in agreement with measurements calculated by a program called DISCOVER which gave a periodicity of phenyl rings on the silicon surface a 1.0 nm distance apart (*Figure 4.77d*). In addition, the program models a side view of the structure shown in *Figure 4.77c* detailing sheet thickness at 0.98 nm.

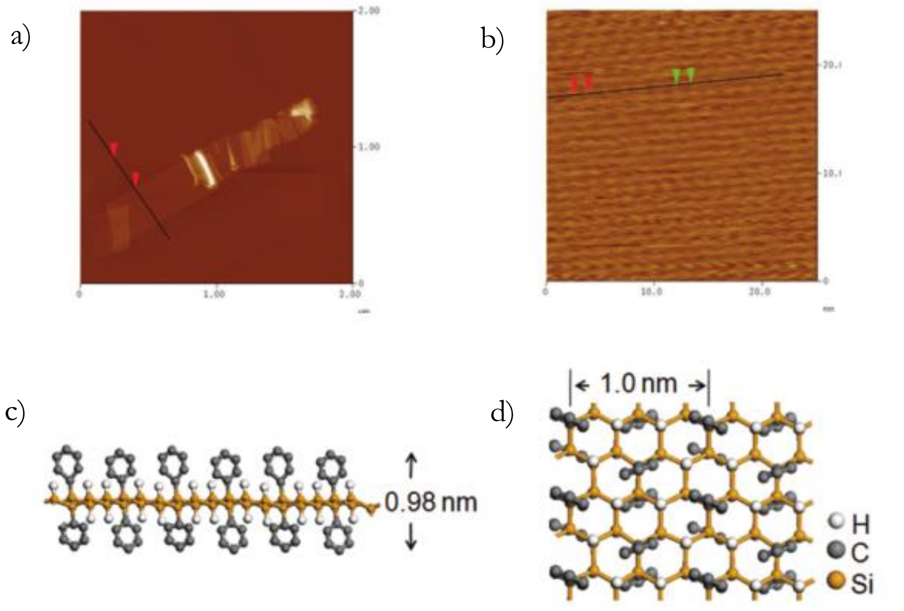

Figure 4.77 a) AFM image of phenyl modified sheets in contact mode, b) atomically resolved image of the surface of phenyl modified sheets. Calculated c) side and d) top view of the model of phenyl modified sheets by DISCOVER.[6]

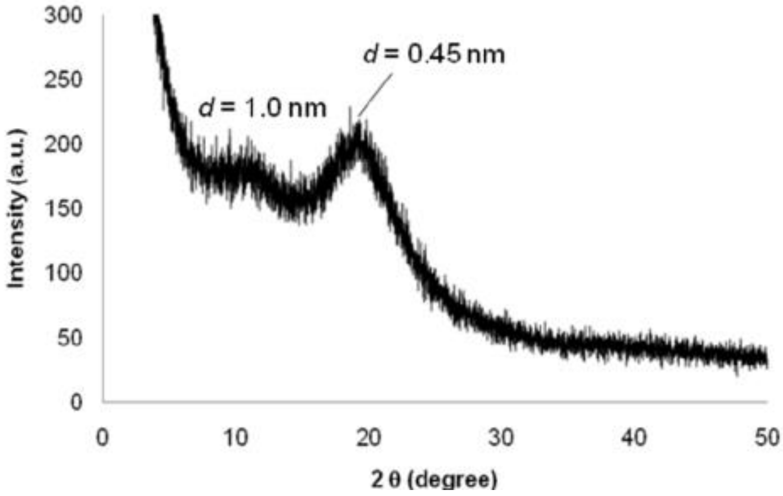

Figure 4.78 XRD pattern of phenyl modified sheets.[6]

The powder XRD pattern of phenyl modified sheets shown in *Figure 4.78* reveals two broad peaks at 2θ = ~9 and ~19° corresponding to *d*-spacing of 0.45 and 1.0 nm respectively. Nakano states that these periodic spacings of the phenyl groups are in agreement with the model structure shown in *Figure 4.77c/d*. It is interesting to note, Nakano did not use microscopic analytical techniques such as TEM or SEM which allow for elemental composition analysis to ensure the material being studied was actually still the silicon sheets.

DFT (density functional theory) and *ab initio* MD (molecular dynamics) simulations were used to investigate the structure and properties of phenyl-modified SiNS. The optimised structure calculated for phenyl-modified SiNS is shown in *Figure 4.79*.[7-9] According to Spencer *et al.* the phenyl groups are separated by a distance of ~6.6 Å and can twist and reorientate themselves, with little interaction between neighbouring groups.[9] In addition, the phenyl groups prevent strong interactions between adjacent silicon layers.[10] In previous theoretical studies of SiNS, similar computational programs have been used.[11-16]

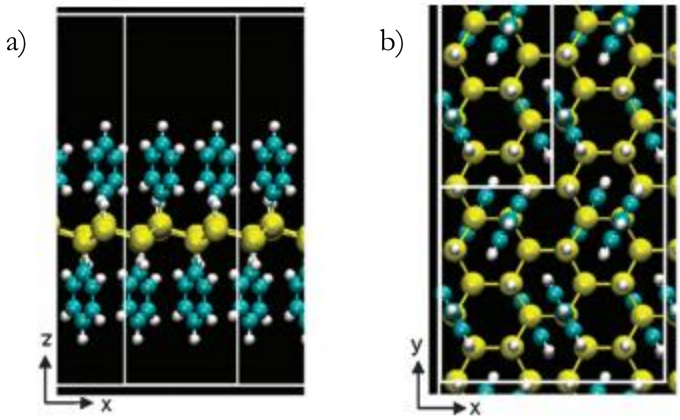

Figure 4.79 Structure of phenyl modified SiNS showing a) side view and b) top view. Atom colours; silicon = yellow, carbon = blue and hydrogen = white.[9]

4.1.3 Hexyl Modified Silicon Nanosheets using an alkene

In 2012 Nakano and co-workers attempted to functionalise layered polysilane *via* a hydrosilyation reaction which is the addition of Si-H across an unsaturated bond using a platinum catalyst.[17] A model structure of the hexyl modified sheets is shown in *Figure 4.80*.

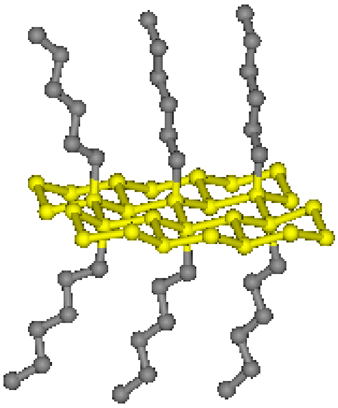

Figure 4.80 A model of hexyl-modified SiNS. All hydrogen atoms have been removed for clarity. Atom colours; silicon = yellow and carbon = grey.

IR spectroscopy was used to characterise the attachment of hexyl groups to the sheets and the spectrum is shown in *Figure 4.81a*.[17] Alkyl stretching and bending absorptions are allocated to frequencies between 2856-2954 and 1259-1459 cm^{-1} respectively and the absorbance at 729 cm^{-1} is assigned to Si-CH_2 vibrational scissoring. Nakano and co-workers pointed out the absence of a C=C absorption band because the double bonds have reacted with SiNS forming C-C single bonds (Si-CH_2-CH_2-). From the powder XRD pattern of hexyl-capped SiNS shown in *Figure 4.81b* Nakano determined that the molecular scale periodicity of the sheets is 0.71 nm. Moreover, the layered structure collapsed and the functionalised product were present as individual sheets.

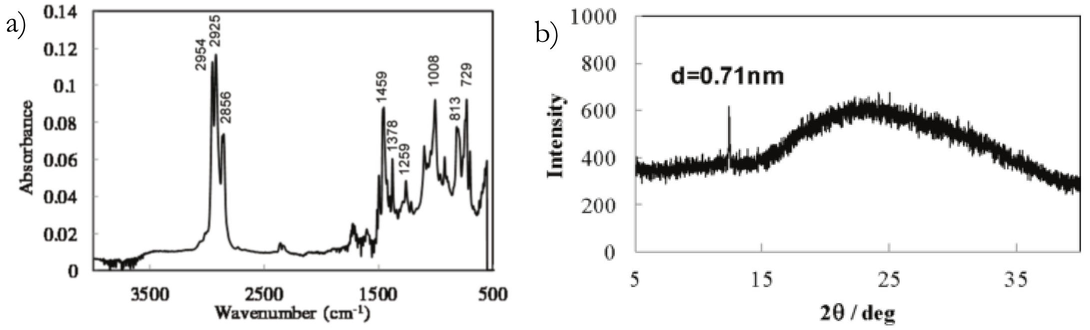

Figure 4.81 a) IR spectrum and b) powder XRD pattern of hexyl-capped SiNS.[17]

A radical-induced hydrosilyation reaction has recently been reported using alkene functional groups.[18] Radical initiators, such as diazonium salts were used to initiate the reaction, however using high temperatures was also successful. The resulting products were characterised using a range of techniques, including AFM imagery, which is shown in *Figure 4.82*. The images revealed that the sheets were free standing with a thickness of approximately 2 nm.

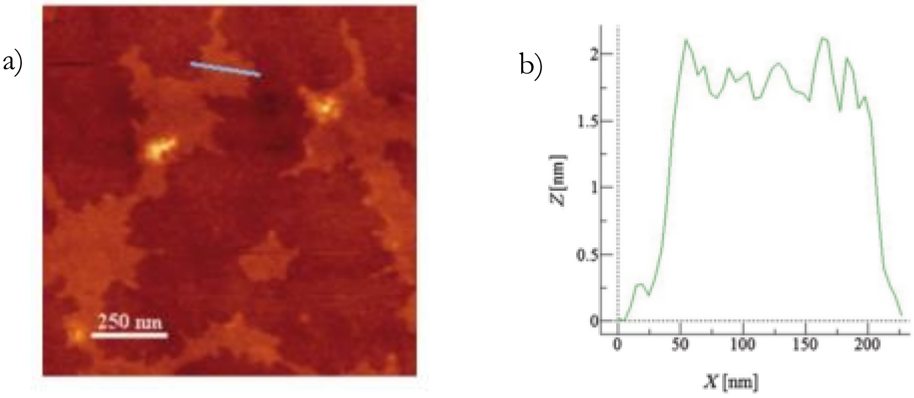

Figure 4.82 a) Non-contact mode AFM image of 1-dodecene functionalised SiNS and b) the line profile taken along the line in a.[18]

4.1.4 Mechanochemical Lithiation of Silicon Nanosheets

Lithiated polysilane was synthesised by Ohta and co-workers in 2014.[19] A mechanical approach was taken where layered polysilane and lithium were placed in a mortar and milled using a pestle. The colour of the material became increasingly darker green with milling time. Si-H bonds terminating the sheets were substituted with lithium to form Si-Li bonds, and a model of the lithiated sheet is shown in *Figure 4.83*. Gas chromatography was used to detect hydrogen gas produced as a by-product when mechanical milling was occurring due to the replacement of hydrogen atoms by lithium cations in the silicon sheets.

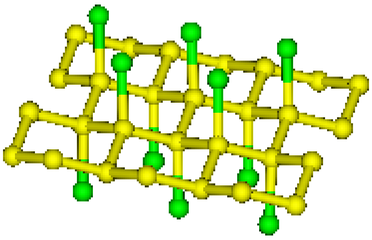

Figure 4.83 A model of lithiated polysilane. All hydrogen atoms have been removed for clarity. Atom colours; silicon = yellow and lithium = green.

It was concluded that increasing the milling time increases the lithiation of the sheets until the sheets do not have any Si-H bonds but are instead completely saturated with lithium. SEM images before and after lithiation are shown in *Figure 4.84a/b*. Ohta and co-workers describe the starting material as plate-like shapes which are completely destroyed during milling to leave aggregates of the lithiated sheets as particles (black spots in *Figure 4.84b*).

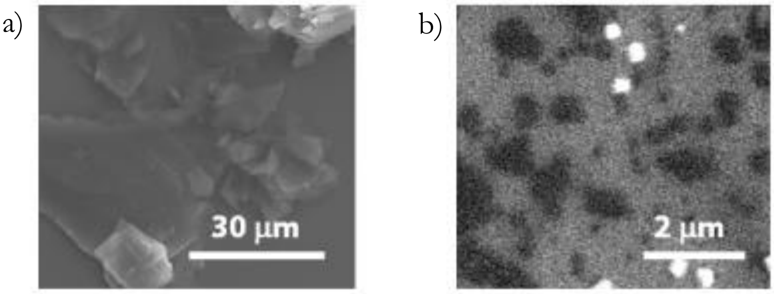

Figure 4.84 SEM images of a) Si_6H_6 and b) $Si_6H_6/6Li$.[19]

Ohta and co-workers studied the IR spectrum of the lithiated sheets, in particular the low wavenumber region, and assigned a new peak at 450 cm^{-1} to the Si-Li stretching vibration mode. They determined this by firstly calculating the partial vibration density of state (DOS) in a Si_6Li_6 model using *ab initio* MD data. From examination of the data, the vibrational DOS peak in the perpendicular direction to the sheet surface can be found at 450 cm^{-1}. The bonds which are perpendicular to the SiNS surface are the Si-Li bonds, and therefore the 450 cm^{-1} peak can be attributed to Si-Li bonds.

4.1.5 Cross-Linking Silicon Nanosheets *via* Amines

In 2015, Nakano and co-workers synthesised cross-linked SiNS using diaminoalkanes with different chain lengths (model shown in *Figure 4.85*).[5] Polysilane was mixed with diaminoalkanes in chloroform at 6 °C for 12 hours. Unreacted amine was removed by repeated distillation under reduced pressure. Further heating at 120 °C for more than 24 hours caused the product to precipitate out of chloroform because the silicon layers were tightly bound together by the diaminoalkanes.

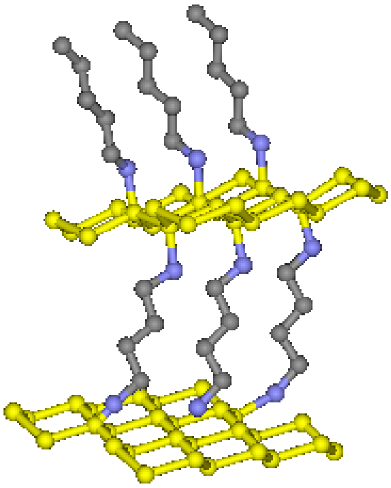

Figure 4.85 A model of cross-linked SiNS via diaminoalkanes. All hydrogen atoms have been removed for clarity. Atom colours; silicon = yellow, carbon = grey and nitrogen = blue.

IR spectroscopy was used to confirm the attachment of the amines to the sheets, and absorption bands at 930 and 1150 cm^{-1} were assigned to Si-N stretches. Two absorption bands at 3265 and 3320 cm^{-1} were assigned to the stretching vibration of the N-H bond. Nakano and co-workers concluded that three types of nitrogen bonding were present including; Si-NH-C, Si-NC-Si and -NH$_2$. It was proposed that every other amine chain was attached to two adjacent sheets. The amine chains that are only attached to one sheet are terminated by a primary amine (-NH$_2$).

4.1.6 Modifications of Silicon Nanosheets *via* Si-O Bond

As previously described in Chapter 3, siloxene is layered sheets of silicon terminated with both hydrogen and hydroxyl bonds (O-H). The hydroxyl bonds can be targeted by using specific reagents and conditions to functionalise the sheets through the O-H bonds. A particular field of research uses zeolite crystals and glass plates, covered with O-H bonds, to attach organic groups building layer-by-layer assemblies.[20-23] The zeolite crystals often pack tightly to form highly ordered multi-arrays on substrates, and are expected to be useful for devices in nanotechnology.[20] The tethering of organic groups onto the substrates is through covalent bonding and an example schematic synthesis is shown in *Figure 4.86*.

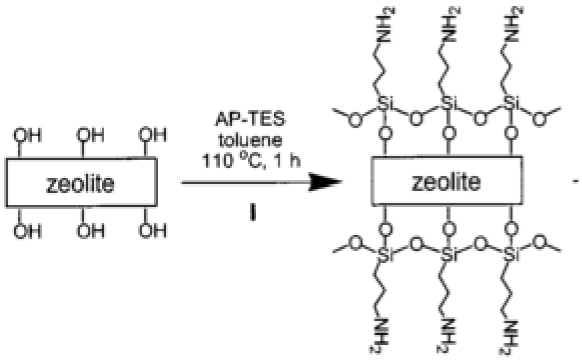

Figure 4.86 Synthesis of zeolite crystals tethered with 3-aminopropyl groups. AP-TES is 3-aminopropyl(triethoxysilane).[20]

The synthesis in *Figure 4.86* produces zeolites tethered with 3-aminopropyl groups. The zeolite surfaces were treated with (3-aminopropyl)triethoxysilane (APS-TES) in toluene and refluxed for 1 hour under an atmosphere of argon.[22] The zeolite powders were collected by filtration and washed with fresh toluene and ethanol. The powders were then placed in an oven to dry. Ninhydrin is a reagent employed to provide confirmation of 3-aminopropyl groups attached to zeolite surfaces. Ninhydrin is easily converted to Ruhemann's Purple in the presence of alkylamines. Ruhemann's Purple has two characteristic features in UV-vis spectroscopy which are absorptions at 405 and 570 nm and the detection of these bands were observed when analysing the alkylamine modified zeolite surfaces.

An interesting development of these functionalised surfaces is the covalent attachment of fullerene balls (*Figure 4.87*). Fullerenes were tethered onto the amine groups *via* N-H addition of the terminal amine into one of the double bonds in the fullerene surface. For identification of this, UV-vis spectroscopy was used which showed a long tail absorption band extending over 500 nm and this is a typical absorption characteristic of an amine inserted fullerene.

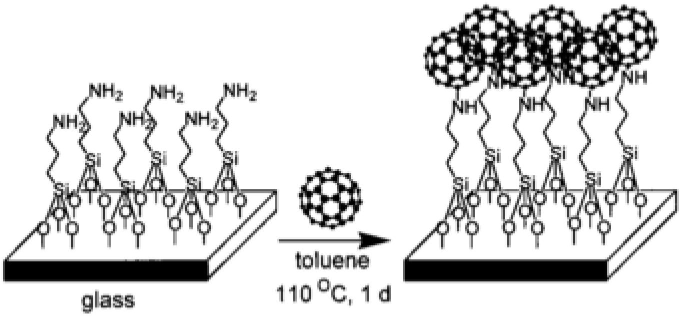

Figure 4.87 Fullerenes mounted onto amine groups which are attached to the zeolite surface. This occurs via N- H *insertion into the double bond of the fullerene.*[22]

4.2 Results and Discussion

Different methods of functionalisation of SiNS are described in this Chapter, and the products are characterised using a variety of analytical surface techniques to probe the structure and bonding within the sheets. Synthetic procedures previously mentioned in the introduction, have been adapted and utilised to fabricate functionalised SiNS. Results are studied and compared to those previously reported in the literature.

4.2.1 Modification of Silicon Nanosheets using an Alkene

4.2.1.1 Synthesis of Functionalised SiNS using a Simple Hexene Molecule (Hexyl-SiNS)

The first attempt to functionalise SiNS used a hydrosilylation reaction, which is the insertion of a Si-H bond across an unsaturated system. Layered polysilane was functionalised *via* a repeat procedure from Nakano, using a platinum catalyst.[17] This tester reaction was used to examine how the nanosheets behaved under certain reaction conditions and therefore establish which conditions were most suitable. 1-hexene, an unsaturated organic compound, was used to produce functionalised sheets creating a Si-C bond linking the silicon surface and alkyl chains. Hexachloroplatinic acid is the precursor of the Pt-catalyst used, known as "Speier catalyst" first discovered in 1957 by John L. Speier.[24] Speier catalyst is commonly used in a wide range of technology, specifically in the silicone industry in the manufacture of coatings, surfactants, mouldings and other consumable goods.[24-26] Layered polysilane, 1-hexene and $H_2PtCl_6.6H_2O$ were stirred in dry toluene overnight under dinitrogen at room temperature. Impurities, such as unreacted starting material, were removed by filtration and subsequently the organic filtrate was washed with water and reduced under vacuum. The obtained hexyl-SiNS, a yellow oily solid, is soluble in typical organic solvents, such as chloroform and hexane.

Scheme 4.8 Reaction mechanism for platinum catalysed hydrosilylation of SiNS via the Chalk-Harrod mechanism. R = $CH_3CH_2CH_2CH_2$-.

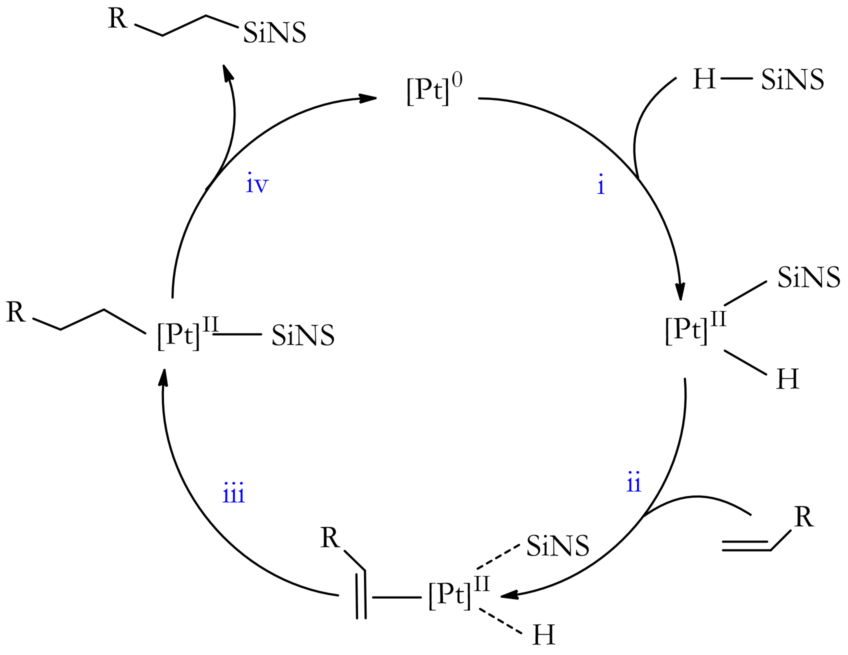

The proposed hydrosilylation mechanism is shown in *Scheme 4.8* and it is generally known as the Chalk-Harrod mechanism.[27, 28] The platinum in hexachloroplatinic acid occupies an oxidation state of 4+, which must be reduced to 0 before it becomes catalytically active.[27] The first step involves an oxidation addition of the Si-H to the Pt(0) metal providing a hydro-silyl complex (i), and following this is the co-ordination of hexene to the Pt(II) (ii). The migratory insertion of the alkene into the Pt-H bond follows (iii) and lastly a reductive elimination of the functionalised nanosheets (iv).

4.2.1.2 *Infrared Spectroscopy of Hexyl-SiNS*

IR spectroscopy was used to analyse the bonding within the sheets and specifically determine the presence of a Si-C bond linking the hexyl groups to the sheets. A list of absorption peaks can be seen in *Table 4.8* taken from an ATR IR spectrum of hexyl-SiNS.

Table 4.8 A table of absorption bands and assignments for hexyl-SiNS.

Absorption (cm^{-1})	**Assignment**
561	Si-Si stretch
784	Si-C stretch
861	Si-O-Si bend
1011	Si-O-Si stretch
1257	C-H bend
2102	Si-H stretch
2846-2959	C-H stretch

Characteristic vibrations of the organic molecules attached to sheets are apparent between 2846-2959 cm^{-1} due to the C-H stretches, and at 1257 cm^{-1} due to the C-H bends as in literature reports.[17] There is a slight reduction in the intensity of the Si-H stretching band at 2102 cm^{-1} compared to SiNS before modification, and therefore it is concluded that some Si-H bonds are still terminating the sheets. No obvious absorption bands are detected in the ~1600 cm^{-1} region, which would suggest that all hexene starting material (C=C) has been used in the reaction or removed during the synthetic work-up.

An absorption band at 784 cm^{-1} shown in *Figure 4.88* is assigned to the Si-C stretches. This assignment is similar to that reported by Nakano and co-workers, who assigned an absorption peak at a lower energy of 729 cm^{-1} for this bond.[17] In addition, Lambert states that Si-C stretches are found in the absorption region of 720-860 cm^{-1}.[29] A large peak at 1011 cm^{-1} corresponds to the Si-O-Si stretches which would suggest the Si-O-Si network remains the framework of the sheets. In addition to these bonds, Si-Si bonds are also present in the framework with an absorption band at 561 cm^{-1}.

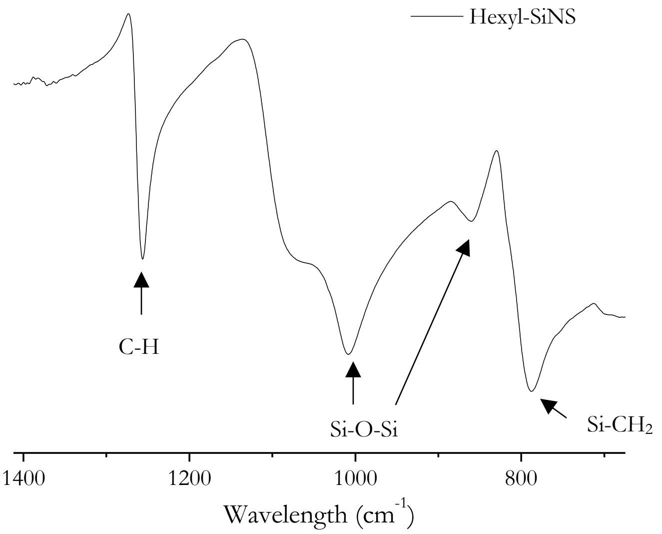

Figure 4.88 High resolution IR spectrum highlighting the region from 1400 to 600 cm^{-1} of hexyl-SiNS.

4.2.1.3 Powder X-ray Diffraction of Hexyl-SiNS

Powder XRD was a technique used to probe periodicities and crystallinity within and between adjacent sheets. The powder XRD pattern of hexyl-SiNS by Nakano, displayed in *Figure 4.89,* shows a peak at $2\theta = 12.4°$ which is assigned to periodicity of the molecular hexyl groups attached to the sheets, rather than the interlayer spacing between the sheets.[17] Nakano and co-workers predicted that the layering structure had collapsed as the peak at 12.4° corresponds to *d*-spacing of 0.71 nm which cannot explain the addition of the *ca.* 1.3 nm hexyl chains.[17]

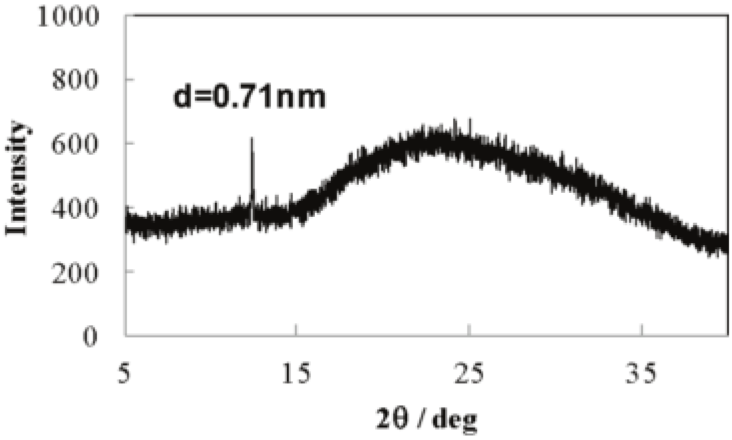

Figure 4.89 Powder XRD of hexyl functionalised SiNS by Nakano et al.[17]

The powder XRD pattern obtained in this work is somewhat different and is shown in *Figure 4.90*. The data was collected by placing hexyl-SiNS onto a circular zero background silicon plate and the sample was bombarded with X-rays produced from a copper anode source (Kα radiation is 1.54 Å). Two clear peaks are observed at 2θ = 39.8° and 46.2°. The diffraction peak at 46.2° is assigned to periodicity within the silicon framework and the corresponding *d*-spacing is calculated using Braggs law:

$$d = \frac{n\lambda}{2sin\theta} = \frac{1.54}{2sin23.1} = 1.96\ \text{Å} \qquad [7]$$

A *d*-spacing of 1.96 Å is slightly larger than the *d*-spacing of 1.92 Å which is calculated for the unfunctionalised starting material in Chapter 3. This is likely to be due to the change in structure of the sheets with small organic groups covalently attached. The new peak at 39.8° corresponds to a *d*-spacing of 2.26 Å and this is similar to the Si-Si bond distance of 2.24 Å and therefore is assigned to the periodicity within the sheets.

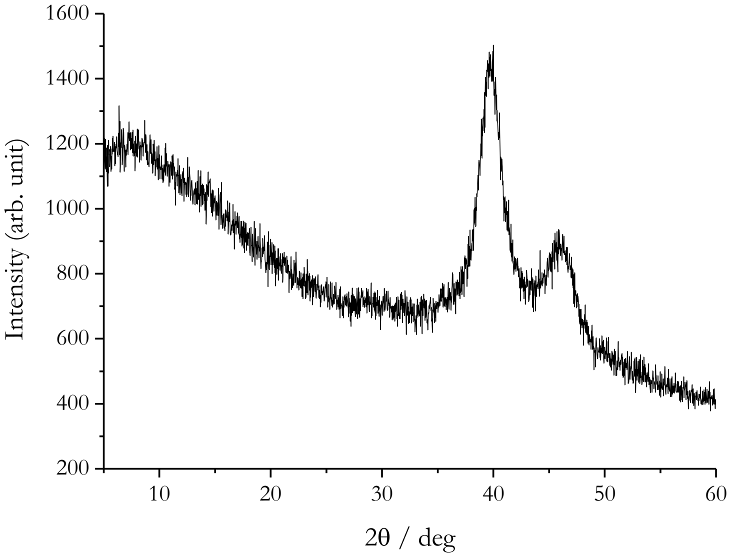

Figure 4.90 Powder XRD pattern of hexyl-SiNS displaying three broad peaks at 2θ = 7.15°, 39.8° and 46.2°.

Focusing at the low angle region there appears to be a large broad peak with a maximum at 2θ = 7.15° (*Figure 4.90)*. The *d*-spacing provided by this peak gives a value of 12.3 Å using Braggs law:

$$d = \frac{n\lambda}{2sin\theta} = \frac{1.54}{2sin3.58} = 12.3\ \text{Å} \qquad [8]$$

This large *d*-spacing accounts for the distance between adjacent sheets if sheets were stacked as illustrated in *Figure 4.91*. The hexyl chain length occupies a distance of 10.3 Å[30] and if the sheets were connected *via* Si-C bonds (bond length of 1.89 Å[31]) the distance between two adjacent sheets would have to be at least 12.19 Å (10.3 + 1.89 Å). The *d*-spacing of 12.3 Å from the peak at 7.15° covers this distance, however peak broadness must be taken into consideration. This peak is very broad which suggests minimal stacking is occurring and the material is fairly amorphous.

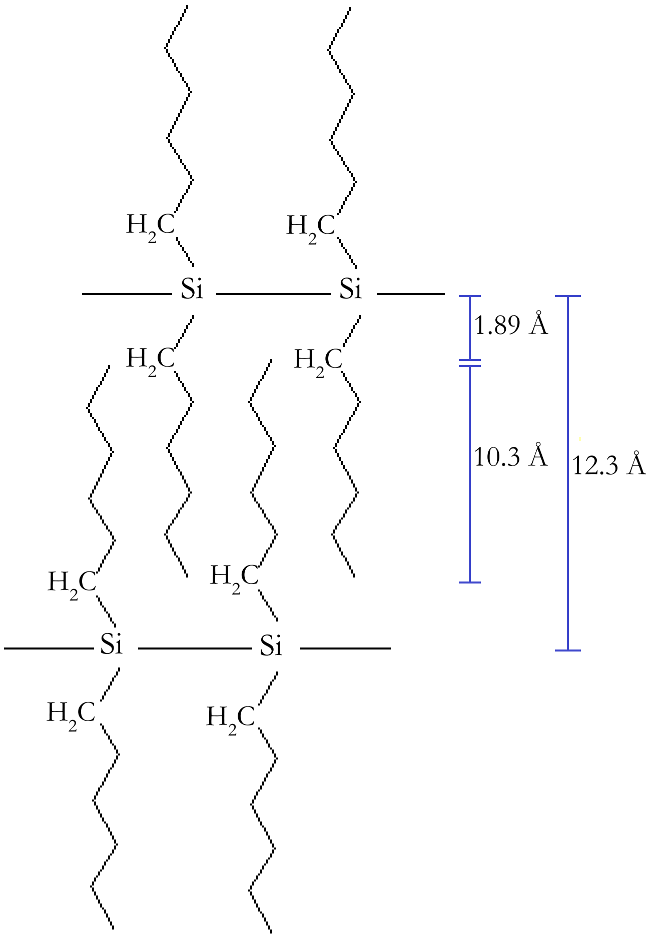

Figure 4.91 An illustration of hexyl-SiNS displaying the interplanar distances between two adjacent SiNS. Si-C bonds occupy lengths of 1.89 Å and the hexyl chains have a length of 10.3 Å.

4.2.1.4 *Transmission Electron Microscopy and Energy Dispersive X-ray Spectroscopy of Hexyl-SiNS*

TEM was used to identify the structure and topology of the material. As in Chapter 3, copper grids with a lacey carbon support film were used for this particular experiment. The sample was sonicated in hexane for 5 minutes to disperse the sample in solution which was subsequently drop-cast onto a grid. *Figure 4.92* displays a typical image of hexyl-SiNS.

The first observation indicates the absence of sheet-like material but rather that a globular structure is present. It is proposed that the sheets were either destroyed during the synthetic procedure, or that a polymerisation reaction occurred between the unsaturated bond in the alkene and the platinum catalyst. If polymerisation occurred and the silicon starting material did not react, insoluble SiNS would have been left in the residue on the filter paper during the synthetic work-up procedure and consequently sheets would not be present in the TEM.

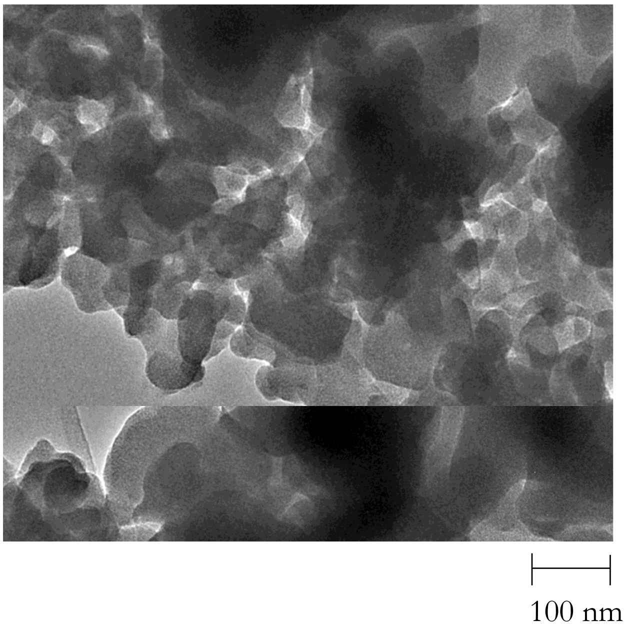

Figure 4.92 TEM image of hexyl-SiNS.

Table 4.9 records the elemental composition of the sample, and the relative atomic percentages. The low detection of silicon informs that silicon is not in the sample observed on the TEM grid, and therefore one can assume that the layered polysilane starting material did not react with hexene. The other possibilities are that the sheets were absorbed into other material, or that there was an inadequate amount of material deposited onto the grids and therefore not all types of material were investigated. EDX analysis detected trace amounts of calcium and chloride which are most likely to have been carried through from the synthesis of layered polysilane. The detection of copper is from the TEM grid and there is approximately 4 % of both platinum and oxygen detected in the sample. The largest abundance of an element detected is carbon with 83.6 % which suggests a reaction between the hexene and catalyst is most likely.

Table 4.9 TEM-EDX elemental analysis of hexyl-SiNS.

Element	**Atomic %**
C	83.6
O	3.7
Si	0.2
Cl	1.6
Ca	0.1
Cu	6.0
Pt	3.8

The paper describing SiNS functionalisation with hexene by Nakano and co-workers did not report any characterisation by electron microscopy in an attempt to identify sheets.[17] However, AFM was used to probe the surface of the material and AFM imagery is shown in *Figure 4.93*. Nakano stated monolayer sheets existed with a thickness of 3.1 nm. The limitation with AFM is the inability to detail the elemental composition of the material and therefore evidence that the material shown in *Figure 4.93a* contains silicon is lacking.

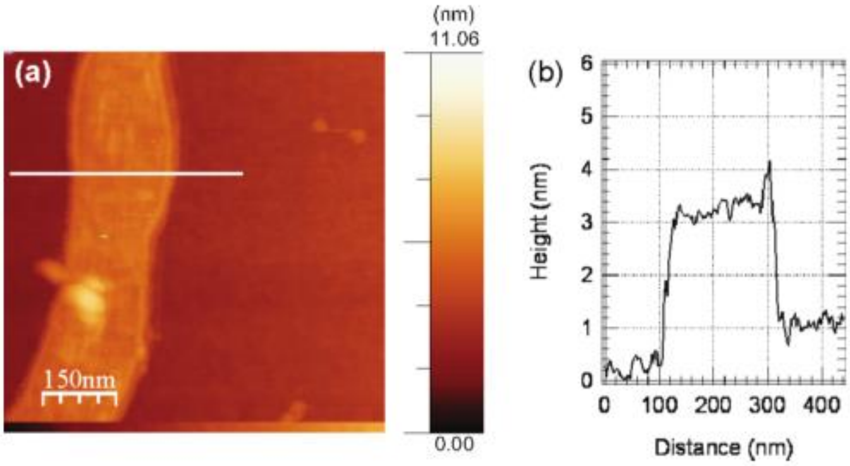

Figure 4.93 a) Non-contact mode AFM image of hexyl modified sheets synthesised by Nakano and co-workers and b) the line profile along the white line in a.[17]

4.2.1.5 Synthesis of Functionalised SiNS using 1-oct-7-enyl-imidazole

Another functionalisation of SiNS *via* a hydrosilylation reaction was attempted using 1-oct-7-enyl-imidazole. This is an unsaturated reagent containing a C=C bond at one end and an imidazole group at the other end of the molecule (product in *Scheme 4.9*). Similarly to the previous example, the aim was to functionalise the sheets *via* the insertion of Si-H bonds (which terminate the SiNS) into the C=C bond of 1-oct-7-enyl-imidazole. 1-oct-7-enyl-imidazole was synthesised from a known literature procedure shown in *Scheme 4.9* where sodium hydride was added in small portions to a mixture of imidazole in THF and refluxed for 1 hour. After cooling to room temperature, 8-bromo-oct-1-ene was added and the mixture further refluxed for 3 hours. The resulting mixture was cooled to room temperature and diluted with diethyl ether. After the synthetic work-up, the resulting 1-oct-7-enyl-imidazole product was a yellow oil in good yield (4.184 g, 94 %).

Scheme 4.9 Reaction scheme of the synthesis of 1-oct-7-enyl-imidazole.

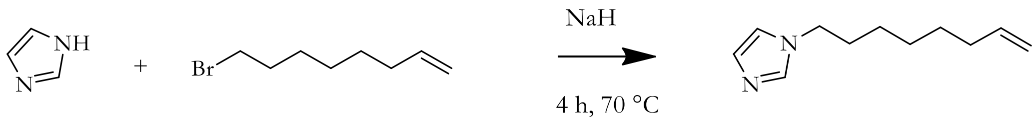

1-oct-7-enyl-imidazole was used to functionalise SiNS in a similar manner as the previous hydrosilyation and this new product is named 1-oct-7-enyl-imidazole-SiNS. 1-oct-7-enyl-imidazole was added to layered polysilane in dry toluene under dinitrogen with a platinum catalyst ($H_2PtCl_6 \cdot 6H_2O$) and the mixture was stirred overnight at room temperature. The yellow solution was filtered to remove unreacted starting material and then washed with toluene and dried with $MgSO_4$. Toluene was removed under reduced pressure to leave a sticky yellow oil, 1-oct-7-enyl-imidazole-SiNS.

4.2.1.6 Nuclear Magnetic Resonance of 1-oct-7-enyl-imidazole-SiNS

The functionalised sheets were soluble in typical organic solvents and therefore were studied *via* NMR. *Figure 4.94* displays the comparison of ^{1}H NMR spectrum of 1-oct-7-enyl-imidazole to 1-oct-7-enyl-imidazole-SiNS. The resonances in 1-oct-7-enyl-imidazole-SiNS NMR correspond to the small organic groups attached to the sheets and they exhibit broader peaks due to the slow molecular tumbling effect anticipated for large nanostructures.[32] This is formally known as the rotational correlation time which is the average time taken for the molecule to change its orientation with respect to the magnetic field. Smaller molecules in general, tumble rapidly compared to larger molecules which tumble more slowly and therefore have characteristic broad peaks in NMR.[32] Due to the restricted freedom of movement of small organic groups attached to the sheets, and therefore broad peaks, the spectra can only be qualitatively used to indicate functionalisation and quantitative analysis, such as integrations, should be interpreted with caution.

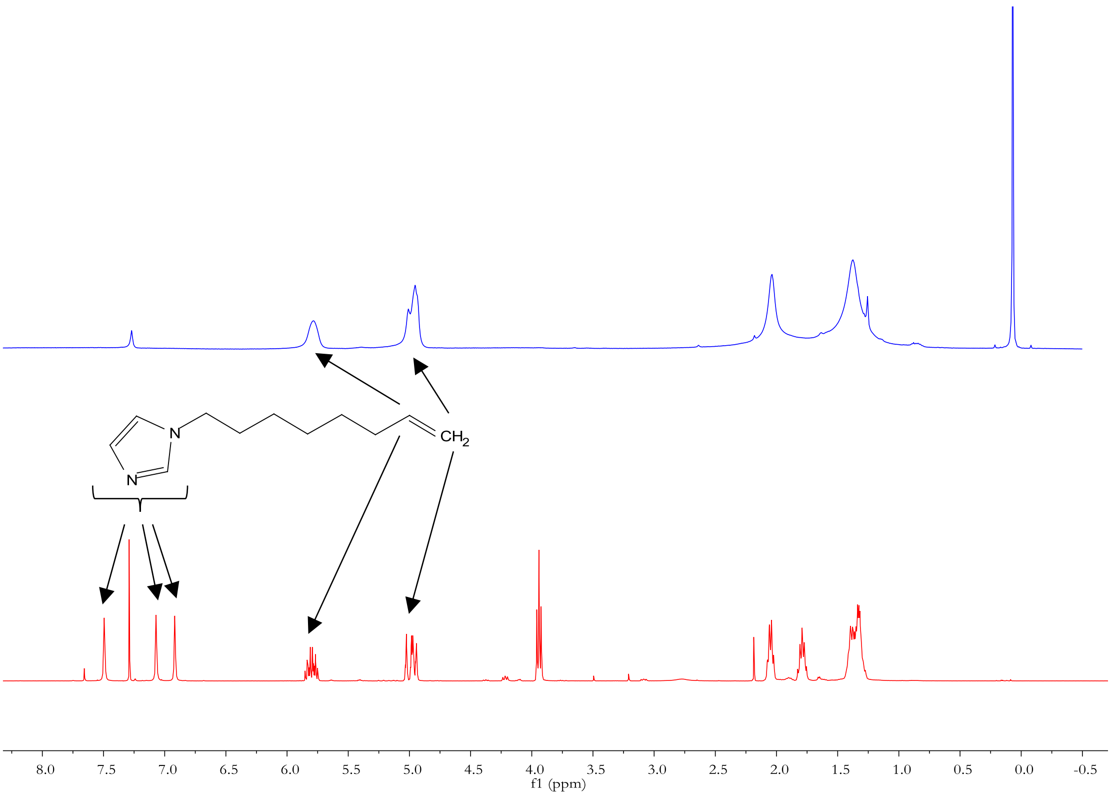

Figure 4.94 ^{1}*H NMR of 1-oct-7-enyl-imidazole-SiNS (blue) and 1-oct-7-enyl-imidazole (red) in chloroform-d.*

Careful comparison of the ^{1}H NMR spectra indicates that the proposed reaction mechanism using the alkene bond to react the organic molecules with the SiNS *via* hydrosilyation did not occur. This is evident from the resonances associated with the alkene bond at chemical shifts of *ca.* 5 and 5.8 ppm still present in the functionalised sheets. If the sheets had reacted with the C=C bond, they would have been removed and therefore those two characteristic resonances would no longer be present. For clarification that the two resonances at chemical shifts of *ca.* 5 and 5.8 ppm had correct assignment of the double bond, a HSQC (heteronuclear single quantum correlation) NMR experiment was carried out and is shown in *Figure 4.95*. The resulting spectrum is a 2D NMR featuring a proton NMR on the x-axis and a carbon NMR on the y-axis displaying a chemical shift correlation map between directly bonded protons and carbons. The spectrum provides connectivity information revealing the two resonances at *ca.* 5 and 5.8 ppm in the proton NMR are correlated to carbons in the characteristic alkene region of 110-140 ppm in the

^{13}C NMR. The three imidazole characteristic resonances at 6.9, 7.1 and 7.5 ppm were noticeably absent in the ^{1}H NMR of 1-oct-7-enyl-imidazole-SiNS, which leads to the conclusion that imidazole had reacted with the SiNS.

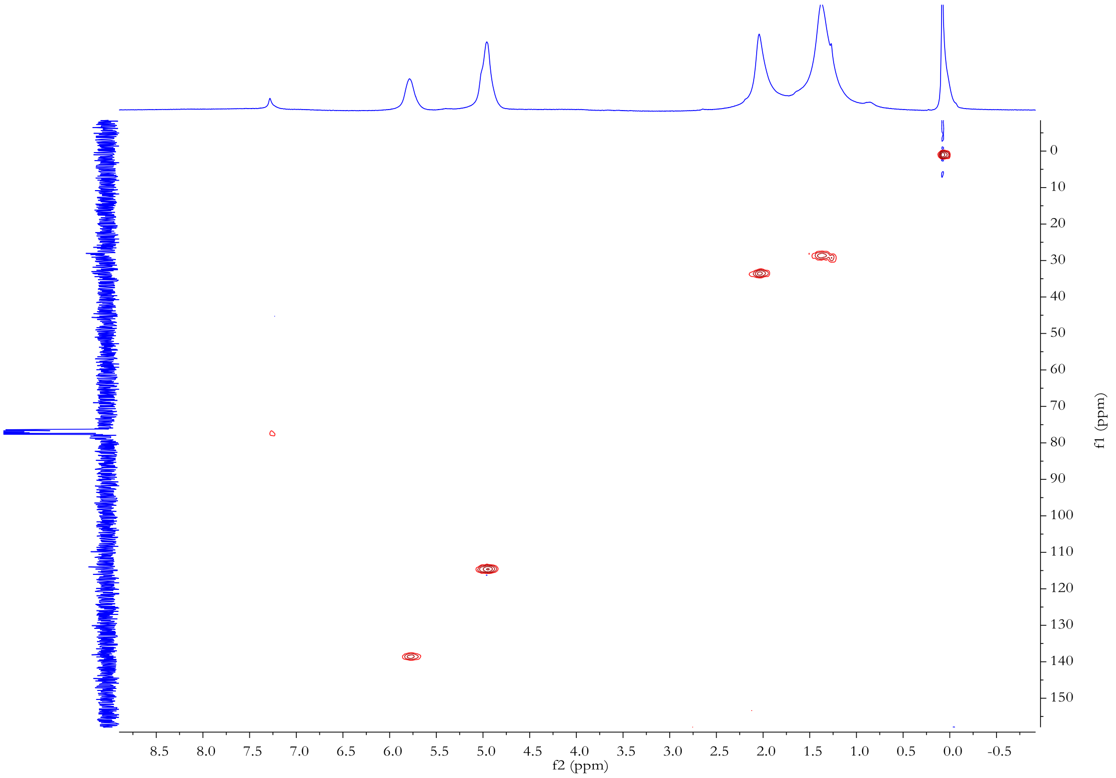

Figure 4.95 HSQC-NMR of 1-oct-7-enyl-imidazole-SiNS in chloroform-d featuring a proton NMR on the x-axis and a carbon NMR on the y-axis.

4.2.1.7 *Synthesis of Octylimidazole-SiNS*

Upon collection of NMR spectra for 1-oct-7-enyl-imidazole-SiNS, it seemed appropriate to probe the functionalisation of sheets using an imidazole compound without an alkene to eliminate any confusion and identify if the imidazole ring was reacting with the sheets or rather the alkene bond (as originally thought). A simple imidazole alkyl chain was synthesised shown in reaction *Scheme 4.10.* 1-octylimidazole was obtained in good yield (3.96 g, 80 %) as a yellow oil.

Scheme 4.10 The synthetic scheme of 1-octylimidazole.

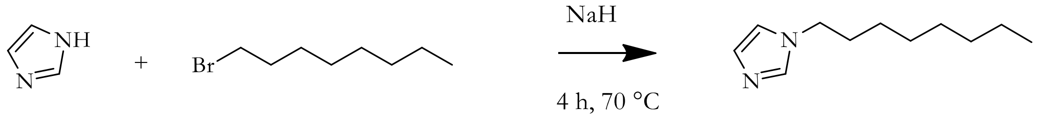

Functionalisation of SiNS was attempted using 1-octylimidazole with a similar method previously employed, however the platinum catalyst was no longer required as the removal of alkene moieties meant hydrosilyation was impossible. 1-octylimidazole was added to a solution of layered polysilane in dry toluene and the reaction was stirred overnight at room temperature. The solution was purified to remove unreacted silicon oxide impurities by filtering and washing with toluene, followed by the removal of toluene under vacuum to leave a yellow oil of 1-octylimidazole-SiNS.

4.2.1.8 *Nuclear Magnetic Resonance of Octylimidazole-SiNS*

The comparison of ^{1}H NMR of 1-octylimidazole to octylimidazole-SiNS is shown in *Figure 4.96*. Similar to before, the imidazole peaks have disappeared after functionalisation of the sheets, and the resonances look slightly broader as expected due to the slow tumbling of the large molecular sheets. Interestingly, the N-CH_2 protons are present after functionalisation in this example as highlighted in *Figure 4.96*, in comparison to 1-oct-7-enyl-imidazole-SiNS where they are no longer present.

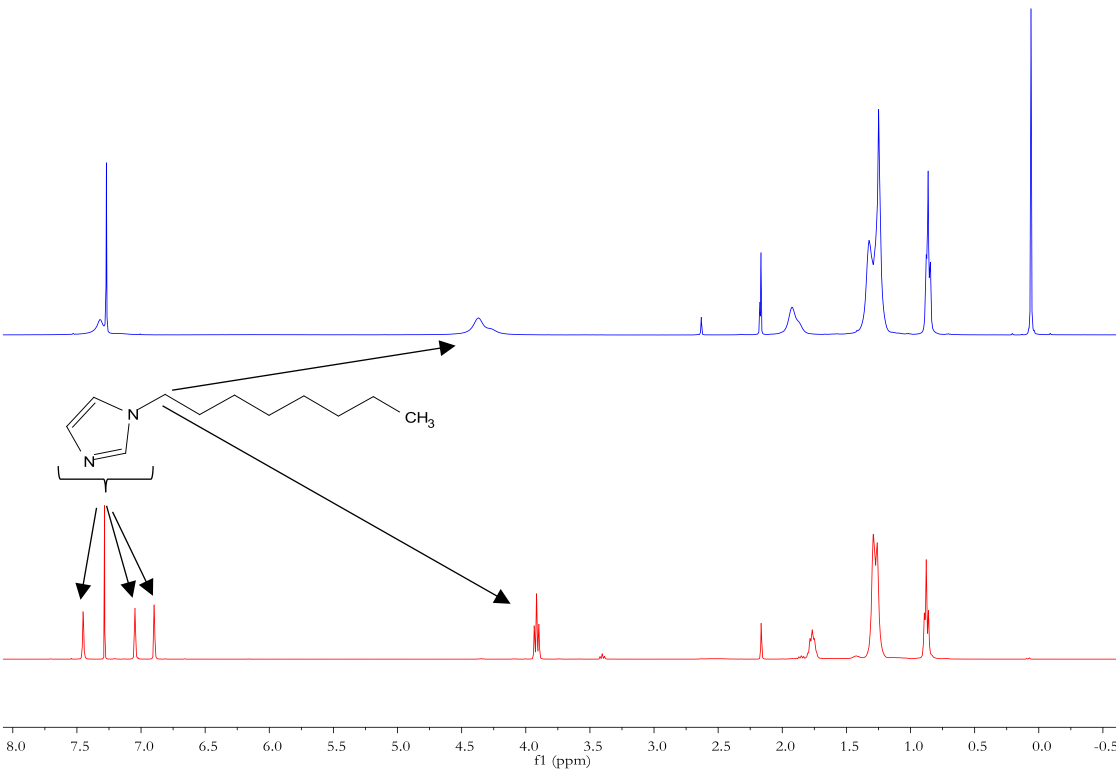

Figure 4.96 ^{1}H NMR comparing octylimidazole (red) to octylimidazole-SiNS (blue) in chloroform-d.

^{29}Si NMR of octylimidazole-SiNS was recorded and is shown in *Figure 4.97*. A large background signal arises from the glass and quartz in the NMR tube at approximately -110 pm and a sharp resonance at -21.94 ppm is observed. Surprisingly, only one silicon environment is observed considering there are potentially many silicon environments present on the sheets including; Si-N, Si-C, Si-H, Si-O. It is suggested that there is a dominant silicon environment which is over-shadowing any other environment. Chemical shifts of silicon derivatives including Si-C, Si-N and S-O, are reported to have a range in the region of -80 to -15 ppm and therefore the sharp peak with a resonance at -21.94 ppm could be assigned to any of these environments.[33]

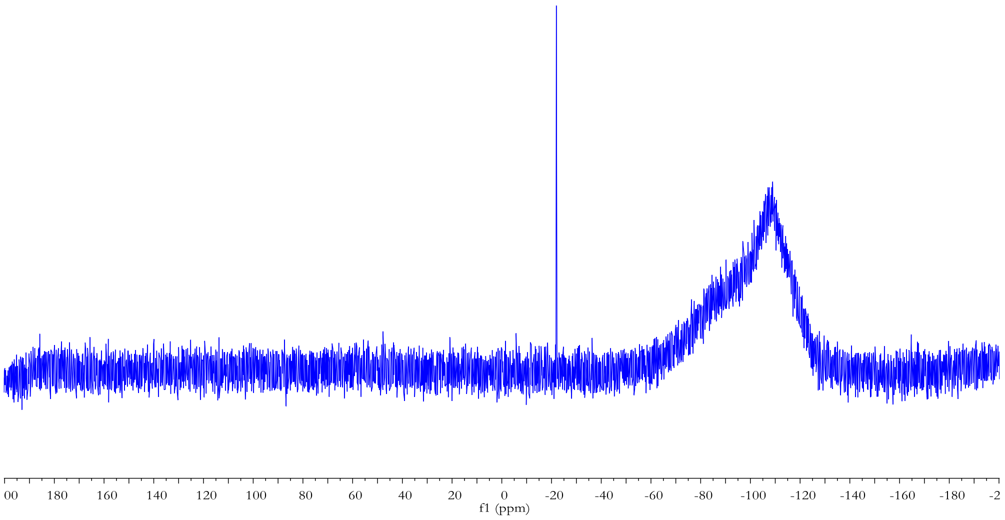

Figure 4.97 ^{29}*Si NMR spectrum of octylimidazole-SiNS in chloroform-d showing two features, firstly a large background signal arising from the glass and quartz in the NMR tube at approximately -110 ppm and also a sharp resonance at -21.94 ppm.*

4.2.1.9 Infrared Spectroscopy of Octylimidazole-SiNS

Absorption bands and their assignments in the IR spectrum of octylimidazole-SiNS are recorded in *Table 4.10*. Absorptions at 489, 801 and 1017 cm^{-1} are assigned to Si-Si stretches, Si-O-Si bends and Si-O-Si stretches from the silicon framework respectively. Comparing IRs of layered polysilane and octylimidazole-SiNS reveals that a new absorption peak arises at 930 cm^{-1}. Si-N bonds absorb is this region which would suggest the attachment of the organic group to the SiNS occurred *via* a Si-N linkage. The small organic groups are responsible for absorption bands corresponding to C-H bends, C-N stretches and C-H stretch at 1240, 1379 and 2925 cm^{-1} respectively. A small absorption peak at 2095 cm^{-1} is observed in the IR spectrum of octylimidazole-SiNS which suggests either Si-H bonds remain terminating the sheets, or silicon impurities are present. An absorption band found at high energy with a frequency of 3306 cm^{-1} is assigned to a N-H stretch.

Table 4.10 Absorption bands and assignments of octylimidazole-SiNS from an IR spectrum.

Absorption (cm^{-1})	**Assignment**
489	Si-Si stretch
801	Si-O-Si bend
930	Si-N stretch
1017	Si-O-Si stretch
1240	C-H bend
1379	C-N stretch
1658	N-H bend
2095	Si-H stretch
2925	C-H stretch
3306	N-H stretch

4.2.1.10 Scanning Electronic Microscopy of Octylimidazole-SiNS

SEM was used to investigate the topographic structure of the material. Octylimidazole-SiNS was dispersed and sonicated in hexane for 5 minutes and deposited onto a copper grid with a lacey carbon film. *Figure 4.98* shows an SE-SEM image of octylimidazole-SiNS revealing thin layers of long wire-type structures and some of these wires are aggregated, while others are slightly separated from the rest of the material. EDX spectroscopy detected minimal silicon in this SEM image, but rather mostly composed of carbon. When investigating the grid as a whole the total material deposited on the grid was insignificant, which would lessen the chance of detecting any silicon material if present.

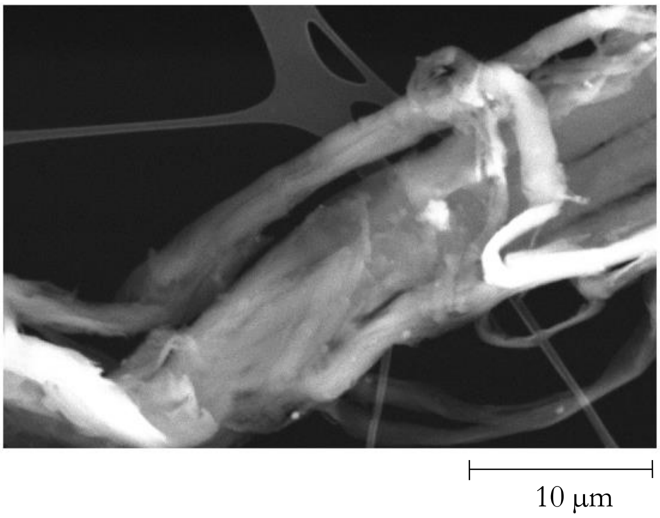

Figure 4.98 SE-SEM image of octylimidazole-SiNS.

Table 4.11 A table summarising the conclusions of SiNS functionalised via an alkene or imidazole.

Conclusion		
Hexyl-SiNS	***1-oct-7-enyl-imidazole-SiNS***	***Octylimidazole-SiNS***
IR: Evidence of Si-H and Si-C bonds revealed the sheets were both functionalised with organic groups (linked *via* Si-C) and terminated with hydrogen. **Powder XRD:** Crystallinity in the material revealed *d*-spacing of 1.96, 2.26 and 12.34 Å. The former two distances are assigned to periodic spacing within the sheets (*i.e.* the arrangement of the hexyl groups). The latter *d*-spacing of 12.34 Å is assigned to stacking of sheets, however the broadness of this peak implies minimal stacking. **TEM:** Only a trace amount of silicon was detected. Sheets were not observed but rather a globular structure with mostly carbon composition.	**NMR** Observations of broad peaks in ^{1}H NMR (due to the tumbling effect) provides evidence for molecules attached to large sheets. Resonances for the octyl chain are apparent, however imidazole peaks disappeared and therefore it is suggested that the imidazole reacted with the SiNS.	**IR:** An absorption band at 930 cm^{-1} is assigned to Si-N stretches, which are responsible for connecting the small organic molecules to the SiNS. **NMR:** There are broad peaks in the ^{1}H NMR signifying a large molecular component. Alkyl resonances are observed, but imidazole resonances have disappeared, indicating the imidazole has reacted. ^{29}Si NMR portrays a sharp resonance at -21.94 ppm assigned to a silicon environment, either Si-C, Si-N or Si-O. **SEM:** Inconclusive results due to limited material deposited onto the grid. Most material detected is composed of carbon.

4.2.2 Functionalisation of Silicon Nanosheets *via* Amine Moieties

4.2.2.1 Synthesis of Octylamine-SiNS

It has been reported that ammonia dissociatively absorbs onto silicon surfaces with little disruption to the surface.[34] The study of alkyamines reacting with chlorinated silicon surfaces under UHV has also been studied by Bergerson *et al.*[35] They reported the organic groups were linked *via* a Si-N bond. In a similar manner, functionalisation of the SiNS synthesised herein was attempted *via* reacting layered polysilane with an amine moiety, targeting the Si-H bonds in the sheets. The reaction proceeded using Schlenk techniques, where layered polysilane was dispersed in dry chloroform under dinitrogen and octylamine was added *via* syringe. The reaction was left to stir for 22 hours at 60 °C and a cloudy solution formed containing a dark grey precipitate. The unreacted starting material, octylamine, was removed *via* distillation at elevated temperature under reduced pressure and this was repeated three times with fresh chloroform added between each attempt to aid removal of unreacted volatile components. The product was dissolved in chloroform and the solution filtered to remove the remaining black solid left over from the reaction. The chloroform solvent was removed under vacuum to leave a yellow oil which had a thick consistency, and this was soluble in typical organic solvents. The reaction mechanism proposed is shown in *Scheme 4.11* . The Si-H bonds in layered polysilane can be considered as a silylhydride, Si^+-H^- allowing the lone pair belonging to the nitrogen of the amine to attack the silicon atom. The hydrogen from the silicon atom combines with the hydrogen from the amine releasing dihydrogen. A further reaction is possible where the nitrogen attached to the SiNS reacts with an adjacent Si-H, and again releasing dihydrogen. The nitrogen is therefore bridging two surface silicon atoms. This idea was first introduced by Bergerson *et al.* when they reported amines attached to a silicon chlorinated surface.[35]

Scheme 4.11 Proposed reaction mechanism for the synthesis of octylamine-SiNS.

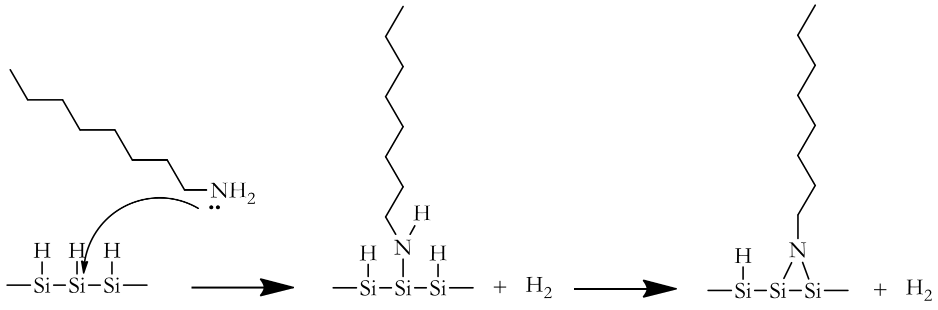

4.2.2.2 *Nuclear Magnetic Resonance of Octylamine-SiNS*

The ^{1}H NMR of octylamine-SiNS was recorded in chloroform; the ^{1}H NMR alkyl region of octylamine (starting material) is compared to octylamine-SiNS in *Figure 4.99*. The resonance at 1.05 ppm, assigned to the NH_2 group, is not present after the reaction and therefore it was concluded that the NH_2 groups react with the SiNS. Other resonances in the alkyl region (shown in *Figure 4.99)* are assigned to protons from the octyl chain. In general, slightly broader peaks are found in the product NMR due to the reasons previously given regarding a slow tumbling rate. It is interesting to note that protons in the octyl chain that sit further away from the silicon surface, like the CH_3 group (chemical shift of 0.85 ppm in *Figure 4.99*) have a similar definition (*i.e.* not broadened) to the starting material indicating increased tumbling rate.

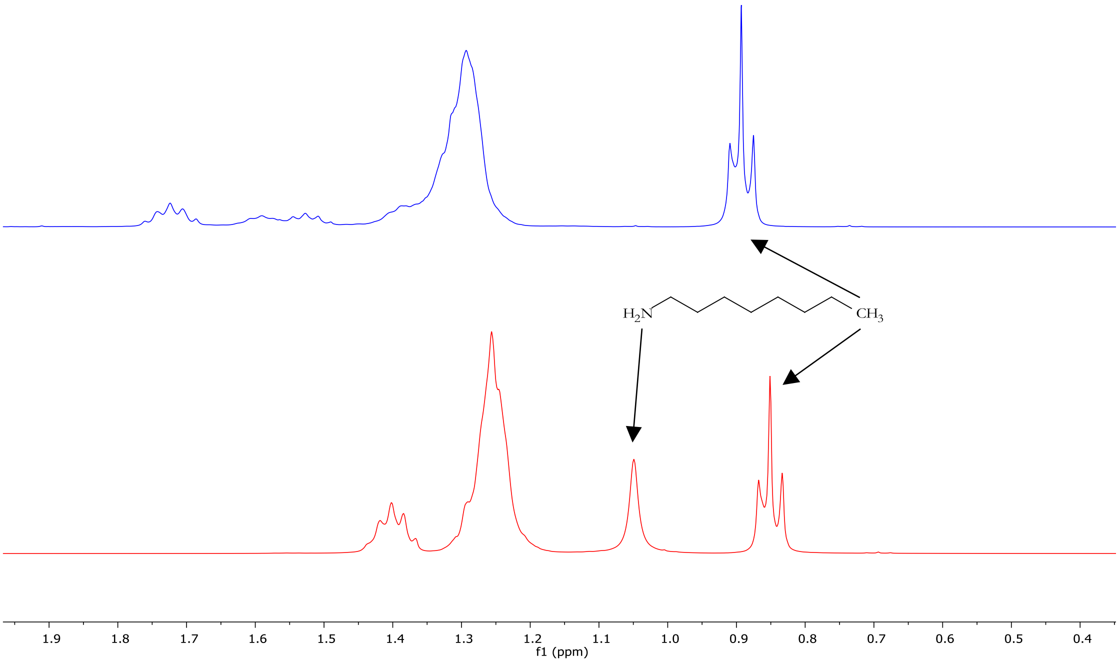

Figure 4.99 Alkyl region of ^{1}H NMR for octylamine (red) compared to octylamine-SiNS (blue) in chloroform d.

4.2.2.3 Scanning Electron Microscopy of Octylamine-SiNS

Octylamine-SiNS was sonicated for 5 minutes in methanol and deposited onto copper grids with a lacey carbon film. The material was studied under electron microscopy and images displayed mostly broken sheets with a planar surface shown in *Figure 4.100*. It is likely that the sheets were destroyed due to the harsh reaction conditions used during synthesis, or because of a prolonged sonification time before deposition onto the grid. Most of the sheets are shattered, however some larger fragments remain, an example highlighted by a white arrow in *Figure 4.100*.

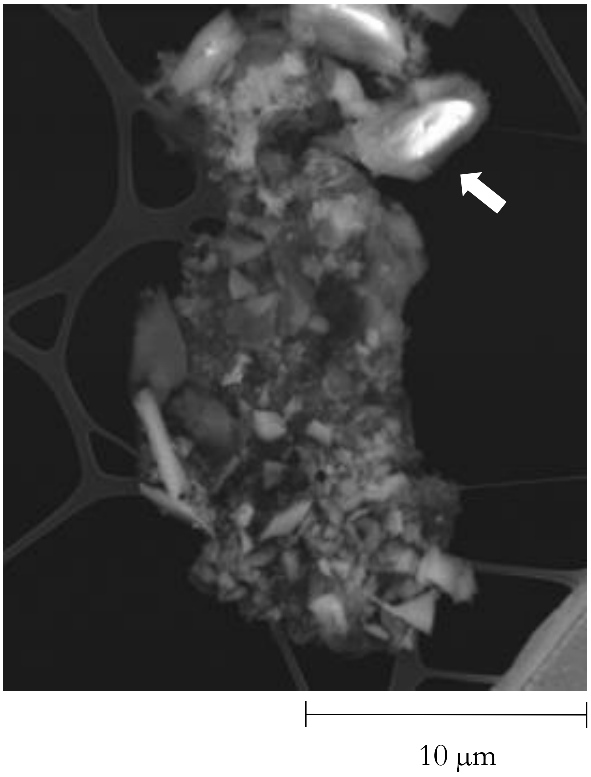

Figure 4.100 SE-SEM image of octylamine-SiNS showing shattered sheets on a lacey carbon copper grid. The white arrow highlights an area of larger sheets.

The SEM-EDX elemental composition maps of silicon, oxygen, carbon and nitrogen with colour superposition are shown in *Figure 4.101*. The silicon composition shown in *Figure 4.101a* displays some areas with a higher concentration of silicon compared to other areas with little, implying that there is a mixture of material amongst the broken sheets. The higher concentrated areas of silicon also appear to have a large amount of oxygen associated with them (*Figure 4.101b*), as well as a small amount of carbon (*Figure 4.101c*). Only a trace amount of nitrogen was detected in these areas (*Figure 4.101d*). The small detection of carbon would suggest functionalisation is occurring sporadically over the sheets. It is interesting that only a small amount of functionalisation was required for the sheets to become completely soluble in organic solvents.

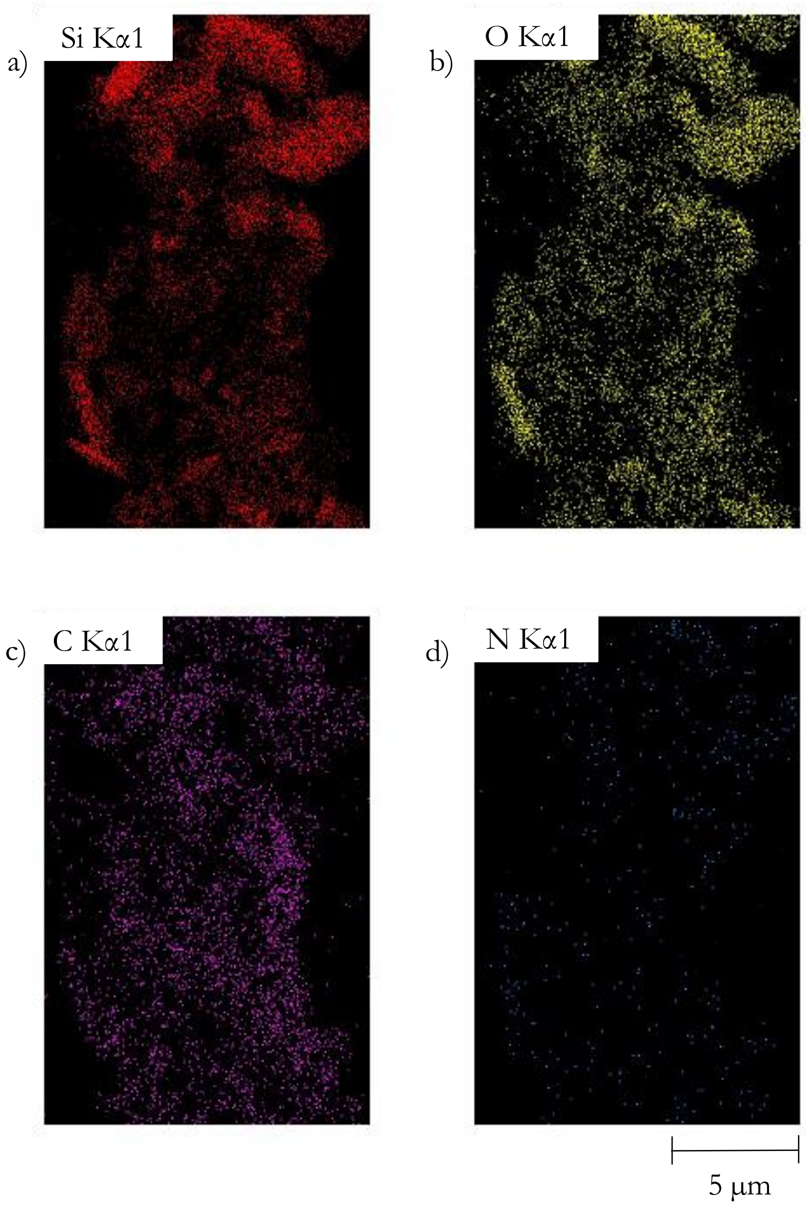

Figure 4.101 Compositional maps of a) silicon b) oxygen c) carbon and d) nitrogen with colour superposition for octylamine-SiNS. Atom colours; silicon = red, oxygen = yellow, carbon = purple and nitrogen = blue.

A single sheet of octylamine-SiNS was also examined. *Figure 4.102a* shows an SEM image of two separate single sheets and they are approximately ~2 μm in width. The elemental composition maps of silicon, oxygen and carbon for this image are shown in *Figure 4.102b/c/d* respectively. The detection of a large proportion of silicon in the two individual sheets can clearly be seen from *Figure 4.102b* and interestingly the sheet on the right appears to have a higher concentration of oxygen associated with it, compared to the sheet on the left. This reinforces the conclusion that there is a variety of material present in the octylamine-SiNS sample. In addition, only a trace amount of carbon was detected (*Figure 4.102d)*, and nitrogen was not detected. Different conclusions can be drawn from this; either the functionalisation was unsuccessful; or functionalisation occurs *via* a different route without the involvement of the amine; or a mixture of material is present, including unfunctionalised and functionalised sheets, with the functionalised sheets modified in a variety of ways. It is proposed that the latter is the correct interpretation, with a variety of material present under microscopic analysis, some functionalised sheets, as well as siloxene present.

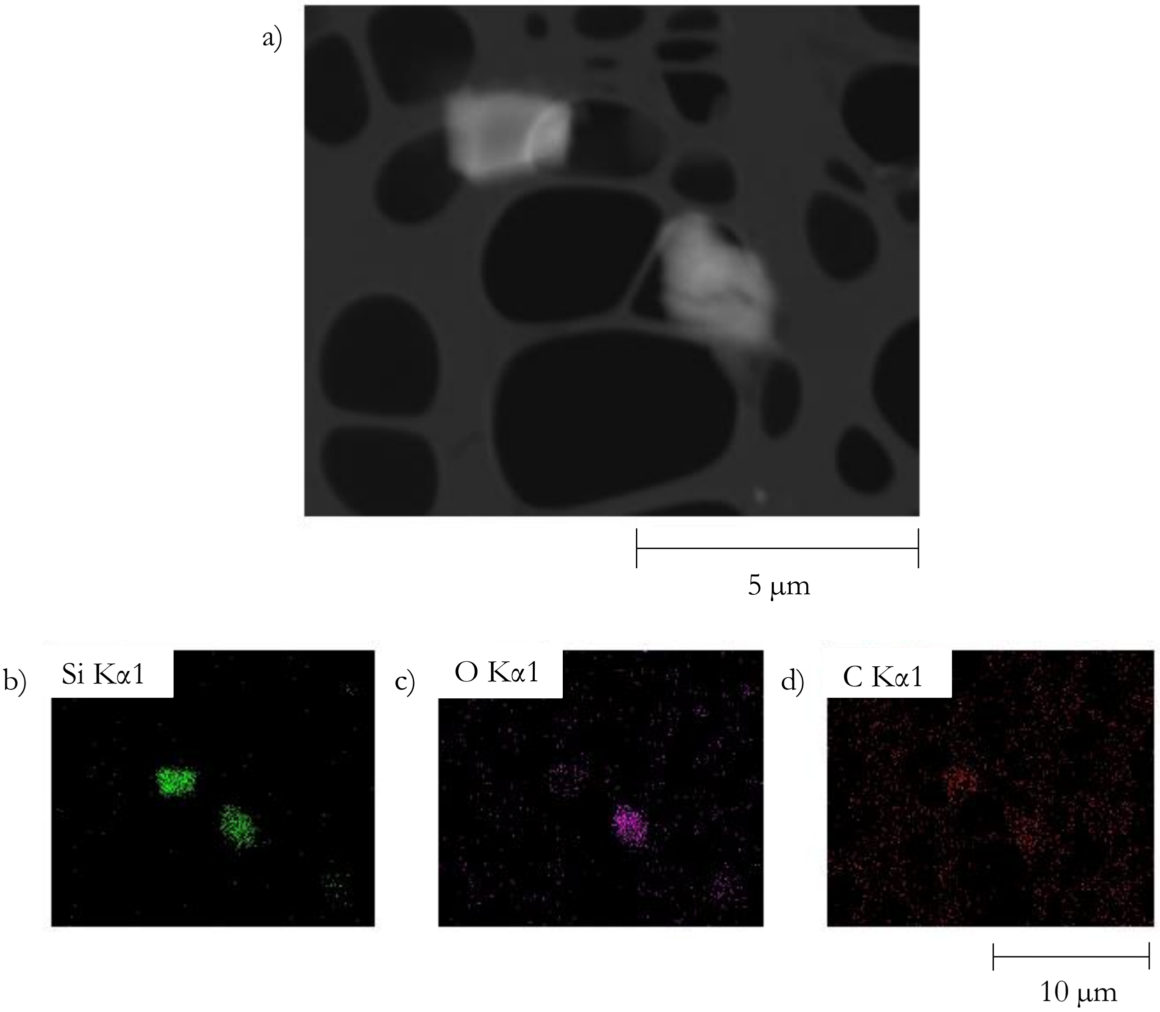

Figure 4.102 a) SEM image of octylamine-SiNS on a lacey carbon copper grid. Elemental composition maps of b) silicon, c) oxygen and d) carbon. Atom colours; silicon = green; oxygen = purple; and carbon = red.

4.2.2.4 Synthesis of Benzylamine-SiNS

Benzylamine was used for the second amine functionalisation of SiNS. The amine was added *via* syringe to a mixture of layered polysilane in dry chloroform and the mixture stirred for 17 hours at 60 °C under dinitrogen. Heat distillation under reduced pressure removed the unreacted benzylamine, and the distillation was repeated 4 times with fresh chloroform. The reaction product was dissolved in chloroform and filtered, and the solvent removed under vacuum leaving a sticky brown oil. *Figure 4.103* compares images of the two starting materials, layered polysilane dispersed in chloroform *(a)* and benzylamine dissolved in chloroform *(b),* with the product, benzylamine-SiNS dissolved in chloroform *(c)*. A similar reaction mechanism for the synthesis of octylamine-SiNS (*Scheme 4.11*) is proposed for benzylamine-SiNS. It is suggested that the large bulky benzyl groups attached to the sheets will aid in further reaction from the amine moieties on the sheets attacking neighbouring hydrogen atoms on the sheets as shown in *Scheme 4.12*.

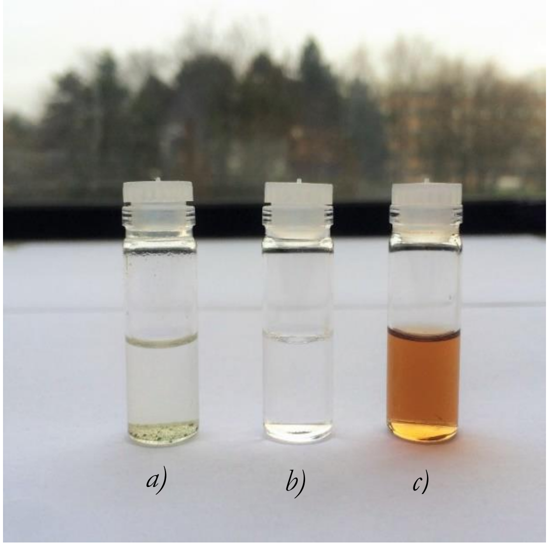

Figure 4.103 Images of a) SiNS dispersed in chloroform, b) benzylamine dissolved in chloroform and c) benzylamine-SiNS dissolved in chloroform.

Scheme 4.12 Proposed reaction mechanism for synthesis of benzylamine-SiNS

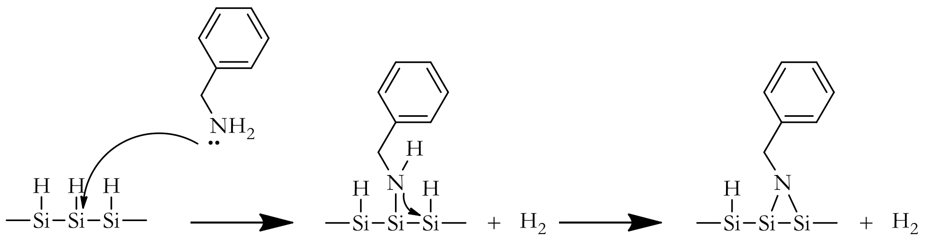

4.2.2.5 Infrared Spectroscopy of Benzylamine-SiNS

The absorption bands listed in *Table 4.12* are found in the IR spectrum of benzylamine-SiNS. An absorption band at 910 cm^{-1} is assigned to a Si-N stretch which was present in the spectrum of benzylamine-SiNS, but not observed in either of the starting materials (benzylamine or layered polysilane). This frequency is comparable to that of the N-Si-N absorption band reported in the literature, between 950-910 and 880-835 cm^{-1}.[36]

Table 4.12 IR absorption peaks of benzylamine-SiNS and their assignments.

Absorption (cm^{-1})	Assignment
494	Si-Si stretch
753, 691	C-H bend (aromatic)
800	Si-O-Si bend
910	Si-N stretch
1027	Si-O-Si stretch
1223	C-N stretch
1494-1378	C-H bend/C-H stretch
1640	C=C stretch (aromatic)
2100	Si-H stretch
2847	C-H stretch (CH_2)
3024	C-H stretch (aromatic)
3267	Broad O-H stretch

The absorption bands at 753 and 691 cm^{-1} are assigned to C-H bends from the monosubstituted benzene ring. Other absorptions bands at 1494-1378, 1640, 2847 and 3024 cm^{-1} are assigned to C-H bends, C-H stretches and C=C stretches from the benzene ring and CH_2 group attached to it. A very weak absorption band at 2100 cm^{-1} was present in benzylamine-SiNS, and is assigned to Si-H stretch. In addition, a weak absorption band at 3267 cm^{-1} was observed which is assigned to O-H stretches. It is concluded that the silicon atoms are either; functionalised with benzylamine; or are terminated by hydroxyl groups (Si-OH) or hydrogen (Si-H). Another absorption peak apparent in the product, but not observed in the spectrum of benzylamine is a large absorption at 494 cm^{-1} assigned to the Si-Si stretches within the sheets.

4.2.2.6 *Scanning Electron Microscopy of Benzylamine-SiNS*

Benzylamine-SiNS was deposited onto copper grids with a lacey carbon film and examined under SEM. The most interesting features indicated that parts of the material were scroll-like shown in *Figure 4.104a* (highlighted by a white arrow) and these structures consisted of a long tube with a hollow core similar to those described in literature.[37] From the images it is difficult to conclude if there are many layers of sheets rolled up known as multiwalled scrolls, or one sheet rolled up, termed a monolayer scroll. Presumptions have been made that the scrolls are multiwalled as sheets stacked on top of each other are most common. The length of the cylindrical nanoscroll is ~15 µm and the width is approximately 1 µm and they are considered nanoscrolls rather than tubes as it appears both ends of the scroll are open, *i.e.* the ends are not fused.

The mechanism for the scroll formation and stability is due to van der Waal's interactions.[38] The overlapping regions in scrolls have an energetic gain associated with them, however bending the structured sheet to form the scrolls requires energy. If the bending process goes beyond a point where two layers overlap, the van der Waal forces give enough energy to stabilise the scroll formation and the process is spontaneous.[39] The driving force of the scroll may be from either deformations in the sheets, or surface strain within the layers consequently causing the edges to lift. In 2009, Xie *et al.* describes graphene sheets rolling up to form scrolls due to solvent molecules occupying the space between the layer and the substrate, causing a bending motion in the graphene sheets.[40] This is another possible mechanism leading to rolled up sheets with an open end morphology.

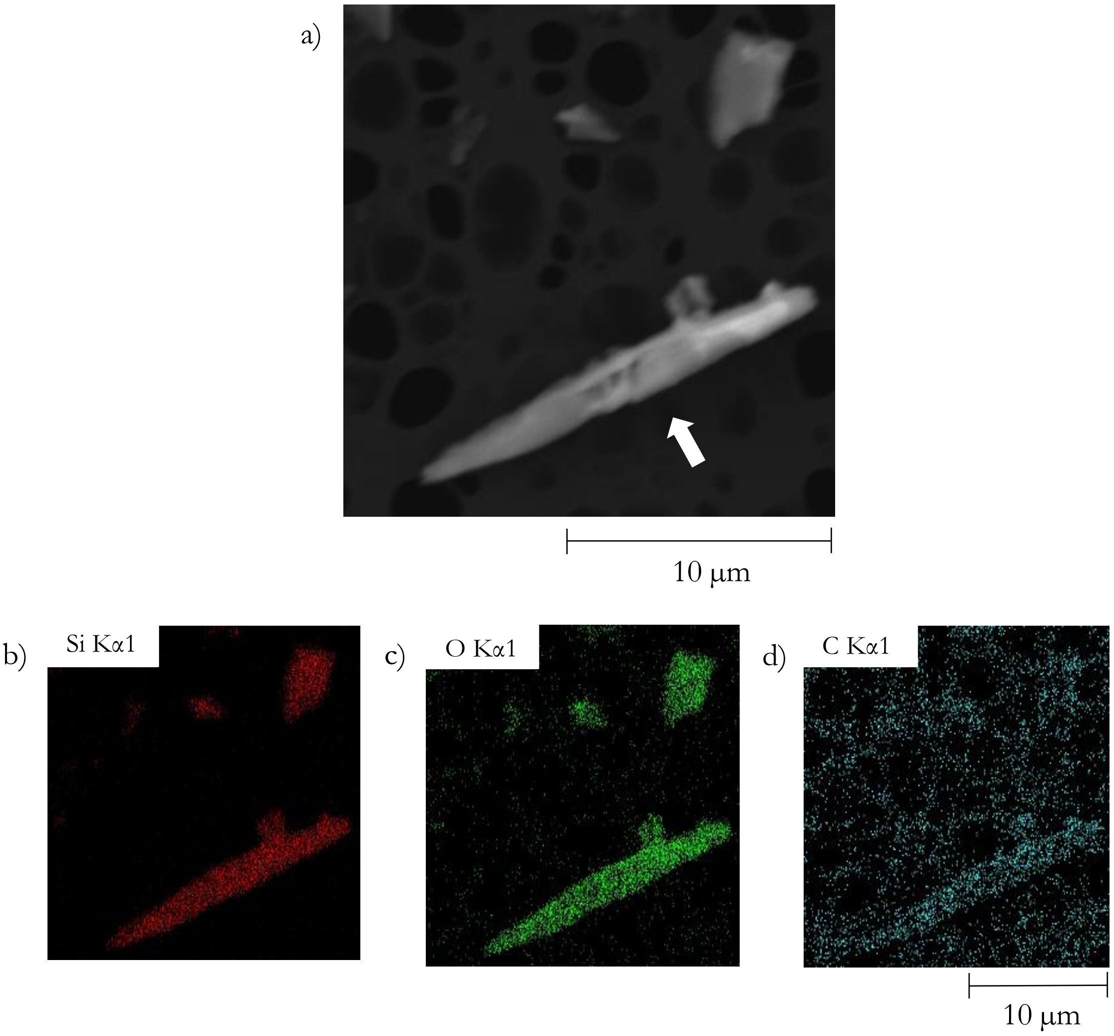

Figure 4.104 a) SEM image of benzylamine-SiNS on lacey carbon copper grid. The white arrow highlights a scroll structure. SEM-EDX elemental mapping of b) silicon, c) oxygen and d) carbon with colour superposition. Atom colours; silicon = red, oxygen = green and carbon = blue.

Elemental mapping in *Figure 4.104* displays the spatial distribution of silicon (*Figure 4.104b*), oxygen (*Figure 4.104c*) and carbon (*Figure 4.104d*) obtained from SEM-EDX. The scroll-type material has a large composition of silicon and oxygen due to the framework of the sheets *i.e.* Si-Si and Si-O-Si bonding network. A shape outline of the scroll is seen in the carbon mapping, however it is difficult to deduce the Si : O : C ratio. Minimal nitrogen was detected in comparison to other elemental compositions, which again implies minimal functionalisation is occurring over the scroll.

4.2.2.7 Transmission Electron Microscopy of Benzylamine-SiNS

Benzylamine-SiNS was deposited on gold TEM grids. Gold TEM grids have some advantages, for example, the absence of a support film such as graphene oxide or lacey carbon, will not perturb the results when examining the EDX of the material. However, a disadvantage to the absence of a support film are the large spaces between the checked grid allowing material to fall though. This often causes the material to accumulate on the gold grid and it is therefore challenging to identify the morphology of the material. The images in *Figure 4.105* of benzylamine-SiNS on gold grids show the silicon sheets protruding from the grid and in some areas the laminar sheet structures is identified (one example highlighted by a white arrow in *Figure 4.105a*). High resolution TEM images of benzylamine-SiNS showed no crystallinity, but rather amorphous structure which would imply attachment of organic groups to sheets is random and without periodicity.

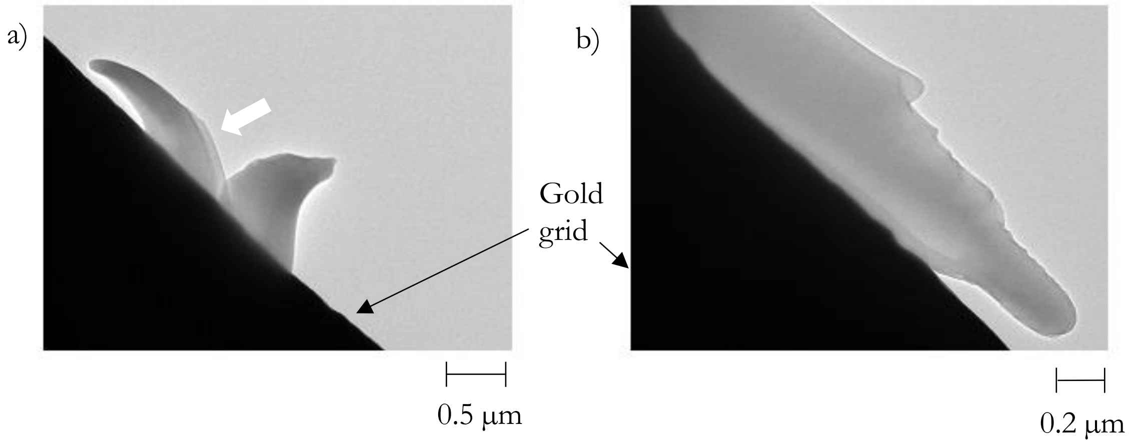

Figure 4.105 TEM images of benzylamine-SiNS deposited on a gold grid showing material collected on the gold grid. The white arrow in a) depicts a laminar structure.

The sheets have a tendency to waver and roll up under the intensity of the electron beam and this is shown in a series of images taken over a few seconds shown in *Figure 4.106*. The nature of material shown in these images also confirms the structure of the scrolls observed in SEM. The rolling-up feature was not apparent when SiNS were studied on gold grids before functionalisation, which would suggest that the functionalisation is bringing about structure change whereby sheets have the ability to bend and roll. The material was challenging to study on gold grids due to the lack of dispersion on the grids and the movement of the material under the beam.

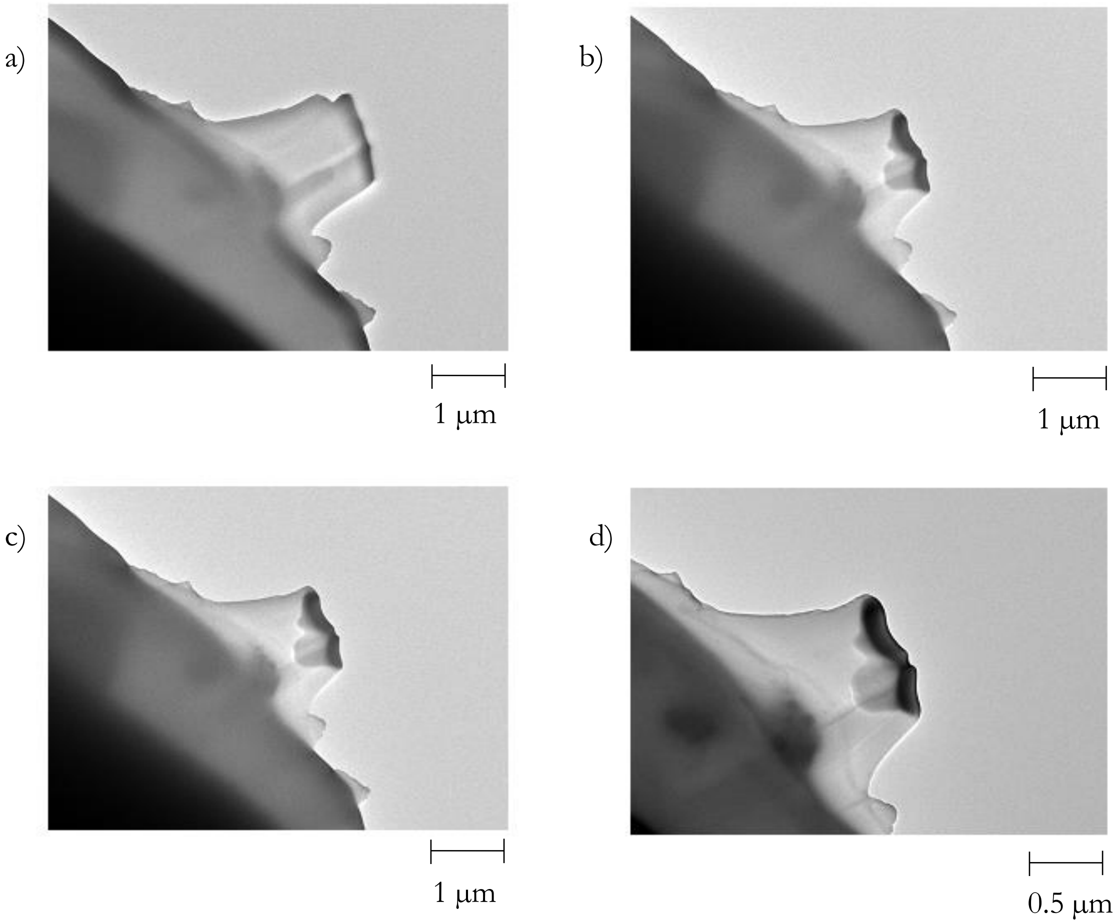

Figure 4.106 A series of TEM images portraying the edges of benzylamine-SiNS curling up over a few seconds. The material was deposited on a gold grid.

EDX was studied for benzylamine-SiNS deposited on gold finder grids and the data is shown in *Figure 4.107*. This data revealed that carbon, silicon, oxygen and nitrogen dominated the composition of the sheets. A large amount of chlorine was also detected for an unknown reason. The detection of carbon was higher than expected which may have been due to a large amount of functionalisation over the sheets, or another carbon-based material present overlapping with the sheets. The latter idea is more likely considering the low amount of carbon detected in SEM-EDX analysis, however identification of the material was challenging due to the build-up and aggregation of sample on the metal grid, making it difficult to distinguish if another material was present.

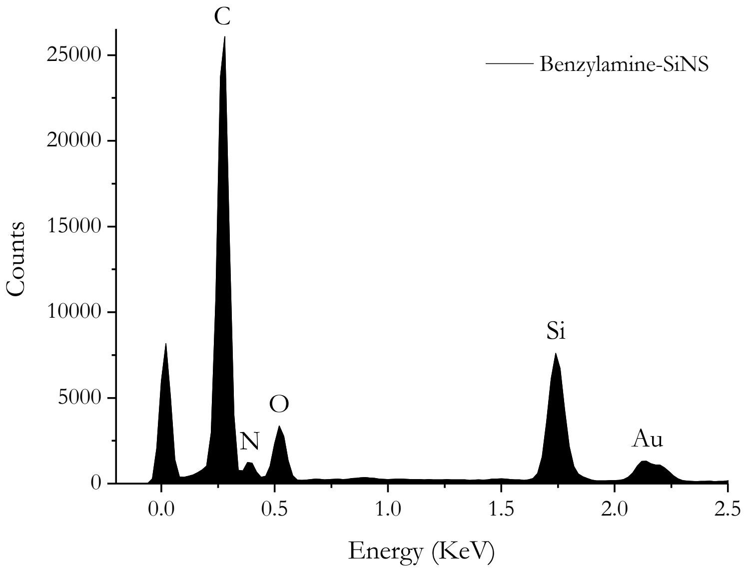

Figure 4.107 EDX spectrum in the energy range 0-2.5 eV of benzylamine-SiNS taken from Figure 4.106d. The material was deposited on a gold TEM grid.

Benzylamine-SiNS was also studied on copper grids with a graphene oxide support film. The material dispersed consistently on these grids and sheet-like material was detected. The thin layers were easily detectable and often holes in the support film were observed underneath the material highlighting the thinness of the sheets. A variety of EDX measurements were taken to examine the elemental composition. Firstly, the silicon sheet over a hole in the graphene oxide film was recorded, however this is not the most accurate analysis due to the scattering of signals upon hitting the material over a hole. Instead, EDX measurements of the carbon support (*Figure 4.108b*) and the material over the carbon support (*Figure 4.108c*) were both recorded. Subtracting the latter from the former gives a chemical analysis of the benzylamine-SiNS only. This data is shown in *Figure 4.108* and it would appear that little carbon is found on the sheets which is very different to the TEM-EDX results obtained from the material deposited on gold grids. The difference in the results highlights the inconsistency of the functionalised material, with both siloxene and other carbon-based material present.

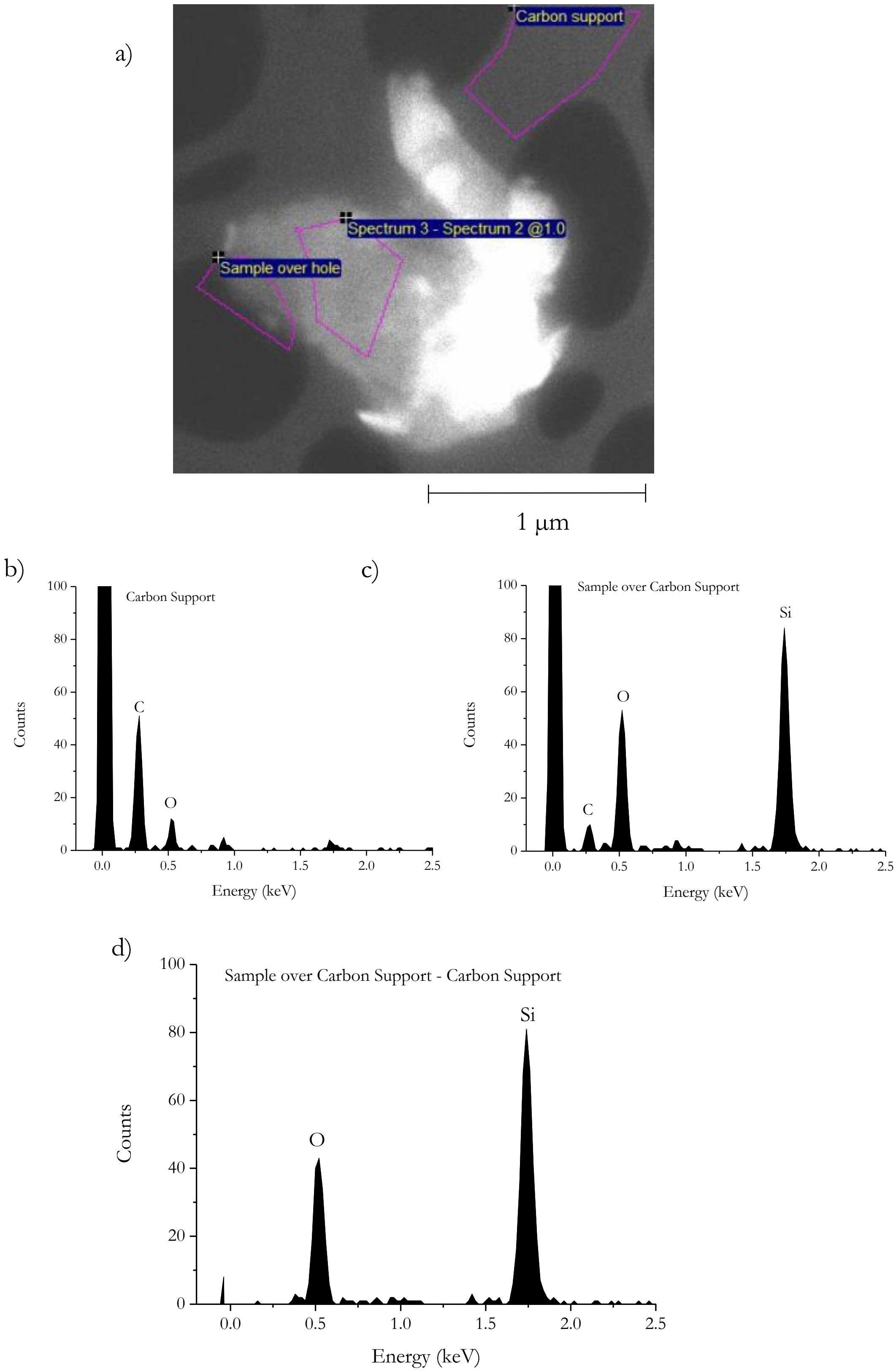

Figure 4.108 a) TEM image of benzylamine-SiNS and corresponding EDX maps of b) carbon support and c) sample over the carbon support. d) Two spectra minus from each other (c-b) to evaluate the EDX of just the sample. Material deposited on graphene oxide copper grids.

4.2.2.8 X-ray Photoelectron Spectroscopy of Benzylamine-SiNS

XPS was used to further analyse the surface of benzylamine-SiNS. A widescan in *Figure 4.109* shows the overall binding energy range from 0-1400 eV of benzylamine-SiNS. Benzylamine-SiNS is a sticky oil, and for XPS analysis, the oil was placed on non-conducting double sided sticky tape. Atomic percentages of carbon, oxygen and silicon are provided in *Table 4.13* comparing functionalised and non-functionalised SiNS data.

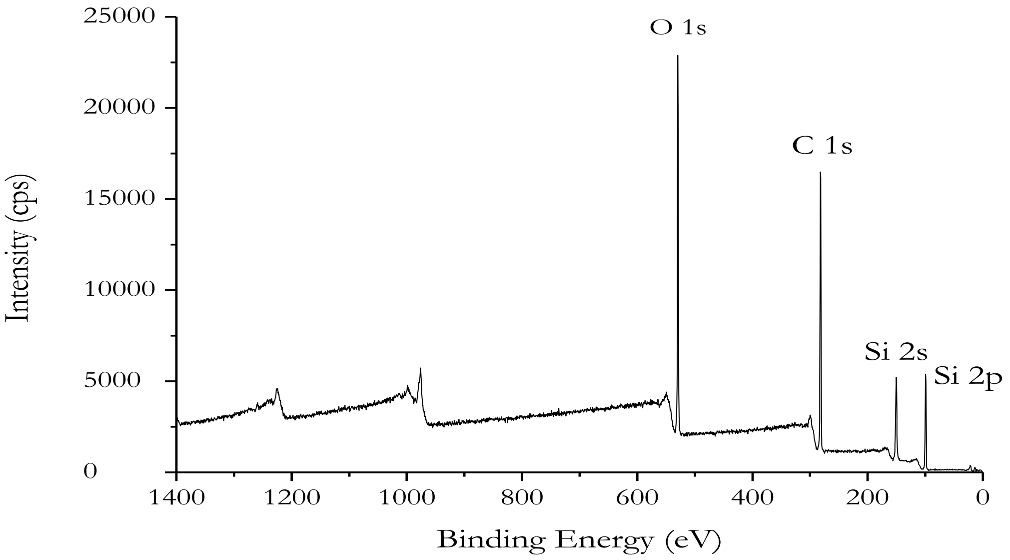

Figure 4.109 XPS widescan of benzylamine-SiNS showing the energy range from 0 to 1400 eV.

Table 4.13 Atomic percentages of benzylamine-SiNS and SiNS detected from XPS.

Element	**Atomic %**	
	Benzylamine-SiNS	**SiNS**
O 1s	21.9	18.2
C 1s	55.8	21.0
Si 2p	22.3	60.8

An increase in oxygen content in relation to silicon (Si : O) changes from 3 : 1 to 1 : 1 after functionalisation, which is expected to be due to the synthetic procedure allowing further oxygen to be inserted in the silicon framework. There is also an increase in carbon content upon functionalisation. *Figure 4.110* shows the binding energy of the carbon 1s orbital and the ratio of Si : C changes from 3 : 1 to 1 : 2.5 after functionalisation. The high proportion of carbon after functionalisation would suggest attachment of carbon to sheets, however a percentage of the carbon increase may also be from adventitious carbon contamination. Nitrogen is not detected and therefore functionalisation is assumed to occur on the evidence of an increase in carbon, however the XPS results suggest functionalisation did not occur *via* Si-N bond as proposed. It is also interesting to note the elimination of fluorine residues, according to XPS measurements, after functionalisation of sheets (refer to XPS in Chapter 3).

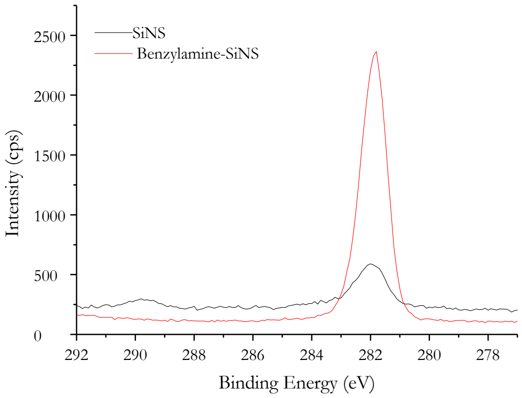

Figure 4.110 High resolution XPS spectra comparing non-functionalised SiNS (black) and benzylamine-SiNS (red) binding energies of C 1s orbitals.

Table 4.14 A table summarising the conclusions of SiNS functionalised via amine moieties.

Conclusion	
Octylamine-SiNS	***Benzylamine-SiNS***
NMR: ^1H NMR of octylamine-SiNS shows a broadening of resonances giving evidence of a large structure. The resonance at 1.05 ppm associated with the protons from the NH_2 group are no longer apparent, concluding that the NH_2 reacts with the sheets. It is suggested that the lone pair on the nitrogen in the NH_2 group attacks the silicon in the sheets, forming an Si-N linkage. Further reaction of this bond can occur with adjacent Si-H bonds, bridging two silicon surface atoms.	**IR:** The comparison of benzylamine and benzylamine-SiNS IR spectra highlight the products new peaks, in particular the absorption assigned to the Si-N stretch at 910 cm^{-1}. Si-Si stretches and Si-O-Si bends/stretches have absorption bands present at 494, 800 and 1027 cm^{-1} from the silicon framework. Other absorption bands present in the products IR spectrum have been assigned to the benzyl ring and CH_2 group.
SEM: Shattered sheets were detected revealing a composition of silicon, however minimal detection of carbon and nitrogen were found.	**SEM:** Images of benzylamine-SiNS revealed a unique scroll-type structure containing an elemental composition of mostly silicon and oxygen, and minimal carbon. In addition, only a trace amount of nitrogen was detected concluding that functionalisation was minimal if not at all.
	TEM: Material was deposited on two types of TEM grids; gold and copper. Identification of material on the gold grids was challenging compared to the copper grids where sheets were easily detected. EDX data showed a large composition of carbon on the gold grids, however a small composition of carbon on the copper grids. Silicon and oxygen were also detected, together with a trace amount of nitrogen. These results indicate there is a mixture of functionalised sheets along with other carbon-based material present.
	XPS: XPS detected carbon, silicon and oxygen, however not nitrogen. It was concluded from the XPS results, that functionalisation of sheets with small organic groups has occurred, however not through a Si-N bond linking the organic groups to the sheets as first proposed.

4.2.3 Functionalisation *via* Si-O Bonds in Silicon Nanosheets

To this point, functionalisation of SiNS targeting the Si-H bond has been described in this Chapter. However, there are a number of Si-OH bonds terminating the SiNS, especially before rinsing with HF as described in Chapter 3. To our knowledge, functionalisation in this way with the SiNS synthesised herein has not been published previously. Materials such as zeolites and glasses have been functionalised *via* the Si-O bond as discussed in the introduction in Section 4.1.6.[21-23] Covalent linkers between the zeolites/glasses and small organic groups are formed, and a similar synthetic procedure is used with our SiNS.

4.2.3.1 Synthesis of 3-aminopropyltrioxysilane-SiNS

For the synthesis of 3-aminopropyltriethoxysilane-SiNS the starting material was siloxene due to the large amount of Si-OH groups terminating the sheets. 3-aminopropyltriethoxysilane was added to a mixture of siloxene in dry toluene *via* syringe and heated to 110 °C for 1 hour. The solution was a pale yellow colour with a grey solid floating on the solution. The reaction mixture was cooled and centrifuged to allow all the sediment (unreacted siloxene) to sink to the bottom of the tube and the pale yellow solution was decanted. The solution was filtered using PTFE membranes (0.2 μm) and the filtrate collected was rinsed off the membrane using a variety of organic solvents. The organic solvents were removed under reduced pressure and a yellow paste/solid remained in the vial. The proposed reaction mechanism is shown in *Scheme 4.13*. Bonding formation between the silicon oxide surface and the aminopropyltriethoxysilane proceeds with the protonation of the alkoxy groups on the aminopropyltriethoxysilane followed by the attack from the hydroxsilane group on the sheets. Two products are possible including; sheets with ethoxy groups from the aminopropyltriethoxysilane which have not reacted, or all epoxy groups reacted with the hydroxyl groups in the SiNS.

Scheme 4.13 The proposed reaction mechanism for the synthesis of 3-aminopropyltriethoxysilane-SiNS.

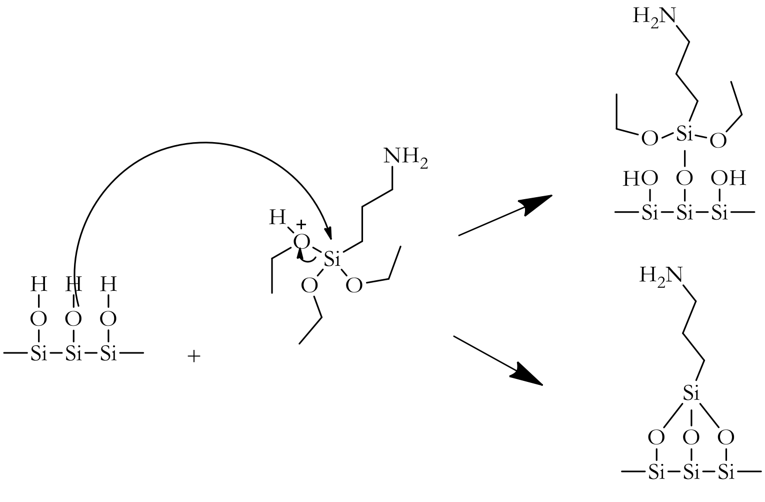

4.2.3.2 *Infrared Spectroscopy of 3-aminopropyltrioxysilane-SiNS*

The IR spectrum of 3-aminopropyltrioxysilane-SiNS was recorded using an ATR attachment. Absorption bands and their assignments are recorded in *Table 4.15.* Absorption bands at 474, and 1067 cm^{-1} are assigned to Si-Si stretches and Si-O-Si stretches, and these form the silicon framework. The organic groups attached to the sheets consist of a 3-carbon chain with an NH_2 group at the end. The carbon chain is responsible for the absorption bands corresponding to C-H stretches and C-H bends at 2965-2873 cm^{-1} and 1441 cm^{-1}, respectively. The N-H stretch with an absorption of 3358 cm^{-1} is assigned to the NH_2 at the end of the carbon chain. An absorption band at 779 cm^{-1} is assigned to the Si-C bond linking the organic group to the sheets.

Table 4.15 IR absorption peaks of 3-aminopropyltriethoxysilane-SiNS and their assignments.

Absorption (cm^{-1})	**Assignment**
474	Si-Si stretch
779	Si-C stretch
949	Si-O-Si bend
1067	Si-O-Si stretch
1297	C-H bend
1392	C-N stretch
1441	C-H stretch
2965-2873	C-H stretch
3358	N-H stretch

4.2.3.3 Transmission Electron Microscopy of 3-aminopropyltrioxysilane-SiNS

The morphology of 3-aminopropyltrioxysilane-SiNS was studied *via* TEM. The sample was dispersed in dry hexane and deposited on lacey carbon copper grids. Sheet-like material was observed, however many artefacts were spread over the surface, for example broken sheets (*Figure 4.111a*). Higher resolution images of the material (*Figure 4.111b*) revealed an amorphous structure where periodicity is not apparent, which suggests functionalisation is random within the sheets. The sheets were composed of mainly silicon, oxygen and carbon as shown by the EDX results (*Figure 4.111c*) and a small percentage of nitrogen was also detected. It is proposed that, similar to previous results, functionalisation occurred in a variety of ways over the sheets, and one of those ways is the proposed mechanism in *Scheme 4.13*. There was a large variety of material spread over the TEM grid.

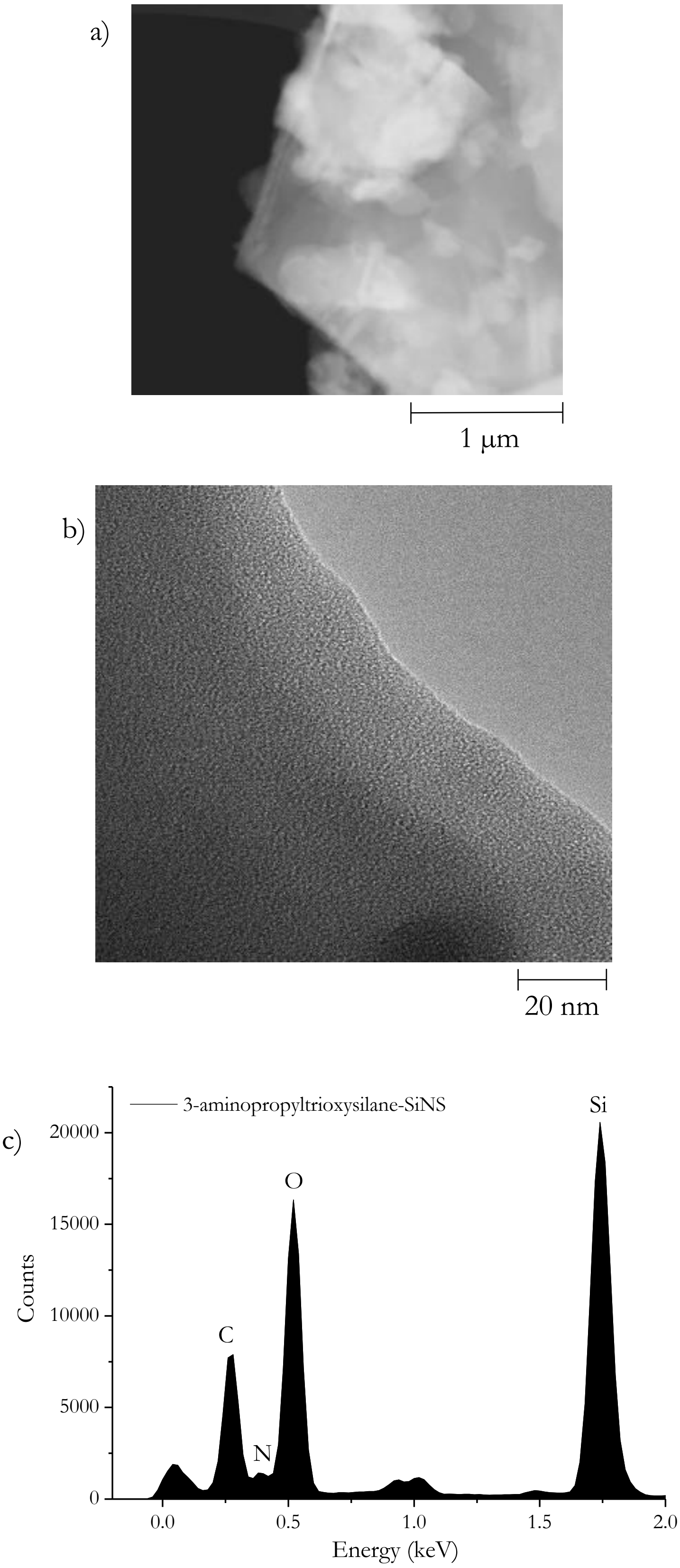

Figure 4.111 a) and b) TEM images of 3-aminopropyltrioxysilane-SiNS. c) EDX data of 3-aminopropyltrioxysilane-SiNS.

4.2.3.4 X-ray Photoelectron Spectroscopy of 3-aminopropyltrioxysilane-SiNS

XPS data for 3-aminopropyltrioxysilane-SiNS was collected. The product was placed on a non-conducting sticky tape similar to previous methods described. The overall XPS scan of 3-aminopropyltrioxysilane-SiNS is shown in *Figure 4.112* and the four main peaks correspond to C 1s, O 1s, Si 2s and Si 2p orbitals. The atomic percentages of these orbitals are compared to data collected for siloxene and are shown in *Table 4.16*.

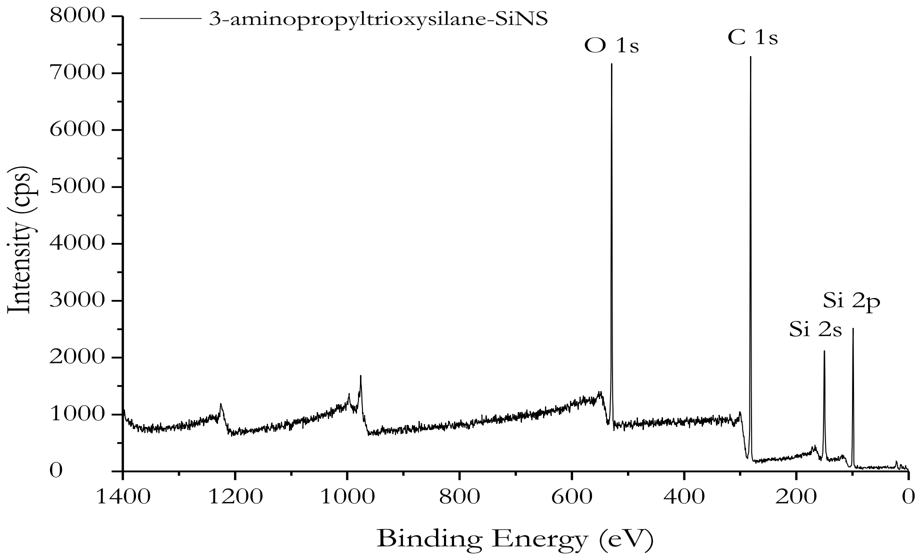

Figure 4.112 XPS widescan of 3-aminopropyltrioxysilane-SiNS in the binding energy range of 0-1400 eV.

The carbon 1s orbital in 3-aminopropyltrioxysilane-SiNS has an atomic percentage of 59.6 % compared to the silicon 2p orbital which has a percentage of 25.1 %. The high proportion of carbon was expected due to the 3-carbon chain length attached to the silicon framework. The ratio of Si : C is approximately 1 : 3 which would suggest that the majority of silicon atoms in the sheets are functionalised. The detection of oxygen is owing to the covalent linkages, Si-O-C, binding the small organic groups to the SiNS as well as the Si-O-Si bonds in the framework. Comparison of the oxygen and silicon percentages, 15.3 and 25.1 % respectively, in the functionalised material, reveals that oxygen has a lower atomic percentage than silicon. This is surprising as it was expected that each silicon atom that is functionalised by 3-aminopropyltrioxysilane would have been linked *via* Si-O-C and in addition, oxygen from within the framework (Si-O-Si) also present would have increased the amount of oxygen detected. Quantitative analysis should be examined with precaution due to the likelihood of adventitious carbon, which is often oxidised, building up on the surface. Nitrogen was not detected in XPS, and therefore other possible functionalisation routes are suggested.

Table 4.16 Atomic percentage data of O 1s, C 1s and Si 2p orbitals of 3-aminopropyltrioxysilane-SiNS and SiNS obtained from XPS.

Element	**Atomic %**	
	3-amino-propyltrioxysilane-SiNS	**SiNS**
O 1s	15.3	50.8
C 1s	59.6	7.8
Si 2p	25.1	41.5

One possibility is that SiNS were functionalised by toluene, the solvent which was used for the reaction. Recently, it has been reported in literature that SiNS have been functionalised *via* a radical hydrosilyation reaction with alkenes.[18] It is proposed that the reaction could proceed *via* the mechanism shown in *Scheme 4.14*, where a reaction commences with the formation of a silyl-radical, which then attacks an unsaturated bond such as that in toluene. A carbon-centre radical then abstracts a neighbouring hydrogen atom producing another silyl-radical and so the chain reaction continues. This would produce sheets with the composition of silicon, oxygen and carbon.

Scheme 4.14 Proposed mechanism for the reaction of toluene with SiNS.

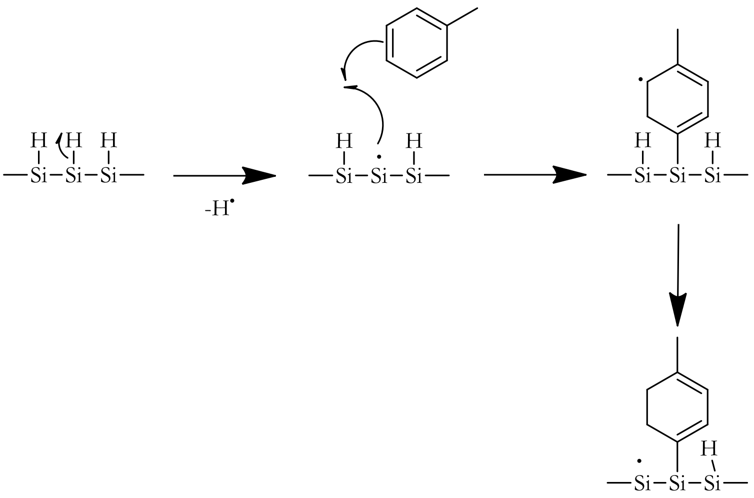

Table 4.17 A table summarising the conclusions of SiNS functionalised via 3-aminopropyltrioxysilane.

Conclusion **3-aminopropyltrioxysilane-SiNS**
IR: IR absorption bands of C-H stretches and bends were observed for the alkyl chain. An absorption band at a higher energy of 3358 cm^{-1} was observed which is assigned to N-H stretches. Absorption bands at 1067, 949 and 474 have been assigned to Si-O-Si stretches, Si-O-Si bends and Si-Si forming the silicon framework. **TEM:** TEM images revealed sheets composed of silicon, carbon, oxygen and nitrogen which suggests the sheets were successfully synthesised using 3-aminopropyltrioxysilane. **XPS:** Large amounts of silicon, oxygen and carbon were detected in functionalised sheets. However, nitrogen was detected. It was possible that the SiNS were functionalised with the solvent toluene.

4.3 Conclusions

The interest of silicon nanomaterials is rapidly growing in the field of nanotechnology, and in the last decade there has been a particular focus on SiNS. SiNS detailed in this Chapter aid in bridging the gap between 1D and 3D materials that have been studied in depth. For fabrication of a nanodevice, it is necessary to control the properties, sizes and shapes of the material synthesised. There are few reports in the literature due to difficulties in synthesising free-standing sheets, however the materials synthesised in this chapter have gone some way towards exploring the synthesis and nature of SiNS. A variety of methods were attempted to functionalise SiNS utilising different functional groups, including hexyl, imidazole, amines and trioxysilanes.

The first method involved a hydrosilylation reaction, where the Si-H bonds were inserted into the C=C double bonds in hexene molecules. The procedure was catalysed by hexachloroplatinic acid. Hexyl-SiNS was analysed *via* IR spectroscopy, powder XRD, TEM and EDX spectroscopy. Absorptions in the 1600 cm^{-1} region of the IR were not observed suggesting that the C=C double bond had reacted. Additionally, in the IR spectrum, a prominent absorption band assigned to Si-C stretch was identified. Extrapolation of data from the powder XRD reveals adjacent sheets are separated by a distance of 12.34 Å, however the peak was broad indicating there is minimal crystallinity and stacking of sheets. These results suggest functionalisation of sheets was successful, however TEM and EDX contradict this as sheets were not identified in TEM but rather a globular-type structure observed. In addition, silicon was not detected in the elemental composition collected by EDX and therefore it is proposed that a polymerisation reaction between the alkene starting material and catalyst occurred. Functionalisation with a different alkene, 1-oct-7-enyl-imidazole, was attempted and results from this lead to functionalising the sheets using imidazole. Functionalisation *via* imidazole seemed successful when analysing the ^{1}H NMR as resonances corresponding to the three protons from the imidazole ring disappeared. The resonances corresponding to the alkyl chains were broader, due to a slow tumbling effect, which is a characteristic of a large molecule (*i.e.* sheets). Inconclusive results were drawn when analysing the material under SEM.

Functionalisation *via* two different amines have been reported and discussed, firstly with octylamine and secondly with benzylamine. The products were investigated using NMR, IR, SEM, TEM and XPS. The ^{1}H NMR of octylamine-SiNS contained some broad resonances due to the slow tumbling of the large molecule. SEM images of octylamine-SiNS on copper grids revealed broken sheets, composed of largely silicon and oxygen with minimal carbon detection. This implies if functionalisation had occurred, it was minimal. Benzylamine-SiNS revealed scroll-type structures when investigated using SEM. These structures were largely composed of silicon and oxygen, and minimal carbon present. However, when the elemental composition of benzylamine-SiNS was studied on gold TEM grids, a large composition of carbon, silicon and oxygen were detected. Identification of the material was challenging due to aggregation of the sample on the gold grids and therefore other material, such as carbon based material, might have been present.

The final functionalisation reported in this Chapter targets the Si-O bonds terminating the SiNS. It involved a simple reaction between 3-aminopropyltrioxysilane and siloxene. The starting materials were heated for 17 hours producing a yellow paste/solid named 3-aminopropyltrioxysilane-SiNS. IR, XPS and TEM were used to analyse the sample. IR results imply successful functionalisation, along with TEM where sheets are present with a composition of silicon, carbon, oxygen and a small amount of nitrogen. XPS revealed silicon, oxygen and carbon present, but no nitrogen is observed, and therefore another route for functionalisation involving toluene has been suggested

The intention had been to functionalise the sheets with different asymmetric perylene monoimide monoanhydride derivatives. However, due to complications when functionalising sheets with smaller organic molecules, a suitable route has not yet been established. (See Chapter 5 for future work suggestions).

4.4 Experimental

4.4.1 Materials

All chemicals were obtained from commercial suppliers (Alfa Aesar, Fisher Scientific, Sigma-Aldrich, or VWR international) and used without further purification. Column chromatography was performed on silica gel (Merck silica gel 60, 0.2 - 0.5 mm, 50 - 130 mesh). Anhydrous toluene was dried by passing through a column packed with 4 Å molecular sieves, degassed and stored over a potassium mirror in a nitrogen atmosphere. Reactions sensitive to air and moisture were performed using a standard Schlenk line, with dinitrogen as the inert gas. Glassware was flame dried under vacuum and backfilled with nitrogen. The sample products were exposed to air during synthetic workup and transfer between measuring equipment. All samples were sealed in vacuum during measurements of XPS, SEM and TEM. IR (~1 minute), Raman (15 minutes) and powder XRD (~20 minutes) measurements had relatively short exposure time.

4.4.2 General Equipment

4.4.2.1 NMR Spectroscopy

Proton and carbon NMR experiments were carried out using either a Bruker DPX 400 MHz , Bruker AV(III)400hd or Bruker AV(III) 400 MHz instrument at room temperature. Chemical shifts are reported with respect to the $CDCl_3$ residual peak at 7.26 ppm (^{1}H), 77.00 ppm (^{13}C).

4.4.2.2 Mass Spectrometry

Electrospray ionisation (ESI) spectra were recorded on a Bruker MicroTOF II spectrometer (Bruker Daltonik, Bremen, Germany), operating in Flow Injection mode, using methanol or acetonitrile as the solvent.

4.4.2.3 *Infrared Spectroscopy*

Infrared spectra were obtained with a Bruker Tensor 27 FTIR spectrometer at room temperature (with an ATR attachment if necessary).

4.4.2.4 *Powder X-ray Diffraction*

Powder XRD data was collected using a PANalytical X'Pert PRO powder diffractometer equipped with a monochromated Cu Kα_1 radiation source (λ = 1.5432 Å, 40 kV, 40 mA). The instrument was fitted with 0.04 rad Soller slits on both the diffracted and incident beams as well as programmable divergent slits on both beams that were set to an irradiative length of 20.0 mm. The powder samples analysed in this thesis were placed on circular zero background silicon plates using PW3064/60 sample spinner and a revolution time of four second. The experiment parameters for the data collection were typically start angle 5°, end angle 60°, step size 0.026°, and scan speed 0.035 °/s

4.4.2.5 *X-ray Photoelectron Spectroscopy*

XPS data was record on a XPS Kratos Axis Ultra LiPPS. For the samples in this Chapter, the oil was placed on double sided sticky tape whereby one end was attached to the sample holder and the other held the powder. The oil covered approximately 0.5 by 0.5 cm area. Spectra were acquired using the Al-Kα monochromatic X-ray source (1486.7 eV) with 0° take of angle (normal to analyser). The vacuum pressure in the analysing chamber was maintained at ~$2\text{x}10^{-9}$ Torr during the acquisition process. The survey spectra were collected with pass energy 160 eV, and 0.5 eV step wise, dwell time 250 ms. Data analyses were done using Kratos Vision (Kratos Analytical Ltd) processing software and CasaXPS Version 2.3.16 PR 1.6. (Casa Software Ltd).

4.4.2.6 *Scanning Electron Microscopy*

SiNS material were dispersed in an organic solvent (usually hexane) using an ultrasonic bath and drop-cast onto SEM grids (Agar). Quanta 650 SEM, equipped with an Oxford Instruments X-Max 150 mm SDD detector for EDX.

4.4.2.7 *Transmission Electron Microscopy*

SiNS material was dispersed in an organic solvent (usually hexane) using an ultrasonic bath and drop-cast onto TEM grids (Agar). Two transmission electron microscopes were used. JEOL 2100F, field emission source TEM equipped with a Gatan Orius CCD camera for imaging and an Oxford Instruments 80 mm X-Max system for EDX. JEOL 2100 Plus TEM, LaB_6 source, equipped with a Gatan Ultrascan camera for imaging and an Oxford Instruments X-Max 80 TLE system for EDX.

4.4.3 Synthesis of Functionalised Silicon Nanosheets

Synthesis of Hexyl-SiNS

The synthesis of this compound was carried out according to a known literature procedure.[17] A flame-dried 2-neck flask was purged three times with dinitrogen and charged with layered polysilane (200 mg) dispersed in dry toluene (25 mL). A solution of 1-hexene (4.3 mL, 34.5 mmol) was added drop-wise, followed by the addition of $H_2PtCl_6·6H_2O$ (0.119 g, 0.23 mmol). The solution was left to stir overnight under dinitrogen at r.t. Unreacted layered polysilane was removed from the solution by filtering and washing with toluene. The toluene solution was purified by washing with water and then dried with anhydrous $MgSO_4$. The solvent was removed under vacuum to leave a yellow oil (0.916 g).

IR (ATR): 2959-2846, 2102, 1257, 1011, 861, 784, 561 cm^{-1}.

Synthesis of 1-oct-7-enyl-imidazole-SiNS

A flame-dried 2-neck flask was purged three times with dinitrogen and charged with layered polysilane (60 mg) dispersed in dry toluene (10 mL). A solution of 1-oct-7-enyl-imidazole (0.1 mL) was added, followed by $H_2PtCl_6{\cdot}6H_2O$ (0.025 g, 0.048 mmol). The solution was left to stir overnight under dinitrogen at r.t. The solution was then purified to remove the unreacted impurities by filtering and washing with toluene. The toluene solution was purified by washing with water and then dried with anhydrous $MgSO_4$. The solvent was removed under vacuum to leave a yellow oil. The pure product was capped with 1-oct-7-enyl-imidazole as a pale yellow oil (0.145 g).

Synthesis of Octylimidazole-SiNS

A flame-dried 2-neck flask was purged three times with dinitrogen and charged with layered polysilane (60 mg) dispersed in dry toluene (20 mL). A solution of 1-octylimidazole (0.4 mL, 2.02 mmol) was added and the solution was left to stir overnight under dinitrogen at r.t. The solution was then purified to remove the unreacted impurities by filtering and washing with toluene. The toluene solution was purified by washing with water and then dried with anhydrous $MgSO_4$. The solvent was under vacuum to leave a yellow oil product which was 1-octylimidazole functionalised SiNS (1.23 g).

IR (ATR): 3306, 2925, 2095, 1658, 1379, 1240, 1017, 930, 801, 489 cm^{-1}.

Synthesis of Octylamine-SiNS

A flame-dried 2-neck flask was purged three times with nitrogen and charged with layered polysilane (60 mg) dispersed in dry chloroform (15 mL). Octylamine (40 mL, 242 mmol) was added *via* syringe while under dinitrogen. The reaction mixture was stirred for 22 h at

60 °C where a grey solution formed and dark grey precipitate was observed. The amine modified SiNS were then obtained after removal of solvent *via* distillation under reduced pressure. Distillation under reduced pressure was repeated twice with fresh chloroform for the complete removal of unreacted amine. The reaction product was dissolved in chloroform and filtered under gravity to remove the black solid. The chloroform solvent was removed under vacuum to leave a yellow oil (0.84 g).

Synthesis of Benzylamine-SiNS

A flame-dried 2-neck flask was purged three times with dinitrogen and charged with layered polysilane (100 mg) and dry chloroform (8 mL). Benylamine (25 mL, 238 mmol) was added *via* syringe under dinitrogen. The reaction mixture was stirred for 17 h at 60 °C. The benzylamine modified SiNS were then obtained after removal of solvent *via* distillation under reduced pressure. A heat gun was used to remove the last 2 mL of solvent. Distillation under reduced pressure was repeated x 4 with fresh chloroform for the complete removal of unreacted amine. The reaction product was dissolved in chloroform and filtered under gravity to remove the left over black solid. The chloroform solvent was removed under vacuum to leave a light brown oil product as benzylamine-SiNS (0.54 g).

IR (ATR): 3267, 3024, 2847, 2100, 1640, 1494-1378, 1223, 1027, 910, 800, 753, 691, 494 cm^{-1}.

Synthesis of 3-aminopropyltrioxysilane-SiNS

A flame-dried 2-neck flask was purged three times with dinitrogen and charged with siloxene (50 mg) and dry toluene (25 mL). 3-aminopropyl)triethoxysilane (0.25 mL, 1.07 mmol) was added *via* syringe and the reaction mixture heated to 110 °C for 1 h. The reaction mixture was allowed to cool and centrifuged to remove the unreacted siloxene. The solvent was filtered through a PTFE membrane (0.2 μm hole size) and the filtrate collected. The filtrate was washed off the membrane using toluene and chloroform and the solvents reduced under vacuum to leave a yellow paste/solid (3 mg).

IR (ATR): 3358, 2965-2873, 1441, 1392, 1297, 1067, 949, 779, 474 cm^{-1}.

Synthesis of 1-oct-7-enyl-imidazole

To a solution of imidazole (1.7 g, 0.025 mol), in THF (50 mL) in an ice bath was added portionwise NaH (60 % in mineral oil, 1.1 g, 0.0275 mol). The resulting mixture was refluxed for 1 h. The solution was then cooled to room temperature and 8-bromo-oct-1-ene (4.6 mL, 0.0275 mol) was added. The mixture was refluxed for 3 h, cooled to room temperature and diluted with diethyl ether. The organic layer was washed with water (x 3) and dried over $MgSO_4$ and the solvent removed under vacuum to afford a yellow oil (4.184 g, 94 %).

^1H NMR (400 MHz, Chloroform-*d*) δ 7.44 (s, 1H), 7.03 (s, 1H), 6.88 (s, 1H), 5.82-5.72 (m, 1H), 5.02 – 4.89 (m, 2H), 3.95 – 3.87 (m, 2H), 2.02 (q, *J* = 6.8 Hz, 2H), 1.76 (p, *J* = 7.3 Hz, 2H), 1.41 – 1.26 (m, 6H). ^{13}C NMR (101 MHz, $CDCl_3$) δ 138.6, 137.0, 129.3, 118.7, 114.4, 46.9, 33.5, 30.9, 28.5, 28.4, 26.3. HRMS $(ESI)^+$ m/z 179.1558 ($C_{11}H_{19}N_2$ $[M+H]^+$ requires 179.1543).

Synthesis of 1-octylimidazole

To a solution of imidazole (1.7 g, 0.025 mol), in THF (50 mL) in an ice bath was added portionwise NaH (60 % in mineral oil, 1.1 g, 0.0275 mol). The resulting mixture was refluxed for 1 h. The solution was then cooled to room temperature and 1-bromooctane

(4.75 mL, 0.0275 mol) was added. The mixture was refluxed for 3 h, cooled to room temperature and diluted with diethyl ether. The organic layer was washed with water (x 3) and dried over $MgSO_4$ and the solvent removed under vacuum to afford a yellow oil (3.96 g, 80 %).

^{1}H NMR (400 MHz, Chloroform-*d*) δ 7.45 (s, 1H), 7.04 (s, 1H), 6.89 (s, 1H), 3.91 (t, *J* = 7.2 Hz, 2H), 1.76 (p, *J* = 7.3 Hz, 2H), 1.31 – 1.22 (m, 10H), 0.93 – 0.79 (m, 3H). ^{13}C NMR (101 MHz, $CDCl_3$) δ 137.1, 129.5, 118.8, 77.2, 47.1, 31.8, 31.2, 29.2, 29.1, 26.6, 22.7, 14.1. HRMS (ESI)$^+$ m/z/ 180.1616 ($C_{11}H_{20}N_2$ [M]$^+$ requires 180.1621).

4.5 References

1. H. Nakano and T. Ikuno, *Appl. Phys. Rev. 3*, 2016, **3**, 040803.
2. K. Xu, L. Ben, H. Li and X. Huang, *Nano Res.*, 2015, **8**, 2654-2662.
3. H. Okamoto, Y. Sugiyama and H. Nakano, *Chem. - Eur. J.*, 2011, **17**, 9864-9887.
4. H. Okamoto, Y. Kumai, Y. Sugiyama, T. Mitsuoka, K. Nakanishi, T. Ohta, H. Nozaki, S. Yamaguchi, S. Shirai and H. Nakano, *J. Am. Chem. Soc.* , 2010, **132**, 2710-2718.
5. H. Okamoto, Y. Sugiyama, K. Nakanishi, T. Ohta, T. Mitsuoka and H. Nakano, *Chem. Mater.*, 2015, **27**, 1292-1298.
6. Y. Sugiyama, H. Okamoto, T. Mitsuoka, T. Morikawa, K. Nakanishi, T. Ohta and H. Nakano, *J. Am. Chem. Soc.*, 2010, **132**, 5946-5947.
7. P. E. Blöchl, *Phys. Rev. B*, 1994, **50**, 17953-17979.
8. J. P. Perdew, K. Burke and M. Ernzerhof, *Phys. Rev. Lett.*, 1996, **77**, 3865-3868.
9. M. J. S. Spencer, T. Morishita, M. Mikami, I. K. Snook, Y. Sugiyama and H. Nakano, *Phys. Chem. Chem. Phys.*, 2011, **13**, 15418-15422.
10. J. S. S. Michelle, R. B. Michael, M. Tetsuya, K. S. Ian and N. Hideyuki, *New J. Phys.*, 2013, **15**, 125018.
11. G. G. Guzmán-Verri and L. C. L. Y. Voon, *J. Phys.: Condens. Matter*, 2011, **23**, 145502.
12. M. Houssa, G. Pourtois, V. V. Afanas'ev and A. Stesmans, *Appl. Phys. Lett.*, 2010, **97**, 112106.
13. D. Jose and A. Datta, *Phys. Chem. Chem. Phys.*, 2011, **13**, 7304-7311.
14. K. Takeda and K. Shiraishi, *Phys. Rev. B*, 1989, **39**, 11028-11037.
15. L. C. Lew Yan Voon, E. Sandberg, R. S. Aga and A. A. Farajian, *Appl. Phys. Lett.*, 2010, **97**, 163114.
16. S. Cahangirov, M. Topsakal, E. Aktürk, H. Şahin and S. Ciraci, *Phys. Rev. Lett.*, 2009, **102**, 236804.
17. H. Nakano, M. Nakano, K. Nakanishi, D. Tanaka, Y. Sugiyama, T. Ikuno, H. Okamoto and T. Ohta, *J. Am. Chem. Soc.*, 2012, **134**, 5452-5455.
18. T. Helbich, A. Lyuleeva, I. M. D. Höhlein, P. Marx, L. M. Scherf, J. Kehrle, T. F. Fässler, P. Lugli and B. Rieger, *Chem. – Eur. J.*, 2016, **22**, 6194-6198.
19. M. Ohashi, H. Nakano, T. Morishita, M. J. S. Spencer, Y. Ikemoto, C. Yogi and T. Ohta, *Chem. Commun.*, 2014, **50**, 9761-9764.
20. G. S. Lee, Y.-J. Lee and K. B. Yoon, *J. Am. Chem. Soc.*, 2001, **123**, 9769-9779.
21. S. Liu, R. Maoz and J. Sagiv, *Nano Lett.*, 2004, **4**, 845-851.
22. S. Y. Choi, Y.-J. Lee, Y. S. Park, K. Ha and K. B. Yoon, *J. Am. Chem. Soc.*, 2000, **122**, 5201-5209.
23. A. Kulak, Y.-J. Lee, Y. S. Park and K. B. Yoon, *Angew. Chem. Int. Ed.*, 2000, **112**, 980-983.

24. J. L. Speier, J. A. Webster and G. H. Barnes, *J. Am. Chem. Soc.*, 1957, **79**, 974-979.
25. B. Marciniec, *Hydrosilylation: A Comprehensive Review on Recent Advances*, Springer Netherlands, 2008.
26. I. Pappas, S. Treacy and P. J. Chirik, *ACS Catal.*, 2016, **6**, 4105-4109.
27. E. N. Jacobsen, A. Pfaltz and H. Yamamoto, *Comprehensive Asymmetric Catalysis: Supplement 1*, Springer Berlin Heidelberg, 2003.
28. T. K. Meister, K. Riener, P. Gigler, J. Stohrer, W. A. Herrmann and F. E. Kühn, *ACS Catal.*, 2016, **6**, 1274-1284.
29. J. B. Lambert, *Introduction to Organic Spectroscopy*, Macmillan, London, 1987.
30. R. M. Barrer and A. Sikand, *J. Chem. Soc., Faraday Trans. 1*, 1979, **75**, 2221-2234.
31. D. R. Lide, *CRC Handbook of Chemistry and Physics*, Taylor & Francis, USA, 2004.
32. N. E. Jacobsen, *NMR Spectroscopy Explained: Simplified Theory, Applications and Examples for Organic Chemistry and Structural Biology*, Wiley, 2007.
33. C. Corminbœuf, T. Heine and J. Weber, *Chem. Phys. Lett.*, 2002, **357**, 1-7.
34. H. Neergaard Waltenburg and J. T. Yates, *Chem. Rev.*, 1995, **95**, 1589-1673.
35. W. F. Bergerson, J. A. Mulder, R. P. Hsung and X. Y. Zhu, *J. Am. Chem. Soc.*, 1999, **121**, 454-455.
36. G. Socrates, *Infrared and Raman Characteristic Group Frequencies: Tables and Charts*, 3rd edn., John Wiley & Sons, Chichester, 2004.
37. E. Perim, L. D. Machado and D. S. Galvao, *Front. Mater.*, 2014, **1**, 1-17.
38. Y. F. Li, *EPL*, 2013, **102**, 26001.
39. R. Ramachandran, D. Johnson-McDaniel and T. T. Salguero, *Chem. Mater.*, 2016, **28**, 7257-7267.
40. X. Xie, L. Ju, X. Feng, Y. Sun, R. Zhou, K. Liu, S. Fan, Q. Li and K. Jiang, *Nano Lett.*, 2009, **9**, 2565-2570.

Chapter 5

Conclusions and Final Remarks

5.1 Conclusion and Future Outlook

The first success detailed in this thesis is the synthesis and characterisation of a series of novel PMIA compounds. The PMIA compounds featured two different moieties at either end of the molecule, including an imide, with four different functional groups employed (butyl, 1-ethylpropyl, cyclohexane and diphenylmethyl-4-methylphenyl), and an anhydride. The crystal structure of a perylene monoimide diester species was studied using Hirshfeld surfaces which allowed identification of the intermolecular forces between the molecules in the solid state. Hirshfeld analysis has proven to be a useful analytical technique which is not often reported in the literature but has the potential use for further analysis of other molecular structures, to aid in the identification of intermolecular interactions within supramolecular structures. Two PMIA units featuring diphenylmethyl-4-methylphenyl pendant groups were linked using organic linkers to fabricate PDI dimers. The more soluble PDI dimer was investigated using a combination of electroanalytical techniques and revealed it possessed two two-electron reduction processes, and the direduced species had an absorption band placed in the middle of the neutral and monoreduced species. The PDI dimer has the ability to form a stable diradical where the unpaired electrons were positioned on each PDI unit and did not communicate with each other.

The second part of this thesis describes the investigation into the synthesis and characterisation of layered polysilane and siloxene. These materials contain layered sheets which feature six-membered silicon rings isolated from each other by silicon-oxygen bridges. The extent of the oxygen bridges is greater in siloxene than in layered polysilane. Infrared spectroscopy revealed that layered polysilane was terminated with hydrogen atoms compared to siloxene which was terminated with a mixture of hydrogen and hydroxyl groups. These particular silicon nanosheet systems were studied using TEM and

SEM for the first time revealing a laminar structure, identified particularly around the edges of the sheets. TEM images revealed the sheets had a rippling feature under the intensity of the microscopic beam and the sheet sizes ranged from 5-10 μm. HRTEM revealed lattice fringes identifying crystalline parts as well as amorphous parts within the sheets. Investigation of powder XRD revealed the spacing between the sheets was approximately 3.25 Å. EDX spectroscopy was used to examine the elemental composition of the sheets, another technique which has not been previously reported for layered polysilane. EDX revealed the composition of the sheets was mostly silicon and oxygen, with a trace amount of copper from the grid. Carbon was often detected when a lacey carbon support film was present. The work herein has focused on the structural aspects of the SiNS as understanding this is important for the use of this material in practical applications.

An area of future work could focus on the investigation into the mechanical properties of the nanosheets. An example of this may be exploring the mechanical strength of the sheets utilsing the bulge test.[1-3] In this experiment the nanosheets are adhered to a steel plate with a 1 mm diameter hole in the centre. As pressure is applied to the nanosheet through the hole, distortion of the nanosheet is monitored measuring the deflection or bulge. Through a series of calculations the ultimate tensile strength (σ_{max}), elongation (ε_{max}) and elastic modulus (E) can be calculated for nanosheets of different thicknesses. This has been carried out on a number of different types of nanosheets including polysaccharide[4] and silicon nitride.[5] Electrochemical properties of many 2D sheet materials have been studied and found application in a variety of electronic devices, such as electrochemical energy storage[6, 7] and electrodes in batteries.[8, 9] In 2016, the study of the effect of nanosheet length and thickness upon the performance in electrochemical devices was reported.[10] The study used WS_2 nanosheets as electrodes and proved that by tuning the nanosheet geometry, whether that be perimeter length or the total accessible suface area within the electrode, the performance of the electronic device was enhanced. This is a relatively new study which has not been reported previously due to the difficulty to control dimensional sizes of sheets, however it would be interesting to carry out similar experiments on the nanosheets described herein.

In addition, layered polysilane can be used as a substrate to grow other species. There has been headway into the investigation of this topic with the use of the material synthesised herein to grow carbon nanocups, which are a sp^1/sp^2 hybridised carbon allotrope. It is proposed that the hollow cavity of the cups can be used as 'containers' for a range of reactions or storage. Investigation of this is very much in its infancy, however exciting outcomes are expected and there is great scope for the use of the 2D material described herein to be used as a substrate to build supramolecular arrays.

Chapter 4 explores modification of the SiNS utilizing small organic molecules, including alkene, imidazole, amine and trioxysilane, to investigate different pathways for sheet modification. The different functionalisation routes are detailed, and results are discussed, with some more successful than others. The intention had been to optimise a route, finding a conclusive pathway for functionalisation of SiNS where a PMIA or asymmetrically substituted PDI could be used to attach the dye molecule to the SiNS. It has been reported in the literature that phenyl-functionalised SiNS have produced a light-induced photocurrent, which is the first reported photocurrent formation in polysilanes.[11] It was thought that PMIA-SiNS or PDI-SiNS systems, would produce a range of interesting properties, including a pronounced photocurrent due to communication between the nanosheets and the attached PMIA/PDI molecules. Furthermore, attachment of perylene derivatives to the SiNS might introduce enhanced photoluminescence and UV-vis properties. The ability to tune the colour of perylene derivatives would suggest that it is possible to tune the colour and absorption properties of PMIA-SiNS/PDI-SiNS systems. Moreover, establishing an ideal route for functionalisation *via* such molecules could lead to more complex supramolecular systems covalently attached to the sheets.

A different approach to modify SiNS with small organic groups could involve functionalising a halogenated SiNS surface rather than surfaces terminated with hydrogen or hydroxyl groups. Several methods to halogenate silicon surfaces have been reported in the literature including, gas phase reactions with molecular halogens[12, 13] (at elevated temperatures[14]) and solution phase reactions using PCl_5 in chlorobenzene for chlorinated surfaces[15] and reactants such as bromochloroform (CCl_3Br) under heat activation for brominated surfaces.[16] It is predicted that the halogenation of silicon surfaces described in the literature can be applied to the material herein and this may enhance the reactivity of the surface for facile functionalisation with small organic groups. There is a large scope for the work of the SiNS synthesised herein and it is hoped that the findings reported advance and expand the field of silicon nanosheet research.

5.2 References

1. C. Li, Z. Liu and H. Xie, *Rev. Sci. Instrum.*, 2014, **85**, 103709.
2. T. Fujie and S. Takeoka, in *Advances in Nanosheets Technology towards Nanomedical Engineering in: Nanobiotechnology*, One Central Press, UK, 2014, p. 68.
3. S. Markutsya, C. Jiang, Y. Pikus and V. V. Tsukruk, *Adv. Funct. Mater.*, 2005, **15**, 771-780.
4. T. Fujie, N. Matsutani, M. Kinoshita, Y. Okamura, A. Saito and S. Takeoka, *Adv. Funct. Mater.*, 2009, **19**, 2560-2568.
5. J. J. Vlassak and W. D. Nix, *J. Mater. Res.*, 1992, **7**, 3242-3249.
6. F. Bonaccorso, L. Colombo, G. Yu, M. Stoller, V. Tozzini, A. C. Ferrari, R. S. Ruoff and V. Pellegrini, *Science*, 2015, **347**, 41-41.
7. M. Chhowalla, H. S. Shin, G. Eda, L.-J. Li, K. P. Loh and H. Zhang, *Nat. Chem.*, 2013, **5**, 263-275.
8. E. Yoo, J. Kim, E. Hosono, H.-S. Zhou, T. Kudo and I. Honma, *Nano Lett.*, 2008, **8**, 2277-2282.
9. G. Du, Z. Guo, S. Wang, R. Zeng, Z. Chen and H. Liu, *Chem. Commun.*, 2010, **46**, 1106-1108.
10. Z. Gholamvand, D. McAteer, A. Harvey, C. Backes and J. N. Coleman, *Chem. Mater.*, 2016, **28**, 2641-2651.
11. Y. Sugiyama, H. Okamoto, T. Mitsuoka, T. Morikawa, K. Nakanishi, T. Ohta and H. Nakano, *J. Am. Chem. Soc.*, 2010, **132**, 5946-5947.
12. S. Rivillon, F. Amy, Y. J. Chabal and M. M. Frank, *Appl. Phys. Lett.*, 2004, **85**, 2583-2585.
13. B. J. Eves and G. P. Lopinski, *Surf. Sci.*, 2005, **579**, 89-96.
14. X. Y. Zhu, V. Boiadjiev, J. A. Mulder, R. P. Hsung and R. C. Major, *Langmuir*, 2000, **16**, 6766-6772.
15. A. Bansal, X. Li, I. Lauermann, N. S. Lewis, S. I. Yi and W. H. Weinberg, *J. Am. Chem. Soc.*, 1996, **118**, 7225-7226.
16. J. He, S. N. Patitsas, K. F. Preston, R. A. Wolkow and D. D. M. Wayner, *Chem. Phys. Lett.*, 1998, **286**, 508-514.

Appendix

Characterisation Techniques

A.1 Infrared Spectroscopy

Infrared spectroscopy is used to identify the bonds in a sample, a technique based on the vibrations of bonds within a molecule. Radiation passes through a sample and the fraction of radiation absorbed at a particular energy is determined and measured as percentage transmittance (*Figure A.*113).[1] The transmittance is the ratio of transmitted beam intensity to that of the incident beam and is calculated using *equation [8]* in *Figure A.*113. The energy of the peaks corresponds to a particular frequency of a bond vibration in the sample. Attenuated total reflectance (ATR) was a sampling tool used to analyse a powdered material, whereby an IR beam is directed into an ATR crystal before going into the solid sample.

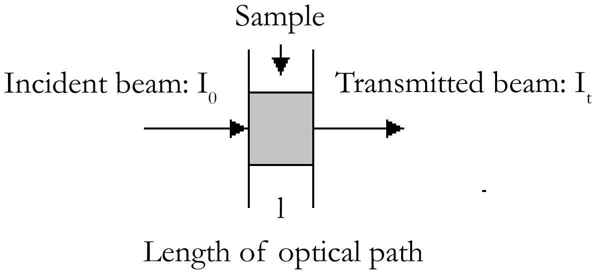

$$T\,(\%) = \frac{I_t}{I_0} \bullet 100 \qquad [9]$$

Figure A.113 Definition of transmittance.

A.2 Raman Spectroscopy

Raman spectroscopy is a valuable technique first observed by an Indian chemist named Sir C. V. Raman which led to the award of his Nobel prize 1928.[2] Raman spectroscopy is used to observe vibrational, rotational and other low-frequency modes in a system for sample identification and complements IR spectroscopy. It works by irradiating a sample with a monochromatic light source (usually a laser) and then detecting the scattered light. The majority of the radiation is scattered from the sample at the same wavelength as the incoming laser radiation which is known as Rayleigh or elastic scattering and is shown as red arrows in *Figure A*.114. However, a very small amount of the scattered light (~10^{-5} % of the incident light intensity) is shifted from the original laser wavelength. This is known as inelastic light scattering or Raman scattering/effect (shown in *Figure A*.114*)*. The shift in energy is due to the interactions between the incident electromagnetic waves and the sample. The interactions lead to two possibilities:

i. Stokes Raman scattering (blue arrow in *Figure A*.114): the sample absorbs energy and the emitted photon has a lower energy than the absorbed photon.

ii. Anti-Stokes Raman scattering (green arrows in *Figure A*.114): the emitted photon has higher energy than the absorbed photon.

Plotting the intensity of the shifted light *versus* the frequency results in a Raman spectrum, and band positions lie at frequencies that correspond to energy levels of different functional group vibrations.

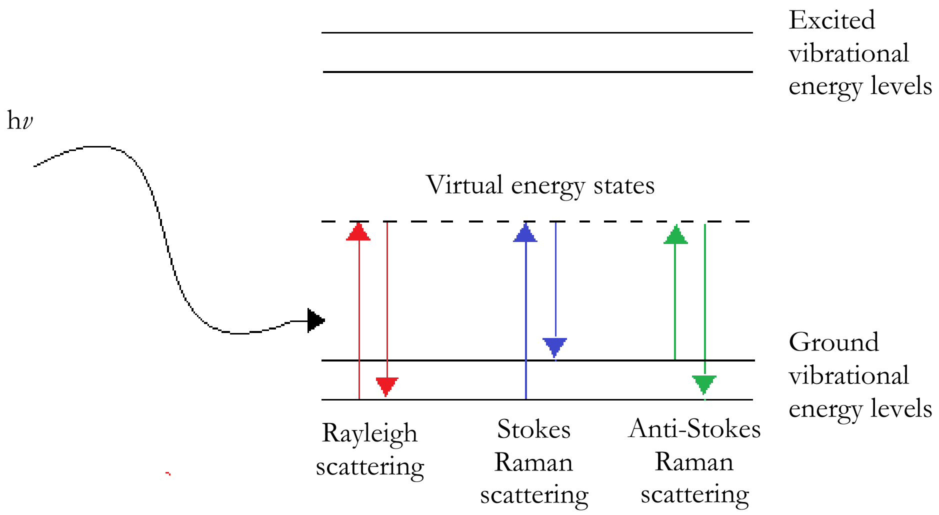

Figure A.114 Graphical representation of the various light scattering processes exploited in Raman spectroscopy.

A.3 Powder X-ray Diffraction

Powder X-ray diffraction (XRD) is an analytical technique which is used to help identify the crystallinity of a material, and provide information on its atomic arrangement. An X-ray beam is directed at a sample and the planes of atoms in the sample, in particular the electron density associated with the atoms, cause the beam to diffract (see *Figure A*.115).

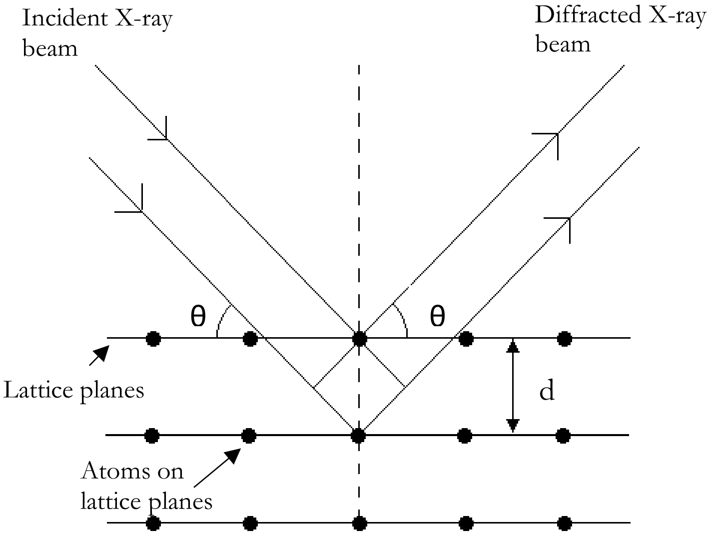

Figure A.115 Diagram showing the diffraction of x-ray beams from atoms.

The intensity of scattered waves as a function of scattering angle is measured to obtain a diffraction pattern. X-rays diffracted in-phase (*i.e.* when a peak of one wave matches the peak of the following wave) will give rise to a signal. These signals are known as Bragg peaks and satisfy Braggs law *[10]*.

$$n\,\lambda = 2\,d\,sin\theta \qquad [10]$$

Braggs law expresses the relationship between the scattering angle of the incident beam and the distance between the lattice planes in a crystal. λ is the wavelength of the incident X-ray beam, *n* is an integer and θ is the angle between the incident ray and the scattering planes. The diffracted beams are recorded by the detector and the plot of diffracted intensity versus the angle produces a powder pattern. A diffracted pattern can be used to determine lattice plane spacing and the crystal's atomic structure.

A.4 X-ray Photoelectron Spectroscopy

An X-ray source of known energy (for the work in this thesis Al Kα at 1486.7 eV is used) irradiates a sample, causing photoelectrons to emit from the sample surface (*Figure A.*116).

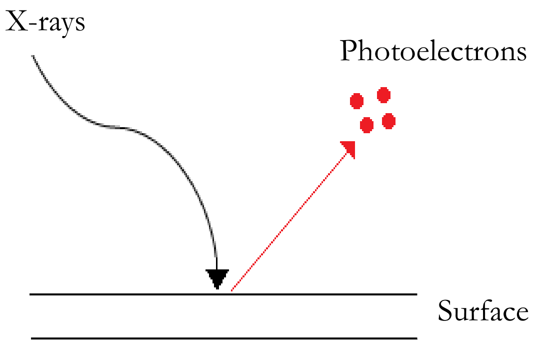

Figure A.116 X-rays excite electrons in a surface sample causing photoelectrons to be ejected.

When surface atoms absorb X-ray photon energy (*hv*), the emitted electron's kinetic energy ($E_{kinetic}$) can be measured by an electron energy analyser.[3] The kinetic energy of the electron depends upon the photon energy (*hv*) and the binding energy ($K_{Binding}$) of the electron. The process is described by Einstein's equation, which can be used to determine the binding energy of the electron.[4]

$$E_{kinetic} = hv - (E_{binding} - \emptyset) \qquad [11]$$

In this equation *hv* is the X-ray source, $E_{kintetic}$ is the kinetic energy, $E_{binding}$ is the binding energy and ø is the work function of the instrument. A spectrum is recorded by counting the ejected electrons of a particular characteristic energy, using the intensity of the peaks to enable quantification. Each element in the periodic table (apart from helium and hydrogen) gives rise to a characteristic set of peaks in the spectrum, allowing identification of elements in the sample.

A.5 Scanning Electron Microscopy

A scanning electron microscope (SEM) (*Figure A*.117) uses a focused beam of high-energy electrons to scan over a surface to create an image. The image is derived from interactions between the electrons and sample and reveals information about the sample, including:

i. External morphology (texture)
ii. Chemical composition
iii. Crystal structure and orientation

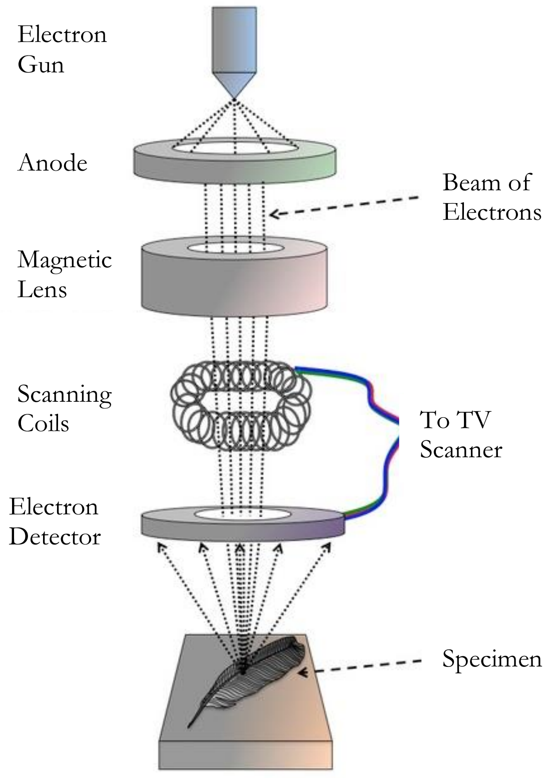

Figure A.117 Diagram showing components of an SEM.

An electron gun is located at the top of an electron column, as seen in *Figure A*.117. It emits electron beams that travel through a series of electromagnetic lenses, targeted at the sample surface. Accelerated electrons in an SEM carry a significant amount of kinetic energy and when they interact with the sample, this energy is dissipated as a variety of signals, including backscattered electrons (BSE), secondary electrons (SE), X-rays and other photons of various energies.[5] The imaging signals of greatest interest are the backscattered and secondary electrons with the former being most valuable for illustrating chemical composition of the sample and the latter for providing topographic information about the sample surface.

A.6 Energy-Dispersive X-ray Spectroscopy

An elemental map is an image showing the spatial distribution of elements in a sample and is obtained from EDX spectroscopy. An electron from an electron column (such as in SEM or TEM) hits the sample and ejects an electron from an inner shell of a sample atom (*Figure A*.118). A hole or vacancy is created and an electron from an outer, higher energy shell fills the hole in the atom. The difference in energy between the higher energy shell and lower energy shell may be released in the form of an X-ray. The number and energy of the X-rays emitted from a specimen can be measured by an energy dispersive spectrometer. Every element in a sample will emit a unique and characteristic pattern of X-rays and therefore the analysis and processing of characteristic X-rays emitted from the sample gives quantitative elemental information. The combination of characteristic X-rays and secondary electrons with respect to location allows for production of elemental maps of a surface.

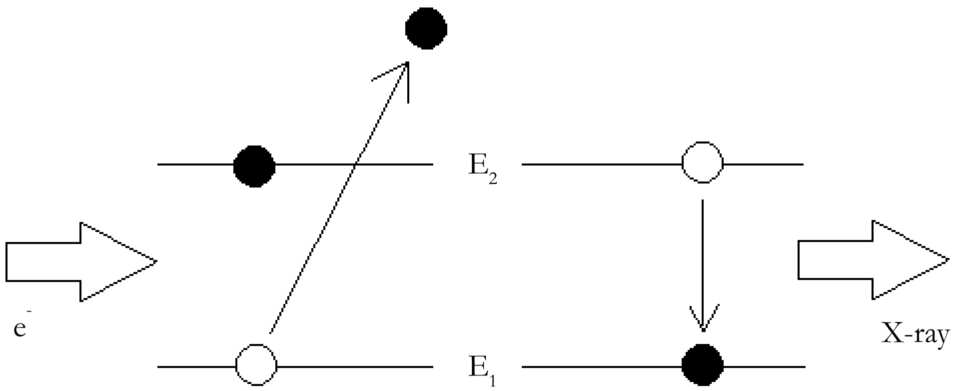

Figure A.118 An illustration of the movement of electronic transitions between atomic shells in EDX spectroscopy. An orbital electron from a shell of lower energy is ejected leaving a hole which is filled by an electron from a shell of higher energy. The lost energy appears as emitted radiation of energy $E_2 - E_1$.

A.7 Transmission Electron Microscopy

In transmission electron microscopy (TEM) a sample is irradiated by electrons with high energy (80-200 KeV). These electrons are transmitted through a thin sample, interacting with the specimen causing loss and scattering of electrons.[6] A sophisticated system of electromagnetic lenses focuses the scattered electrons into an image or diffraction pattern.

A.8 References

1. B. H. Stuart, in *Infrared Spectroscopy: Fundamentals and Applications*, Wiley, Chichester, 2005, pp. 1-13.
2. C. V. Raman and K. S. Krishnan, *Nature*, 1928, **121**, 501-502.
3. D. Briggs and M. P. Seah, *Practical Surface Analysis, Auger and X-ray Photoelectron Spectroscopy*, 2nd edn., Wiley, New York, 1990.
4. J. C. Vickerman and I. Gilmore, *Surface Analysis: The Principal Techniques*, 2nd edn., Wiley, Chichester, 2009.
5. J. Goldstein, D. E. Newbury, D. C. Joy, C. E. Lyman, P. Echlin, E. Lifshin, L. Sawyer and J. R. Michael, *Scanning Electron Microscopy and X-ray Microanalysis*, Plenum, New York, 2003.
6. J. I. Kikuchi and K. Yasuhara, in *Transmission Electron Microscopy (TEM) in Supramolecular Chemistry: From Molecules to Nanomaterials*, Wiley, Chichester, 2012, pp. 633-645.